Thermomechanical modeling of photovoltaic module manufacturing processes

Ichrak Rahmoun

PSL UNIVERSITÉ PARIS

THÈSE DE DOCTORAT
DE L'UNIVERSITÉ PSL

Préparée à MINES Paris-PSL

Modélisation numérique des procédés de fabrication des modules photovoltaiques

Thermomechanical modeling of photovoltaic module manufacturing processes

Soutenue par
Ichrak RAHMOUN
Le 19 Mai 2022

École doctorale n°364
Sciences Fondamentales et Appliquées

Spécialité
Mécanique Numérique et Matériaux

Composition du jury :

Fabrice Schmidt Professeur, IMT Mines Albi, France	Président
Cyrille Sollogoub Professeur des universités, CNAM, France	Rapporteur
Veronica Bermudez Directeur de recherche, QEERI institute, Qatar	Rapporteur
Corinne Alonso Professeur des universités, LAAS-CNRS, France	Examinatrice
Aude Derrier Chef du service SMSP, CEA-Liten, France	Examinatrice
Pierre-Olivier Bouchard Professeur, CEMEF MINES ParisTech, France	Co-Directeur de thèse
Jean-Luc Bouvard Professeur, CEMEF MINES ParisTech, France	Directeur de thèse

MINES PARIS | PSL

Dedication

إلى أمي و أبي الغاليين،
سبب ما حققته حتى اليوم

إلى زوجي الغالي سفيان،
لكل ما قدمته لي من تشجيع ودعم وحب

إلى أخواتي الحبيبات،
لحبكن و تشجيعكن

إلى إبن أختي زين،
مصدر سعادتنا العائلية الجديد

À mes chers parents, Fatima et Hassan,
pour leur amour, leur éducation, leurs sacrifices.
Je vous dois une éternelle reconnaissance.

À mon cher mari Soufian,
pour ton encouragement, ton soutien et ton amour

À mes chères sœurs, Ihsane et Chaymaa
pour tout votre amour et votre encouragement

À mon neveu Zain,
qui as apporté beaucoup de bonheur à notre famille

“ The future belongs to those who believe in the beauty of their dreams “

Eleanor Roosevelt

«««المستقبل ملك لأولئك الذين يؤمنون بجمال أحلامهم»»»

إليانور روزفلت

Acknowledgements

Cette thèse a été fiancée par le Commissariat à l'Energie Atomique et aux Energies Alternatives (CEA) - LITEN au sein du Département des Technologies Solaires (DTS) en partenariat académique avec le Centre d'Elaboration et de Mise En Forme des matériaux (CEMEF) de Mines ParisTech.

D'abord, je souhaite remercier Anis Jouini de m'avoir donné l'opportunité de réaliser ma thèse au CEA-Liten du Bourget-du-Lac au sein du Service des Modules et Systèmes PV (SMSP). J'ajoute à mes remerciements, Yannick Veschetti chef de l'ancien Service des Modules Photovoltaïques (SMPV) et Fabien Chabuel chef de Laboratoire des applications modules (LAM).

J'adresse également ma sincère gratitude à Mme. Veronica Bermudez et à Mr. Cyrille Sollogoub pour m'avoir fait l'honneur d'être rapporteur de ce travail et également à Mme. Corinne Alonso et Mr. Fabrice Schmidt d'avoir bien voulu participer au jury de thèse en tant qu'examinateurs.

Ma plus grande reconnaissance est dédiée à mes directeurs de thèse Jean-Luc Bouvard et Pierre-Olivier Bouchard. Je salue la qualité de leur encadrement et leurs disponibilités pour répondre à toutes mes questions tout au long de ces années. Les échanges que nous avons eus ont été toujours fructueux, source d'inspiration et de motivation et j'en garde d'excellents souvenirs. Merci pour votre soutien, votre encouragement, votre patience et vos conseils menant toujours aux meilleures solutions. Merci à la confiance que vous m'avez témoignée pendant ces années de thèse. Je vous remercie de bon cœur pour toutes vos qualités humaines.

Je tiens également à remercier mon encadrante Aude Derrier pour m'avoir accueillie au sein du laboratoire LMPV et diriger ma thèse. Je la remercie aussi pour le temps qu'elle m'a consacré pour répondre à mes questions, ainsi que ses conseils, et ses encouragements tout au long de ma thèse.

Je souhaite adresser mes remerciements à Christophe, Gilbert, Guillaume, Gaby, Romain, Arnaud, et à tous les permanents du CEMEF qui m'ont aidé à réaliser les expériences, à les comprendre, à exploiter les résultats et à répondre à toutes mes questions. Et surtout merci pour les premiers secours quand je m'étais coincée entre les mors !

Merci également à mes collègues des laboratoires LMPV et LAM qui m'ont bien accueilli durant les deux ans au CEA. Je remercie chaleureusement et particulièrement Bertrand et Eeva qui ont été un grand support technique de cette thèse et qui ont participé à la réussite de ce projet. Enfin, je tiens à remercier grandement mes collègues : Jean-Baptiste, Marion V., Timéa, Marion S., Nicolas E., Corentin, Rolland, Vincent, et Rémi.

Cette expérience fut riche professionnellement ainsi qu'humainement. Merci à mes co-bureau Mehdi, Yacine et Clément du fameux « bureau des légendes » au CEMEF et à mes co-bureau du « bureau des thésards » au CEA : Anders, Tatiana, Nicolas, Victor, Jean-Baptiste pour la meilleure

ambiance. Merci à toi, Mohamed « the go-to person » pour toute l'énergie positive et la motivation pour tenir le coup. Merci Carla, « la meilleure Toulousaine » pour tous les moments agréables partagés ensemble.

Mes reconnaissances vont également à mes meilleures amies Latifa et Yousra qui m'ont toujours soutenue et donné une incroyable motivation en toutes circonstances. Merci à vous pour tous les souvenirs mémorables.

Enfin, ma reconnaissance et mes remerciements les plus vifs vont à ma famille qui a enrichi mon chemin avec espoir, lumière et amour. Merci à ma chère mère Fatima Ouled Addi, pour sa tendresse inépuisable, son amour en or, et ses sacrifices infinis qui ont fait de moi ce que je suis aujourd'hui. Merci au meilleur papa du monde Hassan Rahmoun, pour tout ce qu'il a fait et continue à faire chaque jour pour moi. Un grand merci à mes formidables sœurs Ihsane et Chaymaa qui n'ont pas cessé un jour à me soutenir pendant tous les moments difficiles, merci pour leur tendresse et leur main tendue. Merci à mon mari Soufian Rassili, qui a partagé avec moi tous les moments de bonheur et d'épreuve, merci de m'avoir encouragé quand je baisse les bras, merci pour ton écoute et merci d'être toujours fier de moi. Merci à ma belle-famille Rassili pour leur soutien et encouragement. Merci infiniment à ma chère Abir Mzibra et à ma chère tante Rachida Ghorba pour votre soutien et votre amour inconditionnel. C'est à vous tous que je dédie ce travail, qui est le fruit de votre amour, vos encouragements et vos sacrifices.

Contents

Glossary

1D one-dimension 131

2D two-dimension 131

3D three-dimensional 135

AL-BSF Aluminium Back-Surface Field 17, 123

BB BusBars 10, 12

BIPV Building Integrated PhotoVoltaic 9

CP double-sided cooling press 20, 143, 144

CRS Continuous Relaxation Spectrum 65

CTE Coefficient of Thermal Expansion 29, 80

CTM Cell-To-Module 16

DIC Digital Image Correlation 67, 70, 80

DMA Dynamic Mechanical Analysis 54, 56, 58–60

DRS Discrete Relaxation Spectrum 65

DSC Differential Scanning Calorimetry 20, 54, 83

ECA Electrically Conductive Adhesive 2, 16, 17, 60, 80

EL Electroluminescence 22

EVA Ethylene-Vinyl Acetate 12, 59, 61, 65

FE Finite Element 30, 44, 54, 64, 72, 74, 89, 143

GBS Glass-Backsheet 9, 12, 14

GG Glass-Glass 2, 12, 14

HIT Silicon heterostructures 10

HP1 vacuum/membrane press 18, 143, 144

HP2 double-sided heating press 19, 143, 144

ICAs Isotropically Conductive Adhesives 17

IEA International Energy Agency 21

IRIS Interactive Rheology Information Systems 65

ITRPV International Technology Roadmap for Photovoltaic 10, 12, 15, 47

MBB Multi-Busbar 16

MD Machine Direction 57, 58, 61

PET Polyethylene Terephthalate 14, 56, 57, 62

POE Elastomeric Polyolefin 12

PP Polypropylene 14, 15, 58, 60, 61, 65, 80, 139, 140

PV photovoltaic 1, 56, 64, 130, 131

PVB Poly Vinyl Butyral 12

PVF Polyvinyl Fluoride 14, 56, 57

SHJ Heterojunction 2, 10, 12, 54, 70, 75, 77, 80, 106, 140

SL Short Lamination 2, 19, 139, 141

TC Thermal Cycling 15, 24

TCO Transparent Conducting Oxide 10

TD Transverse Direction 57, 58

TIO Tin-doped Indium Oxide 10

TPO Thermoplastic Polyolefin 12, 59, 61, 65, 140

TPT Tedlar (PVF) / PET / Tedlar (PVF) 15, 56, 57, 61–63, 65, 80

TTE Time-Temperature Equivalence 61

TTS Time-Temperature Superposition 61–63

UV Ultraviolet 13

VIPV Vehicle Integrated PhotoVoltaics 9

VM von Mises 92

VOCs volatile organic components 18, 106

WLF William Landel Ferry I, 62, 63

List of Figures

List of Tables

General introduction

Cette thèse est financée dans le cadre des programmes INES.2S. Institut de la transition énergétique (ITE), porté par le CEA à l'INES, il a pour mission de développer en France une filière industrielle d'intégration de l'énergie solaire photovoltaïque, en appui de la loi de Programmation Pluriannuelle de l'Énergie. L'ITE INES.2S est cofinancé par le gouvernement français dans le cadre du Programme d'Investissements d'Avenir (ANR-10-IEED-0014-01).

Elle s'est déroulée en partenariat académique avec le Centre d'Elaboration et de Mise En Forme des matériaux (CEMEF) de Mines ParisTech.

Motivation

Growth and expansion of solar energy

In the current crisis of climate change and the urgent need to reduce CO_2 emissions, the supply of energy must be ensured as much as possible by green energy. Only 25% of the growth in energy consumption between 2009 and 2019 is provided by renewable energy [1]. Solar photovoltaic (PV) energy has become one of the most competitive sources for electricity generation. In 2020, solar PV achieved a new record-breaking of new capacity installations with an increase of 139 GW reaching a global capacity of 760 GW against 39 GW of capacity in 2010 as shown in Figure 1 [1]. Today, solar PV has achieved an installation capacity of 1 TW globally [2] and is expected to reach 63.4 TWp in the horizon of 2050 providing 69% of the global primary demand (including power and heat, transport, and desalination) [3].

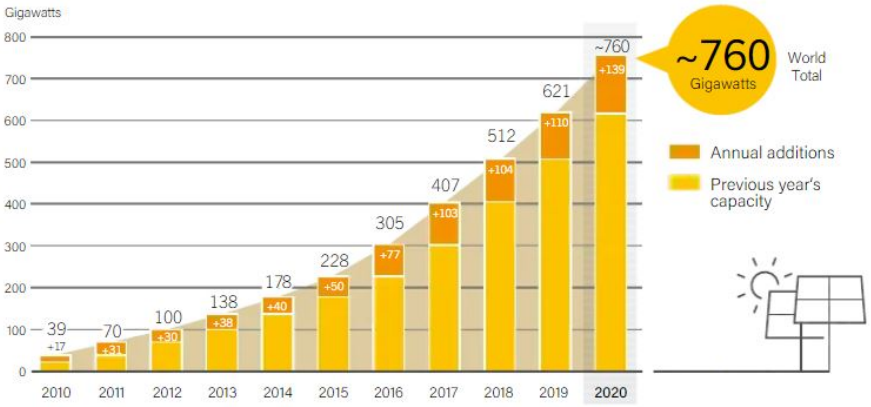

Figure 1: Solar PV Global Capacity and Annual Additions, 2010-2020 [1]

This increase in solar energy capacity is primarily driven by the reduction in PV module costs - which have been reduced by 93% since 2010 - making solar energy one of the cheapest renewable energies available nowadays in the world ahead of fossil fuels [4]. This reduction in PV module cost is ensured through optimized manufacturing processes, reduced labor costs, and improved PV module efficiency.

Aiming to meet the challenges of increasing installation capacity and competitiveness of solar energy, a combination of reduced manufacturing cost and increased performance of PV modules will aid in reducing the cost of PV systems.

This work focuses on the first challenge, through the modeling and optimization of the manufacturing process.

Technological and scientific challenges of PV module manufacturing

From cell to string: interconnection process

The solar cell is considered as the key component towards improving the performance of the PV module. The efficiency of the PV module is related to the efficiency of the solar cell. The p-type mono-si cells - currently dominant in the solar market - achieve efficiencies up to 20%. While n-type cells such as Heterojunction (SHJ) currently provide the highest efficiency of 21% and will increase to 23% within 10 years. The high efficiency of SHJ cells is related to their highest bifaciality factor among all bifacial cell technologies. Thanks to these properties, the SHJ technology will reach a market share of 18% in 2031 [5].

The SHJ cell technology has a particular sensitivity to temperature. The classical soldering interconnection process is not suitable for this technology [6]. These technological challenges have led to a migration to a low temperature interconnection technology, namely bonding by Electrically Conductive Adhesive (ECA). This assembly technique has shared the interconnection market by 6% in 2021 with an expected growth of up to 25% share in the next 20 years [5].

From string to PV module: lamination process

SHJ cell technology is promising for increasing the efficiency of PV modules. However, to take full advantage of its bifacial effect, the development of bifacial modules is essential. Currently, mono-facial modules (i.e. with white backsheet) are dominant in the market with 70% of the market share. By 2031, bifacial modules will dominate the market with approximately 55% share. Glass as a back side will take a large share of this market with 45% share [5]. This sharp growth of the bi-glass module structure requires an adaptation of the PV module manufacturing process, mainly lamination.

Bürkle, a laminator manufacturer, has developed a multi-configuration lamination process, also called Short Lamination (SL), which reduces the processing time by 50% [7]. The advantage of this lamination technique is the additional step especially for Glass-Glass (GG) modules to avoid the defects observed in this type of modules manufactured with conventional lamination. Moreover, the reduction of the manufacturing time provided by this technique meets the requirements of the PV market which expects an increase of the manufacturing process throughput by 125% for

GG modules only [5]. However, this lamination technique has been developed recently and still lacks maturity.

The PV market is experiencing a sharp growth every year, these technologies are alternatives for now but in the future, they will become mainstream. It is, therefore, crucial to anticipate in the understanding of their behavior and the adaptation of manufacturing processes to meet the market expectations. Therefore, there is an urgent requirement to optimize the manufacturing processes and make them more reliable and robust.

From thermomechanical modeling to the reliability of PV modules

Classically, the reliability of the PV module and the validation of new technologies are investigated using experimental accelerated qualification tests according to the IEC 61215 standard [8]. These qualification methods have allowed to achieve a PV module lifetime of 25 years. The performance warranty of PV modules is intended to increase to 30 years from 2021 onwards [5]. However, these experimental tools are not sufficient to study the thermomechanical behavior of PV modules with regard to the technological challenges of the manufacturing process. Therefore, numerical tools are needed to achieve the goal of improving the mechanical reliability of PV modules.

In the field of microelectronic packaging, modeling has been widely used to improve their mechanical reliability [9–11]. Great similarities are encountered between the field of microelectronic packaging and PV module packaging regarding materials (silicon, polymers, metals) and the mechanical reliability requirements. Experimental and numerical characterization of the thermomechanical behavior of PV modules must be an integral step in the development of new technologies.

Numerical modeling is a tool that allows to study thermomechanical problems consuming less time and less material resources. It also allows to study the coupling of complex phenomena such as those present in the case of PV module (coupling of thermomechanical loading, different components behavior laws, bending of thin structure). Most importantly, thermomechanical modeling allows access to local variables such as the stresses that are at the origin of crack initiation.

Nevertheless, the complexity of the PV module structure is a major scientific challenge in the development of numerical tools to study their thermomechanical behavior. The geometrical aspect of the PV module and the dimensional difference between the components of the PV module is one of the major difficulties in the development of numerical models. Furthermore, the large variation in thermomechanical behavior between the PV module components requires the use of complex laws to ensure good accuracy of the numerical calculations. Nevertheless, the great weakness of material behavior laws database of PV module components leads researchers to use simplified behavioral laws [12], which might influence the accuracy of numerical calculations. Therefore, the enrichment of the material behavior database is another scientific challenge addressed in this thesis.

Therefore, enhancing and optimizing the manufacturing process, using advanced experimental characterization and numerical tools, will lead to better reliability of PV modules and

thus reduce their cost.

Objectives and outline

This thesis work aims at understanding the thermomechanical behavior of PV modules during the manufacturing process - interconnection and lamination - in order to identify the process parameters that influence their mechanical reliability. The ambition of this work is to be able to establish recommendations on process parameters of PV modules manufacturing - interconnection and lamination - as well as suggesting process parameters adjustments to limit the potential damage of the solar cell during the manufacturing process. This main goal is ensured by the development of advanced numerical models that allow an accurate and efficient study of the evolution of thermomechanical stresses during the PV module manufacturing process. The implementation of these models with reliable input parameters is ensured by experimental characterizations of the PV module component's behavior. PV modules were fabricated with controllable lamination parameters using CEA-LITEN equipment in order to study their post-process residual deflection with respect to manufacturing parameters and to verify the correlation with the numerical models. The manuscript is structured in six main chapters:

- Chapter 1 provides a state of the art overview of the manufacturing process of PV modules and their damage mechanisms. The structure of the PV module is presented by defining the characteristics and features required for each component of the PV module. The two manufacturing processes of the PV module - interconnection and lamination - and their different techniques are described. The damage mechanisms related to the process are also detailed.

- Chapter 2 gives a literature review dedicated to thermomechanical modeling of PV module manufacturing processes. Thermomechanical simulation available in the literature and modeling the PV module manufacturing processes reported are discussed. The process parameters influencing the residual stresses within the PV module after processing are analyzed. This literature review allowed us to highlight some of the strong hypothesis adopted in the numerical models so far and to define the strategy of this Ph.D work.

- In chapter 3, the thermomechanical behavior of some components of the PV module - naming encapsulants, backsheets, ECAs, copper ribbon, and SHJ solar cell- has been studied. DMA and tensile measurements have been performed to identify the parameters of the constitutive behavior used to model the thermomechanical behavior of the studied components. Then samples of SHJ solar cells were subjected to a 4-point bending loading in order to compare their elastic behavior and fracture strength with silicon literature data. The characterization of thermal properties of the different components were are also presented in this chapter.

- Chapter 4 aims at modeling the evolution of the thermomechanical stresses induced during the interconnection process. A 2D sub-model has been developed for this reason. The influ-

ence of some process parameters such as the temperature and the curing time of ECA, type of ECA, and ECA pad design on the induced stress level has been analyzed.

- Chapter 5 is devoted to sub-modeling the evolution of the thermomechanical stresses induced during the lamination process. A 2D sub-model allowed to study the impact of different type of components behavior laws on the accuracy of the calculations. With the same 2D approach, the influence of some architecture parameters, for instance the cell size, the number of busbars, and the type of the back face on the induced stresses was identified. Another 3D sub-model was introduced to study the stress edge effect and the out-of-plane stresses. A thermomechanical stress analysis during lamination with respect to the ECA interconnect technique was performed.

- In chapter 6, a method for measuring the overall deflection of the PV module was developed. With this method the deflection of PV modules manufactured by varying parameters of lamination process (temperature, architecture, and cooling type) was measured. A 3D model was subsequently used to validate the experimental measurements.

- We finally draw general conclusions of this thesis and open the discussion to useful prospects for future work.

Chapter 1

Manufacturing process of photovoltaic modules, and their damage mechanisms: a literature review

Contents

Résumé du chapitre

Ce chapitre présente une revue bibliographique sur les procédés de fabrication des modules PV et leurs mécanismes d'endommagement. Le module PV est un stratifié de plusieurs couches de natures différentes assemblé en deux étapes successives à l'aide de deux procédés de fabrication : l'interconnexion et la lamination. Les cellules solaires sont le noyau du module PV. Elles sont connectées en série afin de générer un courant suffisant pour le fonctionnement du module PV. Cette étape d'assemblage de plusieurs cellules pour former un « string », est réalisée durant le procédé d'interconnexion. Puis un groupe de string est encapsulé entre des couches protectrices par l'intermédiaire du procédé de lamination.

Dans un premier temps, la structure du module PV est présentée, en définissant le rôle et les caractéristiques exigées pour chaque couche du module PV. Puis un aperçu sur le comportement thermomécanique de chaque composant est discuté. La majorité des composants du module PV, notamment l'encapsulant, la face arrière en polymère et les colles conductrices montrent un comportement viscoélastique dans la gamme de température des procédés de fabrication. Tandis que le ruban du cuivre, qui joue le rôle de l'interconnecteur, a lui un comportement élastoplastique. Le verre et la cellule solaire ont un comportement élastique linéaire isotrope et orthotrope, respectivement.

Dans un second temps, les procédés de fabrication des modules PV sont introduits. Le premier procédé de fabrication est l'interconnexion. La technique d'interconnexion la plus courante est le soudage, également appelé « stringing ». Il existe plusieurs variantes de l'interconnexion en fonction du métal d'apport et de la méthode utilisée pour souder. La technique d'interconnexion par soudage n'est pas recommandée pour plusieurs technologies de cellule solaire notamment l'hétérojonction. Ce type de cellule est sensible au soudage à haute température. En conséquence, d'autres techniques d'interconnexion tel que le soudage à basse température ou le collage par des colles électriquement conductrices sont en pleine croissance. Ces deux techniques sont discutées plus en détails dans ce chapitre.

Le deuxième procédé d'assemblage du module PV est la lamination. Lors de ce procédé, un chargement thermomécanique est appliqué pour ramollir l'encapsulant par chauffage et en appliquant simultanément une pression afin d'assurer une adhésion entre les couches du module PV. Ce chargement peut être appliqué en une seule étape ou en plusieurs étapes selon la technique choisie et l'architecture du module PV. Récemment, un procédé de lamination court a été développé qui permet de réduire le temps de fabrication de 50% en réduisant le temps de chauffe et en utilisant un refroidissement rapide contrôlé.

Dans un dernier temps, les mécanismes d'endommagement observés après fabrication ou à stade précoce après installation des modules PV et documentés dans la littérature sont présentés. Les deux mécanismes rapportés sont la microfissuration des cellules solaires et la délamination. Ces deux mécanismes d'endommagement n'engendrent pas un dysfonctionnement total du module PV, mais ils nuisent à son rendement et sa fiabilité. Enfin, les paramètres procédés qui participent à la création de ces endommagements sont discutés.

The PV module is a laminate of several layers of different nature assembled in two successive steps using two manufacturing processes. In this chapter, the structure of the PV module will be defined by identifying the role of each layer/component and its characteristics. Then, the manufacturing processes of the PV module will be presented. Finally, the damage mechanisms related to the manufacturing process and the choice of materials will be discussed.

1.1 Literature review of photovoltaic modules

1.1.1 Structure of PV modules

The silicon solar cells (c-Si) are the core of the PV module. Each solar cell reproduces, under direct sunlight, approximately 0.6V [13] depending on its type and technology. In order to generate sufficient voltage in the PV module, solar cells of the same characteristics are interconnected in series to form a so-called « string ». This step is made through the **interconnection process**, which consists in connecting the front side of a solar cell to the backside of the adjacent solar cell, often by means of a copper ribbon cover with solder material. In a PV module, there are two types of ribbons: a) the « inter-cell » ribbon, which is used to interconnect the cells; b) the « inter-string » ribbon, whose role is to collect the electrical energy transferred by each string and transport it to the electrical output of the PV module according to the chosen electrical configuration.

Once the solar cell matrix is assembled, it is encapsulated between protective layers on the front and backside through the **lamination process**. The classic architecture is a glass front sheet and a white or transparent multi-layer polymer backsheet as presented in Figure 1.1. For bifacial cell technologies, a transparent back side is required. Modules with a glass back side are widely used for this type of technology. Other architectures with a composite or polymer front sheet are also available in some PV applications as Building Integrated PhotoVoltaic (BIPV) [14–16] or Vehicle Integrated PhotoVoltaics (VIPV) [17]. The focus in this work will be on PV modules with **Glass-Glass(GG)** and **Glass-Backsheet (GBS)** architectures.

After the assembly of the PV module, a junction box is attached to the backside of the PV module to interconnect the strings to generate an electrical circuit. Often the most common electrical configuration for this connection is bypass diodes [13]. For some architectures, an aluminum frame is added to protect the edges of the PV module.

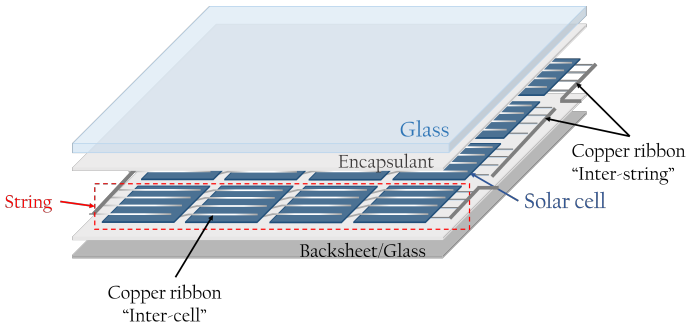

Figure 1.1: Standard architecture of a 4 × 4 cell PV module.

This protection is designed to preserve the PV module from the harsh environmental condi-

tions in which it will operate, including high temperatures, humidity or rain, UV exposure, and wind and snow loads. In addition, this packaging must also ensure safe operation and high reliability and performance over time [13].

1.1.1.1 Crystalline silicon solar cells

The market of solar cells experiences a large variability in the type of crystalline solar cell: Single crystal (concentrator), Single crystal (non-concentrator), Multicrystalline, Silicon heterostructures (HIT), and Thin-film crystal [18]. Crystalline silicon solar cells are currently dominating the PV market with a 95% share [5]. In this study, the focus will be on the **heterojunction solar cell** (SHJ) technology.

The core of the SHJ solar cell structure is a doped crystalline c-Si wafer with a thickness varying between 150 μm and 180 μm [19]. After an etching performed on both surfaces of the wafer to create a pyramid-like texturing and to decrease the reflectivity, an intrinsic hydrogenated amorphous silicon passivation layers of a few nanometers are deposited (see Figure 1.2a). Then thin layers of boron-doped P-type which play the role of emitter and a layer of phosphorus-doped N-type hydrogenated amorphous silicon as an electron contact are deposited on the front face and the back face of the bulk respectively. Then an anti-reflection layer of Transparent Conducting Oxide (TCO), usually Tin-doped Indium Oxide (TIO), is added. Finally, a metallization of the cell is added to create the electrodes that will collect the charged carriers [20; 21]. The metallization layer is in the form of a grid, also called "H-pattern metallization", composed of fingers and BusBars (BB). The busbars are printed perpendicularly to the fingers and are of a greater thickness in order to allow the transmission of the electric charges collected by the fingers (see Figure 1.2b). There are several techniques of metallization [22], according to the International Technology Roadmap for Photovoltaic (ITRPV) 2020 the most widely used technique is the screen printing [5].

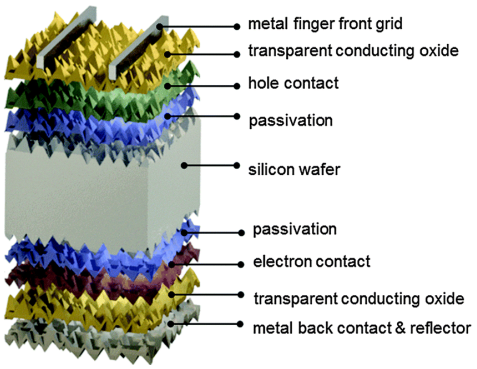

(a) stacking of SHJ cell layers [20]

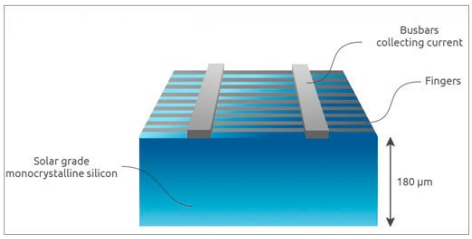

(b) Metallization of crystalline solar cell [23]

Figure 1.2: Structure of a standard HJT cell

The advantage of SHJ cells is that all manufacturing steps are performed at low temperatures below 250°C, which reduces the risk of substrate degradation [21], besides its bifaciality properties. From a mechanical point of view, the thickness of these added layers are negligible compared to the thickness of the silicon wafer, and therefore the mechanical behavior of the cell is often considered identical to the wafer [24].

The photovoltaic industry is continuously moving towards thinner wafers with a large surface area [25], which leads to an increase in the breakage rate in the production processes [26]. Indeed, silicon breakage leads to material and economic losses during the entire production chain of solar cells, from wafer cutting to module assembly [27]. Hence the importance of studying the mechanical properties, and in particular the resistance of these materials to the stresses experienced during the PV module manufacturing cycle.

Mono-crystalline silicon exhibits an orthotropic elastic behavior due to the combination of cubic symmetry and the equivalence of shear conditions [28]. This simplifies the representation of its stiffness matrix into 3 independent terms C_{11}, C_{12}, and C_{44}. Thus, according to Hooke's law, its orthotropic elastic law can be presented as follows:

$$\sigma_{ij} = C_{ijkl}\varepsilon_{kl} \Longrightarrow \begin{bmatrix} \sigma_1 \\ \sigma_2 \\ \sigma_3 \\ \sigma_4 \\ \sigma_5 \\ \sigma_6 \end{bmatrix} = \begin{bmatrix} C_{11} & C_{12} & C_{12} & 0 & 0 & 0 \\ C_{12} & C_{11} & C_{12} & 0 & 0 & 0 \\ C_{12} & C_{12} & C_{11} & 0 & 0 & 0 \\ 0 & 0 & 0 & C_{44} & 0 & 0 \\ 0 & 0 & 0 & 0 & C_{44} & 0 \\ 0 & 0 & 0 & 0 & 0 & C_{44} \end{bmatrix} \begin{bmatrix} \varepsilon_1 \\ \varepsilon_2 \\ \varepsilon_3 \\ \varepsilon_4 \\ \varepsilon_5 \\ \varepsilon_6 \end{bmatrix} \tag{1.1}$$

The experimental values of the elastic constants of silicon oriented in the < 100 > direction of the stiffness matrix are given in Table 1.1.

C_{11}	C_{12}	C_{44}	$E_{<100>}$	$G_{<100>}$	$\nu_{<100>}$
		(GPa)			(-)
165.6	63.9	79.5	130	79.6	0.28

Table 1.1: Elastic properties of mono-crystalline silicon [28; 29]

Silicon has a linear orthotropic elastic behavior up to a brittle failure [24]. Thus, the fracture strength of the wafer will be mainly governed by the surface defects (microcracks, saw damage etc.) [27]. All these material quality and sawing process aspects and their association with silicon wafer failure are well documented in the thesis of Carton [30].

In the PV module industry, the behavior of silicon wafers is often characterized by bending tests (3 or 4 points) [24; 26; 30]. There are other types of tests, such as the twist test or bi-axial tests like "ring-on-ring" or "ball-on-ring" [26; 27; 30].

1.1.1.2 Copper ribbons

The copper ribbons are the collectors of the photovoltaic energy generated by the solar cells. Copper is an excellent electrical conductor with an electrical conductivity of $6.0 \times 10^7 (\Omega.m)^{-1}$ at ambient temperature, the highest in the metals after silver [31]. The copper ribbons used in the photovoltaic field have a rectangular shape and are often coated with a solder layer of approximately $20\ \mu m$. This coating is a tin-based alloy (Sn) approximately $60-97\%$ metal additions such as silver (Ag), lead (Pb), bismuth (Bi) or copper (Cu). Lead coated ribbons are more likely to extinction

because of its toxicity. In addition, the melting point of lead is too high (327°C [32]) which is not suitable for welding on SHJ solar cells since it shows temperature sensitivity. Another alternative is bismuth which has a lower melting point between 120°C and 160°C [6].

Along with the chemical composition of the ribbon, the cross-section is also an important factor. The section of the standard coated "inter-cell" ribbons can vary according to the number of busbars of the solar cell. For 4BB cells, ribbons of 1.1 to 1.2 mm wide can be selected. For a higher number of busbars, 5BB, a width of 0.9 to 1 mm is the most suitable. The thickness is also variable between 0.2 and 0.22 mm [33]. For the inter-string ribbons, they have larger section (for instance 5×0.3 mm^2).

Other than its excellent electrical properties, copper ribbon displays isotropic elastoplastic behavior in the range of its use in PV applications. It is also a fairly ductile material. Good fatigue properties are also required in the case of copper in order to withstand the fatigue it undergoes during the installation of the PV module. The fatigue of the copper ribbons and the solder joint during operation are well documented in the literature [34–37].

1.1.1.3 Encapsulant

The encapsulant is an adhesive polymer foil between the different layers of the PV module. Its role as a solar cells protector is to provide sufficient adhesion with all components of the PV module, high optical transmission, electrical insulation, and protection against humidity.

Two families of encapsulant are available in the PV market:

- Crosslinkable encapsulants: especially Ethylene-Vinyl Acetate (EVA) and the Elastomeric Polyolefin (POE). Silicone is also used for the encapsulation of PV module operating in very harsh environmental conditions such as space [38].

- Non-crosslinkable encapsulants: several types are distinguished, including Thermoplastic Polyolefin (TPO), Poly Vinyl Butyral (PVB), and Ionomers. Their non-crosslinkable nature has the advantage of facilitating the recyclability of PV modules at the end of their life.

EVA is the most mature material in the history of PV module encapsulation and dominates the PV market with 90% share [33]. Unlike polyolefins, which are a new type of encapsulant widely used in the last years with a market share of 7% in 2018 [33]. According to ITRPV, their market share may increase up to 25% by 2029 [5]. Polyolefins are more suitable for GG architecture due to the absence of acid formation during lamination, unlike EVA. The formation of acid in EVA during lamination is an ongoing phenomenon. However, the permeability of the backsheet in the case of GBS architecture enables the acid to escape [39; 40].

For the most advanced module technology, more attention has been paid to the white EVA. This particular encapsulant is used as a bottom encapsulant to increase the light reflection in the inter-cell gaps thereby increasing the module power by 5W. Its market share has increased sharply by 15% in 2019 [41].

Besides all these optical and chemical characteristics, the encapsulant has to meet mechanical requirements as a binder for the different layers of the PV module. The two most sought mechan-

ical properties in an encapsulant are adequate viscosity at high temperature to permeate through the cell matrix and avoid cavities, as well as high adhesion with all PV module components. And most importantly, adequate rigidity to accommodate the internal stresses imposed on the cells by the glass due to the difference in CTE [42]. The thermal conductivity of the encapsulants is also an important parameter. The better the encapsulant conducts heat, the lower the operating temperature will be, improving the electric yield [43].

The encapsulants have viscoelastical properties in the temperature range of the PV module manufacturing [12; 24; 44; 45], and melt at a lower temperature than the lamination process temperature. The thermomechanical behavior of several encapsulant will be studied in the next chapter.

1.1.1.4 Glass

Beyond the protection of internal components of PV module, the front side material has several specific functions. It must ensure good optical transmission, appropriate refraction depending on the properties of the encapsulant, good electrical insulation and good Ultraviolet (UV) stability. It is the first line of defense against any mechanical impact such as hail. This requires a material with high impact resistance and sufficient tensile strength.

There are several types of glass depending on the constituent added with the silica such as sodium carbonate boron or lead. The glass used in the field of PV is a float glass that is shaped in a tin bath to ensure a flat surface and no air inclusion. Glass for PV applications undergoes an additional tempering step to increase its rigidity and improve its resistance to impact and fracture [24]. It often contains low iron particles to ensure better transmission of solar radiation. Other surface treatments can also be added, such as texturing to improve the adhesion with the encapsulant or the addition of an anti-reflection layer to reduce the parasitic reflections on the front of the glass.

In the manufacturing or operating temperature range of the PV module, the glass has an isotropic elastic behavior. Standard glass plates are 3 to 4 mm thick. Its thickness is more than half of a PV module, so its expansion somehow governs the expansion of the PV module. Several authors have studied the mechanical and thermal properties of various types of glass [46; 47]. All the mechanical and thermal properties used in this work for float glass are taken from the literature and presented in Table 1.2.

Young modulus E (GPa)	Poisson's ratio ν	Density ρ (kg/m^3)	CTE α ($10^{-6}1/C$)	Thermal conductivity λ(W/J/K)
73	0.24	2500	8.96	0.937

Table 1.2: Elastic properties of float glass [46; 48]

1.1.1.5 Backsheet

The backsheet acts as a protective layer for the solar cells and prevents PV modules from environmental impacts such as aggressive substances, scratches, etc. Its two main roles are electrical

insulation and protection against moisture as the interconnectors are metallic components and must be protected against corrosion. Humidity conditions vary depending on the site and the operating time. Therefore, the backsheet must be able to withstand and operate in these different conditions [39].

The rear side can be made of glass for GG architectures or of multi-layer polymer for GBS architectures. Polymer backsheets often have a thermoplastic Polyethylene Terephthalate (PET) or Polypropylene (PP) core layer. As PET has a poor UV stability, additional layers often made of fluoropolymers are used to enhance the UV resistance of the backsheet [39]. Among these fluropolymers we find Polyvinyl Fluoride (PVF) which has an excellent weathering stability after ageing tests [49; 50]. Nevertheless, the harmful ecological impact of fluropolymers is forcing manufacturers to introduce other alternatives. The different backsheet configurations available in the market are shown in Figure 1.3.

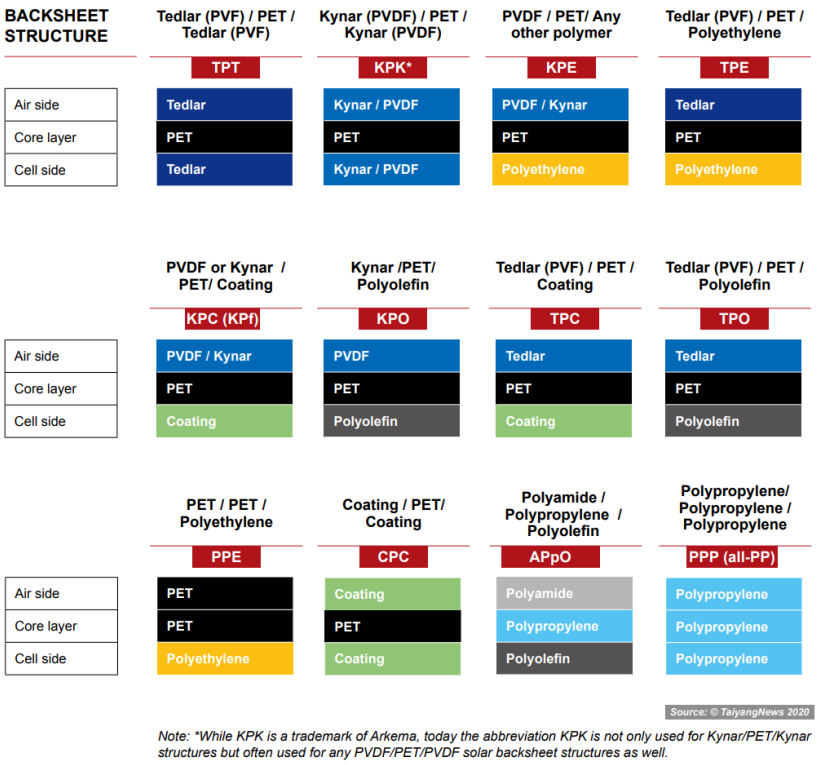

Figure 1.3: Backsheets configuration available in the current PV market [39]

The traditional process used to manufacture backsheets with a PET core layer is by laminating the glued layers together to form a multilayer polymer. With the recent development of PP based backsheets, the co-extrusion process has been adopted. As delamination represents the most critical degradation mode in backsheets [51], this one-step process eliminates the need to glue the layers together, which reduces the risk of delamination of the backsheet layers. In addition, PP provides good reflectance by increasing the power of the PV module by 1.5 – 2.5% compared to a PET-based backsheet module. It represents a good barrier against humidity while allowing the diffusion of acetic acid which inhibits corrosion in metal components. In general, its performances during aging are better than PET backsheets [52].

Given the large deployment of bifacial technology, which will reach 35% by 2030 according to

the ITRPV [53], transparent backsheets are recognized as a good alternative to opaque backsheets. The transparent backsheet offers several advantages over glass. Among these advantages, the light weight of the PV module as well as the reduced cost as the GG structure favors the use of POE which are 30% more expensive than EVA [39].

Backsheets have a viscoelastic thermomechanical behavior as well [12; 24; 48]. They also show an anisotropy of behavior related to their layered structure [12], and the nature of their process. In the experimental chapter 3, we will further detail the thermomechanical behavior of a Tedlar (PVF) / PET / Tedlar (PVF) (TPT) and PP backsheet types.

1.1.2 PV module manufacturing processes

The PV module manufacturing chain consists of several steps from extracting the raw material, particularly silicon, to the installation of the solar system (Figure 1.4). The manufacturing of crystalline silicon solar modules consists of two major and crucial steps: **interconnection** and **lamination**. Other minor steps are cell inspection, glass cleaning, framing, and junction box assembly.

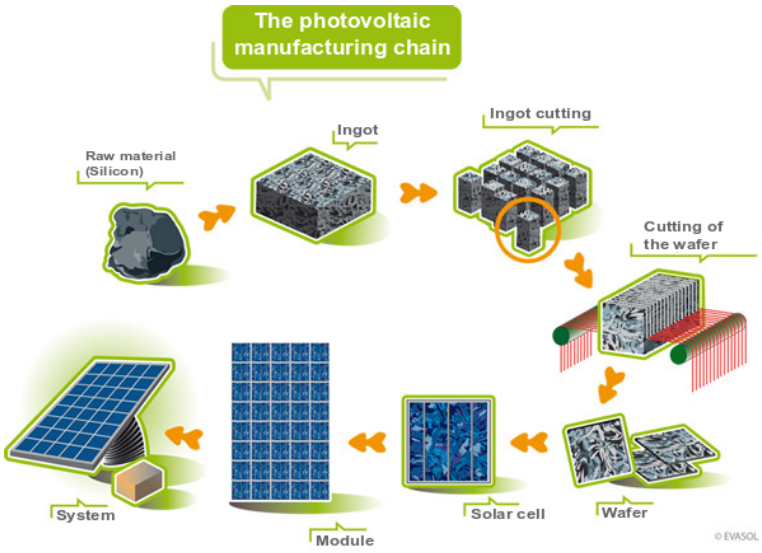

Figure 1.4: The photovoltaic manufacturing chain (Credit EVASOL [54])

After the manufacturing process, the PV module is subjected to several qualification tests according to the standard IEC 61215 [8], also called accelerated tests. One distinguishes the performance characterization tests directly after manufacturing, such as visual inspection, insulation test, maximum power measurement, performance at low irradiance...etc. Another family of tests aims at characterizing the aging mechanisms of PV modules such as Thermal Cycling (TC), UV preconditioning test, Damp-heat test, Outdoor exposure test...etc. Other tests are used to validate the mechanical resistance of the module. For instance, the mechanical loading test is used to characterize the resistance of PV modules under a mechanical load such as snow, and the hail test is performed to identify the resilience of the module against mechanical impacts like hail.

1.1.2.1 Interconnection

The principle of the interconnection process, also called "tabbing/stringing", is to link the solar cells with a conductive material in order to collect and transport the photovoltaic energy generated by each solar cell. There are several interconnection technologies and they are generally adapted to the solar cell technologies used to create PV modules. In each interconnection technology, the solar cells are interconnected in order to improve the performance of the module independently of the solar cell and also to reduce the Cell-To-Module (CTM) losses [55].

The most common interconnect technology used worldwide today is the soldering of tinned copper ribbons on the busbars on the surface of the solar cells. During the last decades, the 3BB technology was predominant on the market and has now disappeared in 2021 [56]. However, the increasing interest in 4 or 6 BB architecture allows an evolution of the interconnection mode to the so-called Multi-Busbar (MBB). MBB technologies, in addition to their power contribution on the modules, allow a better resistance of the modules to accelerated aging tests, a reduction of the quantity of silver paste and thus a reduction of the production cost [57; 58].

The most common interconnection technique is welding, also called stringing. There are several variations of tabbing depending on the filler metal and the method used to solder. The second growing technique is ECA bonding. Other techniques without busbars are used like the Shingle technology which consists in bonding the overlapped cells one to the other with the ECA [59]. A second approach for this type of interconnection is to contact neighboring cells without busbars or 0BBs by wires using a foil. The copper wires are embedded in a polymer foil or matrix and coated with a low temperature solder alloy, mainly indium (InSn) or bismuth (SnBiAg) based with a melting point below 160°C and 138°C respectively. The lamination step of the module allows two actions in one: the melting of the polymer matrix and the welding of the wires to the cell [60; 61].

In this work, the cell technology of interest is SHJ. Therefore, in the following review, we will focus on the welding at low temperatures and bonding by ECA adapted to this cell technology.

1.1.2.1.1 Soldering at low temperatures

Welding is done either by infrared radiation or by ultrasound. Indeed, most of the industrial stringing machines performs the soldering of solar cells and ribbons by localized heating by means of infrared light [62].

As mentioned in Section 1.1.1.2, SHJ solar cells are temperature sensitive, which makes the lead-based soldering process more challenging. InSn alloy could be a potential replacement for SnPb because its melting temperature is 117°C, only depending on the large percentage of indium. The cost of this alloy is however too high for PV applications [63]. SnZn alloys tend to form a substantial oxide layer during soldering, which is a priori not suitable for PV ribbon soldering [64]. Nevertheless, a controllable zinc content of 9% is suitable. Bismuth is an element that is also widely used in low temperature lead-free solder compounds. It is a heavy, brittle, non-toxic and low cost metal. When alloyed with Sn, its melting temperature is close to or below that of eutectic SnPb ($\approx$ 180°C). The quality of a SnBi alloy weld is impacted by the behavior and evolution of bismuth under aging at elevated temperatures, indeed at high temperatures bismuth forms large

grains of material, which can be a failure factor at the weld interface [65]. In spite of this, a lot of research continues to be carried out to study the different aspects of Bi-based welds because its advantages remain, to say at least, non-negligible [66].

Another type of room temperature ultrasonic aluminum (Al) ribbon welding has been studied in the case of Aluminium Back-Surface Field (AL-BSF) cells. Among the greatest advantages of this technique are that cracks due to thermomechanical stresses could be avoided. On the other hand the use of copper ribbons, which are generally more expensive than aluminum ones, could be considerably reduced. The results of the IEC61215 qualification procedure have shown promising results for this technology [67]. However, few works have been published on this type of solder. According to these two studies [67; 68], it seems that this type of soldering works well for Al-BSF cells although it could be that this soldering method has not been investigated further for the new generations of solar cells [55].

1.1.2.1.2 Bonding with Electrically Conductive Adhesives (ECA)

The second technique used to interconnect SHJ cells is ECA bonding. After the adhesive is applied to the solar cell using the screen painting technique, the ribbons are positioned and the adhesive is thermally cross-linked. The cross-linking is progressive as the solar cells pass over the stringer's heating plates. Localized pressure is applied to the ribbons with the pins to ensure good adhesion between the ribbon and the solar cell as illustrated in Figure 1.5. The cross-linking of the polymer chains leads to adhesion to the surfaces. The amount of adhesive printed currently ranges from 6 to 15 mg per busbar and is highly dependent on its composition and viscosity [6].

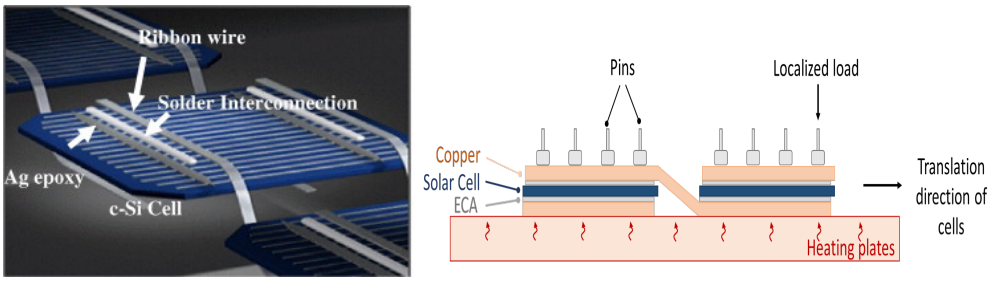

(a) (b)

Figure 1.5: (a) Solder interconnection between copper ribbon and silicon solar cell [69], and (b) schematic representation of stringer used for interconnection by ECA bonding

This technology is increasingly used to manufacture PV modules, with a market share that may reach 20% by 2031 [5]. The adhesive is usually a composite of conductive particles in an acrylate- or epoxy-based polymer matrix. The matrix provides the mechanical properties and the fillers provide the electrical properties. The matrices are polymeric and their electrical conductivity is typically of the order of $10^{-14} - 10^{-7}\Omega^{-1}.m^{-1}$ [70]. The fillers are typically silver with an electrical conductivity of the order of $6 \times 10^{7}\Omega^{-1}.m^{-1}$ [32]. Copper flakes are also rarely used. The ECAs used in the PV application all belong to the category of Isotropically Conductive Adhesives (ICAs). This category is distinguished by its microstructure, which gives it a higher electrical conductivity than the others [71]. Depending on the shape and volume fraction of the particles, the conductive

path, also called "percolating path", is created and can reach a threshold that increases the overall conductivity of the material [72].

ECAs are the main alternatives to solder. They have various advantages such as low toxicity compared to lead, low processing temperatures due to their cross-linking temperature of about 150°C, their ability to assemble materials of different natures, their good resistance to mechanical cycling, their ability to make small assemblies and finally their eventually lower environmental impact [73].

The low peel strength is often considered as a disadvantage for this type of assembly, despite its proven reliability during thermal cycling tests [74]. Generally, the peel strength is greater than 0.5 N.mm^{-1} and can sometimes reach a value greater than 1 N.mm^{-1}, which is usually sufficient for the joint to withstand thermal cycling. It has been shown that inadequate adhesive cure time can cause insufficient peel force [6].

One of the main problems of ICAs is the degradation of their electrical properties over time. Among the phenomena that can affect their electrical properties is oxidation, which explains their sensitivity to humidity [75]. Several strategies have been proposed to limit this effect and make ICAs more stable over time. For instance, the use of polymers with a high cross-linking rate that absorb less moisture [76]. The choice of substrates and particles can reduce oxidation [77]. The most common method is based on the choice of metal for the particles. Silver has a conductive oxide making it very advantageous compared to copper, aluminum or tin. Other ICAs rely on non-metallic fillers (carbon nanotubes, graphite, graphene) which are less likely to react [70].

1.1.2.2 Lamination

Once the cells are interconnected, a subsequent lamination step is necessary to protect them from the external environment during installation. Lamination is a type of thermocompression process, which consists in applying a thermal and mechanical load to join two or more materials together. In the case of lamination, it is the encapsulant that acts as a binder when heated and softened. Then by applying mechanical pressure the encapsulant adheres to all the components to form a laminate. These two loading processes can be applied in one step or in multiple steps depending on the selected process and the architecture of the PV module. Both configurations have been studied in this work. In the following review, we will discuss the differences between these two configurations.

1.1.2.2.1 Conventional lamination process

The layers of the laminate are loaded in the vacuum/membrane press (HP1). It uses a vacuum for pressure control in both the lower chamber (where the PV module is loaded), and the upper chamber. A pressure can be applied on the laminate, by imposing a higher pressure above the membrane than below.

The first phase is preheating with convection, while the PV module is lifted on pins (Figure 1.6a). At this point, zero pressure is applied, in order to avoid bubbles apparition due to volatile organic components (VOCs) released from the encapsulant and the air present between the lay-

ers. Then, the pins are pulled down in the heating plate, improving the thermal contact. Pressure is applied to the module, by injecting air above the membrane (Figure 1.6b). When the lamination temperature is reached, the encapsulant crosslinks/softens. Its formerly infusible polymeric chains form a wide-meshed network structure, ensuring the adhesion between all parts of the structure [24; 78]. The duration required for the cross-linking or softening depends on the chosen encapsulant material. The processing time is generally between 8-20 min for EVA and 10-14 min for TPO for instance. The lamination temperature is often between 140-160°C for most of the encapsulants [43]. The processing time and temperature are quite influencing parameters on the final quality of the PV module. In the case of EVA, the degree of cross-linking impacts the luminescence intensity of the PV module [78].

In a conventional lamination process, the module is cooled down in the ambient air with no pressure control.

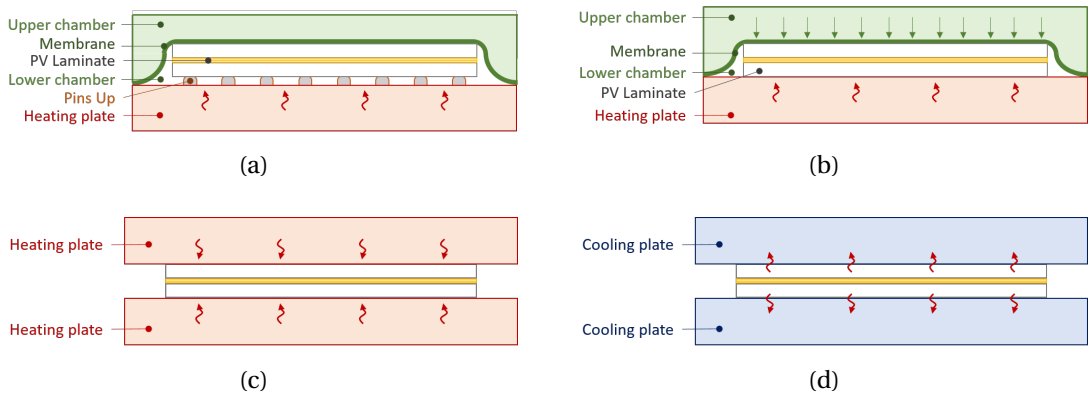

Figure 1.6: Schematic representation of the different laminator configurations: vacuum/membrane press (HP1) (a) with pins-up (b) and pins-down with applied pressure, (c) double-sided heating press (HP2) (d) and cooling press (CP) [79]

1.1.2.2.2 Short lamination process

In 2019, the production throughput of the stringing process is 20% higher than that of the lamination process [80]. This has led to the interest of the lamination process developers to increase the production capacity of the laminators. Bürkle, a laminator manufacturer, has developed a multi-configuration lamination process, also called SL, which reduces the processing time by 50% as shown in Figure 1.7.

Additionally to a vacuum/membrane press used for the classic lamination process, the SL process adds a double-sided heated flat press step, more especially for glass-glass (GG) PV modules [7].

In this type of lamination, the PV module may go in a double-sided heating press (HP2) (Figure 1.6c). This is an optional stage, developed more especially for GG PV modules, as membrane press on this architecture may involve edge pinching, with bad sealing, higher glass breakage and residual stresses [81–83] as illustrated in Figure 1.8. An advantage of this chamber design is faster symmetric heating (while in the HP1 case, the laminate is heated only from the bottom side). However, this is done at air pressure (no vacuum control). Thus it can only be used as a complement

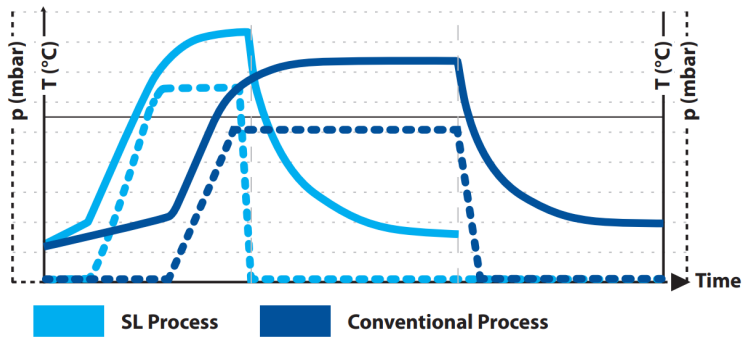

Figure 1.7: Comparison of conventional and short lamination process developed by Bürkle [7]

to the first stage. In this case, the laminate leaves HP1 before reaching the maximum lamination temperature.

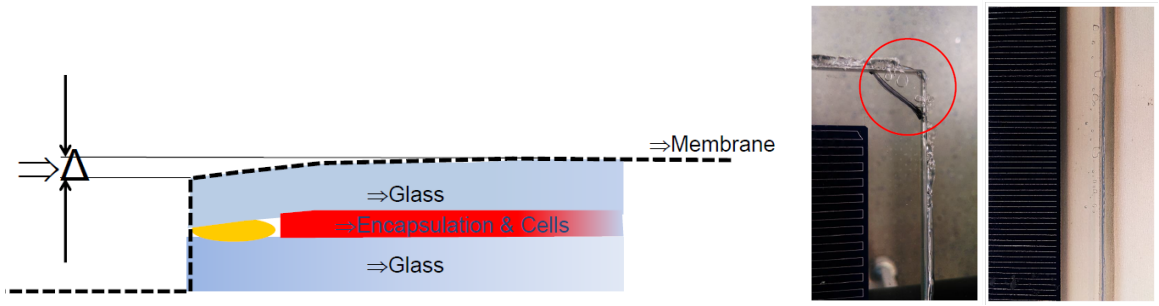

(a) (b)

Figure 1.8: (a) Schematic explanation of edge pinching [84] and (b) induced bubbles on the corner and edge after lamination [82]

Another step that characterizes this type of lamination process is the controlled cooling. During this step the module enters a double-sided cooling press (CP), which cools down the PV module to room temperature while maintaining pressure to impose flatness. Cooling with the cooling press can be up to five times faster than cooling in the open air, which is equivalent to reducing the lamination total time by 62.5%. Therefore, the production throughput of the PV modules is considerably enhanced.

Li *et al.* [85] characterized the influence of the cooling press on the encapsulation properties of PV modules. The adhesion strength between EVA and glass is improved by 10%. Their Differential Scanning Calorimetry (DSC) characterization results showed that the high cooling rate in the CP decelerates the crystalline growth and thus the cross-linked EVA has smaller crystallites.

One of our studies, focusing on the characterization of heat transfer in the PV module in the case of a short lamination, showed that the heat transfer in HP2 and CP is uniform throughout the thickness of the PV module. However, an edge effect was found in the case of the CP which could be caused by the coolant flow. The heat transfer in HP1 is overly influenced by the lamination configuration used as well as the presence of the bubbles which act as a thermal insulator since the heating in this chamber occurs from the bottom only [79].

According to ITRPV, the lamination throughput will increase by 2031 to 25% and 17% for GG and GBS architecture respectively [5]. Hence, more attention should be devoted to the optimiza-

tion of the lamination process along with improving the quality of the PV modules to avoid infant failures.

1.2 Damage mechanism of PV modules and their influence on performances

Efficiency and power are the two key parameters that characterize the performance a PV module. A PV module's efficiency represents its capacity to generate electrical energy from incident solar light per unit area [41]. In the 1980s, the average efficiency of a PV module was limited to 9%. In 2010, the efficiency of PV modules has experienced a remarkable progress, reaching 14.7%. Since then, this progress is growing and reaching 19.2% in 2019 [41]. In the last few years, several records have been achieved up to 22.7% due to the development of new solar cell technologies and the improvement of the quality of the lamination materials.

Any failure in the PV module can lead to a drop in its performance. According to International Energy Agency (IEA), there are three stages of PV module failure during its lifetime: infant-failure, midlife-failure, and wear-out-failure as presented in Figure 1.9. Among the failures related to mechanical issues that occur during the infant time of the PV module are cell interconnect breakage, cracked cell isolation, and delamination [86]. According to statistics on the failure modes of two million PV modules delivered by a German distributor between the years 2006 and 2010, 10% of failure modes were related to defect cell interconnect, and 5% were due to delamination [87].

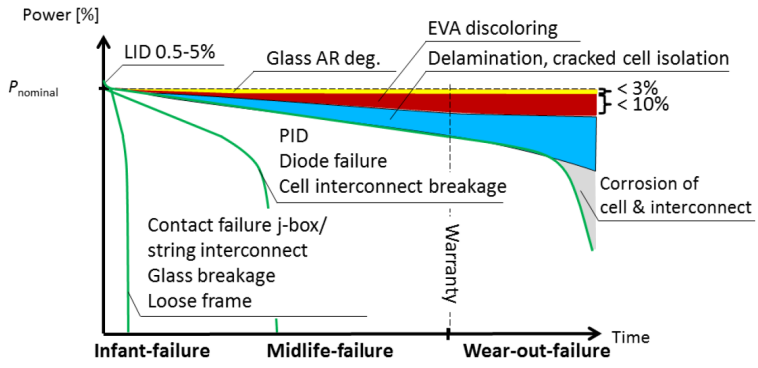

Figure 1.9: Failure scenarios of crystalline based photovoltaic module (LID: light-induced degradation; PID: potential induced degradation; j-box: junction box) [86]

Both types of failure can reach large percentages after several years of operation. Schulze *et al.* [88] collected the failures occurring in 273 PV modules from 3 different manufacturers after 15 years of operation. Delamination was representing 80% of the primary failure mode in some modules. While cell part insulation due to cell cracks was representing 30% of the primary failure mode in other PV modules.

In this section, these two most common damage mechanisms will be discussed along with their influence on PV module performance. The influence of some parameters of the interconnection and lamination processes on the creation of these defects will be reviewed.

1.2.1 Microcracking of solar cells

1.2.1.1 Effect of solar cell cracking on the performance of PV module

Solar cells are subjected to thermomechanical stresses all along their manufacturing chain either in the stringing stage or during lamination. In addition, during their operation time, they are subjected to mechanical loads (such as snow, wind, mechanical impacts, etc.), and to thermal cycling due to the heat difference between day and night. All this loading history contributes to the initiation and possible propagation of microcracks. Cell failure can lead to current blockage and hot spot formation, which significantly compromises module performance [89]. Therefore, minimizing the formation of microcracks is critical to improving module reliability.

The presence of microcracking in photovoltaic silicon is detected using the Electroluminescence (EL) technique, which is a method that allows the detection of electrically inactive areas and cracks in solar cells [90–92] as displayed in Figure 1.10. Microcracks are visualized by dark lines in the EL images, because they either do not emit light or their emission is quite low. Sometimes the cells can even isolate a part of the cell avoiding a current generation [93].

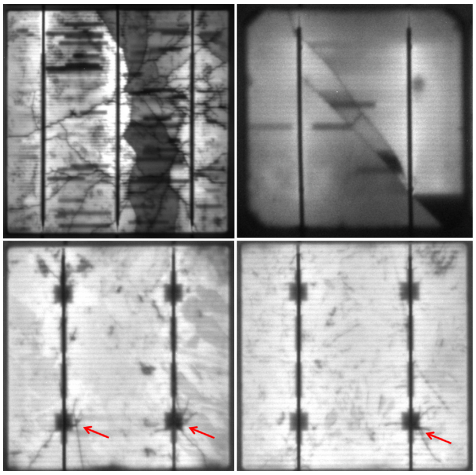

Figure 1.10: Electroluminescence images of cracks in (top left) a multicrystalline solar cell, (top right) a monocrytralline solar cell, and (bottom) at solder pads in two multicrystalline solar cells [13]

The presence of microcracks does not necessarily lead to a total failure of the PV module. However, they can cause phenomena that can limit the performance of the module or completely damage it. Among these phenomena, the hot spots can be noticed. The hot spots are a phenomenon that occurs when the string with a reduced short circuit is forced to work in inverted polarity. This leads to the consumption of the power generated by the other string. Thus, some cells of the string can reach locally high temperatures [94]. Hot spots can be induced by several factors like shadows, localized dirt or cell damage.

Deng *et al.* [95] studied the impact of cell damage on hot spots. Infrared (IR) thermography images showed a local increase in temperature in the cracked areas of the solar cell as presented in Figure 1.11, locally reaching up to 200°C. Causing even a burning and swelling of the backsheet (see Figure 1.11).

The main complexity in term of cracking mechanisms in PV modules is due to the interaction

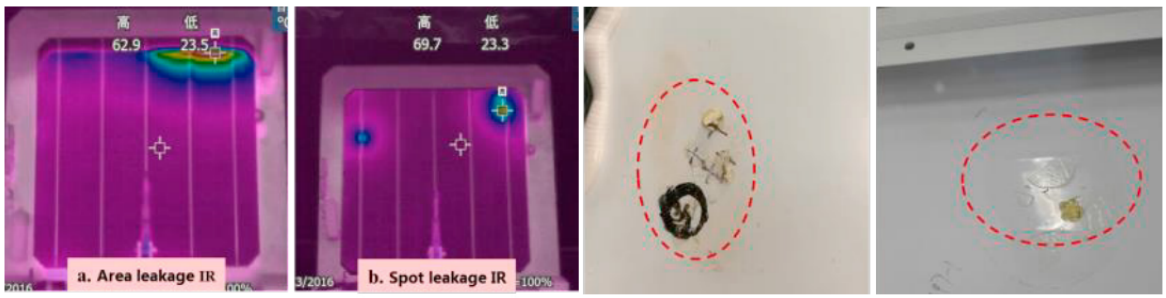

(a) (b)

Figure 1.11: (a) Infrared (IR) thermography images of different defect cells and (b) Appearance of the back-sheet in the damaged area of the PV module [95]

between mechanical, thermal and electrical phenomena. A microcracked cell with 8% of the cell surface electrically inactive shows that the average cell temperature is not constant and highly oscillating during the operating time [96] as illustrated in Figure 1.12. However, an intact cell has a lower and almost constant average temperature. In parallel, the string output voltage oscillates from 1V to 9V in defected cell (see Figure 1.12). This behavior is explained by the fact that the detected microcrack is not electrically insulated and able to conduct heat flow and electricity from one side of the crack to the other. It is assumed that the recovery of the electrical response is the result of the closure of the crack faces due to thermoelastic effects [96].

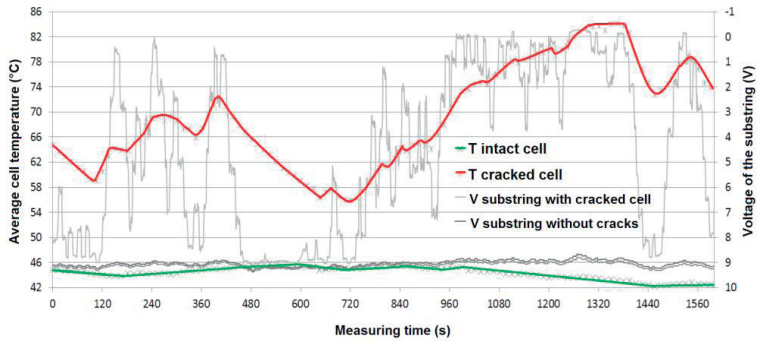

Figure 1.12: Comparison of temperature evolution and voltage of sub-string with and without microcracked cell regarding monitoring time [96]

After evaluating the effect of solar cell cracking on the performance of the PV module, we will discuss the contribution of some parameters of the interconnection and lamination process to the creation of these cracks.

1.2.1.2 The contribution of the interconnection and lamination process to the creation of microcracking

Papargyri *et al.* [97] reviewed the modelling and experimental investigations of microcracks in crystalline silicone PV. They summarized the crack characteristics based on their origins as shown in Table 1.3. The majority of crack distribution is in the interconnection area either at the soldering stage or at the lamination stage.

In the interconnection step, the internal stresses are induced by the difference of CTE between

Origin	How the cracks initiated	Crack distribution	Parameters that affect cracks	Comments
Soldering	Due to thermomechanical stresses in the cell because of the CTE variations of different materials [98]	The region near the end of the soldering path in Si layer is a critical area due to the higher thermomechanical stresses [99; 100]. Cell cracks initiate preferentially at the edge of the front busbar [101] having a diagonal or ±45° orientation [102].	Increasing the speed and decreasing the power of the soldering system [100] and using a low solder melting point [103] reduce the probability of cracking.	The type of the interconnection technology affects the physical contact and therefore the mechanical stresses which are developed.
Lamination	The lamination process of Si cells creates residual stresses in the Si wafers due to high temperature and pressure [104]	Maximum stresses occur close to the edge of the copper interconnector [69; 105–108]. Cracks with a ±45 orientation [109].	Higher encapsulant stiffness results to a lower fracture load [110; 111]. The stresses increase with thickening interconnects [112].	The lamination process is a critical operation in the production cycle because a number of new cracks occurs after this step [107]. The cells located near the frame experience more stresses and displacements [99].

Table 1.3: Summary of crack characteristics based on their origin (Extracted from [97])

the cell and the copper ribbon [98]. As the PV market is moving towards thinner silicon wafers, the risk of microcracking increases [13; 97]. Therefore, a readjustment of the ribbon behavior is necessary, especially the yield strength of the ribbon. Ribbons with a high elastic limit induce a significant warpage of the cell, which can lead to cell failure after welding [113]. A lower yield point allows the ribbon to switch to plastic behavior during cooling, thus reducing the stresses applied to the cell. Reducing the ribbon thickness also has a beneficial effect on reducing the failure rate in the solar cell after welding [114]. A 30% reduction in soldering ribbon thickness reduces the cell breakage rate by 15% after 200 TC cycles [115].

In the lamination stage, the parameters that influence the creation of cracks are mainly related to the mechanical behavior of the materials and the geometry of the PV module. Rowell *et al.* [116] experimentally investigated the effect of PV module composition on the fracture strength of PV modules directly after lamination and after 10 cycles of TC. Their results after lamination showed that for the stiffer encapsulants at room temperature, the fracture load during a mechanical loading test decreased by almost 50%. The comparison between modules with interconnected and non-interconnected cells showed that the fracture force decreased by 35% when using soldered ribbon. Dietrech *et al.* [105] have been interested in the numerical evaluation of the influence of the encapsulant thickness on the PV module deflection (see Section 2.2.2.2). In the work of Rowell *et al.* [116] this aspect has been validated experimentally. As the thickness of the encapsulant increases, the fracture force increases in the PV modules after lamination.

Another aspect regarding the creation of cracks in solar cells, that is related to the lamination step, is the asymmetry in the thickness of the PV module architecture. When the PV module is asymmetrical, and especially in the case of a GBS module, the neutral plane where the normal stresses on the cut section are zero, is located in the glass. And when the module is subjected to

bending loading, all the module components and mainly the cell are loaded in tension leading to a cell crack [117].

The duration of the preheating stage is also an important parameter to ensure a good quality of the PV module. If the duration of this step is not well chosen, the membrane will apply pressure on the PV module before the encapsulant softens, which increases the risk of cell failure [118].

1.2.2 Delamination

Delamination is the most documented failure mode in the PV module field [13]. It can occur at any interface in the module, including the glass/encapsulant, encapsulant/cell, ribbon/EVA, and encapsulant/backsheet interfaces or in the backsheet interlayers [13; 118] as illustrated in Figure 1.13. Degradation of the encapsulant/cell interface is critical to the reliability of the module and its lifetime since it is considered as a direct pathway for moisture, which leads to corrosion of the cell metallization. Subsequently it contributes to the power loss in the PV module [119].

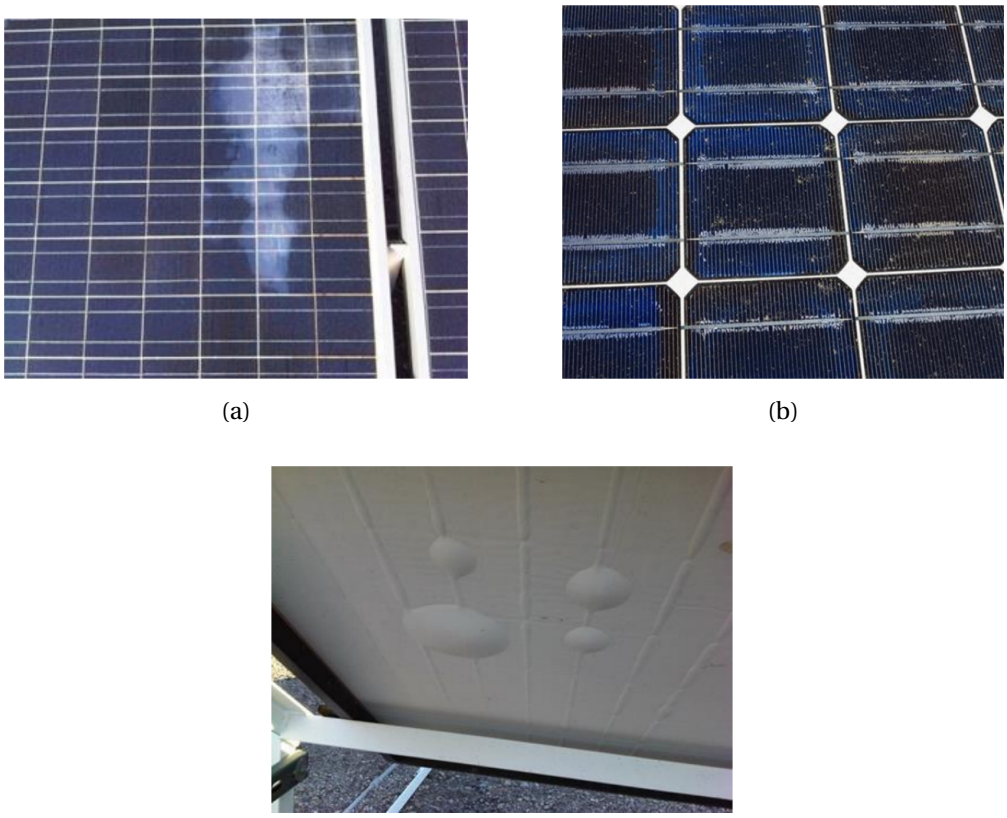

(a) (b)

(c)

Figure 1.13: Example of delamination in PV modules at the interfaces (a) encapsulant/glass (b) encapsulant/cell, and (c) encapsulant/backsheet [119]

In the encapsulant/backsheet interface, without the use of destructive failure analysis, it is often difficult to distinguish whether the delamination has occurred between the encapsulant and the backsheet or between the backsheet layers. This type of delamination is visible by blisters in the outer face of the backsheet as displayed in Figure 1.13c. This type of failure in the backsheet can be detrimental to the safety of the PV module since the backsheet must provide electrical insulation for the PV module [119].

Although not all types of delamination result in a direct failure of the PV module, they significantly compromise its reliability and performance. However, the presence of air in the delaminated layers decreases the interfacial reflectance, and this decrease results in a drop in maximum power due to the reduction of the short circuit current [120].

The delamination is a failure mechanism that occurs from the infant stage. It represents 5% of the degradation mode reported in PV modules after two years of their installation, probably due to improper manufacturing at lamination stage [87].

The lamination process has a major role in the quality of the interfaces between the different layers. The time and temperature in each step of the process, especially pre-heating step, are controlled to optimize the adhesion between the layers and to avoid air trapping in the PV module. If air gets trapped between layers, it can lead to further delamination during the operation of the PV module [118]. In EVA encapsulant, additives such as silane primer are added to improve the adhesion of the encapsulant with the other components. Li *et al.* [121] have shown that this silane adhesion promoter escapes from the EVA at 80°C during heating step. And thus a very long heating time can induce a loss in the adhesion properties of the EVA encapsulant. Hence, this phenomenon leads to poor adhesion strength in the PV module.

The edge-pinching problem in glass-glass modules discussed in Section 1.1.2.2.2 represents an activating factor for delamination. During lamination, the membrane applies a stress concentration to the edges of the PV module. In GG modules, this concentration induces edge-pinching and thus a lower thickness of encapsulant at the edges. The bent glass tends to return to its original shape, and thus induces delamination at the edges of the module at the encapsulant/glass interface. This delamination at the edges opens the way for moisture and impurities to propagate to the center of the module [118].

The PV module is manufactured mainly by two successive processes: interconnection and lamination. With these two procedures the PV module is assembled using several different kinds of components. Each component of the PV module has to meet several characteristics and requirements to ensure a proper operation of the PV module. Nevertheless, the PV module can be damaged either in the manufacturing stage or in the early stage during operation. This damage is mainly related to the manufacturing process, material selection and the combination of the PV module components. Thus, the reliability and lifetime of PV modules is clearly related to these parameters.

The reliability of PV modules is assessed using accelerated qualification tests. These tests require a significant amount of time and sample size to study the performance of the PV module under various environmental conditions. However, these tests do not allow to establish a direct link between the process parameters and the residual stresses induced after fabrication that affect the reliability of the PV module. Several researchers have been interested in using thermomechanical modeling to understand the thermomechanical behavior of PV modules and the phenomena that contribute to the creation of residual stresses.

A bibliographic review of modeling approaches and models available in the literature to study interconnection and lamination processes will be discussed in the next chapter.

Chapter 2

Thermomechanical modeling of PV module manufacturing processes: a literature review

Contents

Résumé du chapitre

Dans ce chapitre, une revue bibliographique sur la modélisation numérique des procédés de fabrication des modules PV est menée. D'abord, les équations mécaniques et thermiques de base qui sont impliquées dans le calcul des contraintes et déformations thermomécaniques sont définies. Puis les facteurs qui accentuent la complexité du développement des modèles 3D complets pour simuler les procédés de fabrications sont discutés en détail. Ces facteurs sont liés principalement à la géométrie et aux comportements thermomécaniques des composants du module PV.

Ensuite, les modèles numériques disponibles dans la littérature qui permettent de modéliser les procédés d'interconnexion et de lamination sont présentés. La modélisation thermomécanique du procédé d'interconnexion par soudage est relativement bien documentée par rapport à l'interconnexion par collage. Il existe un seul modèle qui traite la problématique de contrainte résiduelle dans les cellules solaires après collage. Leurs résultats ont montré que l'interconnexion par collage induit moins de contraintes résiduelles dans la cellule solaire par rapport au soudage. Cependant le niveau de contrainte obtenue dans leur étude de collage par ECA est trop élevé par rapport à des résultats d'autres modèles qui étudient le soudage. Ainsi, leurs hypothèses simplificatrices surestiment éventuellement le niveau de contrainte.

La modélisation du procédé de lamination est une thématique qui a attiré l'intérêt de plusieurs chercheurs dans la dernière décennie. Il existe plusieurs modèles dans la littérature qui étudient soit l'évolution des contraintes durant le procédé ou bien le niveau de contrainte résiduelle à la fin du procédé. Généralement deux stratégies différentes ont été adoptées : la sous-modélisation à l'échelle de la cellule solaire, et la modélisation multi-échelle. Plusieurs modèles disponibles dans la littérature sont assez complets en termes de géométrie et de conditions aux limites choisies. Pourtant, dans la majorité des modèles, des lois de matériaux simplifiés sont utilisées.

Enfin, les paramètres des procédés d'interconnexion de lamination qui influencent l'état de contrainte résiduelle dans le module PV sont examinés. Les paramètres du procédé d'interconnexion les plus étudiés sont la technologie du procédé, la géométrie et la limite d'élasticité du ruban de cuivre. Les rubans de cuivre à faible section transversale génèrent moins de contraintes résiduelles dans la cellule solaire. De plus, une faible limite d'élasticité contribue à la réduction des contraintes dans les cellules solaires.

Dans le cas du procédé de lamination, les paramètres étudiés numériquement sont liés à la géométrie ou aux comportements de certains composants, notamment la cellule solaire, le ruban et l'encapsulant. Le type de refroidissement et son influence sur la déflexion et la contrainte résiduelle sont documentés par une étude expérimentale et analytique.

Ce chapitre est clôturé par une synthèse sur les travaux de la littérature en soulevant plusieurs questions ouvertes. Cette synthèse a permis par la suite de mettre en place la stratégie d'étude de cette thèse.

In recent years, a considerable focus has been devoted to establishing the link between the reliability of PV modules and their manufacturing processes. Given the structural complexity of the PV module and the coupling of thermal and mechanical loading, researchers have adopted a numerical resolution to understand the thermomechanical phenomena that occur in the PV module structure throughout the manufacturing process and even during accelerated testing.

2.1 Theoretical basics of thermomechanics

The relationship between displacements, deformations and stresses of a solid body subjected to temperature changes, force action, phase changes and other internal or external phenomena is defined by the theory of solid mechanics. The basic relationships of solid mechanics theory are well documented in the literature [122–124].

The theoretical problem of thermomechanics of PV modules fits into the theory of small deformation. The relationship between the stress tensor and the strain tensor is called the constitutive equations. They define the mechanical stiffness of the material. In the case of an elastic material, the constitutive equation can be denoted as follows:

$$\sigma = C\varepsilon_{el} \tag{2.1}$$

C is the fourth order stiffness tensor. It is composed of 81 elastic coefficients, relating 9 stress components to 9 strain components. As the strain and stress tensors are symmetrical only 21 components are independent. When the material is isotropic, the stiffness tensor depends on two parameters and the constitutive equation 2.1 can be simplified into Hooke's law:

$$\boldsymbol{\sigma} = \lambda\, \mathrm{tr}(\varepsilon)\mathbf{I} + 2\mu\varepsilon \tag{2.2}$$

here, tr(ε) is the trace of strain tensor, λ and μ are Lamé constants which are related to the elastic constants (E,ν). In the case of non-elastic materials, other constitutive equations are used depending on the behavior of the material and the adapted model.

When the temperature of a material varies due to heating or cooling, the amplitude of vibration of the atoms increases/decreases with respect to their equilibrium position, which changes the interatomic distances. This results in an increase, known as dilatation, or a decrease, known as contraction, of the geometrical dimensions of the material. This relative change in geometry at a temperature variation of 1°C is described by Coefficient of Thermal Expansion (CTE) α_{th}.

$$\alpha_{th} = \frac{L_F - L_0}{L_0\,(T - T_0)} = \frac{1}{L_0} \cdot \frac{\Delta L}{\Delta T} \tag{2.3}$$

Where, L_F and L_0 are the final and initial length of specimen, respectively, T is the temperature of measurement, and T_0 is the reference temperature. ΔL is the expansion/contraction of specimen with respect to its initial length.

When a material is subjected to pure thermal deformation in a temperature range $\Delta T = T - T_0$, the thermal strain tensor is composed of only the normal strains as follows:

$$\varepsilon_{\text{th}} = \alpha_{th}\Delta \text{T}\mathbf{I} \tag{2.4}$$

In thermomechanical problems, the total strain is the sum of the mechanical ε_{mec} and thermal ε_{th} strains. These strains are the result of mechanical loading and thermal expansion due to temperature variations applied to each material.

$$\begin{aligned} \varepsilon &= \varepsilon_{mec} + \varepsilon_{th} \\ \varepsilon_{mec} &= \varepsilon_{el} + \varepsilon_{inel} \end{aligned} \tag{2.5}$$

The mechanical strain has two components, the elastic strain ε_{el} which is given by the Hooke law 2.2 and an inelastic strain ε_{inel} which represents the irreversible strain.

The thermomechanical coupling also requires the solving of the heat equation in the material. The PV module structure is a laminate where each layer contributes to the heat transfer. The amount of heat transferred depends on the thermal and mass properties of the material. The energy equation or heat transfer equation for each module layer is given below :

$$\rho_i \text{C}_{pi} \frac{\partial \text{T}_i}{\partial t} = \lambda_i \Delta \text{T}_i, \quad i = 1, 2, \ldots, n \tag{2.6}$$

Where i represents the layer number, ρ_i stands for the density ($\text{K}g/m^3$), C_{pi} is the specific heat ($\text{J.K}g^{-1}.\text{K}^{-1}$) and λ_i depicts the thermal conductivity ($\text{W}.m^{-1}.\text{K}^{-1}$).

In general, solid mechanics problems can be solved analytically for simplified geometries. However, in the case of complex geometry of PV module, Finite Element (FE) method is often used to solve such a system of equations.

2.2 Thermomechanical modeling of photovoltaic module manufacturing processes

The reliability and lifetime of PV modules is largely related to their manufacturing process. Several experimental accelerated qualification tests of PV modules are developed within the context of the IEC 61215 standard [8]. PV modules undergo a sequence of experimental characterizations that validate their reliability. These characterizations, while effective in studying the reliability of PV modules, are time consuming and require significant material resources. Moreover, very few tests enable to study the thermomechanical behavior of PV modules. Numerical modeling is a tool that allows to study thermomechanical problems consuming less time and less material resources. It also allows to study the coupling of complex phenomena such as those present in the case of PV module (coupling of thermomechanical loading, different behavior laws of components, bending of thin structure). Most importantly, thermomechanical modeling allows access to local variables such as the stresses that are at the origin of crack initiation. Although finite element modeling is efficient, it is necessary to adopt some simplifying assumptions while keeping the maximum coherence with the physical conditions of the problem.

The implementation of a numerical model with the FE method is based on four important

elements: geometry, behavior laws, boundary conditions and loading, and meshing. The space discretization as well as the choice of elements in the mesh are key parameters. In the case of modeling PV module manufacturing processes, there are several complexities related to these elements.

Geometry and meshing

The geometry of the PV module is a thin structure where the thickness is quite negligible compared to the other dimensions, which makes it quite complex. The degree of complexity varies according to the scale of the study.

At the string scale, the solar cell is the largest component in the structure (surface 156 × 156 mm^2 for M0 format) with a rather low thickness/length ratio. On the outer surfaces of the cell, layers of metallization and ECA at the scale of a few micrometers are deposited (see Figure 1.5a). Then comes the copper ribbon which represents the thickest layer in the whole structure with a thickness of up to 220 µm. Thus, during the interconnection stage, all components have a thickness at the micrometer scale.

At the overall PV module scale, the thickness / length ratio is even lower. Table 2.1 shows thickness (t) to length (L) ratio of each component with respect to the number of solar cells of a PV module. In a PV module with a single cell, the lowest ratio is present in the cell. Since its dimensions do not change with increasing number of cells in the PV module, the ratio remains constant. As the number of cells increases, the ratio becomes lower in the other layers. The copper ribbons bind between two cells regardless of the size of the PV module. Therefore, for a number of cells greater than one, the ratio does not change. Also the t/L ratio in the PV module is reduced by increasing the number of solar cells.

Number of solar cells	**t/L ratio** ($\times 10^{-3}$))					
	Cell	**Copper**	**Backsheet**	**Encapsulant**	**Glass**	**PV module**
1 cell	0.96	1.2	1.75	2.25	10	15.75
4 cells		0.63	0.913	1.17	5.2	8.2
60 cells			0.116	0.15	0.66	1.8

Table 2.1: The thickness to length ratio of the components with respect to the number of solar cells of a PV module

In the case of numerical studies of thin structures subjected to bending, a minimum number of elements per thickness is required. Furthermore, flattened elements (3D element with high aspect ratio, i.e. element that are elongated in two directions much more than the third direction) are not recommended for this type of problem. Given the geometric relationship of the PV module layers in both scales, 3D models including all string and PV module details would require millions of elements. Thus, the calculation time would be increased drastically. **Therefore, some geometrical simplifications, such as neglecting some components which have a very low thickness, are crucial for modeling the behavior of the string and PV module during their fabrication.**

Behavior laws

As discussed in the previous section, in thermomechanical problems, the total deformation of a material is governed by the mechanical and thermal deformation. Therefore, the overall behavior of each component is defined by its thermomechanical law and by its thermal expansion.

According to the bibliographic review of PV module components presented in Chapter 1, the encapsulant, backsheets and ECAs have a viscoelastic behavior, while the copper ribbons have an elastoplastic behavior. The solar cell has an orthotropic elastic behavior, and the glass is isotropic elastic. This variety in the thermomechanical behavior of the components increases the complexity of the numerical problem. The consideration of some complex behavior such as viscoelasticity can contribute to the increase of the calculation time. Therefore, some simplified laws can be used as long as it will not affect the accuracy of the simulations.

On the other hand, the thermal expansion of materials depends directly on the temperature variation during thermal loading. For some materials, their expansion may be isotropic and constant over the range of temperatures applied during interconnection and lamination. For others, the expansion may be variable and anisotropic. Considering a constant CTE for materials can be a simplifying approach to the numerical calculation.

Boundary conditions and loading

During both the interconnection and lamination processes, thermal loading is applied to heat up or cool down the structure while simultaneously applying a force or pressure to ensure adhesion of the layers. Therefore, the numerical problem requires the use of a coupled temperature and displacement solver. The thermomechanical coupling uses elements that have both displacement and temperature degrees of freedom, which allows to manage the thermomechanical behavior of materials. In some software, it is not obvious to couple mechanics with thermal equations, which can complicate the numerical models.

During the manufacturing of the string or the PV module, they are placed on heating plates which allow to heat the components by conduction. When cooling occurs in the open air for example, the laminates are cooled by convection. The choice of these thermal boundary conditions is also important for the accuracy of the thermal calculation of the problem.

Contact management is often a source of complexity in numerical models. In the case of modeling the PV module manufacturing process, two types of contact are present. The first type of contact is related to the contacts at the interfaces between all components. The second type is associated with the contact of the structure with the heating plates, which are rigid bodies.

The mechanical contact at the interface can be considered as a perfect contact if we want to simplify the numerical model. Otherwise, contact properties that are defined from the adhesion energies between the different layers can be used. There are several approaches to study the non-perfect contact between materials, including the implementation of cohesive elements which enable to study for instance the interface delamination [125–127].

In recent years, much interest has been given to thermomechanical modeling of PV modules. In the following sections, the existing models in the literature will be reviewed. The assumptions used to build these models will be analyzed. Then the residual stress level after interconnection and lamination will be discussed. Finally, research that investigates the influence of process pa-

rameters will be presented.

2.2.1 Thermomechanical modeling of the interconnection process

The interconnection process represents the first thermomechanical loading applied to solar cells in the PV module manufacturing chain. In the last years, several researchers were interested in modeling the interconnection process and mainly the soldering. In most of the works, the interconnection process is modeled only by the cooling step from the solder solidification temperature to the room temperature [101–103; 108; 109; 128–135]. Very few studies consider the entire thermal heating cycle during the process (i.e. heating from room temperature 25°C to 250°C and then cooling to room temperature) [99].

Esfahani *et al.* [100] used a different approach by modeling the process in two sub-steps. The first one consists in applying a local heating by the crossing of the welding heating head which locally increases the temperature of the heat-affected zone (HAZ) as illustrated in Figure 2.1. The second step simulates the cooling of the cell and the copper to room temperature by convection. A similar approach has been used in [136].

Figure 2.1: Soldering system used in the model of Esfahani *et al.* [100]

In most of the works, the busbars interconnection technology with rectangular ribbons has been studied. Some models take into consideration the pads of metallization layers (see example in Figure 2.2a) while in others the pads of metallization are neglected for simplification reasons. Rendler *et al.* [137; 138] studied the evolution of residual stresses during cooling after soldering in the case of a multi-busbar technology with circular copper ribbons with discontinuous soldering points as shown in the model presented in Figure 2.2b.

As mentioned in Section 1.1.2.1, in this work we are interested in the study of the low temperature interconnection process especially the ECA bonding adapted for SHJ cells. Very few studies are available in the literature that focus on the residual stresses induced by bonding of the cell and the ribbon using ECAs [139–141]. The most recent numerical study was performed by Geipel *et al.* [139] on the residual stresses induced after ECA bonding and welding in order to compare the two techniques. Their model includes the ECA layer, the ribbon, the cell, and the aluminum metallization layer as displayed in Figure 2.3. Geometric simplifications were used such as neglecting the top solder layer and considering the thickness of the busbar and the aluminum layer to be equal. The modeling is performed in steady state, so effects such as creep are not considered. The copper ribbon and solder are modeled using an elastoplastic behavior laws, while for the other components elastic behavior is considered. The stress free state is considered at the solidification temperature which is around 160°C for the adhesives and 179°C for the solder. Therefore, the

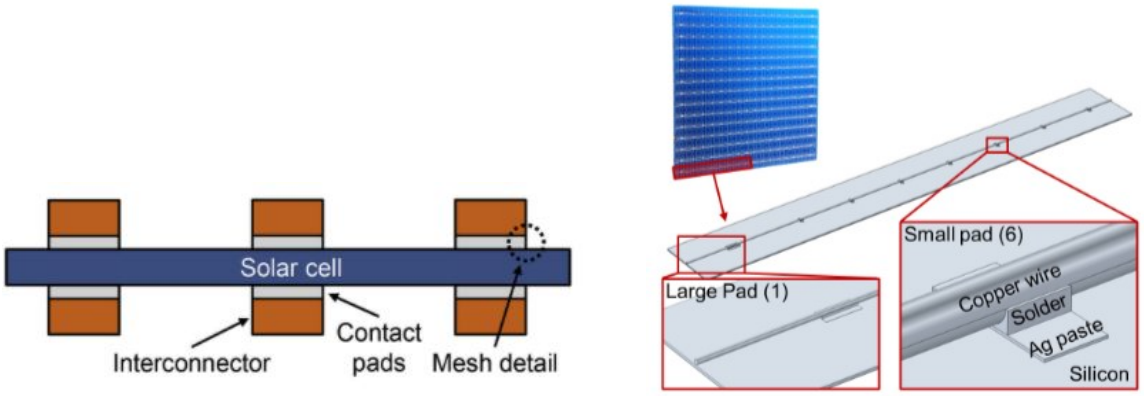

(a) (b)

Figure 2.2: (a) Model geometry details that indicate the mesh distribution in the case of busbars technology (Extracted from [102]) (b) Model geometry consisting of a cell section of $78 \times 10 mm^2$ with half of a MBB pad row and a soldered Cu wire with a diameter of $300 \mu m$ [138]

residual stress state is considered at 25°C after cooling.

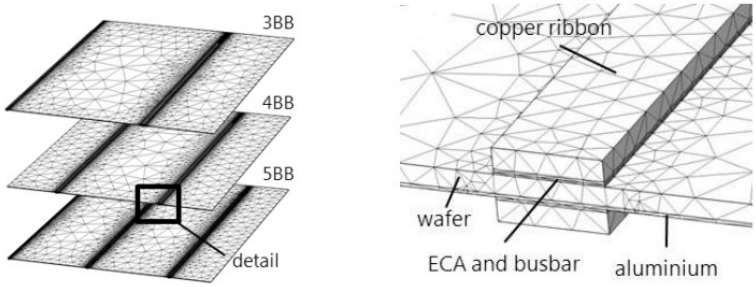

Figure 2.3: Overview of the FEM for the consecutive busbars (left), and detailed view on the layer structure and the mesh (right) (Extracted from [139])

Their model is the most complete one so far in the literature, in terms of geometry, for studying interconnection bonding by ECA. However, it only allows to study the cooling stage and the residual stresses at the end of the process. The cross-linking step and the evolution of thermomechanical stresses during the process are not investigated.

2.2.1.1 Residual stress and strain levels

Beinert *et al.* [129] found a relative residual stress level after soldering of about -22 MPa in the solar cell. While in the study of Song *et al.* [108] the maximum principal stress level in the cell after welding is about 145 MPa. In these two studies, solder was not considered. However, in the study by Song *et al.* [108] the copper ribbon was modeled with an elastoplastic behavior law. Tippabhotla *et al.* [132] showed that the presence of solder and the use of an elastoplastic law in copper and solder reduces the stress level by up to 50%.

In the study by Kraemer *et al.* [101] the behavior of the solder, ribbon and busbars was considered elasto-plastic. The distribution of the third principal maximum stress in the string is presented in Figure 2.4. Due to the large contraction of the copper ribbon, the residual maximum principal stresses in the third principal direction are compressive. Stress concentrations are ob-

served in the interface between copper and silicon since both have a high Young's modulus. Thus higher compressive stresses are observed along the busbar, while the stress level in the rest of the cell is almost stress free. The out-of-plane strain analysis reveals that the edge of the cell undergoes a residual strain of -0.4. In this area, the cell is in contact with the alminum layer of metallization. As the string cools down, the aluminum contracts and applies deformation to the cell since it has a higher CTE.

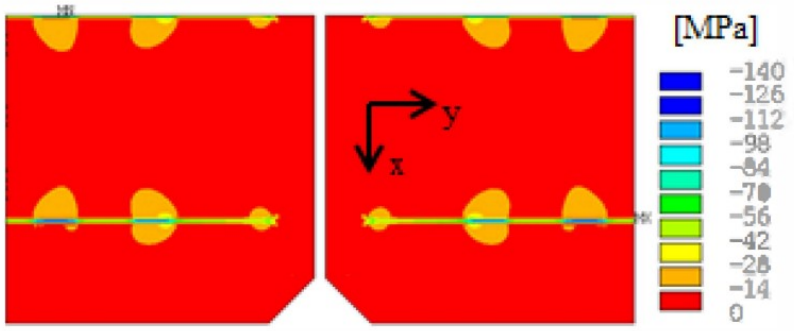

Figure 2.4: Contour plot of the third principal stress in the silicon cells after cooling. Areas beneath the back side solder regions show highest stress [101]

In the case of bonding with ECA, the normal residual stress state is compressive in the copper and solar cell in the x direction as shown in Figure 2.5, while in the y direction the copper is under tension. The compressive residual stresses in solar cell reach a value of -231 MPa [139].

Figure 2.5: Cross section of the interconnection with the normal stress in y-direction highlighted (left), and the same cross section with the normal stress in x-direction (right) [139]

In the study by Geipel *et al.* [139], they showed that the ECA interconnect technique induces less residual stress compared to welding. However, the stress level obtained with an ECA assembly in their study is much higher than that found by Kraemer *et al.* [101] in the case of welding. Kraemer *et al.* [101] used more complex behavior laws, and therefore the stress level is more accurate. Thus, more simplified behavior laws in the case of modeling the interconnection by ECA can lead to an overestimation of the residual stress state.

According to these results, the residual stresses induced during the interconnection process are due to the CTE mismatch between the solar cell and the copper ribbon or the solar cell and the metallization layer in aluminum.

The conventional welding interconnection process is widely studied in the literature [101–103; 108; 109; 128–135]. *However, the bonding interconnection process using ECA is rarely studied* [139–141]. *Mostly, the approach of modeling the cooling down from the maximal temperature of the process is the most used by researchers in studying soldering or ECA bonding interconnection process.*

This approach is based on the fact that the interface bonds between the components are established at the welding temperature. However, in the case of ECA bonding, the cell/ECA/copper interface bonds are established at the ECA curing temperature. In the literature, so far, no research has been conducted on the evolution of thermomechanical stresses in the case of ECA bonding technology.

2.2.1.2 Influence of the process parameters on the residual stress state

The residual stresses induced during the interconnection are mainly due to the CTE mismatch between the string materials [142]. Therefore, the dimensional parameters and the behavior of the materials have a significant impact on the residual stresses.

Dimensions of copper ribbon and yield strength

In a study by Ridhuan *et al.* [131], the thickness of the ribbon t_{Cu} was varied between 0.01 and 0.03 mm keeping the thickness t_{Si} of the solar cell fixed. The post-soldering residual stresses are maximal when the ratio t_{Cu}/t_{Si} is equal to 0.8 for hard ribbon. Analytically, the expression of the maximum principal stress is defined as a cubic function of the ratio of the thickness which explains the peak stress at 0.8. For soft ribbons, the maximum stress is reached at a higher thickness ratio of around 1. This is explained by the variation of Young's modulus ratio between the ribbon and the solar cell which is also involved in the analytical formula of the stress calculation.

Figure 2.6a displays the variation of the third principal stress, since they are higher than the first principal stress, in the solar cell after welding according to different types of ribbons with a yield strength varying between 30 MPa and 120 MPa. Four ribbons with different Young's modulus were analyzed in the study by Wiese *et al.* [135].The curves show that the third principal stress in the silicon is lower as the yield strength of the ribbon decreases. This decrease can reach -60% to -70% for the principal stress in the solar cell. However, the influence of Young's modulus on the residual stresses is negligible. Since an elasto-plastic model was used, the Young's modulus only affects the speed of the stress increase until the yield criterion is fulfilled.

The influence of the ribbon dimensions and the width of the front face busbar (FS-BB) were also studied in [135]. Figure 2.6b shows the evolution of the first principal stress in the cell. The width of the busbar was varied in two widths, one wider and one narrower than the ribbon. The wider busbars induced a residual stress level up to 50% lower than the narrower busbars. A reduction in residual stresses in solar cells is achieved when thin copper ribbons are used. The combination of narrower ribbons and busbars can further reduce the residual stress in the solar cell.

Interconnection technique

Wiese *et al.* [135] performed a comparative numerical study between solar cell soldering techniques by varying the type of solder while adapting the solidification temperature of the alloy. Four study cases were selected by modifying the initial temperature of simulation: no solder (T_{sol} = 183°C), $Sn_{63}Pb_{37}$ (T_{sol} = 183°C), $SnAg_{1.0}Cu_{0.5}$ (T_{sol} = 210°C), and $SnAg_{3.5}Cu_{0.75}$ (T_{sol} = 220°C). Figure 2.7a depicts the first principal stresses in the silicon with the different welding techniques. It is

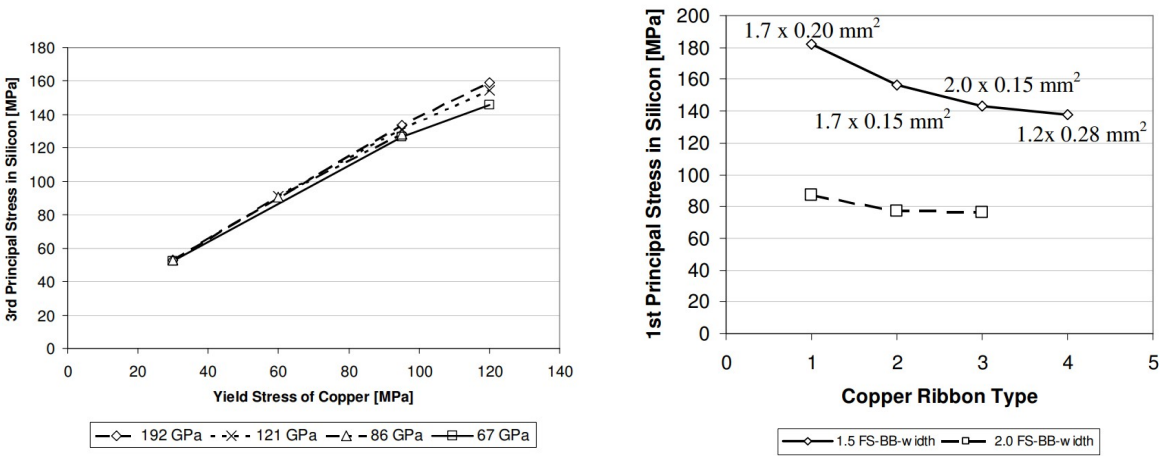

(a) (b)

Figure 2.6: (a) Influence of the copper ribbon's yield stress on the third principal stress in silicon solar cells after soldering with respect to the yield stress of the copper ribbon and (b) Influence of copper cross-section on the first principal stress in silicon after soldering [135]

clear that the presence of solder between the ribbon and the busbar reduces the residual stresses in the solar cell as the stress decreased by almost 100 MPa when solder is added with the same cooling profile. Lead-free solder induces higher residual stresses in the cell. This is due to the higher solder temperature, higher Young's modulus and smaller creep rates. Solder joints with a high silver content involve lower creep rates, which reduces their ability to relax stresses. Therefore, the creep of the solder has a significant influence on the post-soldering residual stress level.

It has also been proved that the soldering temperature and the type of solder influence the warpage of the cell after soldering. Low temperature and Bismuth based solders create less warpage in the solar cell than lead based solders [103].

Geipel *et al.* [139] investigated the level of residual stress induced after bonding by two different types of ECA (thermoset and elastomer) compared to the conventional soldering technique. As mentioned previously, the temperature of ECA curing is lower than temperature of solidification of solder. Figure 2.7b displays the evolution of the first maximum stress in the thickness of the string. The residual stress level in the ECA/solder layer is reduced by 10 MPa when a thermosetting adhesive is used instead of the solder. In the case of an elastomer, the stress level decreases further to 1 MPa. In the ribbon, the stress level is almost identical between thermosetting and soldering, however with an elastomer the stress is reduced by 20 MPa. Similarly in the cell, the elastomer interconnection induces less stresses. This difference is related to the ability of the elastomer ECA to absorb the shear induced by the CTE mismatch between the copper and the cell.

The most studied interconnect process parameters are process technology, geometry and yield strength of the copper ribbon. Copper ribbons with a small cross-section generate less residual stress in the solar cell. Moreover, a low yield strength contributes to the reduction of stress in the solar cells. The presence of solder between the cell and the ribbon greatly reduces the residual stresses. Low temperature welding techniques also have an advantageous effect in reducing the stress level post manufacturing.

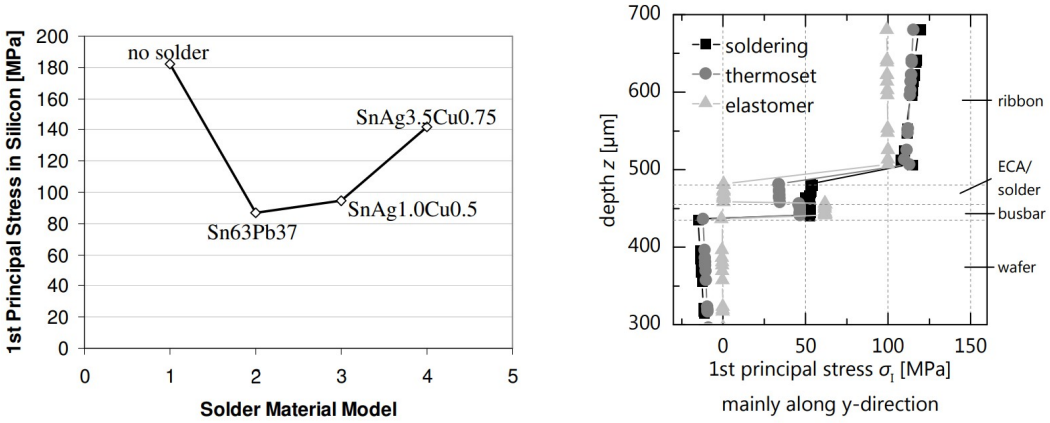

Figure 2.7: (a) Maximum first principal stress in silicon solar cell with different solder alloys [135], and (b) first principal stress along the depth of the interconnection (only sunny side shown) [139]

2.2.2 Themomechanical modeling of lamination process

The research on thermomechanical modeling of lamination processes was initiated by Meuwissen *et al.* in 2006 [141] and U. Eitner in 2008 with several works related to the modeling of the lamination process and thermal cycling [24; 143–145]. Several researchers in different research entities have since developed different thermomechanical models to study the lamination process. Among these teams are the works of:

∗ ***The modeling team of the German Fraunhofer Institute for Solar Energy Systems (ISE)***

Their work consists in the development of models in multi-scale approaches using Comsol Software.

- Eitner [24] developed a 2D plane stress sub-model that represents the inter-cell area of the PV module as shown in Figure 2.8a. Although the geometry requires a plane strain approximation, plane strain modeling has been preferred. This model was used to study the sequencing of the lamination process and thermal cycling to analyze the variation of the inter-cell gap during thermal cycling. The interconnectors between the cells were neglected. The materials behavior was considered elastic except the EVA with two mechanical behaviors (a thermoelastic and viscoelastic model) in order to study the sensitivity of the inter-cell gap estimation according to the behavior law. The stress free state is assumed at lamination temperature of 150°C.

- Another 3D sub-model was established by Eitner *et al.* [143], which is representative of a quarter string stacked with the PV module layers. This model aims to numerically investigate the effect of the interconnector design on the electrical performance of the module and the residual stress state (see Figure 2.8b). A bidirectional coupling mechanism between the solder areas on the cells in the 3D geometry and the solder areas of the 2D-interconnector was implemented. This coupling enables to account for the elastic solder properties. This simplification is justified by the difference in scale between the dimension of the solder and

the string. Thermoelastic behavior laws were used in this model. The stress free state is assumed at lamination temperature of 150°C.

- In his Ph.D. thesis, Eitner developed a 3D model of a quarter string of a 60-cell PV module without interconnects [24] (Figure 2.8c). The model is composed of 15 cells of size 125 × 125 mm in pseudo-square shape. The materials were considered elastic except for the EVA which is viscoelastic. Only the cooling of the PV module is modeled in this case considering a stress free state at 150°C.

- Dietrich *et al.* also used a multi-scale approach with a 3D global model representing a string or several strings of cells encapsulated with the other layers [105; 146] and sub-models representing the structure interconnected with the metallization layer and the copper ribbons as displayed in Figure 2.8f [105; 130; 147].

- Further works on the modeling of the lamination process were pursued in the researches of Beinert *et al.*. In these recent works, two models have been developed. A 3D sub-model which is at the cell scale and focuses on the detail of the metallization and interconnection (see Figure 2.8d) [128; 129]. Another 3D scale model of the PV module similar to Eitner's was used by adding aluminum frame attachment points as presented in Figure 2.8e [148–150]. Larger solar cells were chosen with a square shape. These models have been used in several other works to study the reliability of PV modules [151–155].

Their work did not focus on studying only the residual stresses induced after lamination, but often a sequence between lamination and thermal cycling or mechanical loading is studied to investigate the reliability of PV modules. For this reason, in all their models they simulate the lamination process by cooling from the lamination temperature to room temperature assuming that at 150°C the encapsulant is melted and thus the stress level is considered to be free in the components. During the lamination process, the components of the module are heated up to a temperature around 150°C, and therefore all components expand during the process. With this assumption, it is considered that with the geometry of the model, the components do not change their dimensions due to the thermal expansion. Therefore, the contraction of the components can be exaggerated.

∗ ***The modeling team of the Xtreme Photovoltaics Laboratory in Singapore***

Their methodology to evaluate the residual stresses due to the manufacturing process is different. They are interested in studying each step of the lamination process: preheating, pressure ramping, curing of EVA and post-lamination cool-down and its contribution in the creation of residual stresses. They often use 2D sub-models in plane strain approximation taking into consideration the details in the interconnection area. All their models are developed using Abaqus Software.

- Tippabhotla *et al.* [134] have developed 2D plane strain and 3D sub-models to capture the evolution of residual stresses during the lamination process in the case of conventional lamination process. These sub-models represent a single-cell PV module with a back-contact

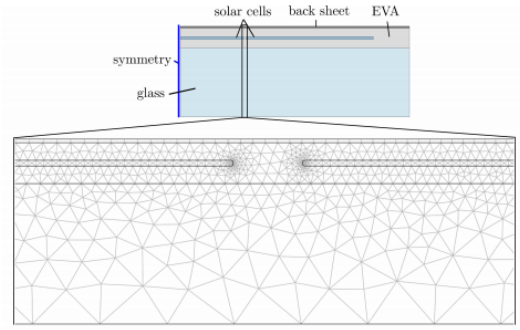

(a) Geometry of the 2-dimensional FEM-model in the simulations with Comsol Multiphysics [24]

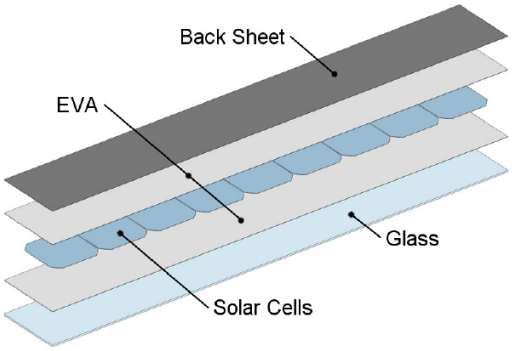

(b) Schematic sketch of the laminated string used in simulations. The interconnections between the solar cells are not shown [143]

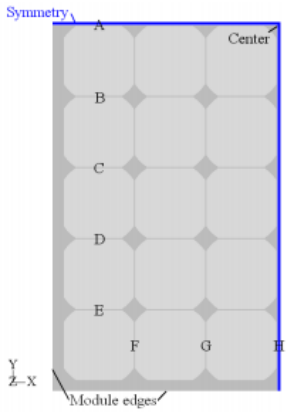

(c) Simulation model of a 60 cells module with symmetric boundary conditions [24]

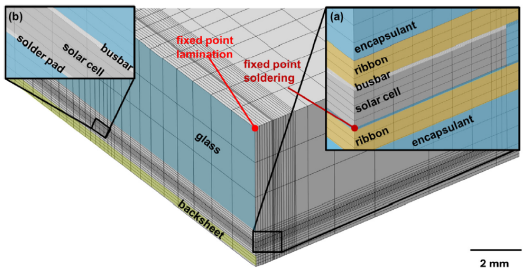

(d) Symmetry corner of the laminate with the used mesh (a) shows the mesh in more detail (b) shows additionally the mesh at a solder pad [129]

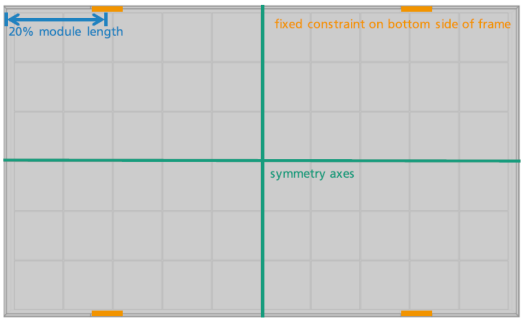

(e) FEM model geometry of the reference module with the symmetry axes depicted (green lines). The orange rectangles show the position of the fixed constraint at 20% of the module length from the edge [150]

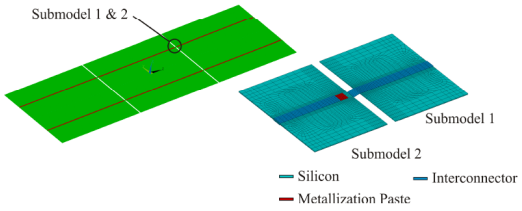

(f) Three dimensional finite element global model (left) and sub model (right) (encapsulant, glass and back sheet is suppressed) [105]

Figure 2.8: Numerical models developed by the ISE team [24; 105; 129; 143; 150]

technology where the cell is interconnected on one side with the copper ribbon. In this study, all layers were considered to be linked during all lamination steps as shown in Figure 2.9a. Soldering was neglected in this model.

- Another approach of sub-step modeling of lamination process, according to the steps shown in Figure 2.9b, was used by Song *et al.* [108]. In the pre-heating and pressure ramping stages, the PV module is modeled by three separate layers without interface bonding. The first layer represents the glass and EVA bonded together, the second layer is the string and the third layer stands for the backsheet and EVA (see Figures 2.9c and 2.9d). At this stage, the encapsulant was assumed not to be softened to fit the shape of the solar cells, for this reason they have considered three separate layers. In the following steps, the PV module layers were considered to be bonded together with perfect interfaces. The layers were considered bonded because the EVA has cross-linked, and therefore the interface bonds are established.

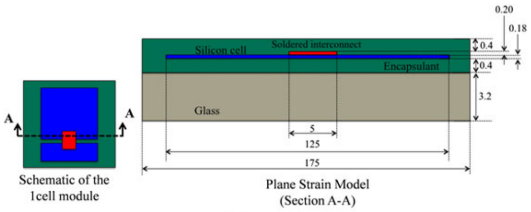

(a) Schematic of the 2D FE model showing dimensions of different components of the mini PV module in mm (not to scale) [134]

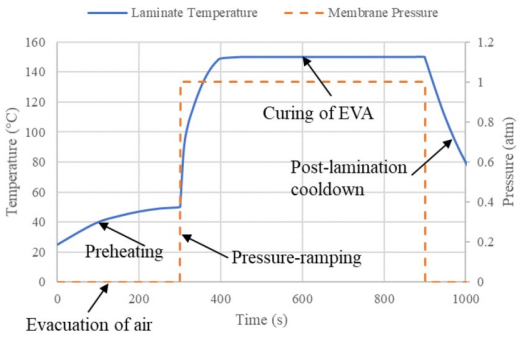

(b) Sub-steps used for modeling the lamination process [108]

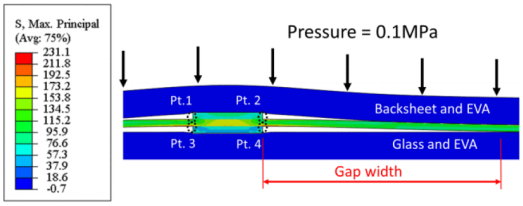

(c) Numerical 2D model used for modelling the pre-heating and pressure ramping steps [108]

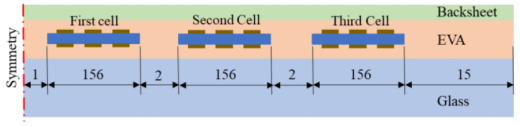

(d) Numerical 2D model used for modelling the EVA curing strep and post-lamination cooldown [108]

Figure 2.9: Numerical models developed by the Xtreme Photovoltaics Laboratory team

These models are used and re-adapted in further works using the same modeling strategy [109; 131; 132; 156; 157]. In all their study, the material behavior is simplified by considering the EVA and the backsheet as thermoelastic except for copper where an elastoplastic bilinear model defined by Wiese *et al.* is used [158].

Other researchers have been interested in the thermomechanical behavior of PV modules either during fabrication, mechanical loading or thermal cycling [48; 99; 103; 106; 159–162]. Other types of PV technologies such as Shingle have been studied thermomechanically [163–165]. Some researchers have made choice to model PV modules using simplified analytical solution [85; 166; 167].

All these works aim at understanding the thermomechanical phenomena that occur during manufacturing or during qualification tests in order to identify the parameters that can improve the reliability of PV modules. In the following we will discuss the level of residual stresses induced in the PV module after the lamination step. We will also review the process parameters that have

shown good optimization of the stress state in PV modules.

2.2.2.1 Residual stress and strain levels

In the study by Beinert *et al.* [129] using the 3D sub-model shown in Figure 2.8d, the residual stresses induced in the lamination step were identified. As explained before, they only model the cooling step from the maximum lamination temperature to room temperature. The residual stress level induced by the soldering of the cell and the copper are implemented in the FEM model. Figure 2.10 represents the relative stress distribution calculated by FEM in the solar cell after cooling from the lamination temperature. The residual stresses in the center of the solar cell are compressive reaching up to -57MPa. As we approach the edge of the compressive cell, the stress level decreases and becomes positive (tension). Areas of solder discontinuity, indicated by white boxes, are visible by compressive stress concentrations in the interconnect line.

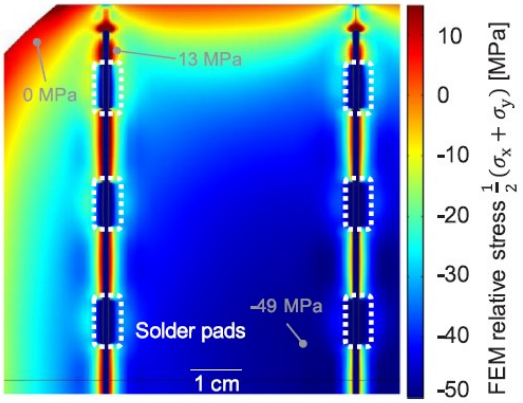

Figure 2.10: Relative stress $\frac{1}{2}(\sigma_x + \sigma_y)$ from the FEM simulation of the solar cell after lamination. The metallization is not part of the FEM model. The dotted white boxes indicate the position of the rear side metallization pads (Extracted from [129])

The modeling of Tippabhotla *et al.* [134] of lamination process in one step showed that the solar cell that was deformed after soldering is forced to flatten during lamination, which induces a deformation concentration near the interconnection area as illustrated in Figure 2.11a. These deformation concentrations at the edge of the interconnection zone are explained by the difference of flexural stiffness in the interconnection zone and the solar cell. This localized deformation in the solar cell induces a rather high level of bending stress in the solar cell reaching locally ≈ 300 MPa as shown in Figure 2.11b. This high stress level is due to the deformation induced in the cell during the soldering step.

The approach of modeling the lamination process in sub-steps with different geometries used by Song *et al.* [108] showed a different level of residual stress. Figure 2.12 displays the level of residual stresses induced after each lamination sub-step at different points of interest shown in Figure 2.9c. The maximum principal stresses in the cell at the end of the pressure-ramping increased by 145 MPa in the backsheet side and 75 MPa in the glass side compared to the post-soldering stress level reaching a maximum of residual stresses up to 275 MPa. This is explained by the transmission of the pressure applied by the backsheet and EVA to the initially flat cell introducing bending

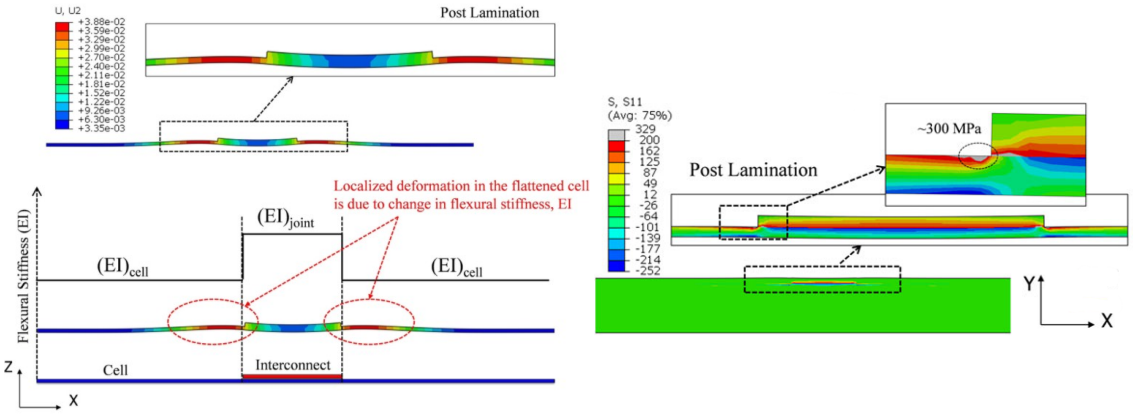

(a) (b)

Figure 2.11: (a) Post-lamination Z-displacement (scaled 5×, the other components have been removed for clarity and full length of the cell is not shown) and (b) residual stress (in X-direction) contours along the cell in MPa post-lamination (only cell and inter-connect are shown in zoomed-in plots) (Extracted from [134])

in the solar cell. The stress level induced after the EVA curing step is the lowest among all the steps ($\approx 20\text{MP}a$). Since the EVA is molten in this step, the thermal stresses related to the temperature difference between the preheating step and the welding 185°C (210-25°C) compared to the temperature difference between the welding and the EVA curing step 60°C (210-150°C) are reduced. Moreover, the deflection induced by the pressure applied by the EVA and backsheet on the cell in the pressure ramping step is reduced by the melting effect of the EVA. After the PV module has cooled down to room temperature, the maximum principal stress level in the cell is 156 MPa in the backsheet side and 100 MPa in the glass side.

As in most studies available in the literature, only the cooling of the PV module is modeled in the lamination process. In this study, they compared this approach, called Simplified post-lamination cooldown (SPLC) and their simulation approach considering heating and cooling step. Using their model, the residual stress level is 20-30 MPa higher which represents 20% of the maximum principal stress in the solar cell as displayed in Figure 2.12.

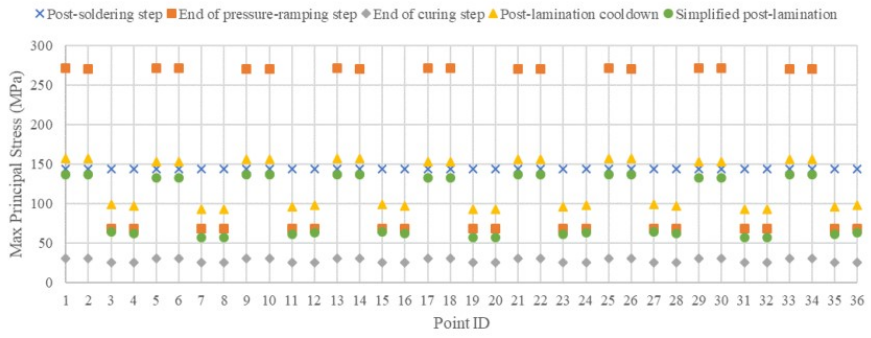

Figure 2.12: Plot of maximum principal stress at 36 critical points (Point ID) in three cells throughout the manufacturing process [108]

In the three approaches compared in this section, the residual stress level is significantly different. Several factors can induce such differences: first, simplified boundary conditions that can influence the accuracy of numerical calculation, then the geometry of the model, and finally the

accuracy of the material behavior laws.

In the work of Beinert et al. [129], the modeling of the lamination process accounting only the cooling step can under/overestimate the stress level. During lamination, the components are heated to the lamination temperature which induces thermal expansion of the materials. By considering only the cooling step, the thermal expansion of the materials is not captured and therefore it is considered that the components will shrink from their initial shape and not from their expanded shape. The pressure applied on the components could also have an effect on the stresses in the solar cells.

Song et al. [108] used a rather realistic approach in their model. However, their analysis was performed at specific points in the cell and at the edge of the interconnection zone where stress concentrations were observed. It is difficult to distinguish whether these concentrations are necessarily related to thermomechanical stresses during the process simulation or to concentration points related to the consideration of a perfect bond between silicon and copper with a geometry with sharp edges that often lead to stress exaggeration problems in FE calculations.

They verified experimentally that the EVA at the end of the preheating step is not melted and is easy to peel off from the solar cell to justify the choice of the geometry adopted in the modeling of the pressure-ramping step. It may be that the interface connection between the encapsulant and the cell is not established, yet the vacuum pressure is intended to evacuate the vacuum between all components and thus ensure contact between the different components.

Tippabhotla et al. [134] used a more simplified geometry to model the entire conventional lamination cycle. However, the residual stress level at the end of the simulation is quite high. This may be due to the non-symmetry of the geometry which favors one-way deflection and also the simplified behavior laws. In their further research, they showed that the use of an elasto-plastic law in copper and thermoelastic law in solder can reduce the stress level by more than 50% *[132].*

2.2.2.2 Influence of the process parameters on the residual stress state

The effect of the cooling press

Li *et al.* [85] investigated experimentally and analytically the influence of the cooling press on the modulus curvature and normal stress in the solar cell. They added a Teflon layer between the glass and the front side encapsulant to separate the glass from the laminate at the end of the fabrication and to measure the curvature of the other layers. Figure 2.13 shows the normal stress in the solar cell in PV modules cooled with and without cooling press. The reduction in residual normal stress in the module cell cooled with the cooling press is 22-27% less than the stress in the module cell cooled in the open air (i.e., without cooling press).

This difference in stress level is related to the residual deflection measured experimentally on the PV modules. The PV modules cooled down with the cooling press have a lower deflection than the PV modules cooled down without cooling press (see Figure 2.13). Therefore, the cooling press decreases the residual deflection in the PV module, thus resulting in a lower residual stress level.

Dimensions of solar cells

Besides thermomechanical parameters, dimensional parameters have an effect on the cre-

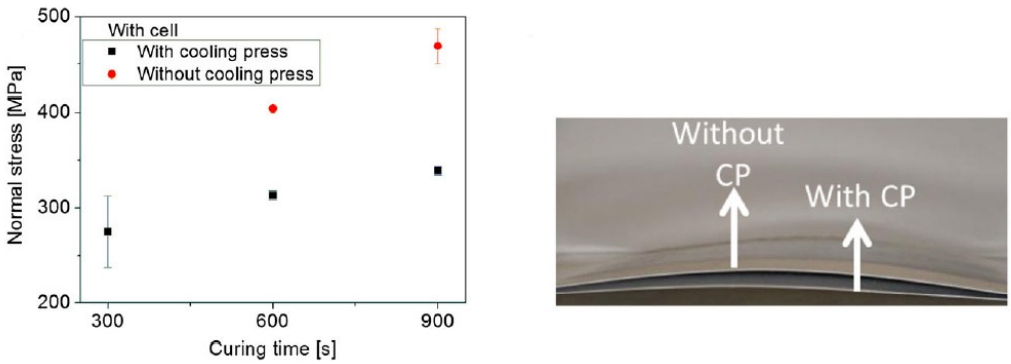

Figure 2.13: Analytical normal stress at the middle layer of Si solar cell in the module with one cell (left), and an image of two modules after cooling and front glass removal, with or without CP (right) [85]

ation of residual stresses in PV modules. It has been shown that the cell thickness acts on the deflection variation and the maximum principal stresses of the PV module after lamination [103; 105; 108; 147]. A smaller cell thickness results in a lower deflection of the laminate, which is the result of a reduced bending moment resulting from thermal stresses [105; 147]. Furthermore, the maximum principal stress in the cell increases by about 27% by reducing the cell thickness from 200 μm to 120 μm as displayed in Figure 2.14a. This is due to the local bending of the copper ribbons [103; 105; 147]. Song *et al.* [108] showed that the level of principal stress after lamination does not change much with the variation of the cell thickness. However, the maximum principal stress after the pressure-ramping step is reduced by 23% for a thickness decreased from 180 to 90 μm. The reduction in cell thickness has also an effect on the long-term reliability of the PV module since thin cells show a reduction in fatigue solder damage [160].

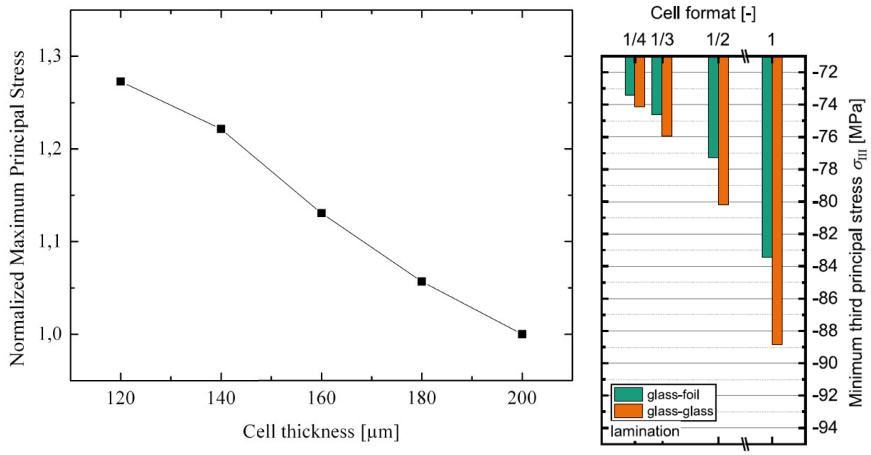

(a) (b)

Figure 2.14: (a) Parameter study of cell thickness regarding maximum principle stress in the silicon after lamination (Ref: 200 μm) [105], and (b) Minimum third principal stress σ_{III} of the solar cells after lamination for the variation of the cell format for glass-foil and glass-glass module (Extracted from [150])

The cell size has also an influence on the stress level induced after lamination. The larger the cell size, slightly higher the maximum principal stress in solar cell is. This slight increase is related to the increase in the size of the modulus associated to the variation of the cell size, and also to the size of the cell itself. Since a larger cell size induces higher compressive stress [150].

The cell shape also has a beneficial effect on the reduction of residual stresses after lamination. By reducing the cell shape from a full cell to a 1/4 cell, the maximum principal compressive stress level is reduced from 83.5 MPa (full format) to 73.4 MPa (quarter cells) as presented in Figure 2.14b. This reduction is equivalent to the reduction in cell size. These effects are identical in glass-glass and glass-backsheet modules.

Properties of interconnect

Song *et al.* [109] numerically investigated the influence of the cross section of the copper ribbon on the creation of residual stresses after lamination. The ribbon width was increased from 1 mm to 1.8 mm. The thickness of the ribbon was also varied by keeping its cross section and its electrical resistance constants. The maximum principal post-lamination stress in the back side of the cell increases as the ribbon width decreases. However, on the front side of the cell, the opposite effect was observed. In their study, they considered that the most critical step was at the end of pressure-ramping, and that the stress level was critical in this step in the widest ribbons. Therefore, they concluded that the increase of the ribbon width has a degrading effect on the solar cells.

Shin *et al.* [103] also showed that the width of the copper ribbon increases the principal stress level in the cell during lamination as depicted in Figure 2.15. They also established the relationship between the number of busbars and the stress level in the solar cell. The results showed that a higher number of busbars increases the stress in the solar cell.

Increasing the copper thickness also alters the reliability of the solder joint by increasing the fatigue damage of the solder joint [160].

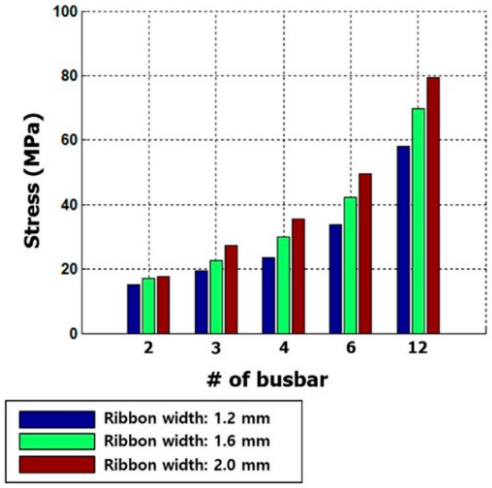

Figure 2.15: Influence of the number of busbars on the maximum first principal stress of the 100-µm-thick silicon wafer during the lamination process (Extracted from [103])

Properties of encapsulant

The encapsulant is the binding element between the layers. It has a role of protection of the solar cells against the loads applied by the glass or the backsheet. Its dimensions, and in particular the thickness, have a primordial role in the level of residual stress after lamination [151].

Increasing the thickness of the encapsulant reduces the deflection induced in the PV module after lamination [105]. Thermomechanical loading on the laminate will induce shear deformation in the encapsulant between the glass and the cell. As the distance between the layers increases, the shear deformations will be more important by decreasing the total deflection of the laminate. On the other hand, increasing the thickness of the encapsulant will allow the cells to move easily. This leads to an increase in the principal stress parallel to the cell as the copper ribbon shrinkage becomes dominant.

Numerically, it has been shown that softer encapsulant induces a lower stress level compared to stiffer encapsulant [168]. Figure 2.16-(a) shows the stress level induced in the solar cell after lamination with respect to the elastic modulus of the studied encapsulants normalized to the elastic modulus of the EVA. In this case, the same encapsulant was used for front and back sides. It can be seen that the stresses are lower when the elastic modulus of the encapsulant is low compared to the EVA. When the elastic modulus exceeds that of the EVA, the stresses increase and reach a maximum even if the elastic modulus increases more. When the elastic modulus exceeds the EVA modulus above 5 times, the stresses decrease sightly.

In other cases, the encapsulant was chosen as the front or back face in combination with another encapsulant in the other face. Figure 2.16 (b) and (c) show the stress level when the EVA is the back and front encapsulant, respectively. The stress levels clearly show that the front side encapsulant and its stiffness have a more important role in creating stress after lamination.

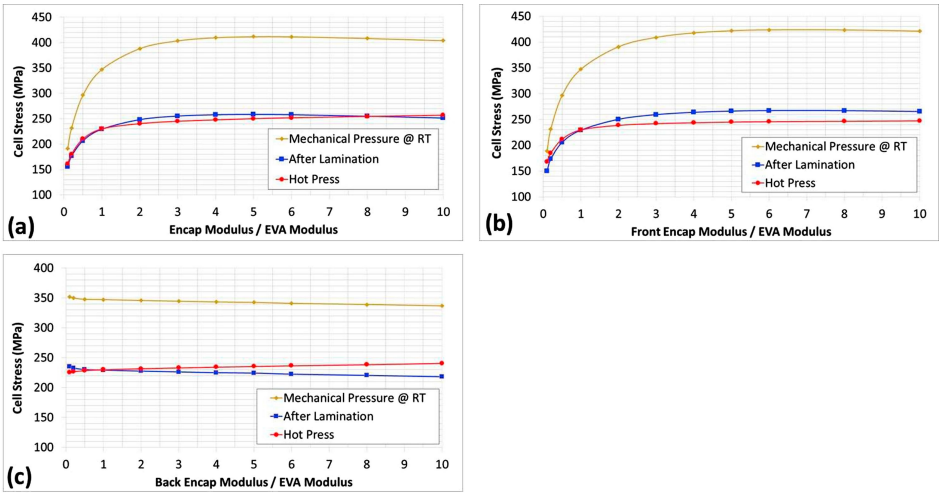

Figure 2.16: Variation of maximum cell stress in tangential direction (for different conditions) with (a) the encapsulant elastic modulus (front and back), (b) front encapsulant elastic modulus and (c) back encapsulant elastic modulus. Note: The encapsulant modulus was normalized by the EVA elastic modulus in all the cases [168]

In this section, the influence of some parameters of the lamination process on the residual stress state are discussed. The parameters studied numerically are related to the geometry or behavioral properties of certain components, including the solar cell, the ribbon and the encapsulant. The type of cooling and its influence on the deflection and residual stress are documented by experimental and analytical study. Therefore, despite the prediction of the ITRPV of the increase of the lamination process throughput [5], the numerical study of the effect of process parameters such as temperature and cooling type on the thermomechanical behavior of the PV modules is still nearly non-existent.

2.3 Summary and open questions

The PV module is a thin and large laminate assembled using two main manufacturing steps: interconnection and lamination. Both steps induce residual stresses that affect the reliability and life cycle of PV modules. Several factors contribute to the creation of residual thermomechanical stresses in the PV module such as different thermomechanical properties of the materials, component geometry, and thermomechanical loading conditions.

All numerical models need to be developed based on input parameters: geometry, behavior laws and boundary conditions representative of the thermomechanical loading applied during the process. In the literature, the database of behavior laws of PV module components is quite poor. Recently, researchers have provided databases on the viscoelastic behavior of some types of encapsulant and backsheet. However, for other materials the data remain weak. **What are the main mechanical tests needed to characterize the thermomechanical behavior of each component ? What are the constitutive behaviors that allow to represent the thermomechanical behavior of the PV module components ? This will be the focus of chapter** 3.

In the first interconnection step, welding is considered as a classical process. For this reason, most of the research available in the literature and presented in this chapter was focused on numerical modeling of the residual stresses after manufacturing. Some cell technologies, especially SHJ technology, are sensitive to high temperature welding. The alternative is the ECA assembly which ensures an adhesion by cross-linking. There are very few modeling studies in the literature that focus on ECA interconnection. However, in all these studies, only the residual stress state after manufacturing was examined. None of the studies presented in this bibliographic review investigated the evolution of thermomechanical stresses during the bonding interconnection process. **How do the thermomechanical stresses in the string evolve during the bonding by ECA interconnection process ? What are the process parameters that allow reducing this level of induced stresses ? Such questions will be addressed in chapter** 4.

The lamination process is considered as the most critical step in the PV module manufacturing chain. Differences in the behavior of the components, the module architecture and the thermomechanical loading are at the origin of the stresses induced during the process and of the final residual stresses.

The interest in thermomechanical modeling of the lamination process has increased in the last decade. Some researchers were interested in understanding the thermomechanical phenomena at the solar cell scale using sub-models. Others have developed multi-scale modeling strategies. Indeed, 2D and 3D submodels were used to study the behavior at a reduced scale of the PV module. Additionally, simplified 3D models were developed to study the global deformation of the PV module by omitting the components with negligible shape such as copper ribbons. **In this work, we also choose a multi-scale strategy to investigate the thermomechanical behavior of PV modules**.

Several components of the PV module have a complex thermomechanical behavior, such as the encapsulant and the backsheet which are viscoelastic and the copper which is elastoplastic. However, in the literature, the behavior laws of these materials are often simplified to elastic or

thermoelastic models. Tippabhotla *et al.* [132] have shown that the use of an elastoplastic law to model the copper ribbon improves the accuracy of the numerical calculations: **how these simplifying material models affect the accuracy of the numerical calculations ? This topic will be the focus on the first part of chapter** 5.

In the sub-modeling of the lamination process, at the solar cell scale, geometrical simplifications are necessary to reduce the complexity of the simulations. In the case of cells interconnected by welding, the metallization and welding layers between the cell and the ribbon are often neglected. Very few studies take them into consideration. However, in the case of cells interconnected by ECA, no study in the literature has focused so far on the evolution of thermomechanical stresses for this type of assembly during the lamination process. **How does the ECA assembled string behave during the lamination process ? This aspect will be discussed in the second part of Chapter** 5.

The sub-modeling at a reduced scale of the PV module is not always sufficient to study the thermomechanical behavior of PV modules. In several numerical models, the global scale of the PV module has been considered in order to study its global residual deformation. Some researchers were interested in numerically evaluating the residual stresses in solar cells by varying some process parameters such as the PV module architecture. Others used an analytical approach to study the effect of the nature of post manufacturing cooling on the deformation of the PV module. These process parameters have an effect on the residual deformation of the PV module. Another important process parameter in the PV module lamination recipe is temperature. Few studies have investigated the effect of temperature on the creation of residual stresses in the PV module. **Thus, how do these three parameters - temperature, architecture, cooling type - influence the numerical deformation of the PV module ?**

Experimental validation of numerical models is a crucial step in verifying the accuracy of numerical simulations. Very few models in the literature are experimentally validated. On the other hand, only two experimental methods for characterizing the deformation of PV modules are reported in the literature: synchrotron X-ray micro-diffraction and confocal micro-Raman spectroscopy. However, both methods are limited to the scale of the solar cell. **Is there an experimental method available to characterize the global deformation of the PV module in order to validate the numerical model ? Chapter** 6 **will be dedicated to the experimental and numerical study of the global deformation of the PV module depending on the process parameters.**

The analysis of the works reported in the literature allowed us to establish a strategy aiming at a better prediction of numerical models. This strategy is divided into three main areas:

- **Area 1**: experimental characterization and establishment of accurate behavioral laws for PV module components
- **Area 2**: sub-modeling of interconnection process and multi-scale modeling of lamination process within the range of temperature of interconnection and lamination processes
- **Area 3**: experimental validation of the global lamination process model

The overall strategy is summarized in Figure 2.17. The strategy of multi-scale modeling of lamination process will be presented in Chapter 5.

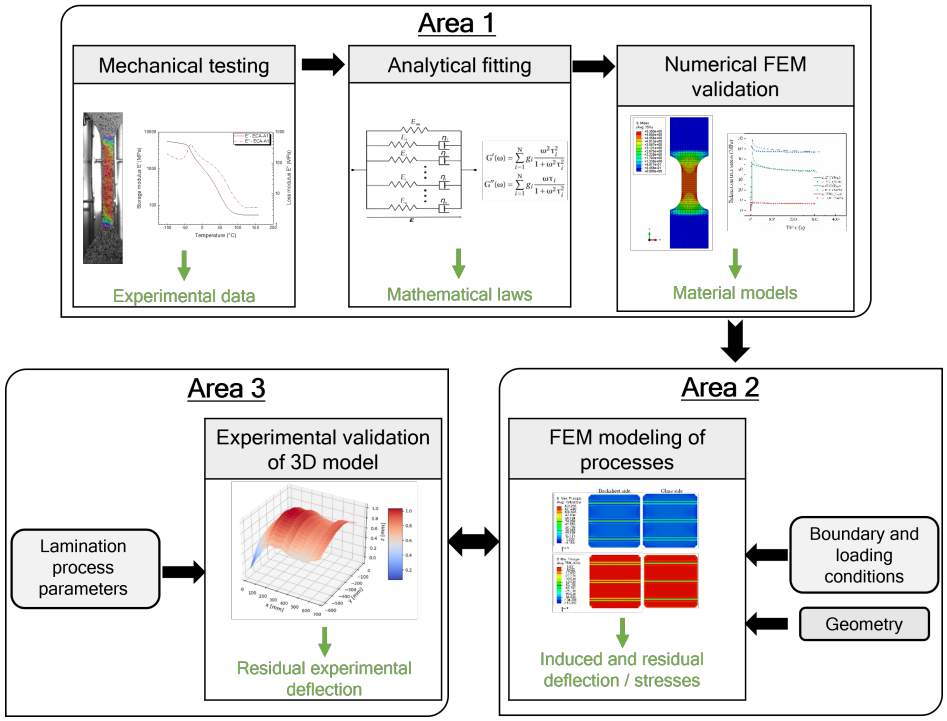

Figure 2.17: Strategy implemented for thermomechanical modeling of photovoltaic module manufacturing processes

Chapter 3

Experimental characterization and numerical modeling of the thermomechanical behavior of the PV module materials

Contents

Résumé du chapitre

La structure d'un module PV est assez complexe. Cette complexité provient de la différence entre les comportements thermomécaniques et des liaisons des interfaces entre les couches utilisées dans le module PV. Cette différence de comportement est considérée comme l'une des sources de contraintes internes dans le module PV pendant sa fabrication. Dans ce chapitre, l'accent sera mis sur la caractérisation expérimentale du comportement thermomécanique de plusieurs composants du module PV.

Tout d'abord, le comportement viscoélastique des matériaux polymères (encapsulant, backsheet et ECA) a été identifié sur la base des courbes DMA via des balayages en température. Les résultats ont montré que l'encapsulant et le backsheet n'ont pas un plateau caoutchouteux très étendu. Ils passent rapidement à l'état fluide après leur transition vitreuse. Il s'agit d'une caractéristique plutôt favorable pour ce type de matériau puisque, pendant le procédé de fabrication, l'encapsulant peut s'écouler pour remplir toute la forme du module PV.

Dans ce chapitre, un modèle mathématique de Maxwell généralisé a été établi pour modéliser le comportement viscoélastique de ces matériaux polymères en utilisant des courbes maîtresses construites par le principe de superpostion temps-température (TTS). Des essais de relaxation expérimentaux et numériques ont été réalisés pour valider le modèle analytique. Un bon accord a été obtenu entre l'expérience et la simulation lorsque la contrainte de relaxation appliquée répond à la condition de viscoélasticité linéaire.

La deuxième partie se concentre sur la caractérisation du comportement thermo-élastoplastique des rubans de cuivre. Les mesures de traction à différentes températures ont montré que les rubans de cuivre présentent une sensibilité à la température de sollicitation. Cependant, aucune sensibilité à la vitesse de chargement n'a été trouvée. Un modèle thermo-élastoplastique de Johnson-Cook a donc été choisi pour modéliser le comportement plastique des rubans en tenant compte de leur sensibilité à la température. Les résultats de la simulation des essais de traction utilisant ce modèle ont montré une bonne corrélation avec les mesures expérimentales.

Dans la troisième partie, notre intérêt s'est porté sur l'étude du comportement élastique et la rupture des cellules solaires SHJ. Sur la base des courbes force-déplacement d'essais de flexion 4 lignes, les modules élastiques dans les directions longitudinale et transversale de la cellule ont été calculés analytiquement et numériquement. L'objectif de cette caractérisation était de vérifier si la transition d'une plaquette à une cellule solaire SHJ a un impact sur ses propriétés élastiques. La corrélation entre les propriétés élastiques théoriques du silicium et les mesures analytiques et numériques a permis de conclure que les propriétés élastiques restent inchangées entre une plaquette de silicium et la cellule solaire SHJ. En outre, le comportement à la rupture des cellules SHJ a été étudié statistiquement à l'aide de la loi de Weibull. La résistance à la rupture dans la direction des busbars est plus élevée que dans la direction perpendiculaire.

Dans la dernière partie de ce chapitre, les propriétés thermiques des composants des modules PV ont été étudiées. Tout d'abord, des mesures de coefficents d'expansion thermique (CTE) ont été

réalisées sur plusieurs composants de modules PV avec différentes variations de composition. Les mesures sur la cellule solaire SHJ ont mis en évidence un effet anisotrope de son expansion thermique. Cette anisotropie est induite par la métallisation en argent de la cellule puisque l'argent se dilate plus que le silicium. La dilatation du ruban de cuivre et du backsheet en PP est également linéaire avec une anisotropie pour le polypropylène (PP). Pour les autres matériaux polymères caractérisés dans cette section, leur expansion thermique n'est pas linéaire et dépend fortement de leurs temperatures de transition ou de leur condition de mise en forme. Enfin, la chaleur spécifique et la conductivité thermique des matériaux polymères ont été mesurées par Differential Scanning Calorimetry (DSC) et lambda-meter, respectivement.

Introduction

The structure of the PV module is quite complex. Such complexity lies from the various layers used in PV module characterized by quite different thermomechanical behavior and interfaces linking materials. This difference in behavior is considered to be one of the sources of internal stresses in the PV module during its manufacturing. Their complex architecture combined with the various behaviors of the PV module components makes the analytical resolution of the system quite impractical. For this reason, FE modeling is required. The accuracy of numerical calculations will depend on the accuracy of the behavior laws used to characterize the different materials. For this reason, the focus of this chapter will be on the thermomechanical behavior of several PV module components.

As the PV module is composed by different material families (polymers, metal, semiconductor), each material category will be investigated separately. In the first section, the viscoelastic behavior of polymeric materials (encapsulant, backsheet, and Electrically Conductive Adhesive (ECA)) will be characterized. Using Dynamic Mechanical Analysis (DMA) tests in temperature sweep, the temperature dependence of polymeric materials will be identified. Then isothermal multi-frequency DMA tests will be used to investigate their time dependency. By introducing the principle of time-temperature superposition, a Generalized Maxwell viscoelastic law will be proposed to model the behavior of these polymers.

In the second section, the thermo-elastoplastic behavior of copper ribbon will be discussed. Based on tensile tests correlated with the Digital Image Correlation technique (DIC), an analytical model of "Johnson-Cook" will be identified and numerically validated.

The third section is devoted to study the mechanical behavior of SHJ solar cells. First, its elastic properties will be defined using force-displacement curves obtained from 4-line bending measurements. Since silicon is a brittle material, its fracture properties will be analyzed using the Weibull probability law.

Then, the fourth section highlights the thermal measurements of the PV module components. More attention will be paid to the thermal expansion coefficient (CTE) measured by the DIC technique. Then, the specific heat of polymer materials measured by DSC will be reported. Finally, the thermal conductivity of backsheet, encapsulants and ECAs will also be outlined. The experimental test matrix detailing the type of test and the parameters used for each material under study is presented in Table 3.1.

Table 3.1: The experimental matrix with different test conditions for all the studied materials

	Dynamic Mechanical Analysis(DMA)		Tensile or Relaxation (DIC) / 4-line bending	CTE measurement (DIC)	Specific heat measurement (DSC)	Thermal conductivity measurement
	Temperature scan	Frequency scan				
Encapsulant	• Temperature range: −70°C to 110°C • Frequency: 1Hz • Amplitude: for TPO-A, TPO-B and Ionomer 5µm for EVA, TPO-C 3µm	• Temperature range: −70°C to 110°C • Frequency range: 0.1 to 10Hz • Amplitude: 5µm for TPO-A and 3µm for EVA	-	TPO-A: • Temperature range: −30°C to 100°C • Temperature ramp: 1°C/min	TPO-A • Temperature range: 10°C to 60°C	TPO-A and TPO-B
Backsheet	TPT: • Temperature range: −40°C to 200°C • Amplitude: 5µm PP white and transparent: −70°C to 170°C • Amplitude: 3µm	• Frequency range: 0.1 to 10Hz TPT: • Temperature range: −40°C to 200°C • Amplitude: 5µm PP white and transparent: • Temperature range: −70°C to170°C • Amplitude: 3µm	Relaxation TPT and PP white: • Temperatures: −30°C, 25°C, 60°C and 150°C • Strain rate: $10^{-3}/s$ • Strain: 2.5%	TPT and PP white: • Temperature range: 40°C to 150°C • Temperature ramp: 1°C/min	TPT and PP white: • Temperature range: 20°C to 130°C	PP white
ECA A1 and A2	• Temperature range: −70°C to 160°C • Frequency: 1Hz • Amplitude: 3µm	• Temperature range: −70°C to 160°C • Frequency range: 0.1 to 10Hz • Amplitude: 3µm	Relaxation: • Temperatures: −30°C, 25°C, 60°C, and 150°C • Strain rate: $10^{-3}/s$ • Strain: 2.5% (at 25°C, 60°C and 150°C) and 1.25% at −30°C	• Temperature range: −30°C to 150°C • Temperature step of 10°C	• Temperature range 20°C to 160°C	ECA A1 and ECA A2
Copper ribbon	-	-	Tensile: • Temperatures: −30°C, 25°C and 150°C • Strain rates: 10^{-2} and $10^{-3}/s$	• Temperature range: −30°C to 150°C • Temperature step of 10°C	-	-
Solar cell	-	-	4-line bending: • Crosshead speed: 10mm/min	• Temperature range: 30°C to 150°C • Temperature ramp: 1°C/min	-	-

3.1 Linear viscoelastic behavior of polymer materials in PV module

A material is called linear viscoelastic when it exhibits a time sensitivity in its linear regime. There are several methods to study the viscoelasticity of materials. Either by directly characterizing the creep or relaxation behavior in their time domain at various isothermal temperatures. Otherwise, by DMA measurements in the frequency domain over a range of frequencies for different isothermal temperatures. Then the complex modulus in the frequency domain is converted into relaxation times to express it in time domain [169; 170].

In this study, a DMA measurement is used to characterize the viscoelastic behavior of two types of backsheet and two types of encapsulant. In the field of PV, few studies are carried out to investigate the viscoelastic behavior of materials used for PV applications [24; 44; 45]. Recently, Bosco *et al.* [12] have provided a large database on the viscoelastic laws of encapsulant and backsheet materials. To complete this database, other types of backsheets and encapsulant have been studied in this work.

3.1.1 Dynamic mechanical analysis (DMA) experiments

The viscoelasticity of polymer can be studied using DMA tests. Dynamic mechanical analysis consists in applying a low amplitude oscillatory strain $\varepsilon(t)$ on a specimen and measuring the resulting stress $\sigma(t)$.

$$\varepsilon(t) = \varepsilon_0 \exp(i\omega t) \tag{3.1}$$

where ε_0 is the amplitude of the strain cycle, $\omega = 2\pi f$ is the pulsation and t is the time.

The stress response of a viscoelastic material is shifted by a factor called the loss factor δ which measures the damping factor in the material. This factor represents the ratio between the storage modulus E' which is a measure of the energy stored in the material representing the elastic part and the loss modulus E'' which is a measure of the energy dissipated during displacement and represents the viscous part.

$$\sigma(t) = \sigma_0 \exp[i(\omega t + \delta)] \tag{3.2}$$

σ_0 is the amplitude of the stress cycle.

Hence, the complex modulus E^* is given by the following relation:

$$\begin{gathered} E^* = \frac{\sigma}{\varepsilon} = E' + iE'' \\ \text{with } E' = \left|E^*\right|\cos(\delta) = \frac{\sigma_0}{\varepsilon_0}\cos(\delta), \quad \text{and} \quad E'' = \left|E^*\right|\sin(\delta) = \frac{\sigma_0}{\varepsilon_0}\sin(\delta) \\ \tan(\delta) = E''/E' \end{gathered} \tag{3.3}$$

Backsheets

DMA tests were performed to characterize the viscoelastic behavior of the TPT backsheet which is composed of the three polymer layers: PVF, PET, and PVF treated. Samples of rectangular shape

with dimensions of $28 \times 4 \times 0.35 mm^3$ were selected in three areas of the plate: center, top, and bottom to check the homogeneity of the plate. To verify the anisotropy of the material, specimens were cut at 0° and 90° with respect to the rolling direction, denoted Machine Direction (MD) and Transverse Direction (TD) respectively, and tested in a temperature range of −50°C to 200°C. The specimens were loaded in tension with a maximum displacement of 5 μm to ensure that the tests were performed in the linear viscoelastic domain.

Figure 3.1 represents the results of storage modulus E′ and the loss factor tan(δ) measured at 1 Hz between −50°C to 200°C on the TPT backsheet. The tan(δ) curves show three peaks related to the glass transition temperatures of PVF and PVF treated at 55°C, and of PET near 110°C. A third peak is observed around 10°C which corresponds to a secondary transition of PET. These glass transitions are reflected on the storage modulus curves by a decrease of the storage modulus near the temperature 55°C. A second strong decrease appears near 110°C as displays in Figure 3.1a.

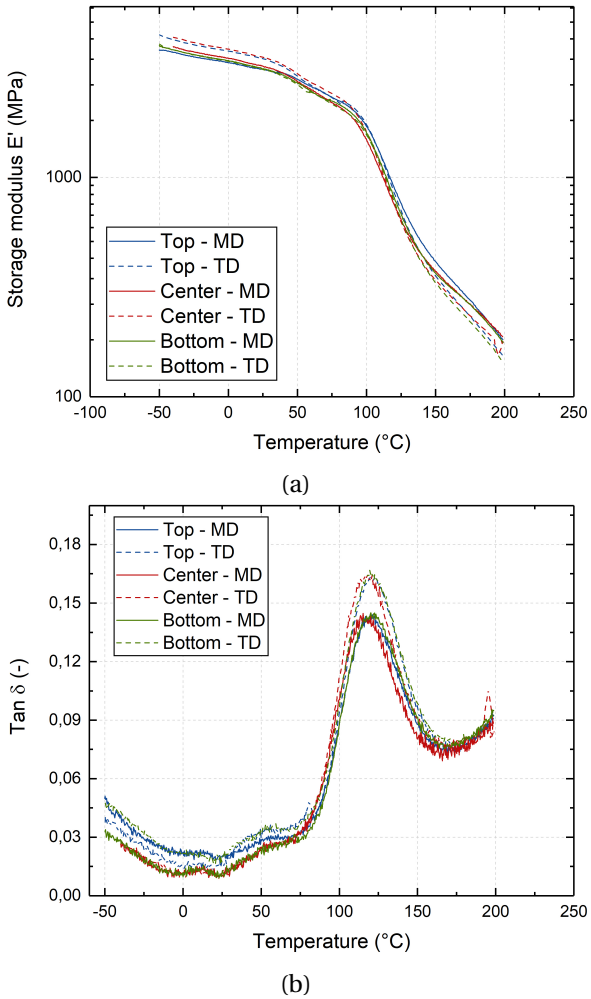

Figure 3.1: The evolution of (a) the storage modulus and (b) the loss factor of the TPT backsheet regarding the temperature in MD and TD directions

At low temperatures, a difference in storage modulus between specimens oriented at MD and TD was observed. This difference decreases as the temperature increases and approaches the glass transition temperature of PVF. Thus, the backsheet plates exhibit anisotropy before the glass transition that diminishes afterward due to the relaxation of residual stresses induced by the process.

As for the homogeneity of the plate, no significant difference was noticed between the samples cut in the three zones of the backsheet plate.

Another type of backsheet composed of co-extruded PP in white and transparent has been studied in this work. Specimens were cut into 5 mm wide strips in both MD and TD directions to study the material anisotropy. The DMA tests were carried out in the temperature range of −70°C to 170°C with a maximum tensile amplitude of 3 µm.

Figure 3.2 represents the storage modulus E′ and loss modulus E″ of backsheet PP white and transparent at MD and TD directions. The curves show a dependency of the storage E′ and loss E″ moduli on the temperature. A primary transition corresponding to the glass transition is observed around −27°C in both variations of the PP backsheet. Two other secondary transitions are identified at −60°C and 10°C. A large decrease of the storage modulus can be observed from 150°C onwards which is related to the flowing state of PP near the melting temperature.

The PP backsheet exhibits an anisotropic behavior since it is stiffer when tested in MD direction. This anisotropy effect is more visible in the transparent PP backsheet. A minor difference in storage and loss moduli was noticed between the white and transparent PP backsheets.

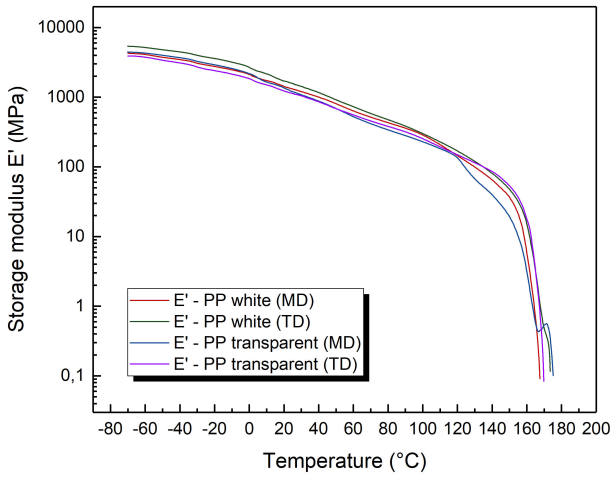

(a)

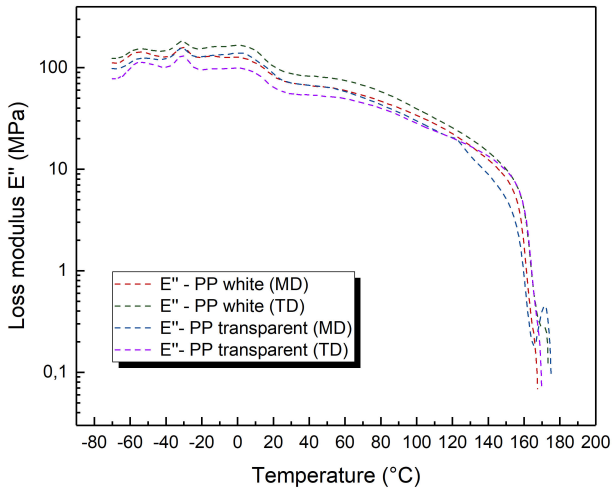

(b)

Figure 3.2: Temperature dependency of white and transparent PP (a) storage and (b) loss modulus in MD and TD directions

Encapsulants

To investigate the viscoelasticity of the encapsulants during the lamination process, DMA tests were carried out on fresh encapsulants. Five types of encapsulant were evaluated in this work: three different types of TPO (A, B and C), Ionomer A, EVA. Samples of rectangular shape with dimensions $30 \times 5\ mm^2$ and a variable thickness depending on the type of encapsulant were used. The specimens were loaded in tension for a maximum displacement between 3 and 5 μm in a range of -70°C to 120°C at 1Hz.

The evolutions of the storage modulus E′ and loss modulus E″ are presented in Figure 3.3. The curves show a decrease in storage modulus E′ in the range -70°C to 0°C for all types of encapsulant except for Ionomer-A which starts to decrease after 10°C. Thereafter, a severe drop in the storage modulus can be noticed at 50°C for TPO-A, B and C, and EVA, and at 75°C for Ionomer-A. This decrease corresponds to the flowing state of the encapsulants. EVA encapsulant is reaching the flowing state at 75°C as its crosslinking starts at 150°C. Therefore, no measurement is captured after 75°C with the type of loading used.

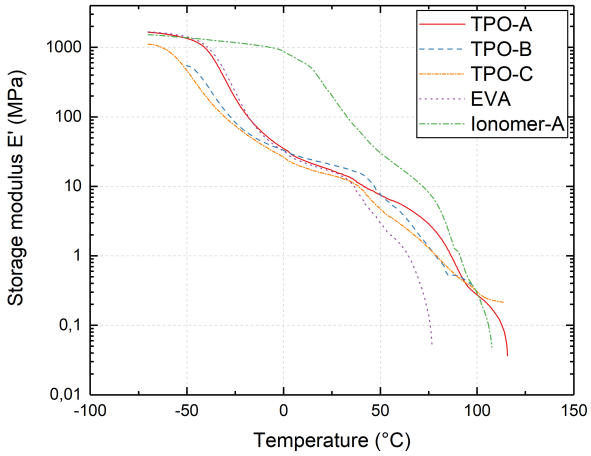

(a)

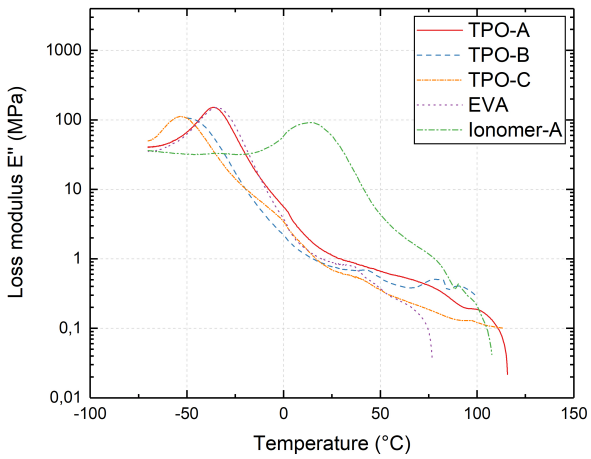

(b)

Figure 3.3: Evolution of (a) storage modulus and (b) loss modulus of encapsulants with respect to the temperature

The loss modulus curves 3.3b display a peak, associated with the glass transition, near -49°C for the encapsulants TPO B and C. For TPO-A and EVA encapsulants the peak of the loss modulus

is around −30°C. However, the ionomer-A presents the highest glass transition temperature of all the tested encapsulant types (T_g = 17.28°C). All the encapsulants exhibit a temperature sensitivity.

To summarize, all tested encapsulants and PP *backsheet did not show a significant rubbery behavior since after the glass transition they switch to flowing state . In general, in molten polymers, the transition between rubbery and liquid behavior is activated from a terminal relaxation time* [171]. *This behavior depends on the critical molecular mass of the macro-molecular chains. The lower the molecular mass is, the weaker the entanglement becomes and therefore the sliding between the macro-molecular chains becomes easier* [171; 172]. *This is consistent with the behavior observed in the encapsulants.*

Electrically Conductive Adhesive (ECA)

The viscoelastic behavior of ECA was also characterized by DMA tests. Two types of acrylate-based ECA of different concentrations of silver particles were tested. The characteristics of each ECA are defined in Table 3.2. Rectangular specimens with a section equal to 5×1 mm^2 were prepared manually using a silicone mold. The specimens were degassed and then crosslinked at 130°C for 10 to 15 min to ensure a total crosslinking of the acrylate. The kinetics of cross-linking is not a parameter considered in our study. A temperature scan was performed in the range of −70°C to 160°C applying a frequency of 1 Hz and an amplitude of 3 µm for both materials.

Name	Binder	Filler type	Metal Weight %	Volume resistivity $\Omega.cm$
A1	Acrylate monomer	Ag	25-50	$2,9.10^{-3}$
A2	Acrylate	Ag	44-48	5.10^{-4}

Table 3.2: Composition of the ECAs selected for the mechanical study

Figure 3.4 illustrates the temperature dependence of the storage and loss moduli. In the curves of the storage module, the two ECAs exhibit three states: the glassy state, glass transition regime, and the rubbery state. Although they have the same base, the ECA-A1 is twice stiffer than the ECA-A2 in the glassy regime. The glass transition temperature of ECA-A1 is low (≈ −30°C). Its stiffness drops before the one of ECA-A2 which has a higher glass transition of 95°C as shown by the loss modulus peak. This difference is possibly related to the chemical formulation of the acrylate between the two types of ECA.

The results discussed in this section show a temperature dependency of the behavior of polymer materials used for the fabrication of PV modules. Characteristic temperatures for the transition from the glassy to the rubbery state have been identified. In the next sections, we will study the time and temperature dependency of the behavior of these materials.

3.1.2 Time-temperature superposition

3.1.2.1 Master curve

To characterize the behavior of the backsheet with respect to the loading isothermal multi-frequency DMA tests were carried out by varying the dynamic loading frequency from 0.1 Hz to 10 Hz every

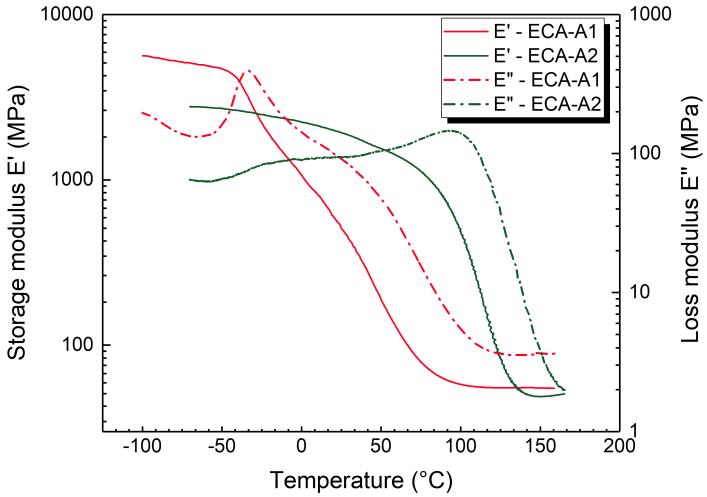

Figure 3.4: Temperature dependency of acrylate-based ECAs storage and loss modulus

10°C between −50°C and 200°C for the TPT backsheet and between −70°C and 160°C for the white PP backsheet, the EVA and TPO-A encapsulant with a heating rate of 1°C/ min. As presented in Section 3.1.1, the tested backsheets showed a low anisotropy in certain temperature ranges. Therefore, for simplification purposes, the master curves are constructed only in the MD direction.

Figure 3.5 represents isothermal measurements of storage modulus for TPT backsheet. An increase of the storage modulus with the frequency increase can be observed.

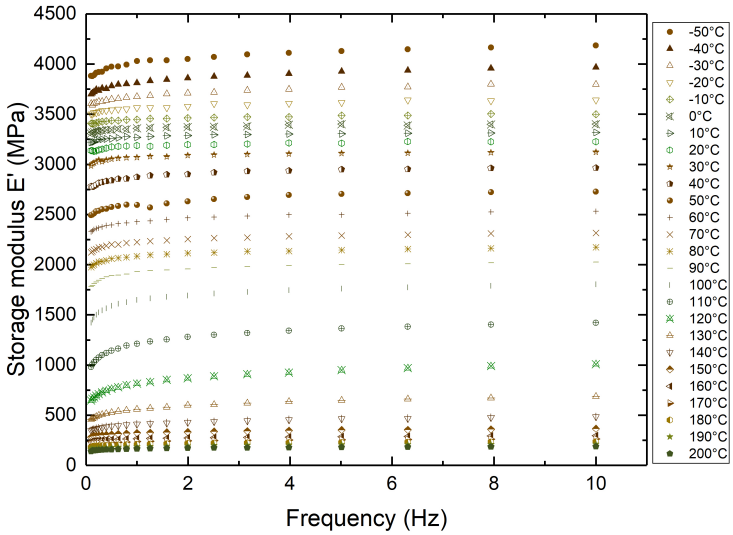

Figure 3.5: Isothermal multi-frequency measurements of storage modulus for TPT backsheet

By increasing the temperature of loading, the macromolecular chains become more mobile, which increases the ductility of the polymer. Moreover, when the loading rate increases, the macromolecular chains do not have time to relax and therefore the polymer becomes more rigid. This double dependency is called Time-Temperature Equivalence (TTE) or Time-Temperature Superposition (TTS) [170; 173].

The purpose of TTS is that a test performed at a high strain rate at room temperature, for ex-

ample, can be equivalent to a test performed at low temperature at a lower strain rate. Indeed, the curves in Figure 3.5 can be shifted in time in a log-log plot to display a master curve. To obtain the master curve for TPT backsheet, the glass transition temperature of PET (T_{ref} = 110°C) was chosen as a reference temperature. By multiplying the frequencies by a shift factor a_T, the isothermal curves can be shifted with respect to the reference curve as shown in Figure 3.6.

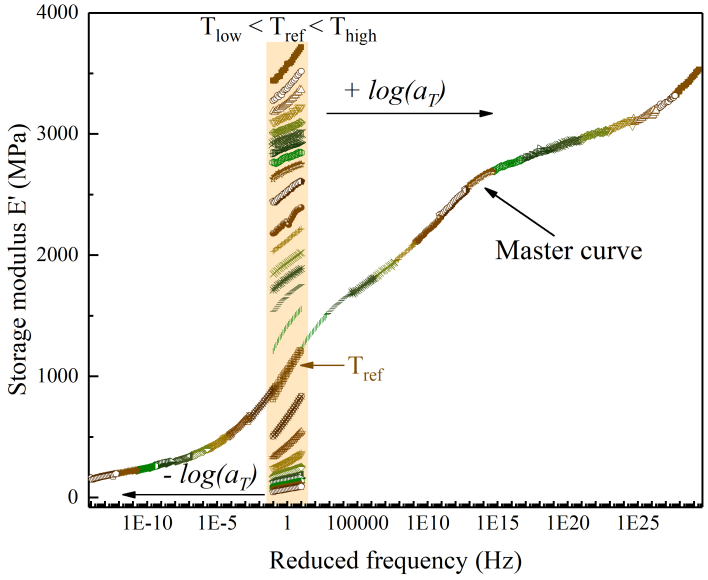

Figure 3.6: Generation of master curve of TPT backsheet using the time-temperature superposition principle

3.1.2.2 Shift functions

Viscoelastic materials, as explained in the previous Section 3.1.2.1, meet the TTS principle. Given this condition, the relaxation modulus E of a viscoelastic material at the actual time t and at a given temperature T is equivalent to the relaxation modulus at a reduced time ζ with respect to a reference temperature T_{ref} as expressed in the following relation [174]:

$$E(t,T) = E\left(\zeta, T_{ref}\right), \quad \zeta = \frac{t}{a_T(T)} \tag{3.4}$$

The shift factor a_T reflects also the change in relaxation time $\tau(T)$ with respect to temperature T, then

$$a_T(T) = \frac{t}{\zeta} = \frac{\tau(T)}{\tau_{ref}} \tag{3.5}$$

where τ_{ref} is the relaxation time at the reference temperature. Thus, the expression of the reduced time when the temperature of measurement varies can be deduced from Equation 3.5 [174]:

$$\zeta(t) = \int_0^t \frac{dt}{a_T(T(t))} = \int_0^t \frac{\tau_{ref}}{\tau(T(t))} dt \tag{3.6}$$

The most widely used shift functions are the William Landel Ferry (WLF) function [175] and the Arrhenius law [169; 171; 173]. The use of either of these two laws depends on the area of analysis

rather centered in the glassy state, in the viscoelastic transition zone or in the flow zone.

For amorphous polymers, and above the glass transition temperature, the WLF equation can be used as empirical function:

$$\log a_T(T) = -\frac{C_1 (T - T_{ref})}{C_2 + (T - T_{ref})} \tag{3.7}$$

where T_{ref} is the reference temperature from which the shifted curves are obtained, C_1 and C_2 are parameters of the WLF law. This shift function is rather valid in the glassy state of the material and mainly in the interval $[T_g; T_g + 100°C]$ [171].

An Arrhenius law can also be used to capture the TTS of secondary transitions in the glassy state. Such model is also valid in the folowing state and is defined by:

$$\log a_T(T) = \frac{E_A}{R}\left(\frac{1}{T} - \frac{1}{T_{ref}}\right) \tag{3.8}$$

where, E_A is the energy of activation in (J/mol), R is the constant of perfect gas. Other empirical functions like polynomial functions have been used to better fit the experimental data [164; 171; 174].

In this work, both WLF and Arrhenius functions were used to define the shift functions. The Arrhenius law (equation 3.8) is applied for $T < T_{ref}$ while the WLF (equation 3.7) is used for $T > T_{ref}$. Figure 3.7 represents the fit of Arrhenius law and WLF function for shift factors regarding TPT backsheet. The WLF fits well the shift factors above the temperature of reference. However, below the temperature of reference (T_{ref} = 110°C), it shows a significant deviation compared to the Arrhenius fit. For the other materials, WLF and Arrhenius parameters are presented in Table A.1 in annex A.

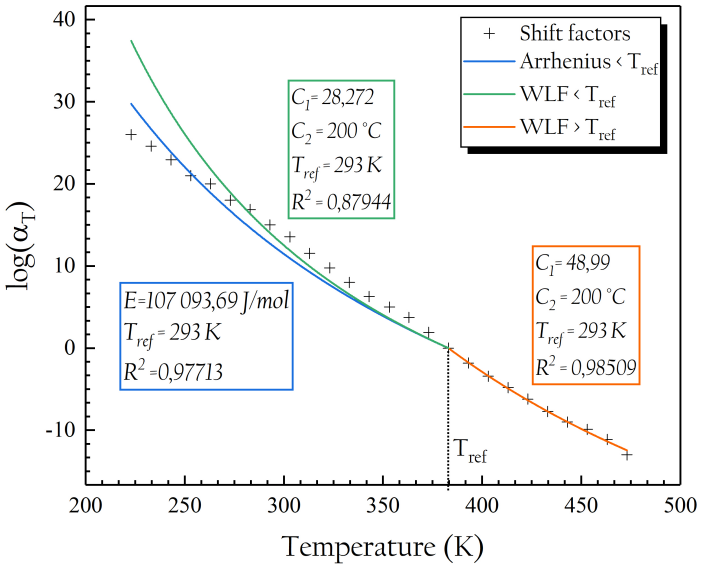

Figure 3.7: Shift factors for TPT bakchseet and comparison of the WLF and Arrhenius shift functions

3.1.3 Description of Generalized Maxwell model

3.1.3.1 Analytical equations

The viscoelastic behavior of polymers used for PV application can be modeled using a Generalized Maxwell model characterized by n branches in parallel, each composed of springs and dashpots as displayed in Figure 3.8. Springs represent elasticity of the material while dashpots represent the viscosity.

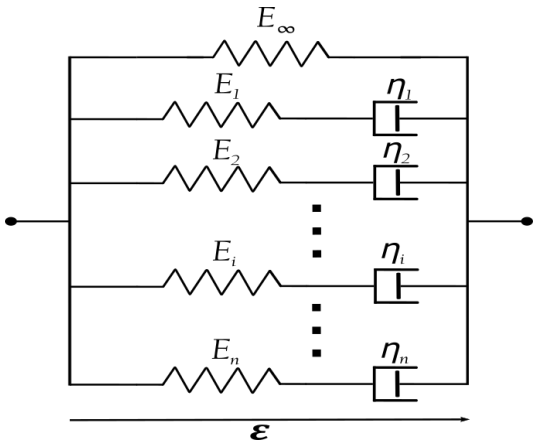

Figure 3.8: Rheological representation of a generalized Maxwell viscoelastic model

A Maxwell element, where a spring and a dashpot are connected in series, is called Maxwell branch. The behavior of each branch is expressed by:

$$\dot{\varepsilon}_i = \frac{\dot{\sigma}_i}{E_i} + \frac{\sigma_i}{\eta_i}, \quad i = 1,2,\ldots,n \tag{3.9}$$

where E_i is the elastic modulus and η_i is the viscosity of the i^{th} branch.

The solution of equation 3.9 for a constant strain ε_0 imposed at $t = 0$ is given by:

$$\sigma_i(t) = E_i \varepsilon_0 \exp(-t/\tau_i), \quad \tau_i = \frac{\eta_i}{E_i} \tag{3.10}$$

Here τ_i is the relaxation time of the i^{th} branch of General Maxwell model. Thus, the constitutive equation of the Generalized Maxwell model can be expressed as follow:

$$\begin{aligned} \sigma(t) &= E_\infty \varepsilon_0 + \sum_{i=1}^{n} E_i \varepsilon_0 \exp(-t/\tau_i) \\ &= \varepsilon_0 \left[E_\infty + \sum_{i=1}^{n} E_i \exp(-t/\tau_i) \right] \end{aligned} \tag{3.11}$$

The relaxation modulus can therefore be defined as a Prony series [174]

$$E(t) = \sigma(t)/\varepsilon_0 = E_\infty + \sum_{i=1}^{n} E_i \exp(-t/\tau_i) \tag{3.12}$$

with, E_∞ is the long term modulus, and related to the instantaneous modulus by $E_0 = E_\infty + \sum_{k=1}^{n} E_k$. Most FE software interprets the relaxation modulus in terms of relative modulus g_i as below:

$$\begin{aligned} \mathrm{E}(t) &= \mathrm{E}_0 \left[g_\infty + \sum_{i=1}^{n} g_i \exp\left(-t/\tau_i\right) \right] \\ g_i &= \frac{\mathrm{E}_i}{\mathrm{E}_0} \\ g_\infty &= 1 - \sum_{i=1}^{n} g_i \end{aligned} \tag{3.13}$$

Set of g_i and τ_i is referred to as Prony parameters.

In the literature, there are several methods to calculate the terms of Prony series from experimental master curve. Citing among these methods, the Procedure X, Multidata Method and the Collocation Method [169], the algorithm of Emri and Tschoegl [176–178], the method by Bhattacharjee *et al.* [179], and the method by Babaei *et al.* [180]. In this work, the method developed by Takeh and Shanbhag [181] in ReSpect code was used to calculate the terms of Prony series. Their method consists in deducing a Continuous Relaxation Spectrum (CRS) $h(\tau)$ from the complex experimental shear modulus $\mathrm{G}^*(\omega) = \mathrm{G}'(\omega) + i\mathrm{G}''(\omega)$ based on the following equation:

$$\begin{aligned} \mathrm{G}'(\omega) &= \int_{-\infty}^{\infty} \frac{\omega^2\tau^2}{1+\omega^2\tau^2} h(\tau) d\ln\tau \\ \mathrm{G}''(\omega) &= \int_{-\infty}^{\infty} \frac{\omega\tau}{1+\omega^2\tau^2} h(\tau) d\ln\tau \end{aligned} \tag{3.14}$$

Here, ω is the frequency and τ is time of relaxation. The nonlinear Tikhonov regularization strategy of Honerkamp and Weese is used to calculate the CRS [182]. Then, the CRS is used to calculate the Discrete Relaxation Spectrum (DRS) defined by the modes $\{g_i \ \tau_i\}, 1 \le i \le \mathrm{N}$ based on two approaches. On one hand, by using the method of Interactive Rheology Information Systems (IRIS) program [183], the number of modes of the DRS and the location of the τ_i in the logarithmic scale are considered as adjustable parameters and their choice is guided by the CRS. On the other hand, an incrementally overlay of the simple strategy of equispaced τ_i is allowed on the choice of the DRS modes. Given the τ_i, a linear least squares problem can be established using the DRS expression:

$$\begin{aligned} \mathrm{G}'(\omega) &= \sum_{i=1}^{\mathrm{N}} g_i \frac{\omega^2\tau_i^2}{1+\omega^2\tau_i^2} \\ \mathrm{G}''(\omega) &= \sum_{i=1}^{\mathrm{N}} g_i \frac{\omega\tau_i}{1+\omega^2\tau_i^2} \end{aligned} \tag{3.15}$$

Based on the experimental master curves discussed in Section 3.1.2.1, the storage and loss moduli are converted to shear conversion moduli and shear loss moduli. This conversion is done by varying Poisson's ratio as a function of temperature using the following relation:

$$\begin{cases} \mathrm{G}' = \frac{\mathrm{E}'}{2(1+\nu)} \quad and \quad \mathrm{G}'' = \frac{\mathrm{E}''}{2(1+\nu)}; \quad \nu = 0,3 \quad \text{when } \mathrm{T} < \mathrm{T}_g \\ \mathrm{G}' = 3\mathrm{E}' \quad and \quad \mathrm{G}'' = 3\mathrm{E}''; \quad \nu = 0,49 \quad \text{when } \mathrm{T} \ge \mathrm{T}_g \end{cases} \tag{3.16}$$

Then, analytical curves have been fitted to calculate the terms of Prony series. Figures 3.9, 3.10, and 3.11 display, respectively, the experimental master curves and the analytical fit of Generalized Maxwell model for TPT and PP backsheets, EVA and TPO-A encapsulant, and ECA-A1. A good cor-

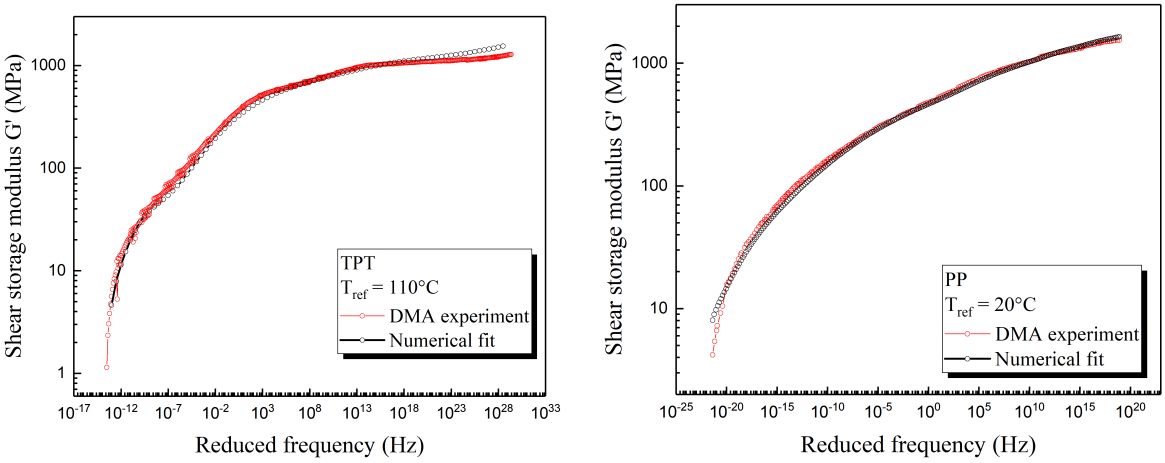

Figure 3.9: Experimental master curves and Maxwell Generalized fit for (a) TPT, and (b) PP backsheets

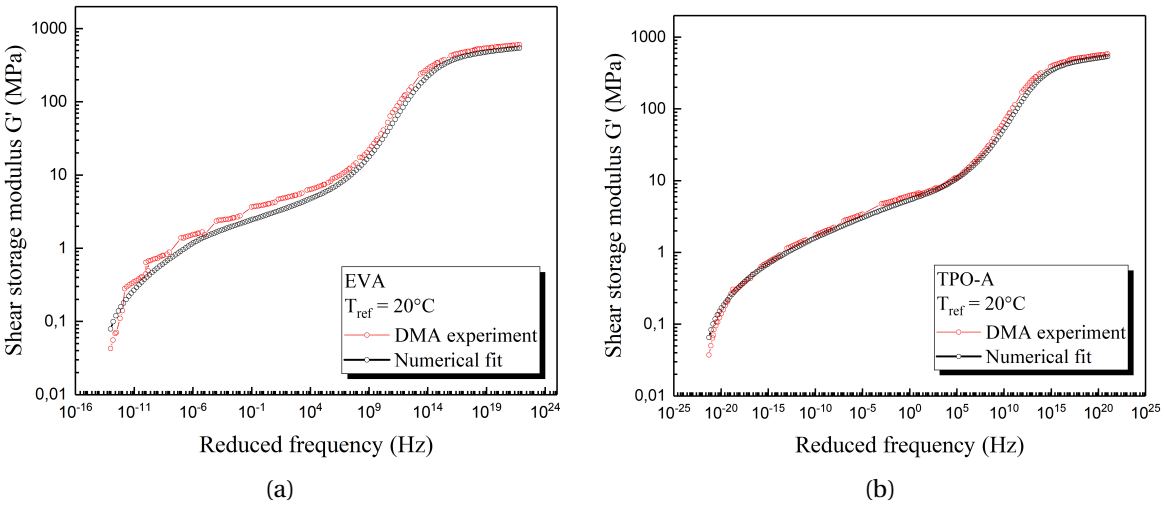

Figure 3.10: Experimental master curves and Maxwell Generalized fit for (a) EVA and (b), TPO-A encapsulants

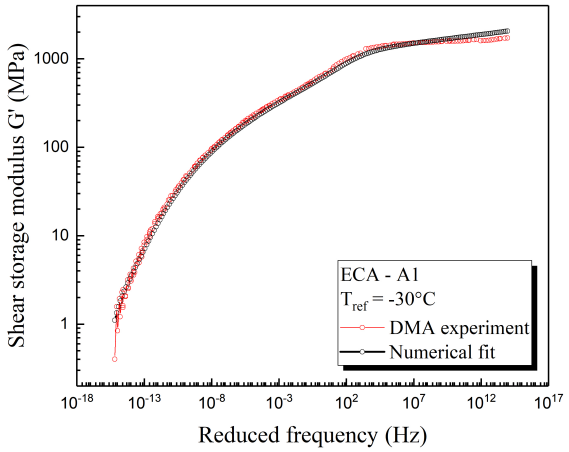

Figure 3.11: Experimental master curve and Maxwell Generalized fit for ECA-A1

relation can be observed between the experimental curves and the analytical ones. Nevertheless, a small deviation can be observed at low frequency (i.e. high temperature) which is due to the flowing state of the materials. The Prony series terms of each material are presented in Annex A

Table A.1.

3.1.3.2 Verification of viscoelastic model using FEM simulations

As presented in Section 3.1.2.2, two shift functions were chosen to represent the TTS depending over the large range of temperature. As all numerical calculations in this study are performed using the FE Abaqus software, the use of two shift functions is not possible with the traditional viscoelastic model available in Abaqus. To overcome such limitation, a user subroutine with combined shift function was used. To check the accuracy of the subroutine calculation, the shift factors were recorded as an output of simple tensile tests by varying the loading temperature. Figure 3.12 represents the comparison with the experimental and Abaqus viscoelastic model coupled with shift function subroutines.

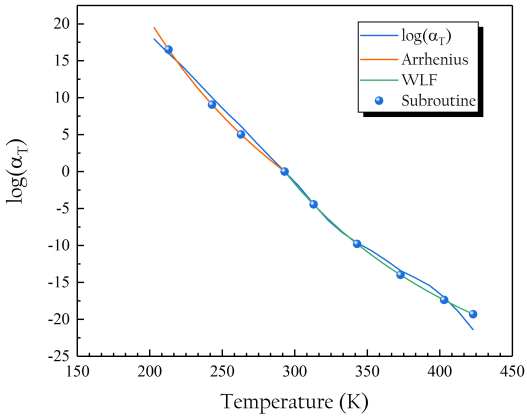

Figure 3.12: The correlation between the shift factors calculated by the subroutine with the experimental values and the analytical fit

To assess the accuracy of the analytical Maxwell Generalized model, relaxation tests have been performed experimentally at different temperature and strain conditions and then correlated with numerical tests. A tensile test set up by Instron Instrument coupled with Digital Image Correlation (DIC) technique was used for these measurement. The principle of the DIC technique will be presented in details in Section 3.2.1. Standardized specimens of 10mm width are used to test TPT and PP backsheets. For ECA-A1 4mm wide specimens were prepared manually using the same method explained in Section 3.1.1. The maximum relaxation strain was varied between 1.25% and 2.5% based on the temperature sensitivity of the specimen. After the application of the strain initial ramp, the displacement is fixed and the force and displacement fields are recorded. The measurement time is 300 seconds. The relaxation tests were performed at four temperatures:−30°C, 25°C, 60°C, and 150°C. For the ECA-A1, its stiffness becomes quite low at 150°C and its force response is quite close to the accuracy limit of the load cell. So for this material the measurements will be conducted at 60°C. A soak time of 15 minutes was applied before each measurement to ensure that the temperature is homogeneous in the material. For the tests performed at low temperatures, liquid nitrogen was used as purge gas.

Figures 3.13 give a comparison between the experimental and numerical relaxation curves for TPT and PP backsheets and for ECA-A1 at different temperatures. On the experimental curves a

decline of the relaxation stress just after fixing the maximum displacement is observed. Then a viscoelastic relaxation is observed on all materials. Higher temperatures result in lower relaxation stress values. For the TPT backsheet, a good correlation between the experimental and numerical curves is obtained except in the area of maximum relaxation stress where a deviation of 9.7% was observed in the curve at 25°C for example. This deviation decreases when the test temperature increases and a better correlation is achieved. In the case of the PP backsheet and ECA-A1, the deviation between the experimental and numerical measurements is even larger than for the TPT backsheet. Similarly, this deviation decreases with increasing test temperature. In general, it can be seen that the model overestimates the stiffness of the material compared to the experiment.

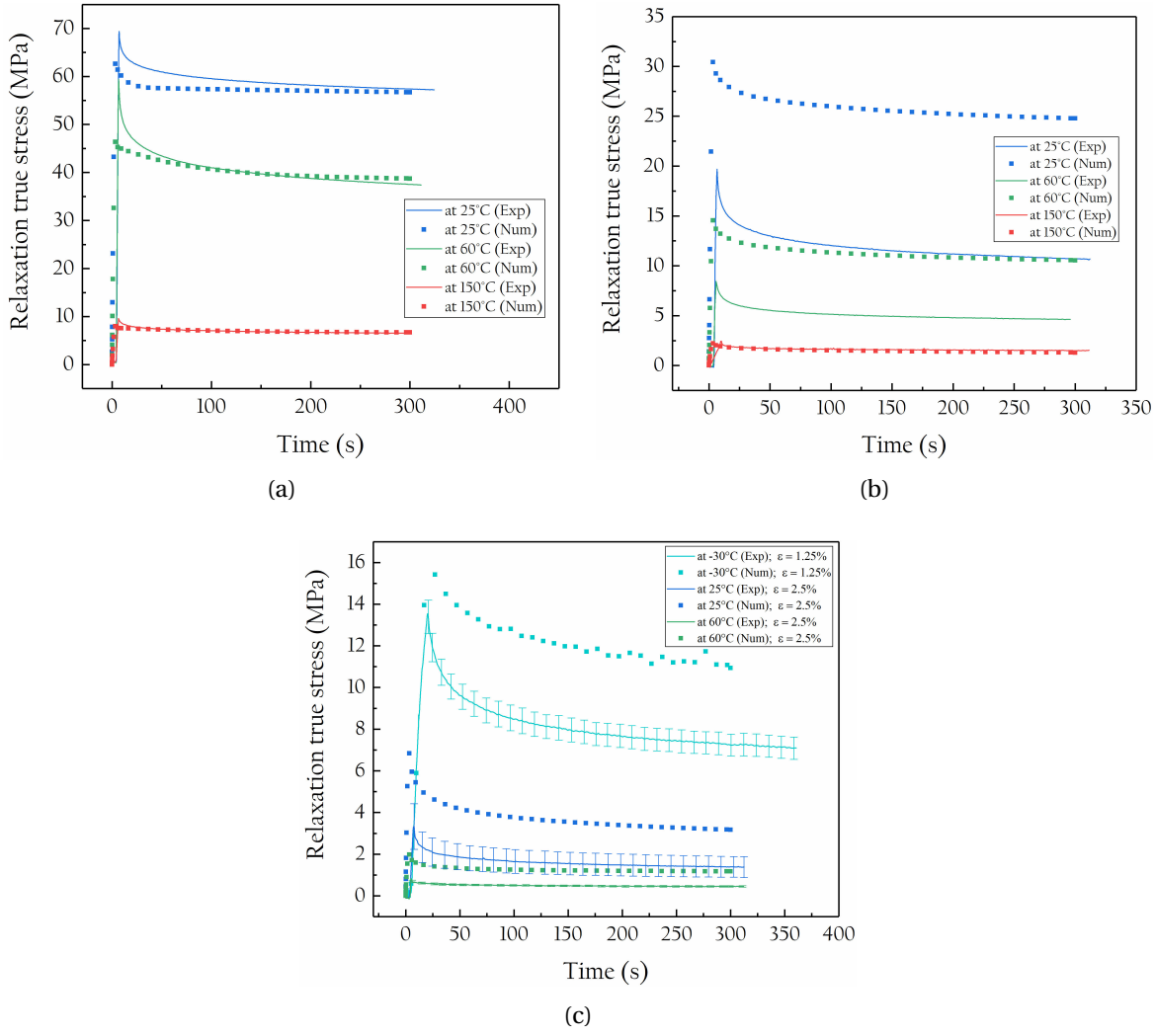

Figure 3.13: Comparison between experiment and numerical stress relaxation curves for (a) TPT and (b) PP backsheets, and (c) ECA-A1 using Maxwell Generalized model

To investigate the source of this deviation between the experimental and numerical relaxation curves, the evolution of the stress-strain curve was analyzed when applying the initial strain ramp before setting the maximum displacement. The results showed that for the curves where the deviation is too large between the experimental and numerical measurements, the stress-strain curve is not linear. Therefore, the experimental measurements are not performed under the same conditions of linearity used to build the viscoelastic model. This explains the overestimation of the

relaxation stress by the numerical model.

In order to verify this conclusion, an experimental relaxation test was performed with a strain of 1% at 25°C where the highest deviation was found between the experimental and numerical measurements. The 1% strain is normally included in the viscoelastic linearity interval.

Figure 3.14 shows the experimental and numerical relaxation stress curves at 25°C for both strains. It can be seen that the experimental and numerical curves at 1% strain are better correlated. Thus, the 2.5% strain applied in the case of the other measurements exceeds the linear viscoelastic limit which induces an overestimation of the material stiffness with the numerical model.

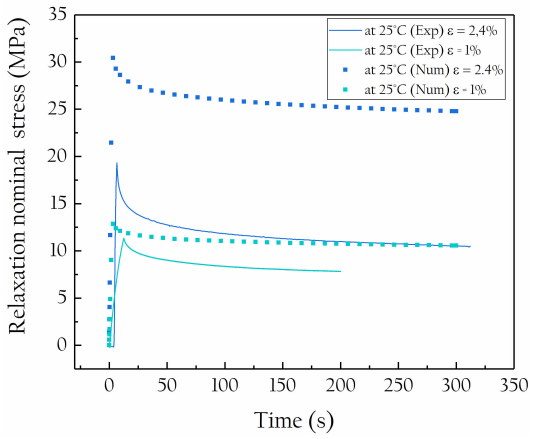

Figure 3.14: Comparison between experiment and numerical stress relaxation curves for PP backsheet at 25°C with two different strains

As mentioned before, the 1% strain is normally included in the linear viscoelastic range, however the correlation between the experimental and numerical curves is not optimal. The relaxation tests were performed with an Instron tensile instrument which loads the material at a macroscopic scale. On the other hand, the numerical model is based on DMA measurements that load the material at a mesoscopic scale. Therefore, the difference in the scale of the material loading and the change of the measuring instrument may induce a variation. The correlation between the two types of measurements can be improved by minimizing the relaxation strain as much as possible to get closer to the DMA measurements on which the numerical model is constructed.

In the case of ECA-A1, the deviation induced between the experimental and numerical curves is not totally related to the viscoelastic linearity. Insufficient repeatability was obtained between measurements on three different specimens subjected to the same test conditions as shown by the error bars in Figure 3.13c. As the specimens were prepared manually, we have analyzed microscopically their shape and distribution in the thickness. Figure 3.15 shows the section of a specimen loaded at 25°C. The presence of porosities near the skin and the core of the specimens was noticed. The skin of the specimen has a different color and microstructure than the core. Moreover, the microstructure and thickness of the specimen section are not homogeneous. These defects present in the specimens, and especially the presence of porosity, contribute to the underestimation of the stiffness of the material experimentally.

In conclusion, the numerical model shows reasonable results. Nevertheless, the experimental

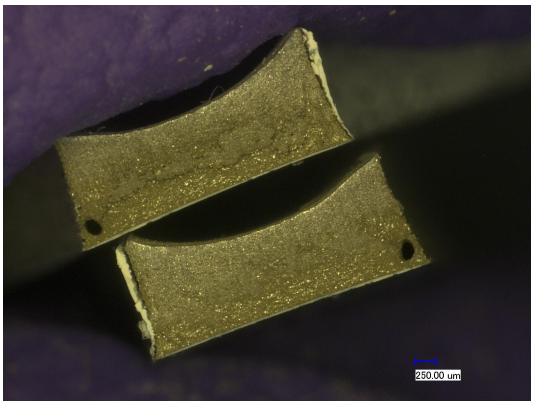

Figure 3.15: Micro-structure of the section of an ECA-A1 specimen tested at 25°C

conditions of the relaxation tests have not been well adapted. To achieve a good correlation with the model, it is necessary to minimize the relaxation strain to validate the hypothesis on which the Generalized Maxwell model is based. Furthermore, the method of manufacturing the ECA specimens should be improved.

In this part of the chapter, the thermomechanical behavior of different polymer materials used to fabricate PV modules has been investigated. In the following, the thermomechanical behavior of copper ribbons and SHJ solar cells will be studied.

3.2 Elasto-plastic behavior of copper ribbons

3.2.1 Tensile tests correlated with digital image correlation (DIC) technique

In this study, tensile tests coupled with a DIC system were performed. The purpose of this technique is to measure the local displacement field in the useful area of the specimen. The test setup is presented in Figure 3.16. It is composed of two cameras in stereo correlation that allow to capture the out-of-plane displacements. A thermal chamber was used to perform temperature controlled tests.

A speckle pattern of black dots on a white background, with dots of irregular size/shape were preformed on the surface of the specimen with a temperature resistant spray paint. During the test, cameras capture images. Using the image correlation software "VIC" [184], the displacement fields are then calculated by post-processing. From the gradient of displacements, the software calculates the local deformation fields on the surface of the specimen.

The software decomposes each image into several sub-images and calculates the displacement by comparing the position of each sub-image to its initial position in the reference image (see Figure 3.17). The average displacement of each sub-image is stored at each calculation iteration and then the software calculates the final displacement field. The global reference coordinate for both cameras is determined by a calibration step, which is performed by taking a number of images of a calibrated test pattern oriented along different orientations.

The DIC technique allows to determine the true strain and then to estimate the true stress as follows:

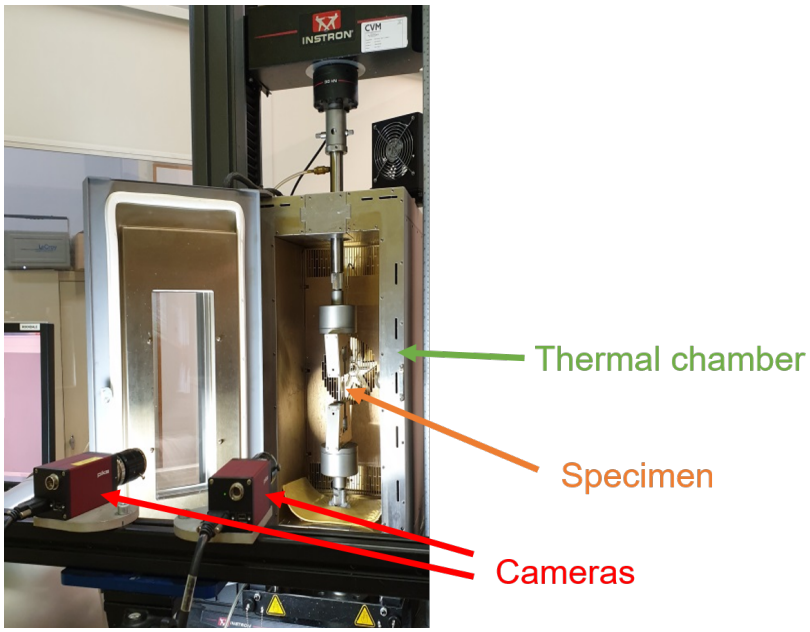

Figure 3.16: Experimental setup of the tensile test with 3D image correlation system

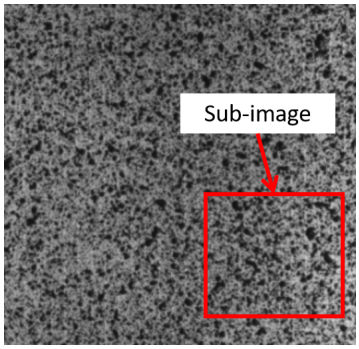

(a) Reference image

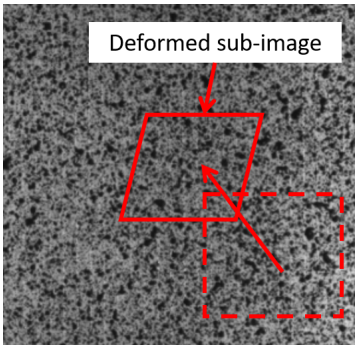

(b) Deformed image

Figure 3.17: Principle of the image correlation algorithm

$$\sigma(t) = \mathrm{F}(t)/\mathrm{S}(t) \tag{3.17}$$

with $\mathrm{F}(t)$ is the force and $\mathrm{S}(t)$ is the section variation of the specimen. $\mathrm{S}(t)$ can be determined by the following expression:

$$\mathrm{S}(t) = w(t) \times e(t) = w_0 \cdot e_0 \cdot \exp^{(}\varepsilon_{yy} + \varepsilon_{zz}) \tag{3.18}$$

where $w(t)$ and $e(t)$ are, respectively, the width and the thickness of the specimen at the time t. w_0 is the initial width of the specimen, and e_0 is the initial thickness of the specimen. ε_{xx} and ε_{zz} are the transverse strains in the width and thickness of the specimen respectively.

Equation 3.17 can be simplified with the assumptions of transverse isotropy (i.e. $\varepsilon_{xx} = \varepsilon_{zz}$), or the assumption of incompressibility (i.e. conservation of volume $\varepsilon_{xx} + \varepsilon_{yy} + \varepsilon_{zz} = 0$). These assumptions lead respectively to equations 3.19 and 3.20:

$$\sigma(t) = \frac{F}{w_0 \cdot e_0} \cdot \exp^{-2\varepsilon_{xx}} \tag{3.19}$$

$$\sigma(t) = \frac{F}{w_0 \cdot e_0} \cdot \exp^{\varepsilon_{yy}} \tag{3.20}$$

Copper ribbons with $Sn_{62}Pb_{36}Ag_2$ coating and a section of $5 \times 0.3 mm^2$ were tested. The different tests conditions are presented in the testing matrix (see Table 3.1). The temperatures of tests were chosen based on temperature ranges applied to the PV module during lamination and thermal cycling tests.

Figure 3.18a shows the tensile curves of the copper ribbons in the zone of maximum deformation at 25°C and 150°C using incompressibility assumption. The tensile curve at −30°C is not shown because it is noisy in the plastic domain due to deterioration of the speckles. Only results in the elastic domain will be used for −30°C. The results showed a sensitivity of the material to the temperature. As the temperature increases, the stresses decrease. Figure 3.18b displays tensile curves of the copper ribbons for two different strain rates at 25°C. Since the stress-strain curves of the two strain rates are overlaid, we assume that the copper ribbons do not exhibit any strain rate sensitivity for the different temperatures.

Young's modulus and Poisson's ratio were calculated for the different temperatures. The results are shown in Table 3.3. The experimentally measured Young's modulus values are slightly different than theoretical value of polycrystalline copper Young's modulus (E_{CuPoly}(T = −30°C) = 130.61GPa, and E_{CuPoly}(T = 22°C) = 128.17GPa) [185]. In the study of H.M. Ledbetter [185], the Young moduli were measured using an ultrasonic pulse-echo velocity measurement system. This method allows the calculation of the dynamic elastic constant of the material, which corresponds to long-wavelength phonons. However, in this study, a quasi-static method was used to measure the elastic constants which explains the differences observed between the values. G.S. Brady *et al.* [32] provided Young's modulus for several types of copper. The value measured experimentally corresponds well to a soft, wrought copper.

Temperature (°C)	Young modulus E (GPa)	Poisson's ratio ν
150	35.6	0.34
25	103.4	0.33
-30	133.2	0.33

Table 3.3: Elastic properties of leaded ($Sn_{62}Pb_{36}Ag_2$) copper ribbons

The dependency of the Young modulus to the temperature will be used to define the elastic properties of the material in FE analysis.

3.2.2 Constitutive model of Johnson-Cook

Wiese *et al.* [158] have studied the elasto-plastic behavior of copper ribbons. In their study, a Ramberg-Osgood model was fitted to the experimental curve. For simplicity reasons, a bilinear plasticity model has been adopted for their FE calculations. However, this model does not take

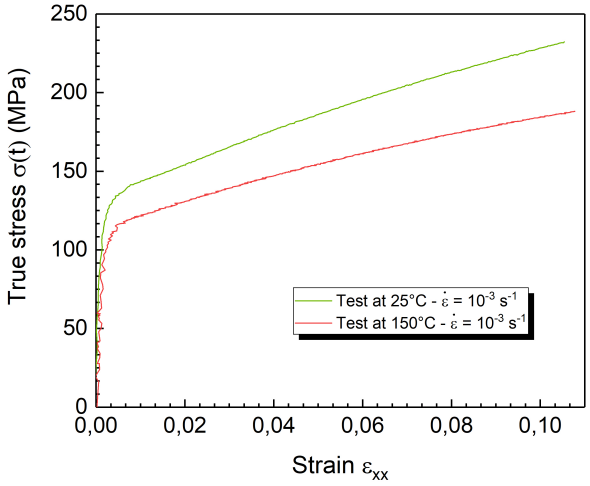

(a)

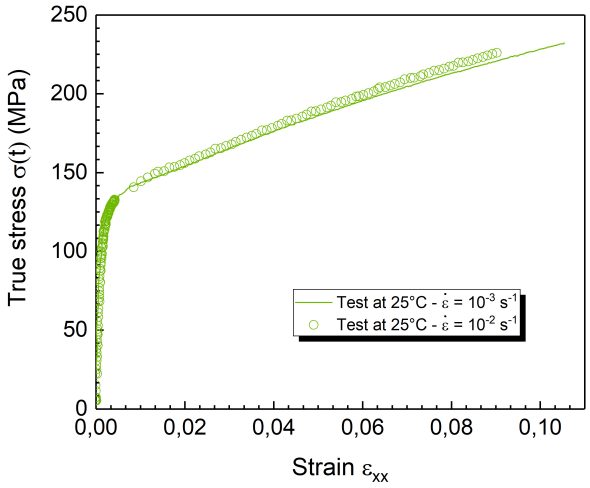

(b)

Figure 3.18: Tensile curves of copper ribbons at (a) different temperature and a strain rate of $10^{-3}/s$ and (b) 25°C and two different strain rates

into consideration the temperature dependency of the copper ribbon.

In this study, based on the tensile curves presented in Figure 3.18a, an elasto-plastic model of Johnson-Cook with isotropic hardening was identified analytically. The constitutive equation for the von Mises flow stress σ_p is given as below [186]:

$$\sigma_p = \left[A + B\left(\bar{\varepsilon}^{pl}\right)^n\right]\left[1 + C\ln\dot{\epsilon}^*\right]\left(1 - \hat{T}^m\right) \tag{3.21}$$

where $\bar{\varepsilon}^{pl}$ is the equivalent plastic strain, $\dot{\epsilon}^* = \dot{\epsilon}/\dot{\epsilon}_0$ is the dimensionless plastic strain rate for $\dot{\epsilon}_0 = 10^{-3}s^{-1}$, A is the yield stress at room temperature, B and n represent the hardening modulus and work-hardening exponent, respectively, C is the strain rate effect, m depicts the thermal softening coefficient and $\hat{T}$ is the homologous temperature of the sample defined as [187]:

$$\hat{T} \equiv \begin{cases} 0 & \text{for} \quad T < T_{room} \\ (T - T_{room}) / (T_{melt} - T_{room}) & \text{for} \quad T_{room} \leq T \leq T_{melt} \\ 1 & \text{for} \quad T > T_{melt} \end{cases} \tag{3.22}$$

where T is the current temperature, T_{room} is the room temperature and T_{melt} is the melting temperature.

In this study, no strain rate effect was observed in the experimental results as shown in Figure 3.18b. Thus, coefficient C is not considered and the equation 3.21 can be simplified [188]:

$$\sigma_p = \left[A + B\left(\bar{\varepsilon}^{pl}\right)^n\right]\left(1 - \hat{T}^m\right) \tag{3.23}$$

The equivalent plastic strain can be defined with the von Mises equation as follows [189]:

$$\bar{\varepsilon}^{pl} = \frac{\sqrt{2}}{3}\left[\left(\varepsilon_x^p - \varepsilon_y^p\right)^2 + \left(\varepsilon_y^p - \varepsilon_Z^p\right)^2 + \left(\varepsilon_z^p - \varepsilon_x^p\right)^2 + 6\left(\varepsilon_{xy}^p\right)^2 + 6\left(\varepsilon_{xz}^p\right)^2 + 6\left(\varepsilon_{yz}^p\right)^2\right]^{1/2} \tag{3.24}$$

$\varepsilon_x^p, \varepsilon_y^p, \varepsilon_z^p, \varepsilon_{xy}^p, \varepsilon_{xz}^p$, and ε_{yz}^p are the components of the plastic strain tensor.

In the case of uniaxial tensile test in the x direction, strains appear in the axial direction and both transverse directions. For an isotropic material that is incompressible during plastic deformation (i.e. $\varepsilon_y^p = \varepsilon_z^p = -\frac{1}{2}\varepsilon_x^p$). Thus, for a state of uniaxial stress the equivalent plastic strain may be simplified as below:

$$\bar{\varepsilon}^{pl} = \frac{\sqrt{2}}{3}\left[\left(\varepsilon_x^p + \frac{1}{2}\varepsilon_x^p\right)^2 + \left(-\frac{1}{2}\varepsilon_x^p - \varepsilon_x^p\right)^2\right]^{1/2} = \frac{\sqrt{2}}{3}\left[\frac{18}{4}\left(\varepsilon_x^p\right)^2\right]^{1/2} = \varepsilon_x^p \tag{3.25}$$

This model allows to describe the elasto-plastic behavior of copper ribbons taking into consideration the temperature dependency of the behavior as discussed in Section 3.2.1. The analytic model of Johnsoon-Cook was fitted to the experimental curves. The parameters of the model are presented in Table 3.4.

A (MPa)	B (MPa)	n	m	T_{room} (°C)	T_{melt} (°C)
101.57	331.58	0.42	0.81	10	1085

Table 3.4: Parameters of elasto-plastic Johnson-Cook model for leaded ($Sn_{62}Pb_{36}Ag_2$) copper ribbons

The analytical model was numerically validated by FE modeling of tensile tests. Figure 3.19 displays the experimental, and numerical stress-strain curves of leaded ($Sn_{62}Pb_{36}Ag_2$) copper ribbons at two different temperatures. The numerical results show a good correlation with the experimental stress-strain curves.

In this section, the thermomechanical behavior of copper has been studied using tensile measurements correlated with the DIC technique. The results showed a temperature dependency of its behavior in the temperature range of the PV module manufacturing. However, no dependency on the loading rate was found. Accordingly, a mathematical model was established based on the experimental curves of the tensile tests, which takes into consideration the temperature dependence.

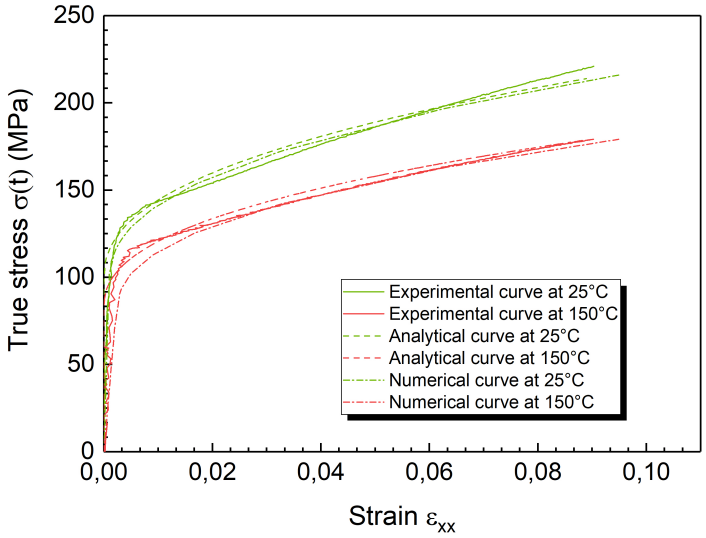

Figure 3.19: Comparaison between experiment and numerical stress-strain curves using Johnson-Cook elasto-plastic model

3.3 Study of the mechanical behavior of solar cells

3.3.1 Elastic properties

As discussed in section 1.1.1.1, silicon wafers go through several processes: from passivation to metallization to obtain the final product which is the solar cell. Eitner [24] has studied the variability of the elastic properties of the RISE-EWT solar cells compared to a silicon wafer, by calculating Young's modulus analytically based on the 3-point bending tests using the classical beam theory. His results show that the Young's modulus remains invariant between the RISE-EWT solar cell and the silicon wafer. However, the beam theory is based on the assumption that the material is isotropic and homogeneous and neglects the Poisson's effect. This cannot be valid in the case of solar cells, thus the analytical calculation of Young's modulus must be taken with caution. Therefore, in this study, a numerical analysis was conducted alongside the analytical method.

In this work, the focus is on SHJ solar cells. Based on 4-line bending tests performed on $156,75 \times 156,75 mm^2$ pseudo-square SHJ solar cells, Young's modulus has been calculated analytically. Then the same test was modeled numerically using the silicon wafers elastic properties to determine the impact of surface treatments on the elastic constants of the silicon wafer.

The 4-line bending tests were performed with 4 steel cylindrical rollers of $8mm$ diameter based on the method developed in [30; 190]. The upper and lower rollers are spaced between them by a distance of $60mm$ and $100mm$ respectively as shown in the setup presented in Figure 3.20. A constant crosshead speed of $10mm/min$ was set for the rollers' displacement in order to perform the tests in a quasi-static loading condition. Twenty solar cells with an average thickness equal to $163\mu m \pm 3$ were tested. Half of the cells were arranged with BB parallel to the rollers and the other half with BB perpendicular to the rollers (see Figure 3.20).

Figure 3.21 displays experimental force-displacement curves of the twenty solar cell samples. The curves showed a very large deflection up to $22mm$, which is due to the small thickness of

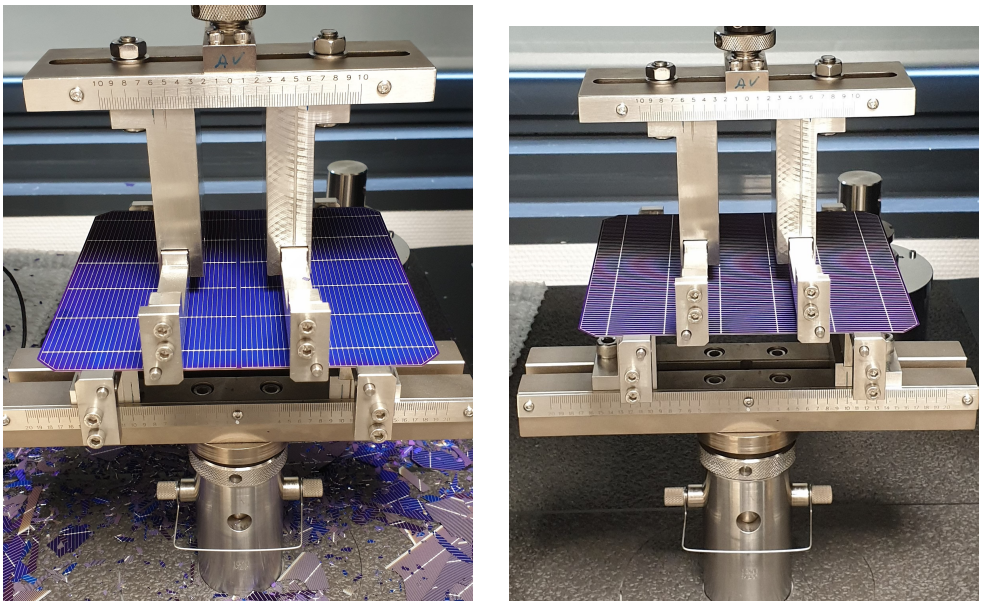

(a) Busbars perpendicular to the cylinders (b) Busbars parallel to the cylinders

Figure 3.20: The 4-line bending experimental test setup used to test solar cells

the samples. Good reproducibility was also observed in the elastic domain contrary to the large variability in the displacement at failure and thus the stress at failure.

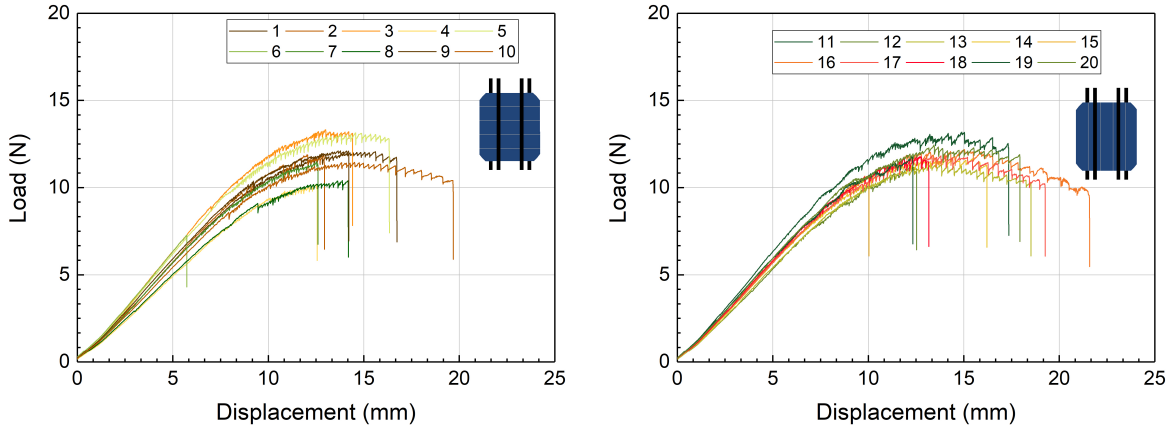

(a) Busbars perpendicular to the cylinders (b) Busbars parallel to the cylinders

Figure 3.21: Experimental force-displacement curves for 4-line bending tests

Young's moduli in both perpendicular and parallel directions were calculated analytically using the beam theory in the case of small displacements. When the specimen undergoes 4-line bending, the upper surface is subjected to compression and the lower surface is under tension. The particularity of the 4-line tests is that the maximum zone of stress fields is always placed in the center of the plate, and it is quite homogeneous. During loading, the thickness of the specimen remains unchanged and therefore the maximum stress and strain are located at the surface of the specimen (see Figure 3.22). Based on these conditions, the Young's modulus can be expressed as follows [191]:

$$\mathrm{E} = \frac{\mathrm{P}(a-d)^2(a+2d)}{4bh^3\delta} \tag{3.26}$$

where $a = 100mm$ and $d = 60mm$ represent the distance between the lower and upper rollers respectively, P is the load in (N), δ indicates the crosshead displacement in (mm), and b and h stand for the width and thickness of the specimen respectively. The Young's modulus is calculated for each sample by linear regression between $\delta = 1mm$ and $\delta = 2mm$.

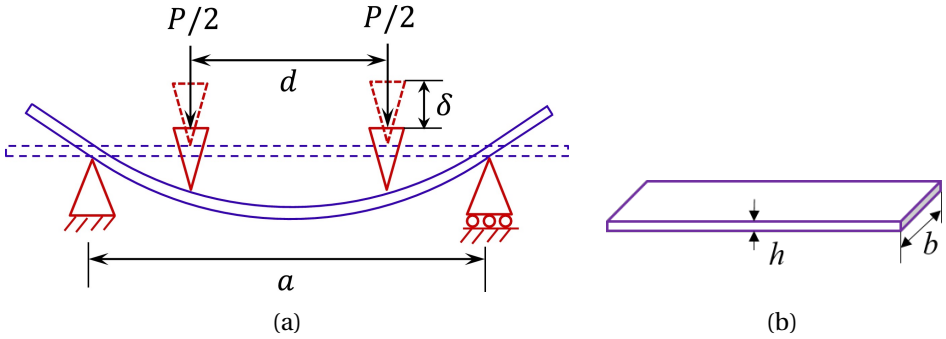

Figure 3.22: Schematic representation of 4-point bending test [191]

Figure 3.23 displays a comparison between the average analytical Young's modulus of SHJ solar cell samples, oriented perpendicularly and in parallel respectively to the busbars, and the elastic properties of the silicon wafer [28]. The largest deviation between the analytical value and the Young's modulus of the silicon wafer is in the case of cells oriented parallel to the busbars up to 2.4GPa. This deviation is considered acceptable taking into consideration the validity of the beam theory in the case of the solar cell and also the measurement dispersion due to the variation of the samples thickness.

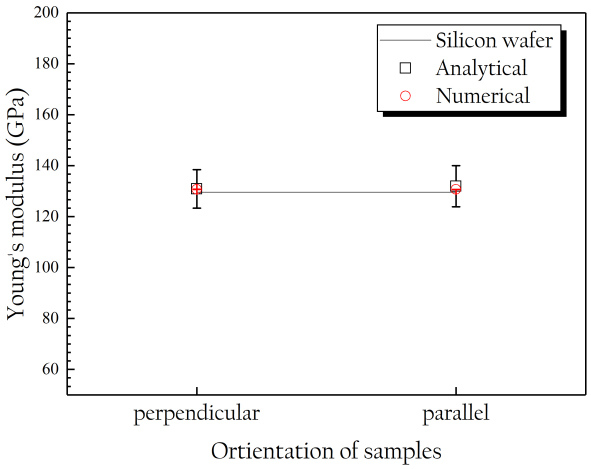

Figure 3.23: Extracted analytical (□) and numerical (○) Young's modulus for SHJ solar cells in both directions parallel and perpendicular to the rollers. The straight line denotes the elastic properties of silicon [28]

The test modeling was performed with a 3D model of a quarter of the 4-line bending device as shown in Figure 3.24a to validate the analytical solution. The model is composed of a quarter of the cell and a half of the top and bottom roller. Symmetry conditions were applied to the symmetrical edges. A displacement was applied on the upper roller and a fixed boundary conditions on both displacements and rotations was imposed on the lower roller. The model contains 6000 linear shell elements with reduced integration (5 integration points in the thickness). The friction between the rollers and the cell is modeled using a Coulomb model with a friction coefficient equal to 0.1 [188].

An exponential law was used to manage the contact pressure between the rollers and the solar cell in the normal direction. An orthotropic elastic behavior of silicon was used from Table 1.1.

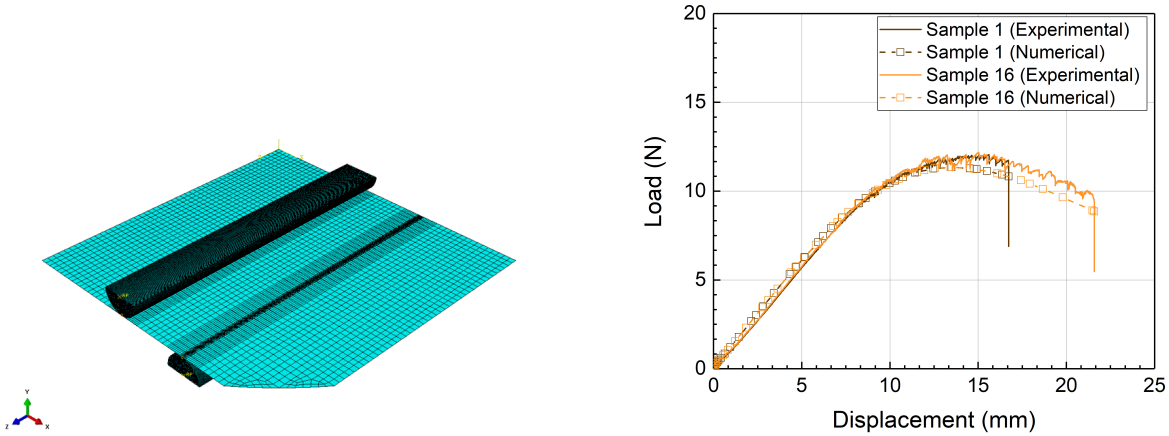

(a) (b)

Figure 3.24: (a) Model meshing of the 4-line bending test set-up, and (b) Experimental and numerical correlation of load-displacement curves for sample 1 and 16

Figure 3.24b displays the numerical and experimental force-displacement curves of the 4-line bending tests regarding specimens 1 and 16 as their thickness corresponds to the average thickness of the samples. The force-displacement curves obtained numerically are in good agreement with the experimental curves. Based on these numerical simulations, the elastic modulus in both directions was calculated numerically by varying the thickness of the solar cell. The average values are presented in Figure 3.23. *The Young's modulus calculated numerically is well consistent with the theoretical values and the values calculated analytically. Therefore, the manufacturing processes of the solar cell do not have a significant influence on the elastic behavior of the silicon wafer.*

3.3.2 Fracture strength of SHJ silicon solar cells : 4-line bending test

As discussed in Section 3.3.1, the dispersion of the displacement at failure observed in the force-displacement curves is significant. For some SHJ solar cells, the displacements of the crosshead at failure reach quite high values, which induces large rotations of the solar cell. Therefore, the beam theory based on the assumption of small displacements and small perturbations is not valid for the calculation of the failure stress. The stress at failure for each specimen was calculated numerically by varying the displacement at failure and the thickness of the specimen in each calculation case. Figure 3.25a shows the tangential stress distribution corresponding to the displacement at failure of sample 16. The upper face of the cell is subjected to compression and the lower face is subjected to tension. As the geometry of the cell is modeled using shell elements, the post-processing of the data is considered on the layer subjected to tension. A homogeneous maximum stress distribution is noticed in the central zone in the solar cell between the two upper rollers.

For brittle materials such as silicon, the calculation of the stress at failure needs to be evaluated statistically. The most used method is the statistic fit with a Weibull distribution [192]. This distribution is based on the weak link theory which represents the failure mechanism of brittle structures. The probability of failure is defined as follows:

$$P_f(\sigma) = 1 - \exp\left[-\left(\frac{\sigma}{\sigma_\theta}\right)^m\right] \tag{3.27}$$

where σ_θ is the stress at which 63.2% of the samples break (i.e. where $P_f(\sigma = \sigma_\theta)$) defined also as the characteristic fracture strength, and m is the Weibull modulus. These Weibull parameters are calculated from the numerical stress data using the maximum-likelihood estimation (MLE) method. Details of this method are available in the works of many authors, e.g. [193; 194].

Figure 3.25b displays the Weibull probability logarithmic scale fit regarding the failure stress of solar cells oriented in perpendicular and parallel direction to the BB. The curves reveal that the fracture strength in the perpendicular direction is lower than the one in the parallel direction. Thus, the solar cell exhibits an anisotropic fracture strength.

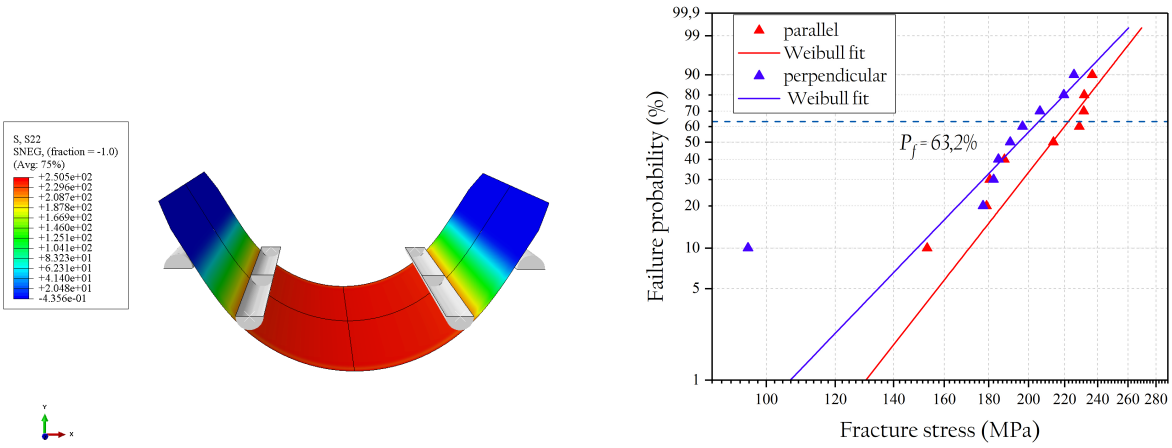

(a) (b)

Figure 3.25: (a) The tangential stress distribution in the solar cell corresponding to the displacement at failure (in MPa), and (b) Weibull probability logarithmic scale plot for SHJ solar cells tested in 4-line bending in the directions parallel and perpendicular to the BB

Table 3.5 shows the characteristic fracture strength σ_θ and Weibull modulus m calculated with 90% confidence bounds, based on the standard ASTM C 1239-07 [195], regarding the testing direction. The accuracy of estimation of these parameters depends on the size of the sample. L. Carton [30], studied the influence of the sample size on the weibull parameters in the case of silicon wafers. To achieve an accuracy of less than 5% in the parallel direction and 2% in the perpendicular direction, a minimum sample size of N = 30 is required. However, more than twice the sample size is needed to achieve an average relative error under 5% in the Weibull modulus m [30]. The number of samples selected for our study does not correspond to these precision ranges. But the general purpose of this study is to compare the fracture strength of solar cells with that of wafers to check if there is a large and significant difference. Comparing the fracture strength of the wafers [30] and the solar cell presented in Table 3.5, the wafer in the parallel direction has a higher fracture strength of $\approx$ 20 MPa than the cell. On the other hand, the difference is larger (i.e. 86.35 MPa) in the perpendicular direction with a higher fracture strength in the solar cell. Although the difference is less important in the parallel direction, but in both cases it is not negligible.

Testing direction	Characteristic fracture strength σ_θ (MPa)	Weibull modulus m (-)
Parallel to BB	222 (208.42...236.67)	8.6 (5.58...13.24)
Perpendicular to BB	205.35 (190.12...221.81)	7 (4.54...10.8)

Table 3.5: Weibull strength parameters with 90% confidence bounds (based on ASTM C 1239-07 [195]) for both tested directions of solar cell

3.4 Measurement of thermal properties

3.4.1 Coefficient of thermal expansion (CTE)

The CTE of PV module components is an essential parameter to characterize since it governs the thermal strain. As mentioned in Section 2.2.2, the mismatch of CTE has an important role in creating internal stresses in the PV module. Springer *et al.* [164] studied the thermal expansion of mainly epoxy-based ECAs. Bosco *et al.* [12] have provided a large database of CTE data for encapsulants and backsheets. In both studies, measurements were performed with a dilatometer. U. Eitner [24] was interested in the thermal expansion of glass using the DIC method.

In this work, the thermal expansion measurement was performed using digital image correlation system. Several authors are interested in this technique of measurement e.g. [196–198]. In this study, CTE measurements were performed for several PV module components: SHJ solar cell, leaded ($Sn_{62}Pb_{36}Ag_2$) copper ribbons, laminated TPO-A encapsulant, the TPT and PP backsheets, and two types of acrylate-based ECA. The encapsulant TPO-A used in this measurement was laminated at 150°C between two glass plates. These glass plates were covered with Teflon to prevent the encapsulant from adhering to the glass. The ECA test specimens were prepared manually using the same method presented in Section 3.1.1. The conditions for experimental CTE measurement are presented in Table 3.1. A thermal chamber was used to apply thermal loading to the specimen. For low temperatures, liquid nitrogen was used as a coolant.

The measurement protocol has been adapted to the type of material:

- Copper: a pre-load of 10N was applied to the ribbon to avoid any possible buckling of the sample at high temperatures.
- SHJ solar cell: the clamps hold it on the top side and it is free at the bottom.
- Polymer materials: normalized specimens of 4mm width were clamped between the upper clamps and left free between the lower clamps. The lower tip of the specimen was cut to avoid any influence of gravity on the measurement of the thermal strain.

Since the thermal expansion of copper ribbon and solar cell is assumed to be linear, thermal loading by 10°C steps were applied. At the end of each step, one hundred images of the sample have been captured. Using DIC analysis, the thermal strain of the material is calculated. The final thermal deformation is obtained for each temperature by averaging over one hundred values collected over the different temperature steps.

Regarding polymer components, the test consists in applying a temperature ramp of 1°C/min to the sample and measuring its thermal strain. An image acquisition frequency of 4 images/min was used. The final strain obtained for each sample corresponds to the average of the thermal strain in three virtual extensometers of the same length at different positions in the region of interest of the specimen.

Figure 3.26a shows the thermal strain of the SHJ solar cell in the BB direction (MD) and in the direction perpendicular to the BB (TD). Since the strain is linear, a parabolic fit of the curve is chosen to determine the CTE of the cell in both directions by deriving the thermal strain with respect to the temperature as described below:

$$\alpha_{th} = \frac{\partial \varepsilon_{\text{th}}}{\partial \text{T}} = c_1 + 2c_2\text{T} \tag{3.28}$$

This method is used for materials with linear thermal expansion, including solar cell, copper ribbon and PP backsheet. The other materials have exhibited non-linear thermal expansion, and therefore another method will be used later to determine their CTE.

The values of the CTE calculated as a function of temperature for the solar cell and in both directions of measurement are presented in Figure 3.26b. An anisotropic thermal expansion is noticed, with more expansion in the TD direction which corresponds to the direction of the metallization fingers. These metallization fingers are composed of a polymer based adhesive with a high concentration of silver particles. Silver has a higher CTE ($\approx 19 \times 10^{-6}$1/°C [32]) than silicon, and given the density of the fingers in the solar cell, its thermal expansion in the direction of the metallization lines increases.

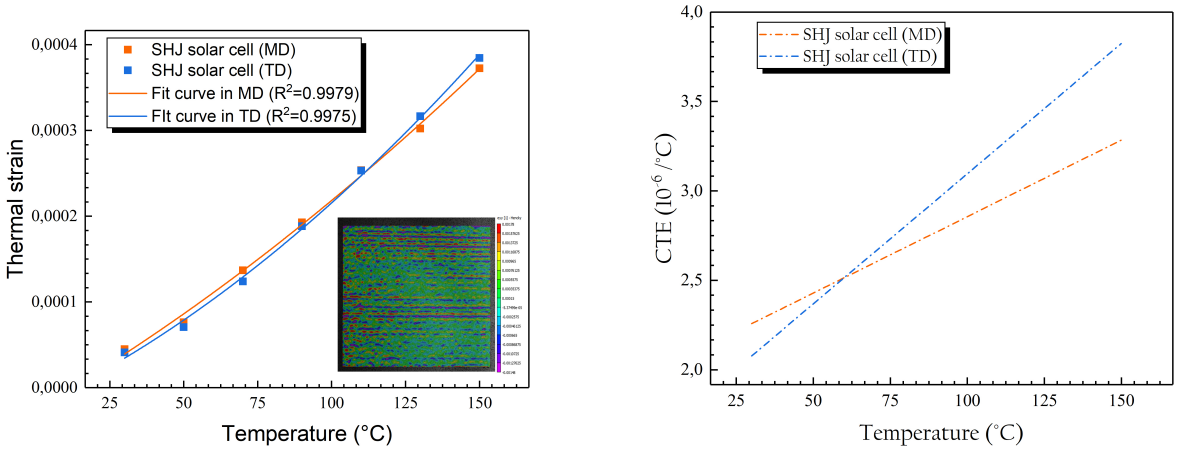

(a) (b)

Figure 3.26: (a) Thermal strain (with a representation of the strain gradient), and (b) Coefficient of thermal expansion (CTE) of SHJ solar cell in both direction MD and TD in the range of temperature of 30°C to 150°C

Figure 3.27a and 3.27b illustrate the thermal expansion of leaded ($Sn_{62}Pb_{36}Ag_2$) copper ribbons and PP backsheet respectively. As their thermal strain is linear, a parabolic fit has also been used and the CTE is calculated based on Equation 3.28. The PP backsheet shows a minor anisotropic thermal expansion.

Figure 3.28a shows the evolution of the thermal strain of the laminated TPO-A encapsulant

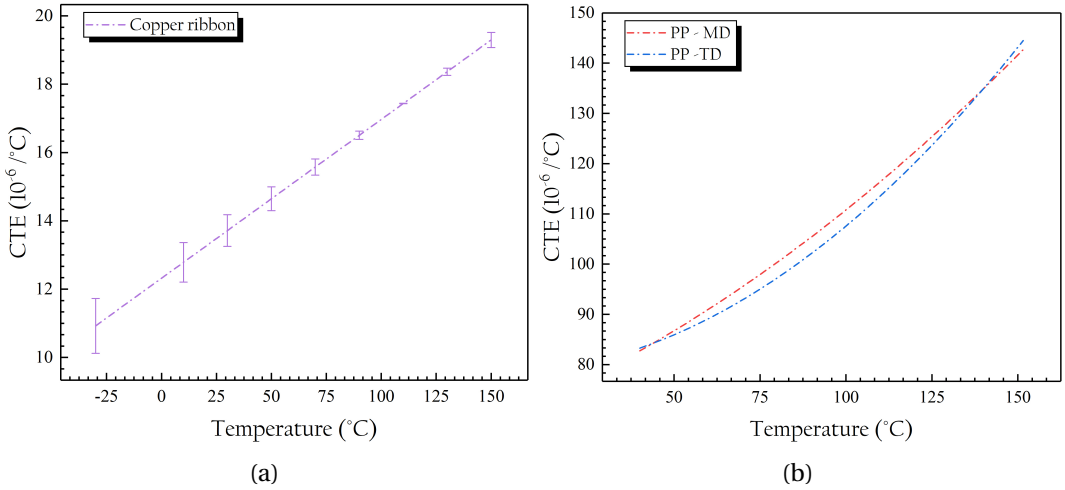

Figure 3.27: Coefficient of thermal expansion (CTE) of (a) leaded ($Sn_{62}Pb_{36}Ag_2$) copper ribbons and (b) PP backsheet

with respect to temperature. The thermal strain of the encapsulant is increasing up to the temperature of 60°C where it starts to decrease. This decrease is induced by material contraction. Lamination of samples might induce residual stresses. Therefore when the specimen are reheated, these stresses relax and the sample shrinks.

Figure 3.28b shows the thermal strains of ECAs A1 and A2 with respect to the loading temperature. For ECA - A1, the thermal strain of sample 1 is almost linear while sample 2 expands with a rather exponential trend and with a higher level of strain. This difference is mainly related to the presence of porosity in the samples. On the other hand, the measurements on ECA-A2 do not show such a large difference between the thermal strains. The difference becomes more pronounced when approaching its glass temperature around 95°C. Furthermore, the slope of the thermal strain changes after the glass transition, which means that the material expands differently between the glassy and the rubbery phase.

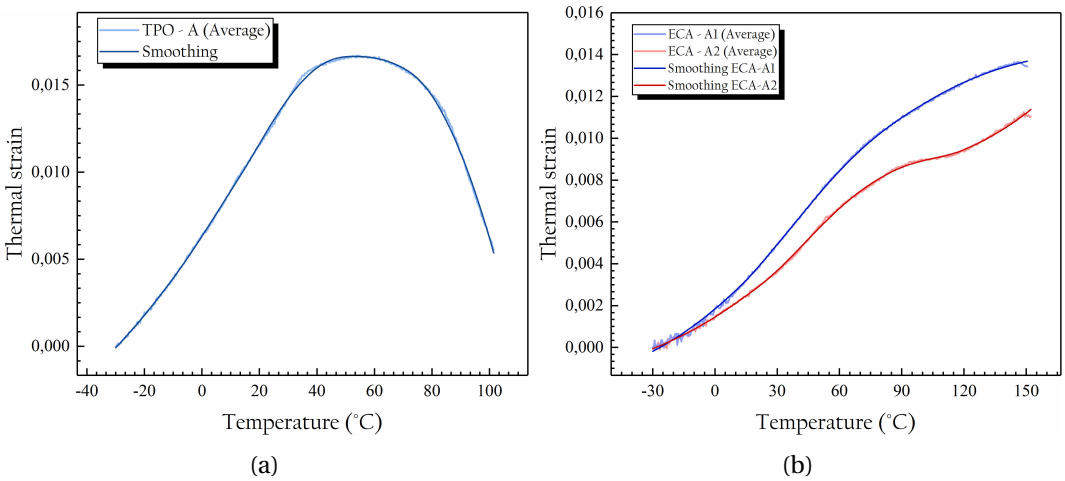

Figure 3.28: Thermal strain and smoothing of curves using the Savitzky-Golay method of (a) encapsulant TPO-A and (b) ECAs A1 and A2

These materials show a non-linear thermal strain evolution. Therefore the method of calculation of the CTE used in this case has been adapted. The CTE is calculated from the smoothed

thermal strain curve using the Savitzky-Golay method [199] as explained in Appendix B.

Figure 3.29 represents the CTE measurements for the TPO-A encapsulant and the A1 and A2 ECAs. As expected, the CTE of the TPO-A encapsulant turns negative when the residual stresses related to lamination are released. However, its expansion in the temperature range between -30°C and 20°C is almost constant. Concerning ECAs, both types of adhesives have an increasing CTE in the temperature range between -30°C and 50°C and then decreasing beyond this temperature. However, the CTE of ECA-A2 increases again after reaching its glass transition temperature.

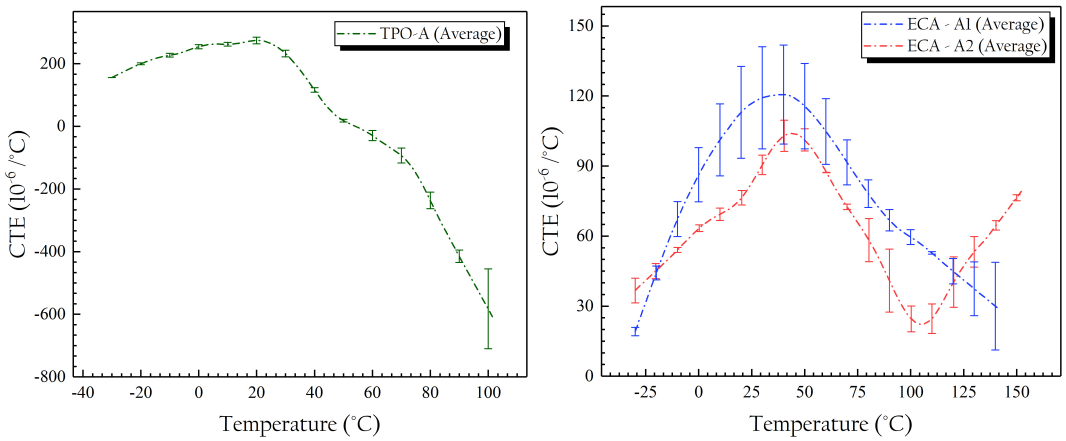

(a) (b)

Figure 3.29: Coefficient of thermal expansion (CTE) of (a) encapsulant TPO-A and (b) ECAs A1 and A2

3.4.2 Specific heat (modulated DSC test)

Specific heat is one of the three material constants that contributes to the heat equation as described in Section 2.1. It represents the ability of the material to absorb or release heat when the temperature changes. This capacity varies according to the nature and type of the material. In the case of our study, an interest was devoted to the polymer material as their heat capacity varies according to their chemical formulation. To measure the specific heat, the modulated DSC method was used. This method consists in applying a sinusoidally modulated temperature ramp to differentiate the contribution of temperature from heating rate in the heat flux response of a sample. Thus the measured specific heat C_p is obtained from this equation [200]:

$$\mathrm{Cp} = \frac{\mathrm{A_{MHF}}}{\mathrm{A_{MHR}}} \times \mathbf{K} \tag{3.29}$$

where $\mathrm{A_{MHF}}$ is the modulated heat flux variation, $\mathrm{A_{MHR}}$ is the modulated heating rate variation, K is a calibration coefficient equal to the ratio of the measured specific heat of a sapphire sample to the theoretical specific heat value of the sapphire. Hermetic aluminum pans were used to encapsulate samples of mass between 15-20 mg. A heating ramp of 1°C/min was applied with a modulation of 1°C for 120s. Different type of materials were characterized, TPO-A encapsulant, PP and TPT backsheets, both acrylate based ECA A1 and A2. The temperature range applied in each case is presented in Table 3.1.

Figure 3.30 shows the evolution of the specific heat for the tested materials in different temper-

ature ranges. The encapsulant has a specific heat almost twice higher than the backsheets, which means that it absorbs more heat and thus slightly insulates the heat transmission between the different layers of the PV module. ECAs have the lowest specific heat in the characterized material group. This is due to their high concentration of silver particles which release heat better than polymers.

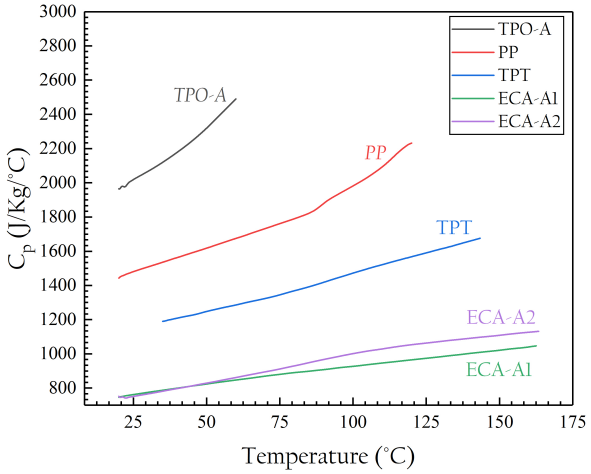

Figure 3.30: Specific heat C_p of TPO-A encapsulant, TPT and PP backsheets, and ECA A1 and A2 with respect to the temperature

The specific heat of all materials is increasing with temperature. To estimate the influence of this variation on the numerically calculated output temperature, a comparative numerical verification was performed considering in one case a constant C_p and in the other case a variable C_p. A temperature ramp is applied on a surface of a cubic element, the nodal temperature is compared between the two cases. A maximum error of 2% is obtained. As a result, the specific heat can be considered as constant in the thermomechanical modeling of the interconnection and lamination processes.

Material	TPO-A	TPT	PP	ECA-A1	ECA-A2
Specific heat (J/Kg/°C)	1848,7	1010.85	1272.11	762.04	751.13

Table 3.6: Specific heat at ambient temperature of TPO-A and TPO-B encapsulant, PP backsheet and ECA A1 and A2 (acrylate based).

3.4.3 Thermal conductivity

The thermal conductivity of the PV module layers has a significant contribution to the heat transfer during the fabrication of the PV module. The thermal transfer is coupled with the thermal deformation of the components, and thus can influence the numerical thermal stress. In the literature, few researchers have been interested in this thermal property of materials for PV applications [48; 162]. For this reason, experimental measurements of the thermal conductivity of the materials used in our numerical studies have been performed. There are several methods for measuring thermal conductivity [201]. In our study, a lambda-meter was used.

Rectangular shaped samples with a minimum size of $5 \times 5 \times 1 cm^3$ were prepared. In the case of the encapsulant and the backsheet, about twenty layers were laminated. For the ECAs, a deposit of thin layer by layer in a mold was made. Each layer was degassed and then cross-linked before adding more material. The measurements are performed at room temperature. The measuring probe is put in surface contact with the measured sample. In order to eliminate the contact resistance between the two, a silicone grease was spread on the measuring surface. Table 3.7 shows the results of the thermal conductivity measurements on the studied materials. The thermal conductivity values measured for the two types of encapsulant are quite close due to their quite identical chemical composition. The thermal conductivity of ECA-A2 is higher than ECA-A1 due to its high concentration of silver particles.

Material	TPO-A	TPO-B	PP	ECA-A1	ECA-A2
Thermal conductivity (W/m/K)	0.46	0.45	0.32	0.61	0.71

Table 3.7: Thermal conductivity at ambient temperature of TPO-A and TPO-B encapsulant, PP backsheet and ECA A1 and A2 (acrylate based).

Conclusion

The purpose of this chapter was to characterize the thermomechanical behavior of the PV module components. First, the viscoelastic behavior of the polymeric materials: encapsulant, backsheet and ECA was identified based on DMA curves in temperature sweep. The results showed that **the encapsulant and backsheet do not have a long rubbery state. They go quickly to flowing state after their glass transition**. This is a rather favorable characteristic for this type of material since during the manufacturing process the encapsulant can flow to fill the entire shape of the PV module.

Then, a mathematical Generalized Maxwell Model was established to model the viscoelastic behavior of these polymer materials using master curves constructed through the TTS principle. Experimental and numerical relaxation tests have been performed to verify their correlation and validate the analytical model. A correct correlation was obtained between the experiment and the simulation when the applied relaxation strain meets the condition of linear viscoelasticity.

The second part focuses on the characterization of the thermo-elastoplastic behavior of copper ribbons. Tensile measurements at different temperatures have shown that **the copper ribbons exhibit sensitivity to the loading temperature**. However, no sensitivity to the loading rate was found. A Johnson-Cook thermo-elastoplastic model was chosen to model the plastic behavior of the ribbons taking into consideration their temperature sensitivity. Simulation results of the tensile tests using this model showed a good correlation with the experimental measurements.

In the third part, an interest was given to the study of the elastic and fracture behavior of SHJ solar cells. Based on force-displacement curves of 4-line bending tests, the elastic moduli in the longitudinal and transverse direction of the cell are calculated analytically and numerically. The aim of this characterization was to verify if the transition from a wafer to a SHJ solar cell impacts its

elastic properties. **The correlation between the theoretical elastic properties of silicon and the analytical and numerical measurements allowed to conclude that the elastic properties remain unchanged between a silicon wafer and the SHJ solar cell**. Moreover, the fracture behavior of SHJ cells was statistically investigated using Weibull's law. **The fracture strength in the busbars direction is higher than that in the perpendicular direction.**

In the last part of this chapter, the thermal properties of the PV module components have been studied. First, CTE measurements were performed on several PV module components with different composition variations. **The measurements on the SHJ solar cell have highlighted an anisotropic effect of its thermal expansion. This anisotropy is induced by the silver metallization of the cell since silver expands more than silicon**. The expansion of the copper ribbon and the PP backsheet is also linear with anisotropy for the PP. For the other polymeric materials characterized in this section, their thermal expansion is not linear and strongly depend on their thermal transition or their processing condition. Finally, the specific heat and thermal conductivity of the polymeric materials were measured.

All these experimental characterizations and the established behavioral laws represent the first step to the construction of numerical models to capture the thermomechanical behavior of the PV module during its manufacturing. All the results presented in this chapter show that each component of the PV module has a unique thermomechanical behavior. One of the objectives of the next chapters will be to identify the influence of this variation of the components' behavior on the internal stresses induced in the PV module during its manufacturing.

Chapter 4

Thermomechanical modeling of interconnection process

Contents

Résumé du chapitre

Dans ce chapitre, nous nous sommes intéressés à étudier numériquement la contribution du procédé d'interconnexion dans la création des contraintes résiduelles du module PV. Le procédé d'interconnexion consiste à assembler la cellule et le ruban de cuivre à l'aide d'une colle électriquement conductrice (ECA), formant ce qu'on appelle un « string », pour assurer la collection et le transport de l'énergie photovoltaïque générée par les cellules solaires. Cet assemblage est réalisé par le biais d'un chargement thermomécanique appliqué sur le string pour réticuler l'ECA et assurer une adhésion entre le ruban et la cellule solaire. Ce chargement, en plus de la différence entre le comportement des matériaux assemblés, induit des contraintes résiduelles dans le string.

Dans un premier temps, nous avons présenté la géométrie et les simplifications adoptées pour construire le modèle 2D avec des hypothèses de déformations planes. Puis les matériaux et leur loi de comportement thermomécanique sont présentés. Les conditions aux limites appliquées sont également détaillées. Enfin, une analyse de convergence du maillage est réalisée.

Les niveaux de contrainte et de déformation ont été analysés durant le procédé et après refroidissement de la structure. Cette analyse a été réalisée sur trois zones d'intérêt : la zone où la force est appliquée par les pins, l'inter-cellule et une zone intermédiaire entre deux pins. Les résultats ont montré que la force appliquée par les pins génère une concentration de contrainte dans le ruban et la cellule solaire, ce qui entraîne une déflexion locale de ses composants. Dans l'inter-cellule, le ruban est cisaillé en raison de sa forme géométrique et de l'asymétrie de la structure. Dans la zone où aucune charge mécanique n'est appliquée, l'effet de la différence entre les CTE des matériaux est plus visible. En termes de déformation, le ruban de cuivre franchit sa limite élastique durant le procédé ce qui induit une déformation plastique irréversible.

Dans la suite du chapitre, nous avons étudié l'impact de certains paramètres du procédé sur le niveau de contraintes thermomécaniques. Trois paramètres procédé ont été sélectionnés dans cette étude : temps et température du procédé, le type d'ECA, et le design des pads d'ECA. Une analyse est réalisée en modifiant la température du procédé. Elle a montré que plus la température est élevée, plus les contraintes thermomécaniques seront importantes. Le temps de réticulation d'ECA et le type d'ECA ont été considérés comme des paramètres de deuxième ordre puisque leur impact sur les contraintes internes est minimal.

Quant au design des pads d'ECA, les résultats montrent que la discontinuité des pads ECA a un effet bénéfique sur l'état de contrainte dans la cellule et le ruban de cuivre, que ce soit pendant le processus ou après le refroidissement. Ceci est lié à la réduction du contact de l'interface cellule/cuivre et donc à la diminution de l'effet lié à la différence de CTE.

Introduction

The interconnection process is the first step in the assembly of the PV module. Its purpose is to assemble the cell with the copper ribbon using a binder to ensure the collection and transportation of the photovoltaic energy generated by the solar cells. This assembly is done through a thermomechanical loading applied on the stack. This loading, in addition to the difference between the material behavior laws, induces residual stresses in the string. It is crucial to identify the contribution of this manufacturing step in the generation of thermomechanical stresses because these stresses will be cumulative during the entire manufacturing process with irreversible behavior for the materials.

In this fourth chapter, a 2D sub-model in plane strain approximation will be used to study the stress state induced during the bonding interconnection process. Firstly, the numerical model will be presented by specifying its geometry and the simplifications adopted. Then, the thermomechanical behavior laws used in this model will be detailed with a focus on the evolution of the ECA adhesive stiffness with respect to temperature using rheological measurements. Then, boundary conditions chosen to model the thermal and mechanical loading as well as the contact management with the heating plates will be identified. A mesh analysis will be performed to select a convergent mesh solution.

Secondly, the state of thermomechanical stress and strain induced during the process will be discussed in different zones of the string where the geometry is not identical and considering the thermomechanical loading applied on each area.

Finally, the influence of some process input parameters on the numerical simulation response (stresss and strains) will be analyzed. The first parameters studied are the process parameters: temperature and time. Then we will focus on the type of ECA and its influence on the stress level induced in the cell and the copper ribbon. Finally, three different ECA pad designs will be investigated to quantify their contribution to the residual stresses in the string.

4.1 2D Finite element sub-model

4.1.1 Presentation of the model

4.1.1.1 Geometries and simplifications

In order to model the thermomechanical stress evolution induced in the solar cell and the copper ribbon during the interconnection process, a 2D sub-model was developed using the FE Abaqus software. This model represents a 2D simplification in plane-strain of two half-cells of type M2 (i.e. Solar cell with 156.75 mm side length) interconnected with a copper ribbon through an ECA adhesive as presented in Figure 4.1. The 2D structure represents a stack of two copper ribbons bonded with a SHJ cell through a thin layer of ECA ($\approx 24\mu m$). The metallization layer and the busbars have been omitted. One of the ribbons bonds the front side of the cell and the back side of the adjacent cell. Physically, this ribbon is not bonded all the way to the edge with the cell. This is a simplification that has been adopted numerically to avoid loading the ribbon in cantilever.

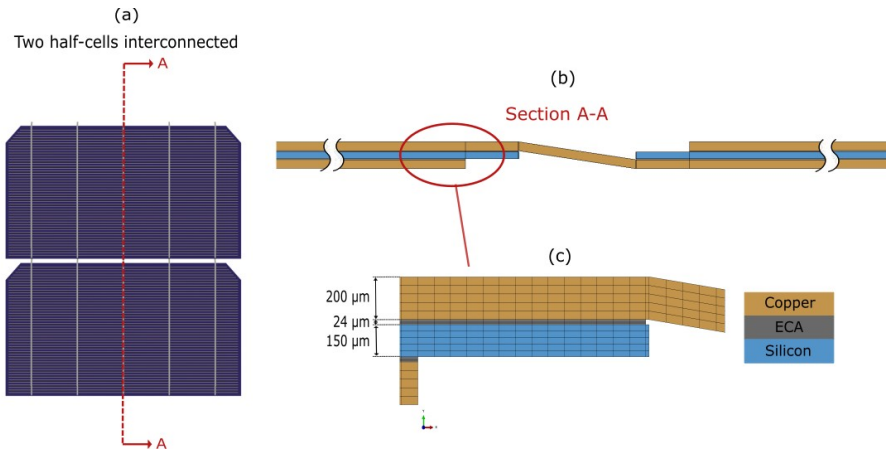

Figure 4.1: (a) Schematic of two half solar cells interconnected with copper ribbon, (b) Geometry of plane-strain FE model (Section A-A) and (c) Mesh details of the structure at interconnection zone

4.1.1.2 Materials behavior laws

During this process the ECA is deposited between the copper ribbon and the solar cell, and then heated to a temperature to crosslink it. To get closer to the physical behavior of the ECA during this phase of cross-linking, rheological experimental measurements of the shear modulus according to the temperature of two types of ECA A1 and A2 are carried out. A quantity of non-crosslinked adhesive was deposited between the two planar measuring tools with an inter-gap of 2.5 mm. The samples were loaded with a radial frequency of $1 rad/s$ and a strain of 1%. The normal force has been considered to be null to prevent the torque from exceeding its critical value when the samples stiffen during cross-linking. A heating rate of $1°C/min$ was chosen. Admittedly, this speed is very slow compared to the rate of cross-linking of the ECAs during the interconnection process, but the purpose of this study is not to characterize the kinetics of cross-linking of the ECAs but to measure their moduli during a heating ranging from room temperature to the process temperature ($\approx 160°C$).

Figure 4.2 illustrates the measurements of storage modulus and shear loss of the two types of ECA characterized according to the temperature. ECA-A1 begins to crosslink around 57°C, however ECA-A2 has a slightly higher crosslinking initiation temperature around 67°C. The glass transition occurred in ECA-A2 just after cross-linking. This phenomenon is represented by a slight drop in the storage module and a peak in the loss module around 95°C. These glass transition properties are in good agreement with the DMA measurements presented in Section 3.1.1. These shear moduli are converted to storage and loss moduli in tension to be used in the modeling of the interconnection process. The behavior laws and thermal properties used for each material in the 2D sub-model are presented in Table 4.1.

4.1.1.3 Boundary conditions

As described in Section 1.1.2.1, during the interconnection process the solar cells with the ribbon are regularly translated on a heating plate to crosslink the ECA. Simultaneously a punctual compression is applied by pins on the copper ribbons to ensure an adhesion with the ECA. In order to

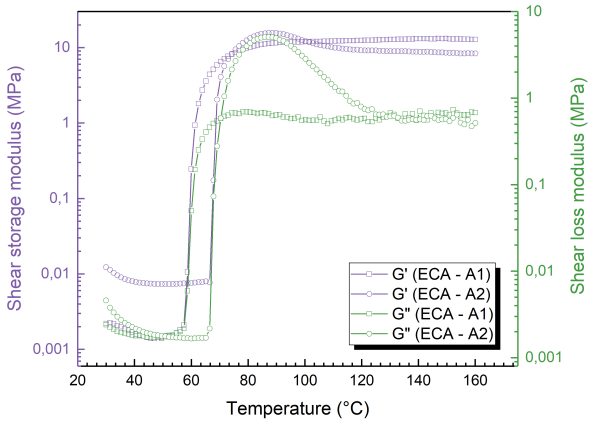

Figure 4.2: The evolution of the storage and shear loss moduli of two types of acrylate-based ECAs during cross-linking

Material	Elastic properties (GPa)	Poisson's ratio ν	Thermal conductivity (W/m/K)	Density (Kg/m^3)	CTE . 10^{-6} (1/°C)	Specific heat (J/Kg/K)
Copper	E(T) (table 3.3) and J.C. (table 3.4)	ν(T) (table 3.3)	401 [48]	8890 [48]	α(T) (table B.1)	386 [48]
Solar cell	elastic anisotrope (table 1.1)		130 [48]	2329 [48]	α(T) (table B.1)	677 [48]
ECA-A1	E(T)	0.35 [164]	0.61 (table 3.7)	4400 [164]	α(T) (table B.2)	762.04 (table 3.6)
ECA-A2	E(T)	0.35 [164]	0.71 (table 3.7)	4400 [164]	α(T) (table B.2)	751.13 (table 3.6)

Table 4.1: Behavior laws and thermal properties used of each component in 2D sub-model

model this, a fixed rigid body was set in contact with the bottom surface of the bottom ribbons. A surface-to-surface contact with hard normal and tangential frictionless properties.

The temperature profile applied to the string as it passed over the stringer plates was measured experimentally using K-type thermocouples bonded directly to the cell in four different positions. Figure 4.3 shows the position of the thermocouples and the temperature profile measured for a recipe of 170°C and a curing time of 2.5s. The temperature monitored by the TC_3 and TC_4 thermocouples is lower than that recorded by the other thermocouples. Thermocouples TC_3 and TC_4 are bonded on the top of the stack of two copper ribbons and the cell interconnected by two layers of ECA. And so the thermal gradient is influenced by the thermal conductivity of the stack. Knowing that the conductivity of the ECA is the lowest, it isolates a bit the temperature transmitted from the ribbon to the cell. The stress free state is chosen at the process start temperature, i.e. at room temperature. The temperature profile monitored by TC_1 was applied numerically on the bottom side of the copper ribbon assuming that the temperature gradient between the ribbon and the cell is negligible due to the high thermal conductivity of copper.

The force applied by the pins is modeled by a concentrated force applied at nodes spaced by the distance between the center of two pins. To manage the rigid body motion, gravity is applied to all the deformable body. To block all degrees of freedom, one node of the cell has been fixed in translation in the longitudinal direction e_x.

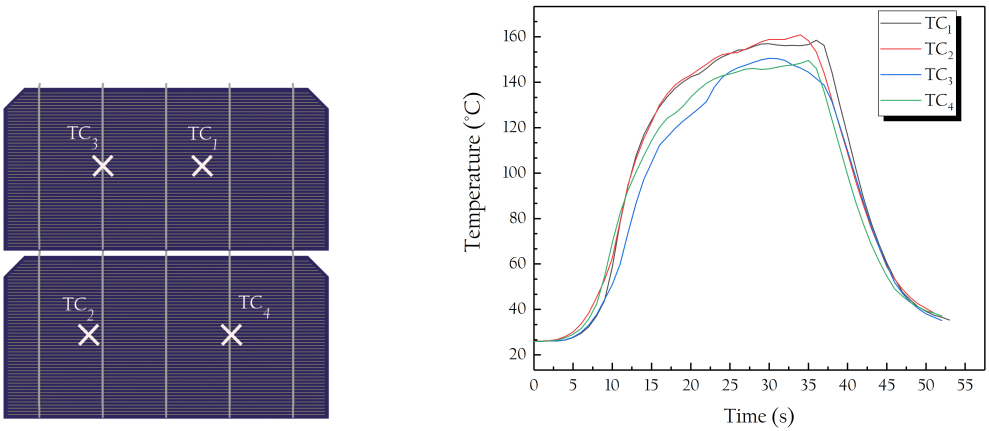

(a) (b)

Figure 4.3: (a) Position of thermocouples K-type for experimental monitoring of temperature and (b) temperature profile for a recipe of 170°C and a curing time of 2.5s

4.1.1.4 Meshing

In this sub-model, quadrangles elements coupled temperature-displacement have been used. First order elements with reduced integration have been chosen with hourglass control to avoid zero-energy modes. A mesh convergence analysis was performed based on the maximum von Mises (VM) stress and the maximal principal stress in the solar cell since it represents the most loaded component in the structure. The element discretization was varied between 0.3 and 0.1 mm. Figure 4.4 displays the evolution of VM and maximal principal stress in the most loaded element located in the solar cell as a function of the number of elements in the structure. The maximum stresses increase with further refinement of the mesh until a number of elements equal to 39110 where the stress stabilizes even when increasing the discretization of elements in the structure. Hence, this number of elements was chosen to mesh the structure.

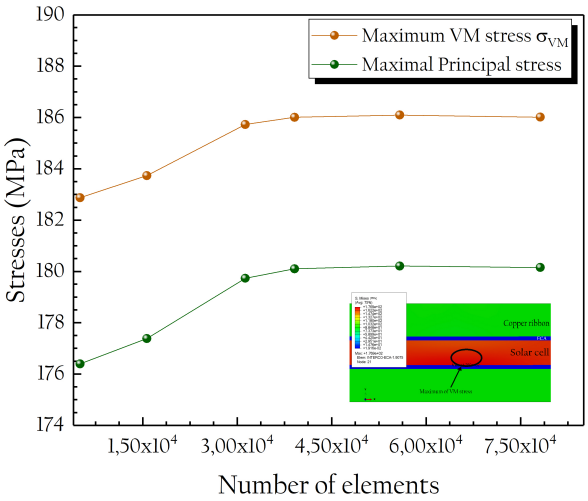

Figure 4.4: Maximum von Mises and maximal principal stresses as a function of the number of elements at 160°C (with a representation of the mesh analyze zone)

4.1.2 Thermomechanical stress and strain level

4.1.2.1 Thermomechanical stress level

The internal stress distribution in the string is not uniform. Therefore, we selected three study areas that have an identical longitudinal stress distribution. Figure 4.5 shows the longitudinal stress distribution in the three zones of interest at two different stages during the interconnection process. These stress distributions are analyzed and discussed by zone:

- **Zone I**: it is representative of the zones where a localized force is applied by the pins simultaneously with the heating from below. At 160°C, the ribbon is under compression with a stress concentration in the zone where the force is applied with a slight deflection. After cooling, the ribbon is strongly bent locally upward ($\sigma_{xx} = \pm 70$ MPa) as its stiffness increases with increasing loading temperature.

- **Zone II**: represents the inter-cell area where no loading is applied, so the stresses in this area are induced by the differed bending due to the asymmetry of the structure and the loading. At 160°C, the ribbon linking two adjacent cells is under shear. This shear is mainly due to its inclined geometric shape and the difference in loading between the left and right sides. The left side undergoes more mechanical deformation due to the force applied plus the loading applied by the other layers, while the right side undergoes thermal deformation since it is the side by which the structure is heated.

  As the cell is not interconnected up to the edge on both sides, they are cantilevered at the edge with a lower stress level compared to the interconnected area on both sides.

  When the stringer cools down, it bends downwards. Consequently, the ribbon connecting two cells is compressed from below and stretched from above.

- **Zone III**: is located in an area where no pin forces are applied. At 160°C, it can be seen that the ribbon and the ECA layer are compressed, with $\sigma_{xx} = -81.6$ MPa for the copper, and the cell is under tension with stresses up to 173 MPa. As the copper ribbon has a higher CTE than the solar cell, it expands more at high temperature. The connection with solar cell using ECA prevents the copper ribbon from expanding as its CTE requires. After cooling, as seen in other areas, the string bends downwards by introducing compressive and tensile stresses into the copper and solar cell, respectively.

The overall longitudinal stress distribution during the ECA bonding process indicates that the cell is under tension while the ribbon is compressed due to the CTE mismatch. After cooling the structure contracts and is deflected downward with a deflection in the opposite direction in the areas of localized pin forces. This reversal of bending direction causes a local buckling of the upper ribbons.

The residual stress level induced in the solar cell at the end of the process does not exceed 3.8 MPa in tension and -0.87 in compression. On the other hand, the residual stress level in the copper reaches locally 3.7 MPa in tension and -7 MPa in compression. However, the average stress level in the ribbon is between 1 and -3 MPa.

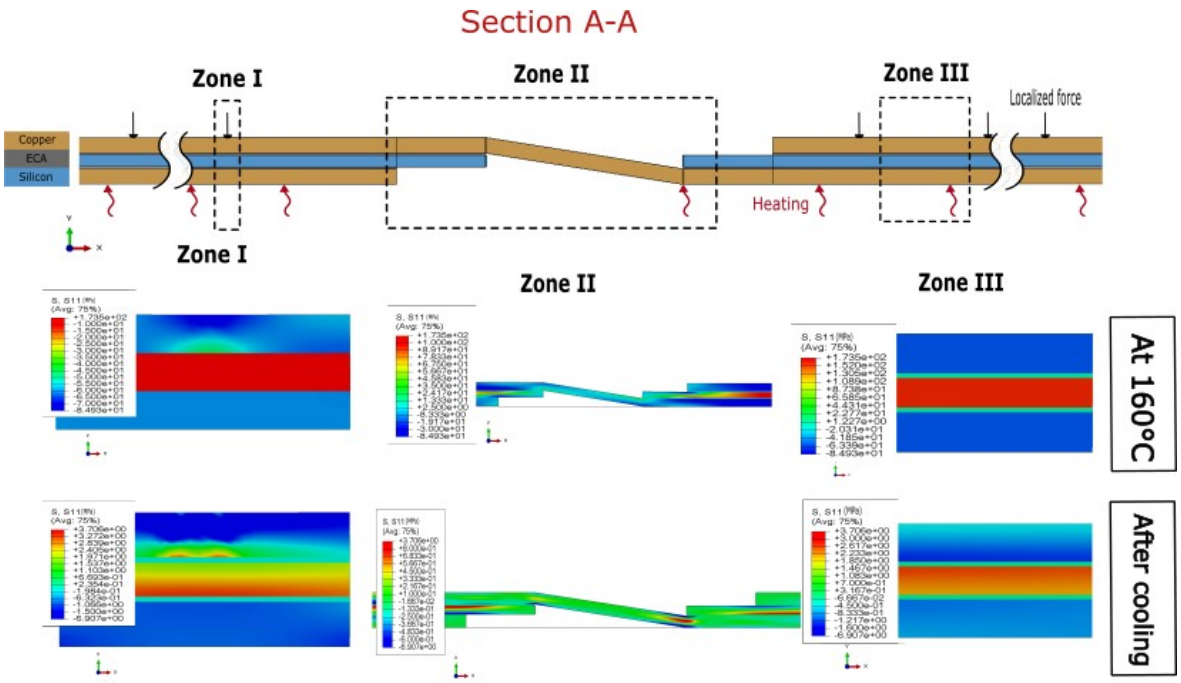

Figure 4.5: Longitudinal stress distributions σ_{xx} in three zones of interest at 160°C and after cooling

4.1.2.2 Thermomechanical strain level

During the interconnection process, thermomechanical loading is applied to the stack. However, the thermal loading applied is quite important compared to the mechanical loading localized on the ribbons. Consequently, the thermal strain is the predominant strain in all components of the string. As the thermal expansion of the components is quite different as shown in Section 3.4.1, the induced thermal strains are correspondingly variable.

Figure 4.6a displays the thermal strains of the three string components during the interconnection process. As discussed in Section 3.4.1, ECA-A1 CTE increases between -30°C and 50°C where it tends to decrease. This effect is noticeable on the evolution of the thermal strain of ECA-A1. The ECA-A1 expands at the beginning of the heating process and from 50°C onwards it contracts. During cooling, the temperature is decreasing so the thermal strain is increasing since the CTE is decreasing at high temperature. Once the string reaches 50°C, the ECA starts to contract back again.

The copper and the cell expand linearly following the temperature evolution during the ECA bonding. Besides, the copper ribbon expands six times more than the solar cell, which explains its compressive stress mode.

Only the copper ribbon was modeled with an irreversible behavior. Figure 4.6b shows the maximum equivalent plastic strain in the copper ribbon during the interconnection process. The copper deforms plastically for the first time when it reaches 60°C, and then this deformation accumulates during the process due to other loads applied to it, including cooling to room temperature. The level of plastic strain of copper is within the small deformation range. Nonetheless, it demonstrates that the ribbon has exceeded its yield strength at the first stage of PV module manufacturing and hence a part of its deformation will be irreversible.

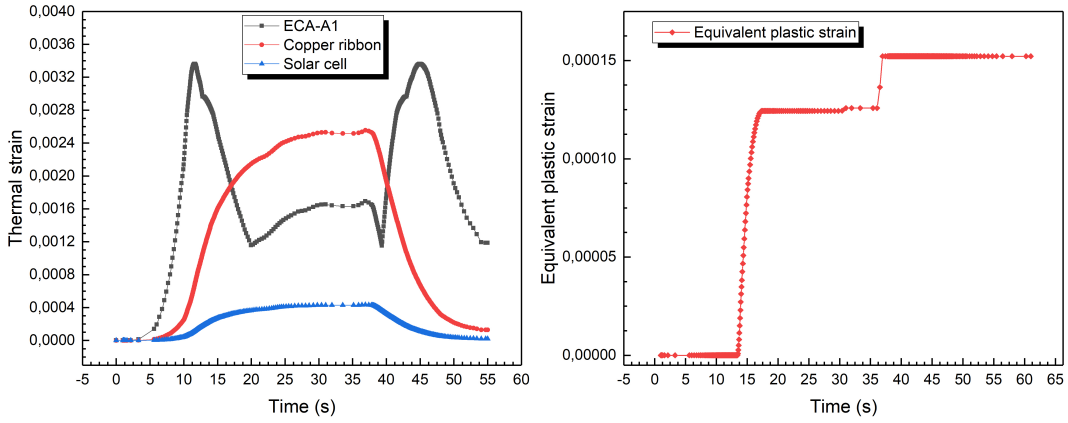

(a) (b)

Figure 4.6: Evolution of (a) thermal strains in the three components and (b) maximum equivalent plastic strain in copper ribbon during interconnection process

4.2 Influence of the interconnection process parameters on the thermomechanical stresses

After assessment of the level of stress and thermomechanical deformation induced during the bonding interconnection process, in this section, we are interested in evaluating the influence of some parameters on the internal stresses induced during the process. Three input parameters have been selected: temperature and time of assembly, the type of ECA used to interconnect the string, and finally, the design of the ECA pads deposited on the cell.

4.2.1 Influence of time and temperature of ECA curing on thermomechanical stresses

The two controllable parameters in the bonding interconnection process are tack time and the curing temperature of the ECA adhesive. Typically, the cross-linking temperature of ECA is around 60-70°C, however they are heated during the process to temperatures above 120°C to ensure complete cross-linking and good adhesion with the other components. The tack time describes the time that the cell remains on the heated plate before being transferred to the adjacent plate. The tack time is determined based on the cross-linking kinetics of ECA. These two parameters were varied in the numerical simulation to quantify their influence on the stress state in the solar cell as it represents the core of the string and also the most loaded component in the structure. Three process temperatures were selected 120°C, 170°C which represents the standard temperature and 200°C. The tack time was varied between 2500 ms and 5000 ms.

Figure 4.7a represents the evolution of the maximal principal stress in the solar cell during the process at different ECA curing temperatures and for the same tack time. As the thermal stress is predominant in the solar cell, the principal stresses curve follows the temperature profile applied to the structure in each case. The curves are almost identical with a shift in the curve at 200°C, which is due to a higher shift in gradient of the temperature imposed on the heating plate in this case. It is clearly noticeable that the higher the cross-linking temperature is, the higher the stress level of the solar cell is as well. The stress level reached in the case of a curing temperature of 200°C

is quite close to the characteristic fracture strength of the solar cell (see Table 3.5). In this model, half cells were considered. According to research performed by Kaule *et al.* [202], half cells have a much lower characteristic fracture strength. Thus, these stresses allow potentially initiation of microcracks.

Figure 4.7b outlines the evolution of the maximal principal stress in the solar cell during the process at the same curing temperature and two different tack times. The stress curve is almost identical in both cases with a longer duration for the tack time of 5000 ms. As the cell is exposed for a longer period of time on a hot plate before being moved to the adjacent plate, it has enough time to absorb more heat and therefore the temperature gradient will be different compared to a cell that is exposed to the hot plate for a shorter period of time. Hence, the stress level is slightly higher in the case of the 5000 ms tack time compared to 2500 ms.

Since the tack time is based on the kinetics of the ECA cross-linking, the stress level can be varied by considering a behavior law that describes these kinetic effects. However, the stiffness of the ECA is negligible compared to the cell and the copper ribbon, the variation could be quite minor.

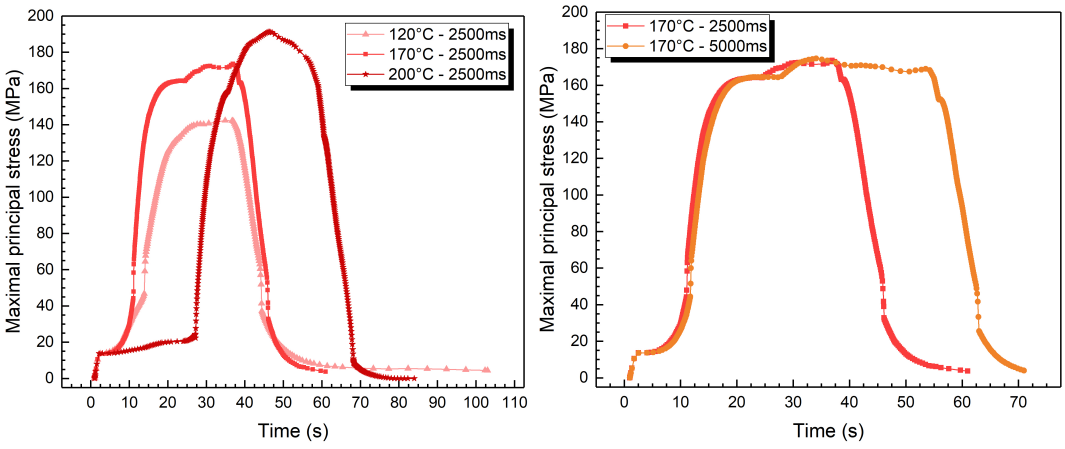

Figure 4.7: The evolution of maximal principal stress during the bonding interconnection process with different (a) curing temperatures of ECA-A1 and (b) tack times

4.2.2 Influence of ECA type on thermomechanical stresses

The thermomechanical behavior of the ECAs selected in this work has been studied in chapter 3. The results showed that the ECAs have a non-identical behavior in spite of their similar composition. Here, the influence of the difference between these two types of ECA on the internal stresses induced in the solar cell and the copper ribbon during interconnection process is identified.

Figure 4.8 depicts the longitudinal stresses σ_{xx} in the normalized thickness of the solar cell and the copper ribbon at 160°C according to the type of ECA used to interconnect the string. The evolution of the stresses for both components and in both cases shows that they are subjected to bending. However, the bending gradient is moderately high in the case of ECA-A2 ($\approx$ 2MPa). ECA-A2 has a particular thermomechanical behavior, its cross-linking and glass transition temperature are quite close. Therefore, during the process, as soon as its rigidity increases due to the cross-

linking effect, it falls back due to the glass transition effect. This characteristic influences as well its thermal expansion (see Figure 3.29b). Therefore, it becomes less rigid than ECA-A1 and cannot handle the CTE mismatch between the cell and the copper ribbon by inducing more internal stresses.

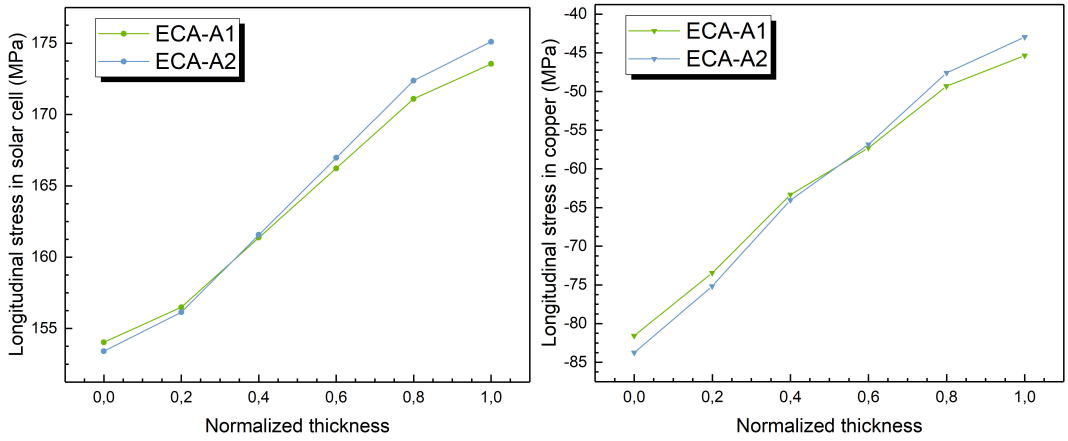

Figure 4.8: Longitudinal stresses σ_{xx} in (a) solar cell and (b) copper ribbon regarding their normalized thickness at 160°C during interconnection process

According to these results, the influence of the type of ECA can be assumed as a second order parameter in the creation of thermomechanical stresses in the interconnection step. Nevertheless, after cross-linking, ECA-A2 is stiffer than ECA-A1 in the range of the lamination process and thermal cycling. Therefore, this assumption cannot be valid in the further manufacturing steps of the PV module.

4.2.3 Impact of ECA pad design on thermomechanical stresses

Silver is the basic metal used as conductive particles in ECA. As the PV industry tends to decrease the amount of silver per module in order to reduce their cost, several approaches are being explored. Among these approaches at the PV module level is the reduction of the amount of ECA deposited on the cell to interconnect it with the copper ribbon.

Theunissen *et al.* [203] studied the impact of the amount of ECA deposited to interconnect cells with shingle technology on their power loss after thermal cycling. Their results show that, with an ECA amount of 8% relative weight/cell, the maximum power loss after 600 thermal cycles reaches 2.9% whereas only 1.1% of power loss for modules with 22% relative weight/cell.

In this work, we investigated the impact of reducing the amount of ECA from a thermomechanical point of view. Three pad designs were chosen for this study: the continuous pad (standard i.e. 100%), Pad A with 32% relative weight/cell, and Pad B with 47% relative weight/cell. As shown in Figure 4.9, pad A is deposited in smaller amounts and with a smaller inter-pad than pad B. The inter-pad presents a contact discontinuity surface between the solar cell and the copper ribbon.

The same numerical model presented in Section 4.1.1 with the same conditions was used in the case of pads A and B. The contact management was changed to a general contact instead of surface to surface contact to manage the contact between the cell and the copper ribbon in the

inter-pad area where a mechanical co-contact can take place. ECA-A1 adhesive was used to model the pads as the impact of the ECA type was considered to be secondary.

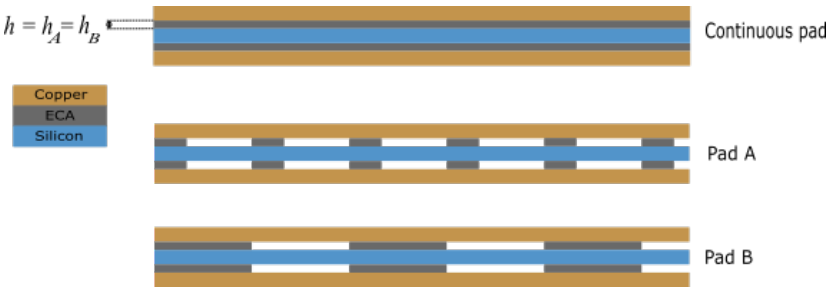

Figure 4.9: The three ECA pad designs investigated in this study

Figure 4.10 shows the longitudinal stress in a segment of the solar cell and the copper ribbon between two ECA pads at 160°C where the maximum stress during the process was found. In the inter-pad of the selected portion, a longitudinal force is applied by the pins. In Figure 4.10a, the stress curve of solar cell with a continuous pad is constant along the length with a stress level of 164 MPa except in the area where a force is applied by the pins. Pad A, which represents a small amount of ECA deposit and an inter-pad larger than the pad, shows a stress level of 161 MPa in the pad area and a stress decrease to 150 MPa in the inter-pad. Pad B depicts an intermediate stress level between the two cases in the pad area and a stress level rather close to pad A in the inter-pad.

In Figure 4.10b, the longitudinal stress in the copper is also constant along the length with a compressive stress level of -60 MPa, the same peak in stress related to the localized force is seen. With pad designs A and B, the stress level in the pads is also lower as in the case of the solar cell. However, in the inter-pad the stresses are higher ($\approx -90\text{MP}a$). This is due to the absence of the ECA layer in the area where the force is applied which results in bending of the ribbon and thus more compressive stress.

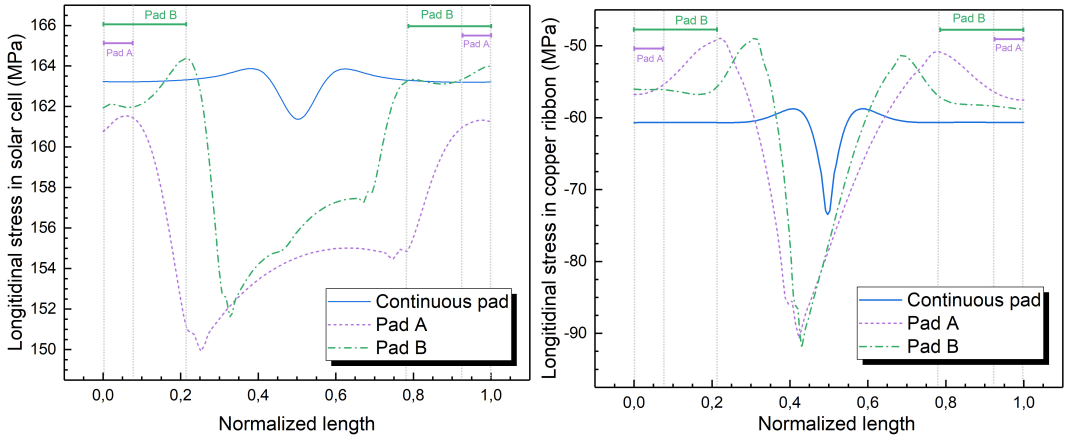

Figure 4.10: Longitudinal stresses σ_{xx} in a segment of (a) solar cell and (b) copper ribbon between two successive pads at 160°C during interconnection process

Figure 4.11 shows the longitudinal stresses in the cell and the copper ribbon in the same segment after cooling the string to room temperature. In the solar cell, the stresses in the continuous pad remain quasi-constant. The stresses in pads A and B are lower than the stresses in the con-

tinuous pad with a minimum difference of 50%. In addition, the same fluctuation is noticed in the design of pad A and B where the stresses in the pads remain higher than the stresses in the inter-pad. On the other hand, in the copper ribbon the stress level in the continuous pad is almost null compared to the stress level in pads A and B.

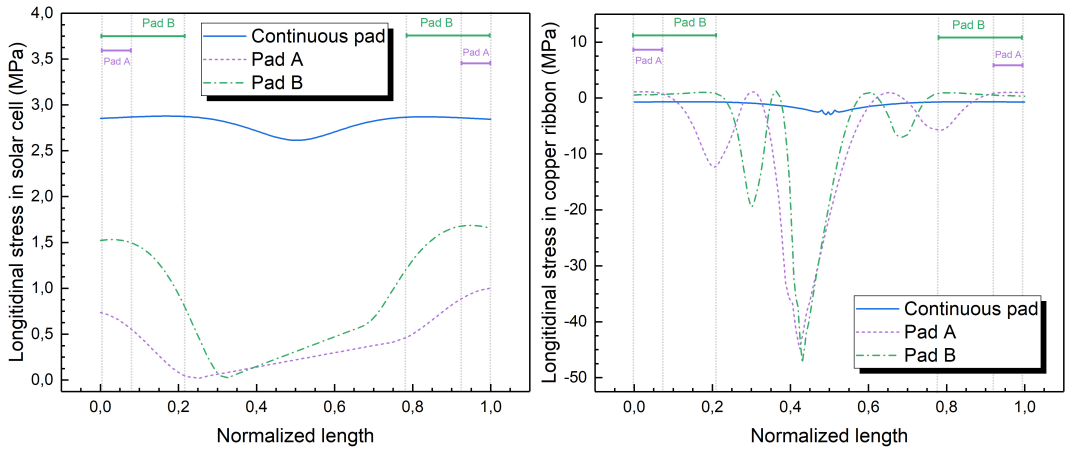

(a) (b)

Figure 4.11: longitudinal stresses σ_{xx} in a segment of (a) solar cell and (b) copper ribbon between two successive pads after cooling during interconnection process

In addition to the advantages of reducing the amount of silver in the module, the deposition of ECA in discontinuous pads may have advantages from a thermomechanical point of view. The presented results revealed that the use of a discontinuous pad induces less residual stress in the solar cell mainly and the copper ribbon. This is due to the repetitive breaking of the bond between the ribbon and the cell, which allows the components to expand and contract without as much stress related to their bond. The shorter the pad, the less stress there will be at the interface compared to a wider pad as in the case of pad B. In addition to that, the inter-pad has a significant role in the creation of residual stresses. With a wide inter-pad, the components will expand or contract more since there is no bonding to constrain them, which will introduce a greater deflection.

The main critical parameter in the interconnection with disconnected pad is the area of application of the force by the pins, at least for copper. When the load is applied in an area of ECA discontinuity (i.e. inter-pad), the ribbon undergoes a greater bending, which generates more compression on the ECA in the neighboring pads and this compression is subsequently transmitted to the solar cell. This phenomenon is illustrated in Figure 4.12a, where a stress concentration up to 190 MPa is observed in the area of the cell at the edge of the pad. As the solar cell is under tension during the whole process, and since the silicon is especially sensitive to tension, this can be damaging. We can also observe that in the inter-pad area, the ribbon comes in direct contact with the cell thus applying a bending force to the solar cell. In the areas where the force is applied at the center of the pad, this phenomenon is not present as shown by the longitudinal stress distribution in Figure 4.12b. Therefore, the remedy to this problem could be to design the position of the pads to coincide with the position of the pins.

Numerical results have shown that the discontinuous pads are advantageous in reducing the thermomechanical stresses during the interconnection process. To our knowledge, there are no ex-

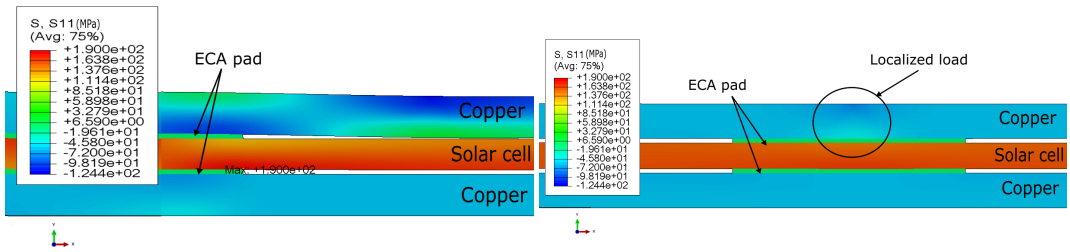

(a) (b)

Figure 4.12: Distribution of longitudinal stress σ_{xx} (a) near inter-pad and (b) in the pad in case of design A

perimental studies in the literature that validate these numerical results. Experimental characterizations, including the mechanical peel strength of these types of interconnects, need to be carried out to verify if the discontinuous pads are effective.

As discussed in Section 2.2.1, few numerical studies were found in the literature that address the thermomechanical behavior of bonded assemblies with ECA.

In the work of Beinert *et al.* [129] the residual stress level induced in the solar cell after welding is -5MPa. In the case of welding assembly, the assembly between the cell and the ribbon is done at the solidification temperature of the filler metal (i.e. at 179°C). Therefore, numerically they model only the cooling step, which explains the level of compressive stress in the solar cell. However, in the ECA bonding process, the bonding between the cell and the ribbon occurs once the ECA is cured at (≈ 60°C) and well before the maximum process temperature. Therefore, it is necessary to model the whole heating cycle or at least from the starting temperature of the cross-linking where the physical contact between the three components is ensured. This explains the fact that at the end of the bonding process the residual stresses (3.9 MPa in tension and -0.87 MPa in compression) are different compared to the one observed in the welding process.

In the study by Geipel *et al.* [139], they showed that the ECA interconnect technique induces residual stress up to -200 MPa in solar cells. As discussed previously in Section 2.2.1.1, these residual stresses are likely overestimated due to behavior laws of components simplification.

Conclusion

The manufacturing of PV module relies on two assembly steps. The interconnection represents the first assembly step of the PV module core, the string. The bonding interconnection is done by a combination of mechanical and thermal loading to ensure adhesion between the ECA glue, the solar cells and the interconnector. The three components involved in this manufacturing step have a totally different thermomechanical behavior as discussed in chapter 3.

In this fourth chapter, we were interested in evaluating the level of induced stresses in the bonding interconnection step and in identifying its potential impact on the stress state in the rest of the manufacturing chain. First, the model used in this study was presented, specifying the behavior laws, the boundary conditions and the mesh adopted. Then we discussed the level of stresses and thermomechanical strains in a string of two half-cells with a fixed set of process parameters. The analysis was performed on three zones of interest: the zone where the force is

applied by the pins, the inter-cell, and an intermediate zone between two pins.

The results showed that the force applied by the pins generates a concentration of stress in the ribbon and the solar cell resulting in a local deflection of these components. In the inter-cell, the ribbon is sheared due to its geometric shape and the asymmetry of the structure. In the area where no mechanical loading is applied the effect of the CTE mismatch is more visible. It must be noticed that the copper ribbon exceeds the yield stress for the first time during this interconnection stage. This induces irreversible plastic strain.

The level of residual stress induced in the string after cooling is negligible, but the level of thermomechanical stress during the process is not. For this reason we have given more importance to the impact of certain process parameters on the maximum thermomechanical stress level in the rest of this chapter.

The first varied process parameter is the loading time and temperature. Secondly the type of ECA was varied. As the thermal stress in the solar cell is predominant, a direct effect on the temperature was found, i.e. **the higher the process temperature is, the higher thermomechanical stress occurs**. The time and the type of ECA were considered as second order parameters since their effect on the internal stress is minimal. And finally, the design of the ECA pad and its influence on the internal stress state was studied.

The results showed that the **discontinuity of the ECA pads have a beneficial effect on the stress state in the cell and the copper ribbon either during the process or after cooling**. This is related to the reduction of the cell/copper interface bonding and thus less effect related to the CTE mismatch. On the other hand, the stress concentration in the solar cell related to the position of force application by the pins is a critical phenomenon that has been observed.

To conclude this chapter, **the level of residual stress induced at the end of the interconnection process remains negligible, which allows us to neglect it later in the modeling of the lamination process in order to simplify the numerical model**. Nevertheless, the level of internal stresses during the process must be taken into consideration during the development of new recipes, because the level of stress reached during the interconnection process can initiate microcracks in the cell that can harm their assembly during lamination.

Several simplifying assumptions were considered in this study. For the behavior of ECAs, the kinetics of cross-linking was not accounted for in this study, but the effect of cross-linking on Young's modulus was considered. It would be relevant to take it into account in future studies to investigate its impact on the stress state. As we model the whole interconnection process, the same thermo-elastic behavior of the ECA is defined at the same temperature points during heating and cooling. Therefore the stiffness considered in the cooling step is lower than the true stiffness of the material after cross-linking. Despite this, the stiffness of the ECA remains quite negligible compared to that of the cell and the ribbon and therefore its influence is assumed to be minimal.

In this study, we were interested in the evolution of the thermomechanical stresses in the interconnection line. In the areas of the cell where there is no bonding to the copper, the stress level is probably lower. A transition from a 2D to 3D approximation could verify this hypothesis and also study the edge effects of this assembly.

Chapter 5

Thermomechanical sub-modeling of lamination process

Contents

Résumé du chapitre

Dans le but d'étudier la modélisation du procédé de lamination, nous avons adopté une stratégie de modélisation multi-échelle. Dans ce chapitre, la sous-modélisation en 2D et 3D du procédé de lamination est étudiée. L'évolution des contraintes thermomécaniques au cours du procédé à l'échelle de la cellule solaire est également analysée.

Tout d'abord, au début de chaque section relative au sous-modèle, les modèles sont présentés avec les simplifications géométriques adoptées et les lois de comportement utilisées dans chaque cas pour modéliser les matériaux. Ensuite, une analyse de la convergence du maillage est réalisée pour chaque simulation.

En utilisant le sous-modèle 2D, une étude sur la précision du calcul en améliorant la fiabilité des lois de comportement relatives aux composants du module PV est d'abord réalisée. Des modèles élastoplastiques et viscoélastiques ont été utilisés pour décrire le comportement thermomécanique du ruban de cuivre, du backsheet et de l'encapsulant respectivement. Les résultats ont montré une surestimation ou une sous-estimation des contraintes thermomécaniques dans tous les composants si des lois de matériaux simplifiées, i.e. élastiques, étaient utilisées. La relaxation de l'encapsulant et du backsheet protège la cellule solaire contre la déflexion appliquée par le verre. Des concentrations de contrainte ont été observées dans les zones d'interconnexion.

Ensuite, trois configurations différentes de l'architecture des modules PV en modifiant le nombre de busbars, la taille des cellules et le type de face arrière ont été sélectionnées pour évaluer leur impact sur les contraintes thermomécaniques. La position des busbars exerce une influence sur les contraintes thermomécaniques induites dans la cellule solaire. Les cellules solaires dont les busbars sont décalés par rapport au centre sont moins chargées. La non-symétrie du chargement thermomécanique et de la structure augmente la déflexion du module PV, ce qui entraîne un niveau de contrainte plus élevé dans un module verre-backsheet par rapport à un module verre-verre.

Un sous-modèle 3D est introduit pour identifier la distribution des contraintes hors plan dans la cellule solaire ainsi que les effets de bord. Les résultats de la sous-modélisation 3D ont montré que la cellule subit des contraintes liées aux effets de bord, notamment au bord des lignes d'interconnexion. Ces effets de bord sont liés à la pression de contact appliquée par les autres matériaux sur les bords de la cellule.

Enfin, la probabilité de défaillance de la cellule solaire en fonction de la technologie d'interconnexion est caractérisée et discutée. Il a été observé que la présence de l'ECA entre la cellule solaire et le ruban de cuivre relaxe le niveau de contrainte induit par la différence du CTE puisque l'ECA se dilate fortement et est moins rigide. Par conséquent, la probabilité de rupture dans le cas d'une cellule interconnectée par ECA est inférieure à celle d'une cellule interconnectée par soudure, quel que soit le type de cellule solaire.

Introduction

The lamination process is the backbone of the PV module manufacturing chain. It is the assembly step that has the greatest impact on the reliability of the PV module. The reliability of the PV module after lamination is classically studied experimentally using accelerated qualification tests. However, these tests consume a lot of material resources and last several days or months. Therefore, the study of the mechanical reliability of PV modules by numerical means is a necessary strategy to save time and resources.

As discussed previously, several modeling strategies are possible to investigate numerically the reliability of PV modules manufactured via the lamination process. In this work, we have adopted a multi-scale modeling strategy as presented in Figure 5.1. In this chapter, the sub-modeling of the lamination process will be studied. The evolution of the thermomechanical stresses during the lamination process at the solar cell scale will be investigated.

First, in the beginning of each section related to the sub-model, the models will be presented with the adopted geometrical simplifications and the behavior laws used in each case to model the materials. Then a mesh convergence analysis will be presented for each simulation.

Using the 2D sub-model, first a study on the accuracy of the calculation by improving the reliability of the behavior laws regarding the PV module components will be performed. Then, three configurations of PV module architecture by varying the number of busbars, the cell size and the type of back side are selected to identify their impact on the thermomechanical stresses.

In a second part, a 3D sub-model will be introduced to identify the out-of-plane stress distribution in the solar cell and also the edge effects. Finally, the probability of failure of the solar cell as a function of the interconnection technology will be characterized and discussed.

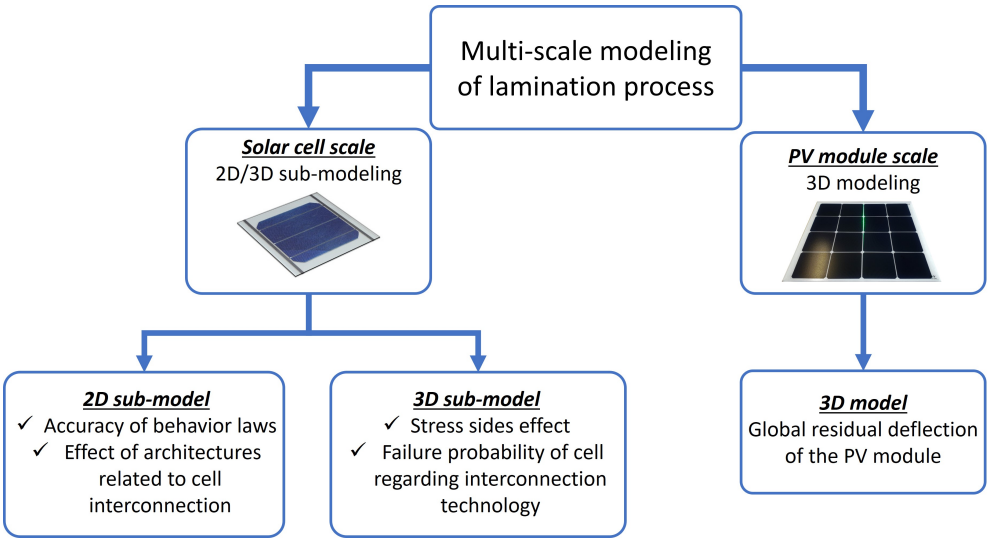

Figure 5.1: Multi-scale modeling strategy for the lamination process analysis

5.1 2D Finite element sub-model

This section of chapter is quoted verbatim from an article submitted for publication by Rahmoun et al. [204].

In this section of the chapter, the 2D sub-model is defined to study the impact of behaviour laws of PV module components on the calculations accuracy. Then, tree different PV module architectures and their impact on thermomechanical stresses will be modeled and analysed.

5.1.1 Presentation of the sub-model

5.1.1.1 Geometry of the model and loading conditions

In this work, a simplified 2D model was developed using the FE ABAQUS software to simulate the evolution of induced stresses in the thickness of the PV module during lamination. The 2D FE model (Figure 5.2-(b)) is a plane-strain approximation for the PV module with a single SHJ solar cell to better apprehend the evolution of induced stresses during PV module manufacturing. The structure geometry allows to model half of the PV module by applying a symmetry boundary condition on symmetrical edge. During lamination, the PV module is placed on the laminator. For this purpose, a fixed rigid body has been added in contact with the front face of the glass. A normal rigid and tangential frictionless contact is used. Perfect contact constraints are considered at each interface. A gravity load is applied to the PV module to avoid rigid body motions. The ECA pads between solar cell and the interconnects were omitted in this model. Transient thermal conditions were applied in the different steps of the simulation. A stress free temperature was set at ambient temperature 25°C. The lamination process was modeled in the following three sub-steps based on the lamination recipe shown in Figure 5.3:

- Step I: preheating to 60°C, in this step the VOCs located in the encapsulant and the air trapped between layers are evacuated to the outside by applying vacuum pressure in order to prevent bubbles from forming in the PV module.
- Step II: heating to the lamination temperature of 150°C while simultaneously applying a pressure of 0.1 MPa for 7 to 15 minutes to ensure optimal adhesion between the encapsulant and the other layers.
- Step III: cooling to room temperature (25°C), by applying a convection boundary condition with ambient air with a heat exchange coefficient of 20 $W/m/K$ representing free air cooling calculated analytically using the method presented in [79].

5.1.1.2 Material modeling

In this sub-model, a conventional EVA encapsulated architecture of a single-cell module was chosen. A TPT backsheet was used for the GBS architecture. The thermomechanical behavior of the materials is discussed in Chapter 3. In this study, the behavioral laws of the EVA encapsulant, TPT backsheet and copper were varied according to the study case. In the thermoelastic case, the DMA

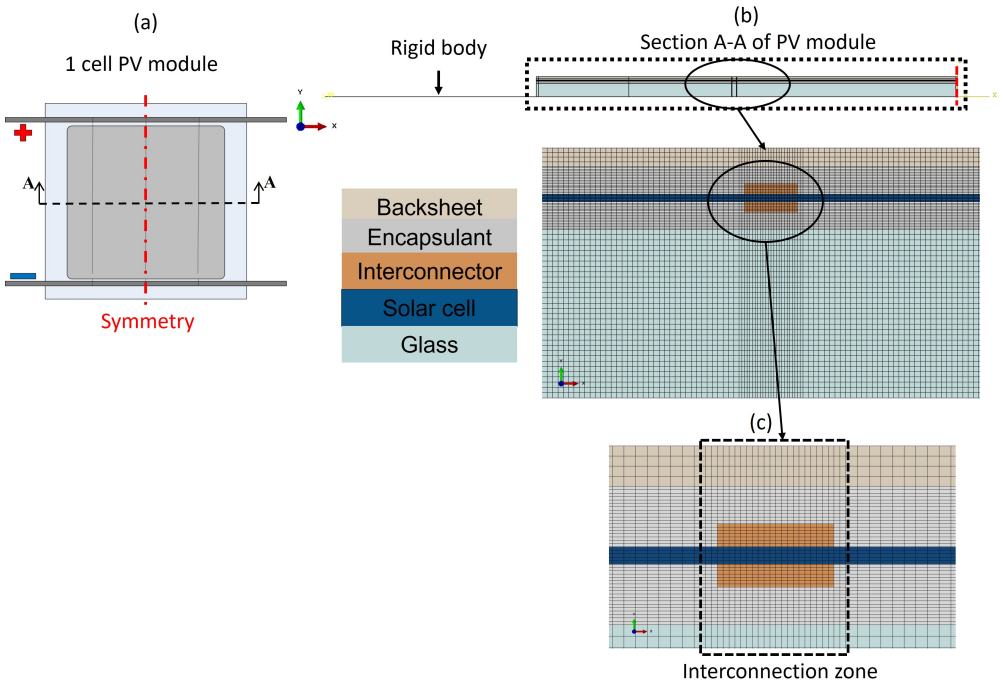

Figure 5.2: (a) Schematic of a PV module with one solar cell, (b) Geometry of plane-strain FE model (Section A-A) and (c) Mesh details of the structure at interconnection zone

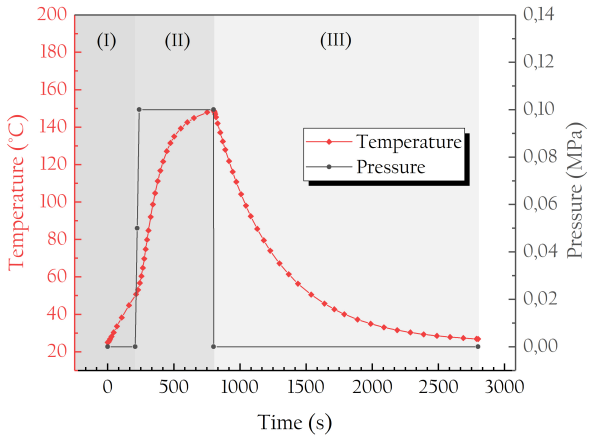

Figure 5.3: Conventional lamination conditions with outdoor cooling

curves of EVA and backsheet were used. The CTE of the copper and the solar cell are considered to be temperature dependent while for the other components a constant CTE is considered. The material behavior used in this sub-model is presented in Table 5.1.

5.1.1.3 Model mesh

In this study, coupled temperature-displacement elements were used. Quadrangle elements were chosen to avoid the problem of high stiffness displayed in some conditions by triangular elements. Based on a convergence study regarding size and three types of elements (quadratic with reduced integration, linear with full integration and linear with reduced integration), the quadratic elements with reduced integration were chosen as the most suitable ones to predict the studied configuration. In order to have a suitable calculation accuracy in the case of bending problems, these

Component of PV module	**Young's Modulus (GPa)**	**Poisson's ratio ν**	**Thermal Conductivity** ($W.m^{-1}.K^{-1}$) [48]	**Density** (Kg/m^3) [48]	**CTE** $.10^-6$ ($1/C°$)	**Specific Heat** ($J.Kg^{-1}.K^{-1}$) [48]
Copper	E(T) (table 3.3) and J.C. (table 3.4)	ν(T) (table 3.3)	401	8890	α(T) (table B.1)	386
Encapsulant EVA	E(T)/G.M. (table A.1)	0.4 [134]	0.311	960	270 [48]	2090
Backsheet TPT	E(T)/G.M. (table A.1)	ν(T)[1]	0.36	2520	50.4[48]	1010
Glass	73 [48]	0.235 [134]	0.937	2500	8 [48]	913
Solar cell	elastic anisotrope (table 1.1)		130	2329	α(T) (table B.1)	677

J.C., Johnson Cook plasticity model; G.M., Generalized Maxwell viscoelastic model.

Table 5.1: Material properties of PV modules components. [1]: Measured parameters

elements must be used with reasonably fine meshes in the thickness (minimum of 3 elements in the thickness) [188]. A more refined mesh was used in the interconnection zones where stress concentrations were observed (see Figure 5.2). A convergence analysis of the mesh was performed based on the maximum von Mises (VM) and maximal principal stresses during lamination in the solar cell since it represents the most loaded component in the structure. The stresses are taken at the integration points. This convergence study was performed for quadratic elements with reduced integration (minimal discretization 0.01mm) where all the materials were assumed thermoelastic except copper which is considered thermo-elastoplastic. Figure 5.4 displays the evolution of the von Mises and maximal principal stresses in the most loaded element located in the solar cell as a function of the number of elements in the structure. We can observe a big variation of the slope near to 77462 elements. This variation is due to the mesh refinement in the interconnection zones which slightly increases the accuracy of the stresses by less than 1 MPa. A convergence of the solution for a number of elements greater than or equal to 78386 elements is reached. In the subsequent simulations, a number of element of 78386 was chosen.

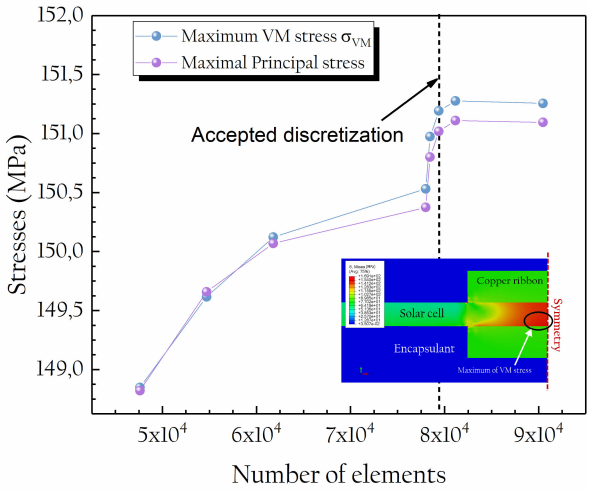

Figure 5.4: Maximum von Mises and maximal principal stresses as a function of the number of elements at 150°C (with a representation of the mesh analyzed zone)

5.1.2 Influence of material models on induced stresses

As the structure of the PV module is complex, several simplifications can be considered in FE models to reduce computation time such as the use of thermoelastic behavior laws. However, these simplifications must have a negligible influence on the accuracy of the numerical calculation. We will discuss the influence of material models on the induced stresses in the PV module during manufacturing process. Four study cases were conducted, while increasing each time the complexity of the material's model. The thermomechanical behavior law used in each case are presented in Table 5.2.

Figure 5.5a displays the vertical displacement and the principal maximum stress for Case 4 at 150°C during the lamination process. We can notice in Figure 5.5a that the PV module is bent upwards with a maximum displacement around 0.133mm. Figure 5.5a shows the principal maximum stress in the PV module when discharged from the laminator. The overall stress level in the PV module is between 21 MPa and -12.2 MPa. Stress concentrations were observed numerically in the solar cell and more especially in the interconnection zones. To observe the effect of these stress concentrations, we have compared the tangential stress profile along the length of the solar cell in Cases 1 and 4. Figure 5.6 shows the tangential stress profile in Case 1 and Case 4. Case 1 represents the simplified case and Case 4 is the most complex in thermomechanical behavior laws of the components. The stress concentrations can be visualized by stress peaks reaching 138.8 MPa on the stress profile in Case 4 along the length of the solar cell. However, the stresses in the solar cell beyond the interconnection areas are between 7.63 MPa and -0.04 MPa. Copper ribbon has a much higher coefficient of thermal expansion than the solar cell, so as it expands and applies a significant stress to the solar cell in the contact areas. By adding ECA pads between the copper and the solar cell, these stress concentrations may eventually be reduced as the ECA adhesive is softened.

Study case	Glass	Solar cell	Copper	Encapsulant	Backsheet	Time of calculation	Number of processors
Case 1	Elastic	Elastic	Elastic	Elastic	Elastic	3h11min38s	28
Case 2	Elastic	Elastic	Elastoplastic	Elastic	Elastic	3h6min19s	28
Case 3	Elastic	Elastic	Elastoplastic	Viscoelastic	Elastic	3h15min7s	28
Case 4	Elastic	Elastic	Elastoplastic	Viscoelastic	Viscoelastic	2h59min30s	28

Table 5.2: The behavior laws used in the four study cases with the calculation time and the number of processors in each case

In Case 1, the thermomechanical stress level exceeds 18 MPa throughout the length of the cell except at the extremity where we noticed a compressive stress of -0.02 MPa. A severe stress fluctuation is noticed in the interconnection zones. The stress deviation in the interconnection zones between Case 1 and Case 4 is 6.78%. However, it is greater beyond the interconnection zones where it reaches 61.94%. This error is mainly related to the softening and relaxation of the encapsulant and backsheet at high temperature. When the encapsulant is softening, it will protect the solar cell and keep it flat against glass bending due to thermal expansion. Using a viscoelastic mode, these effects of softening and relaxation of the encapsulant as lamination temperature increases are considered. Thus with an elastic model, the level of thermomechanical stresses is

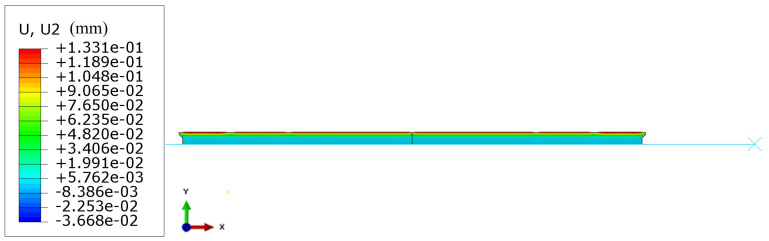

(a) Vertical displacement in mm of PV module at 150°C (y-scaled ×5)

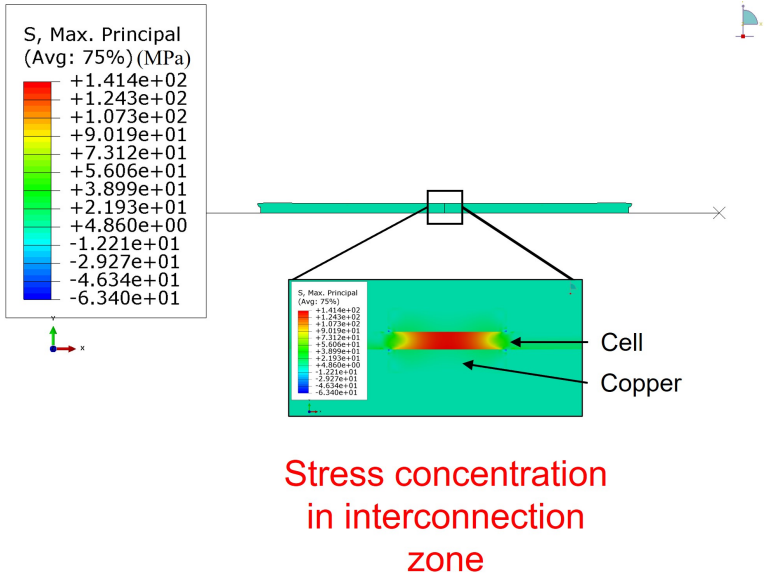

(b) Principal maximal stress σ_I^{max} in MPa showing the stress concentration in the interconnection zone at 150°C in Case 4 (y-scaled ×5)

Figure 5.5: Vertical displacement and principal maximum stress for Case 4 at 150°C during the lamination process

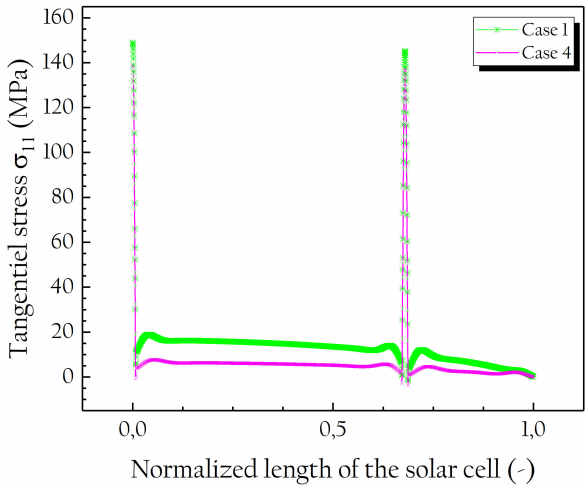

Figure 5.6: Level of tangential stresses σ_{11} along the length of the solar cell at 150°C in cases 1 and 4 (the center of solar cell corresponds to zero)

overestimated.

5.1.2.1 Elastoplastic behavior of the interconnector

Copper ribbon has a thermo-elastoplastic behavior with rigidity decreasing when increasing the temperature. This decrease of rigidity can make it more sensitive to plastic deformation. A study reported by Wiese et al. [158] assessed the constitutive behavior of copper ribbons. It was found that Young modulus of copper ribbons decreases as the temperature increases. We also noticed this temperature sensitivity in the experimental measurements presented in Section 3.2.1.

The evolution of the tangential stress in Cases 1, 2, and 4 during lamination in the volume of a copper ribbon assembled on the backside of the solar cell is presented in Figure 5.7. Unlike the cell, the copper ribbon is subject to compression during lamination due to the difference in CTE between the ribbon and the cell. Ribbon has a higher CTE than silicon, so it expands more, but the interface bond with the cell prevents it from expanding as much as its CTE requires. In the pre-heating stage, the tangential stress in all three cases is identical, and as the pressure is applied by the membrane and the temperature increases in stage II the copper ribbon undergoes plastic deformation. Therefore, in Case 1 where the behavior of copper is considered elastic, the stress is overestimated by 6.2% due to the absence of plasticity in the copper. In the cooling step III, the stress level in each case is distinguished. In Case 1 the stress is null since the ribbon is considered elastic, so all its deformation is reversible. On the other hand, in Cases 2 and 4, residual stresses are induced in the ribbon due to its irreversible plastic deformation. However, the stress level in Case 4 where the EVA and the backsheet are considered viscoelastic, the stress level is 51.72% lower than in Case 2 due to the relaxation of the encapsulant and backsheet. The relaxation of the viscoelastic materials, the encapsulant and the backsheet, relaxes the deformations applied to the copper ribbon.

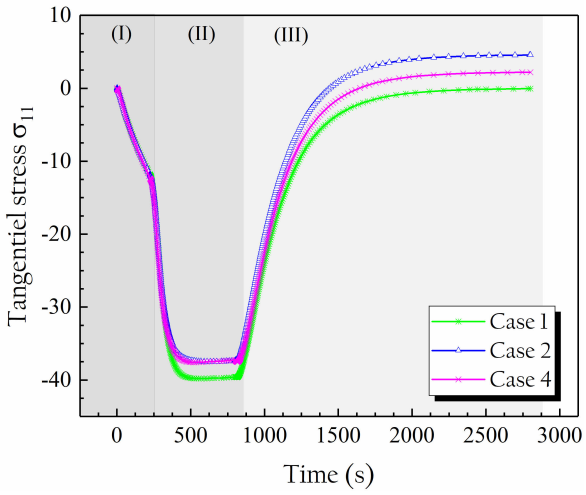

Figure 5.7: Evolution of the average tangential stresses σ_{11} in Cases 1, 2 and 4 during lamination process in the volume of a copper ribbon assembled on the backside of the cell

5.1.2.2 Viscoelastic behavior of the encapsulants

The purpose of the lamination process is to soften the encapsulant and apply pressure on the structure for assuring an adhesion between the layers that protect the solar cell. Considering the

encapsulant as an elastic material, no effect of softening and relaxation will be observed in the numerical results. Figure 5.8 shows a comparison between the tangential stress evolution during lamination in Case 1 and Case 3 for which the encapsulant is considered as viscoelastic. In Case 1, the maximum tangential stress is reached at 150°C, and is around -0.113 MPa. However, the maximum tangential stress in Case 3 is equal to -0.09 MPa, i.e. a decrease of 20.67%. During the second lamination step, a constant pressure is applied on the PV module. This pressure leads to a relaxation of the encapsulant at 80°C.

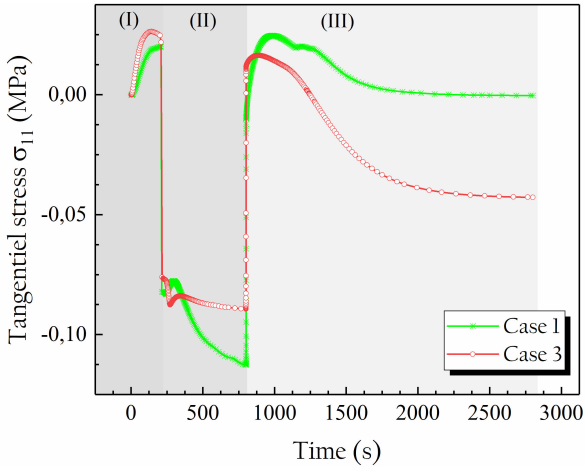

Figure 5.8: Evolution of tangential stress σ_{11} in cases 1 and 3 during lamination process in the volume of encapsulant in interconnection zone

The stress in the encapsulant are compressive ones though very low. Figure 5.9 presents the total, elastic, viscous and thermal strains evolution in the encapsulant during the lamination process. We can observe that the total and viscous strains are negative while the thermal strain is positive. Due to the relaxation of the encapsulant, the viscous tangential strain becomes predominant with a maximum value of -0.058. The proportion of the tangential thermal deformation is also important ($\approx$ 3.36%). The elastic deformation is negligible. The sum between these three components gives a negative total deformation in the encapsulant, describing the compressive stresses observed in Figure 5.8.

5.1.2.3 Viscoelastic behavior of the backsheet

In a large number of numerical studies found in the literature, the thermomechanical behavior of the backsheet is considered as thermoelastic [24; 48; 128; 129; 134]. Bosco *et al.* [12] have studied experimentally the viscoelastic behavior of the backsheet and provided Prony series for several types of backsheets and encapsulants. In the current work, a study on the viscoelasticity of TPT backsheet was carried out. A Generalized Maxwell model was developed and used in our model. The evolution of the tangential stress in the backsheet during lamination and cooling is shown in Figure 5.10 for Cases 3 and 4. Compressive stresses are located in the backsheet during the lamination step. But once the structure cools down, the backsheet is under tension. In the preheating step (I), the tangential stress is identical for both Cases 3 and 4. At the end of this step, the backsheet softens and relaxes due to the increase of temperature and the applied pressure by

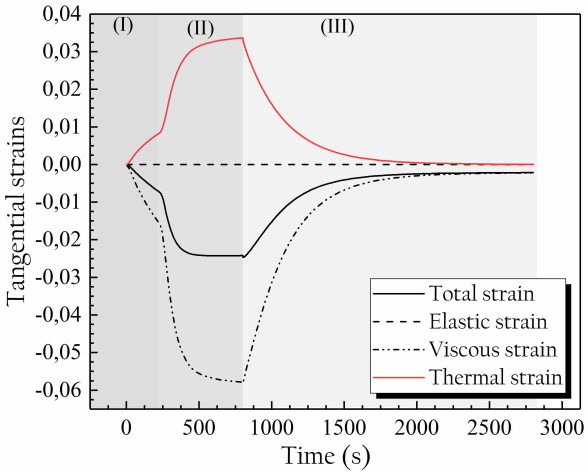

Figure 5.9: Evolution of tangential strains in case 3 during lamination process and cooling in the volume of encapsulant in interconnection zone

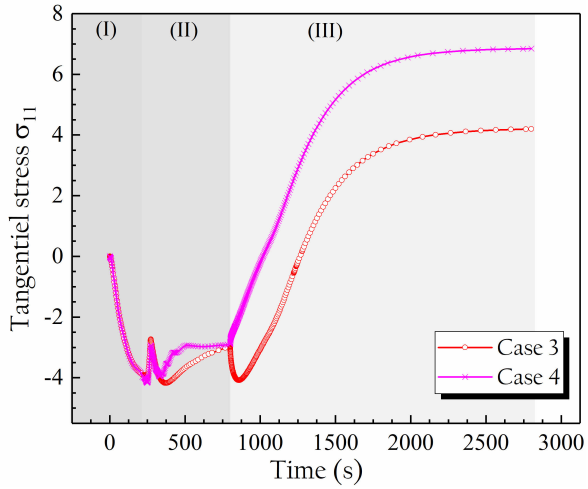

Figure 5.10: Evolution of tangential stress σ_{11} in cases 3 and 4 during lamination process and cooling in the volume of backsheet near the interconnection zone

the membrane. Therefore stress level decreases by 19.84% in Case 4 compared to Case 3. After cooling, in Case 4 the residual stresses induced in the backsheet equals 6.84 MPa which is higher compared to Case 3. As mentioned previously, after cooling the PV module bends upwards resulting in tension stresses in the backsheet. This tension stresses are more important when the material is very soft compared to glass. This is the case when the viscoelastic mode is added in the backsheet behavior.

We discussed the influence of all material behavior laws on the thermomechanical stresses in the PV module. Complex constitutive models have been used which should require considerable computational resources. In Table 5.2, we have presented the different case studies with the calculation time required for each case for the same number of processors. The computation time in all cases is almost identical. On the other hand, by choosing a more realistic material model for the encapsulant, the computation time increased by few more minutes. Case 4 is the most complete in terms of realistic behavior law. The computation time is less than Case 3 by 15min. In addition, more realistic behavior model helps to better manage numerical problems in simulations such as singularities

which could explain the decrease of time calculation between cases 3 and 4. Thus, the computation time is not an issue if a good accuracy is sought in the computations.

This study revealed that the use of simplified material models can have a poor predictive accuracy with an overestimation of deflection or an over/underestimation of thermomechanical stresses.

5.1.3 PV module architecture and its impact on thermomechanical stresses induced during lamination

The PV module architecture has evolved significantly over the last decade. Any variations in the architecture can impact the stress state in the PV module. Eitner *et al.* [143] demonstrated that the interconnect design affects the residual stresses in the solar cell after lamination. Dietich *et al.* [105] reported the dependence of PV module deflection on the thickness of the solar cell and the encapsulant. Rendler *et al.* [102] studied the influence of contact pads on the thermomechanical stresses induced in the solar cell after the interconnection process. Beinert *et al.* [150] conducted a recent study on the size and number of solar cells as well as the size of PV modules and their impact on thermomechanical stresses after lamination, during a thermal cycle and mechanical loading. They studied two architectures related to glass-glass (GG) and glass-backsheet (GBS) architectures on large modules. Moreover, in their simulations thermoelastic laws were used as material models.

In this present work, the evolution of residual stresses in a PV module during manufacturing was studied for different parameters for three different architectures as presented in Table 5.3:

- Heterojunction solar cell size: Two solar cell sizes where chosen, M0 which is a standard size and M2 which is larger (2.25% surface area increase). With an efficient cell technology of 19.5%, the M2 cell size provides a gain of 0.1 W of output power compared to M0 [33].
- The number of BusBars (BB): Increase from 3 BB to 6 BB. Depending on the cell technology and PV module design, a power gain of 5 to 10 W can be provided by multi-bar technology [33].
- PV module backside type: The backside of the module can be made of white or transparent backsheet polymer or glass. According to International Technology Roadmap for Photovoltaic (ITRPV) 2019, the degradation rate of standard backsheet modules is 0.25% higher than the glass-glass modules. The degradation of glass-glass PV modules reduces energy production by 15% after 30 years [33].

Three numerical models were built by varying the architectures. Realistic material models were taken into account as in Case 4 presented in Section 5.1.2. The maximum stresses in each component during lamination and after cooling to room temperature are shown in Figure 5.11. During lamination, the maximum stress in all components is a compressive stress except in the solar cell which is in tension. As the PV module cools down, the maximum stress is reversed compared to the lamination step with a lower level of stress. The stress level in the encapsulant, backsheet and glass is negligible compared to the maximum stresses observed in the solar cell and the interconnector. From a thermomechanical point of view, the increase in cell size does not have an effect on the tangential stress state. The size of the solar cell is mainly related to the number of busbars.

Model	Format of solar cell	Number of BB	Design
Architecture N°1 [M0-3BB-GBS]	M0	3	GBS
Architecture N°2 [M2-6BB-GBS]	M2	6	GBS
Architecture N°3 [M2-6BB-GG]	M2	6	GG

M0, Solar cell with 156 mm side length; M2, Solar cell with 156.75 mm side length; BB, BusBars; GBS, Glass-Backsheet; GG, Glass-Glass.

Table 5.3: PV module configurations studied to assess the impact of the architecture on the thermomechanical stress

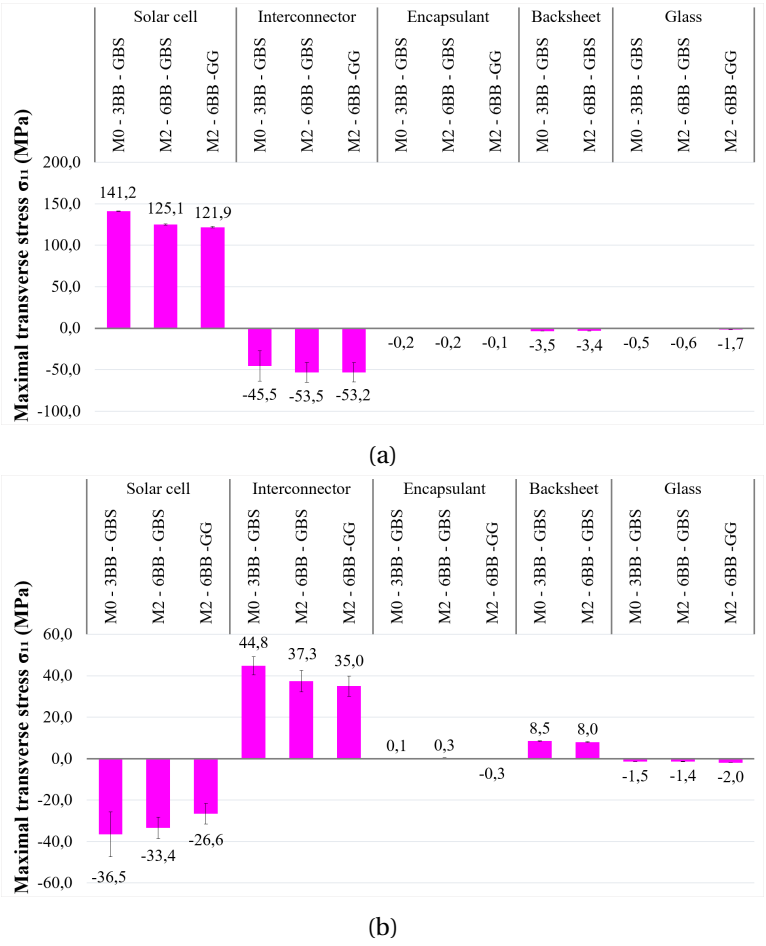

Figure 5.11: The maximal tangential stress in each component in different PV modules architecture (a) during lamination step and (b) after cooling to ambient temperature

During lamination and even after cooling in a glass-backsheet module, the maximum stress in the 6BB solar cell always remains lower than the stress in the 3BB solar cell. As the interconnector is offset from the center of the solar cell, the residual stress will be lower since the maximum deflection is mainly located in the center of the PV module. Comparing the two architectures with the same M2 cell size in 6 BB and a different backside, the level of maximum residual stresses induced in the solar cell in a glass-glass module decreases by 6.8 MPa (i. e. 20.38%) after cooling and by 2.3 MPa (i. e. 2.6%) in the lamination step (II) compared to the glass-backsheet module. Glass represents the thickest layer in the PV module (67% of the total thickness) and has a rigidity of 75 GPa. Hence the neutral plane of the laminate is located in the glass plate. The backsheet has a very high CTE compared to glass. However its softening during lamination makes it insufficiently rigid

compared to glass. Therefore the expansion of the glass governs the expansion of the PV module, which results in higher stresses in the other components. The heating during lamination is non-symmetrical, even if the structure of glass-glass PV module is symmetrical, and therefore the temperature gradient is different in the two glass layers. Thus the expansion of the glass placed against the rigid support remains dominant and the stress level in the other components is not much reduced compared to a glass-backsheet structure.

In this study, with the simplified 2D sub-model, we have highlighted the impact of the behavior laws on the computational accuracy. The realistic behavior laws ensure a good computational accuracy in the case of simulation of the manufacturing process. The effect of some architecture has also been studied. The cells with multibusbars show a lower level of thermomechanical stresses. The GG modules also have a positive effect on the reduction of residual stresses.

The modeling of the lamination process in 2D is a simplified approach that allows fast and efficient simulations to study the effects of architecture, process, and/or material behavior in the thickness of the PV module. However, some effects such as edge effects and out-of-plane stress levels are not identified. For this reason, we opted for another sub-model with 3D geometry at the cell scale to study these effects.

5.2 3D Finite element sub-model

In this section of the chapter, a 3D sub-model is constructed to study edge effects and out-of-plane stresses during PV module lamination. Based on the results of the 2D sub-model, a glass-backsheet architecture with 3 busbars was selected as it represents the most critical case. Since the interconnection area represents the most critical area in the PV module, a study on the effect of the presence of ECA between the copper and the cell will be performed.

5.2.1 Presentation of the sub-model

5.2.1.1 Geometry of the model and loading conditions

In order to study aspects of edge effects and out-of-plane stress distribution, a 3D sub-model was developed using the FE Abaqus software.The sub-model represents the geometry of a single cell PV module as illustrated in Figure 5.12. The symmetry of the geometry allows to model only the quarter of the PV module by applying boundary conditions to the symmetric planes. Perfect contact constraints are considered at each interface. A gravity load is applied to the PV module to eliminate rigid body motions. The ECA pads between solar cell and the interconnects were considered in this model (see Figure 5.12-(b)) and metallization details of solar cell were omitted. Transient thermal conditions were applied in the different steps of the simulation. A stress free temperature was set at ambient temperature 25°C. The lamination process was modeled using the same lamination steps of a conventional lamination process used in 2D sub-model and presented in Figure 5.3.

During lamination, the PV module is placed on the laminator. For this purpose, a fixed rigid body has been added in contact with the front face of the glass. A normal rigid and tangential

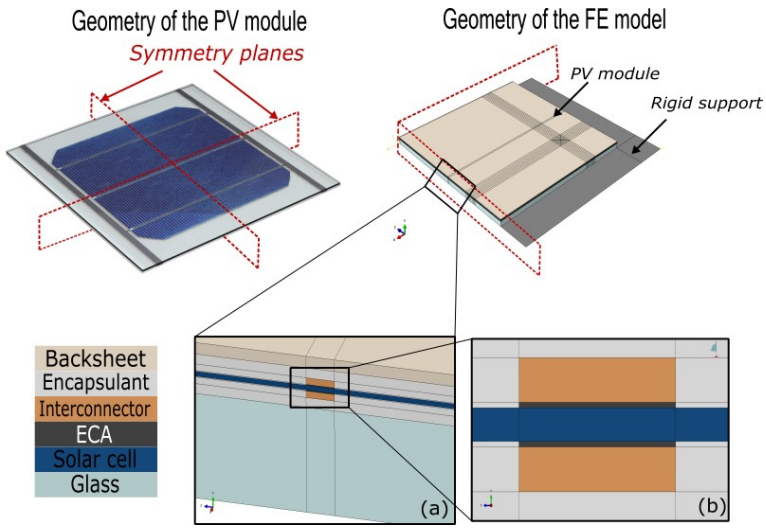

Figure 5.12: Schematic of geometry and FE model of a single-cell PV module. The enlargement (a) shows the thickness in more details and enlargement (b) shows the interconnection zone details

frictionless contact is used. Contrary to the simplified 2D case, in the 3D sub-model the PV module undergoes a double curvature due to thermomechanical loading. This double curvature induces a concave deformation of the PV module and thus the edge of the glass layer slightly penetrates the rigid support as displayed in Figure 5.13a. This leads to divergence problems. To solve this numerical problem, a fit interference function available on Abaqus Software was added to the model to handle the problems of penetration of the deformable body into the rigid body.

By default, the imposed contact between two surfaces is defined without penetration when $h(t) \leq 0$. It is considered that the contact penetration exists when $h(t)$ is positive. The definition of interference fit in the contact properties allows to manage the overclosure problems in the initial step or during the calculation steps. By defining a limit v of allowed penetration (so that $h(t) - v(t) \leq 0$), the algorithm pushes the slave surface to correct the penetration of the deformable body into the rigid body as shown in Figure 5.13b.

This surface displacement has no effect on the level of stress and strain in the case of our problem since the penetration is of the order of a few micrometers. In fact, this allows to reduce the contact pressure and to block the glass from bending more than it should during the lamination process.

5.2.1.2 Material modeling

As discussed in Section 5.1.2, the use of realistic behavior laws ensures good computational accuracy. Therefore, in this study viscoelastic behavior laws were used for the encapsulant, backsheet and ECAs. A thermo-elastoplastic law was used to model the copper. The thermal expansion of the components is considered variable with temperature except for glass where a constant value is defined. In the case of TPT backsheet and solar cell, an orthotropic thermal expansion coefficient is defined.

Romer *et al.* [152] have studied the effect of an anisotropic and negative backsheet CTE on the residual stress distribution after lamination cooling. Their simulations showed that the stress

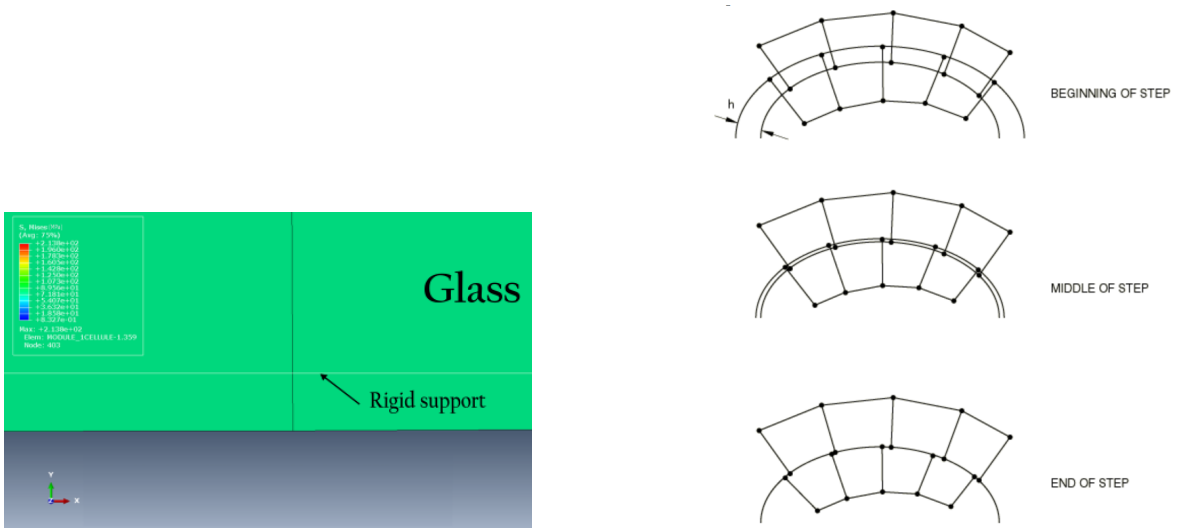

(a) (b)

Figure 5.13: (a) Example of glass penetration in rigid support during the pre-heating step (I), and (b) Interference fit with contact surfaces [188]

distribution is asymmetric in solar cells. Backsheets with a partly negative CTE show a lower compressive stress level compared to a backsheet with a strictly positive CTE. For this reason, in our study, we consider the effect of anisotropic thermal expansion in the backsheet. All materials' properties and behaviour laws are presented in Table 5.4.

Component of PV module	**Young's Modulus (GPa)**	**Poisson's ratio ν**	**Thermal Conductivity** ($W.m^{-1}.K^{-1}$)	**Density** (Kg/m^3)	**CTE** $.10^{-6}$ ($1/C°$)	**Specific Heat** ($J.Kg^{-1}.K^{-1}$)
Copper	E(T) (table 3.3) and J.C. (table 3.4)	ν(T) (table 3.3)	401 [48]	8890 [48]	α(T) (table B.1)	386 [48]
Encapsulant TPO-A	G.M. (table A.1)	ν(T)	0.46 (table 3.7)	944*	α(T) (table B.2)	1848.7 (table 3.6)
Backsheet PP	G.M. (table A.1)	ν(T)	0.32 (table 3.7)	2520 [48]	α(T) (table B.1)	1272.11 (table 3.6)
Glass	73 [48]	0.235 [134]	0.937 [48]	2500 [48]	8 [48]	913 [48]
Solar cell	anisotropic elasticity (table 1.1)		130 [48]	2329 [48]	α(T) (table B.1)	677 [48]
ECA-A1	G.M. (table A.1)	0.35 [164]	0.61 (table 3.7)	4400 [164]	α(T) (table B.2)	762.04 (table 3.6)
ECA-A2	G.M. (table A.1)	0.35 [164]	0.71 (table 3.7)	4400 [164]	α(T) (table B.2)	751.13 (table 3.6)

J.C., Johnson Cook plasticity model; G.M., Generalized Maxwell viscoelastic model.

Table 5.4: Material properties of PV modules components. *: provided by manufacturer

5.2.1.3 Model mesh

In this 3D sub-model, coupled temperature-displacement elements were used. Hexahedral elements were used in the model and a combination of hexahedral and prismatic elements was used especially in the pseudo-square area of the solar cell to improve the mesh quality as illustrated in Figure 5.14a. First order linear elements with reduced integration have been chosen (minimal discretization 0.04 mm) where all the materials were assumed thermoelastic. A more refined

mesh was used in the interconnection zones where stress concentrations were observed (see Figure 5.14b).

A convergence analysis of the mesh was performed based on the maximum von Mises (VM) and maximal principal stresses during lamination in the solar cell since it represents the most loaded component in the structure. The stresses are taken at the integration points. As explained before, the complexity of the structure and the low length to thickness ratio requires a large number of elements in 3D geometry. With the coarsest mesh, the initial number of elements is around 50 000 elements. By refining the mesh, the number of elements exceeds half a million elements. Therefore, this increase of elements increases considerably the numerical computation time and therefore in this analysis the computation time is also taken into consideration.

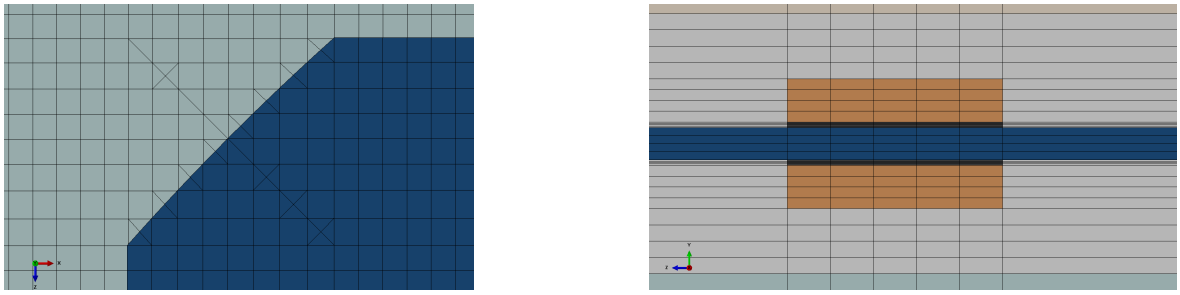

(a) (b)

Figure 5.14: Mesh details in 3D sub-model (a) in the plane of PV module near the pseudo-square corner of solar cell (only solar cell and glass are represented), and (b) in the thickness of PV module

Figure 5.15 displays the evolution of the von Mises and maximal principal stresses in the most loaded element located in the solar cell as a function of the number of element in the structure. It has been noticed that the level of von Mises and maximal principal stresses increase by refining the model mesh. By reaching a number of elements close to 300 000 elements, the stress level reaches a maximum level. The first four simulations were run on a local computer on 8 processors and the maximum computation time reached 165 hours. The fifth case of calculation launched on a virtual machine with 10 processors reaches a rather high calculation time (approximately 540 hours). However, the difference in measurement accuracy between 300 000 elements and 375 000 elements is only improving by 0.1%. The last case of calculation with a number of elements higher than half a million elements chosen to verify the total convergence of the mesh solution was launched in parallel on a cluster using 28 processors. In this case, the computation time dropped and reached a level of computation time almost identical to the cases with a coarse mesh. Therefore, considering the important reduction of the computation time using a parallel configuration on the cluster, a mesh refinement until a good computation accuracy as the case of 300 000 elements is adopted.

5.2.2 3D Stress distribution and side effects

Figure 5.16 shows the distribution of the maximal and minimal principal stresses in the backsheet side and the glass side of the solar cell at the end of lamination and before cooling. Stress concentrations are noticed all along the interconnection lines. The maximal principal stresses are tensile

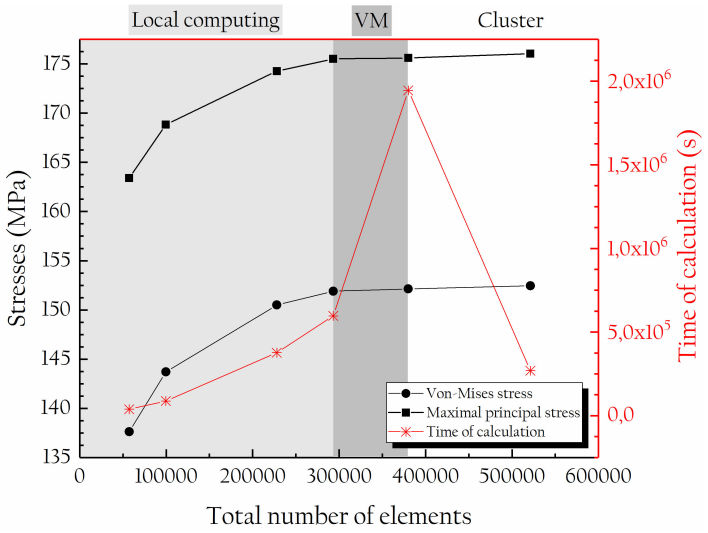

Figure 5.15: Maximum von Mises and maximal principal stresses with respect to the number of elements at 150°C

ones throughout the cell except at the edge of the interconnect line where they are compressive. An inverse stress distribution is observed in the minimal principal stress distribution.

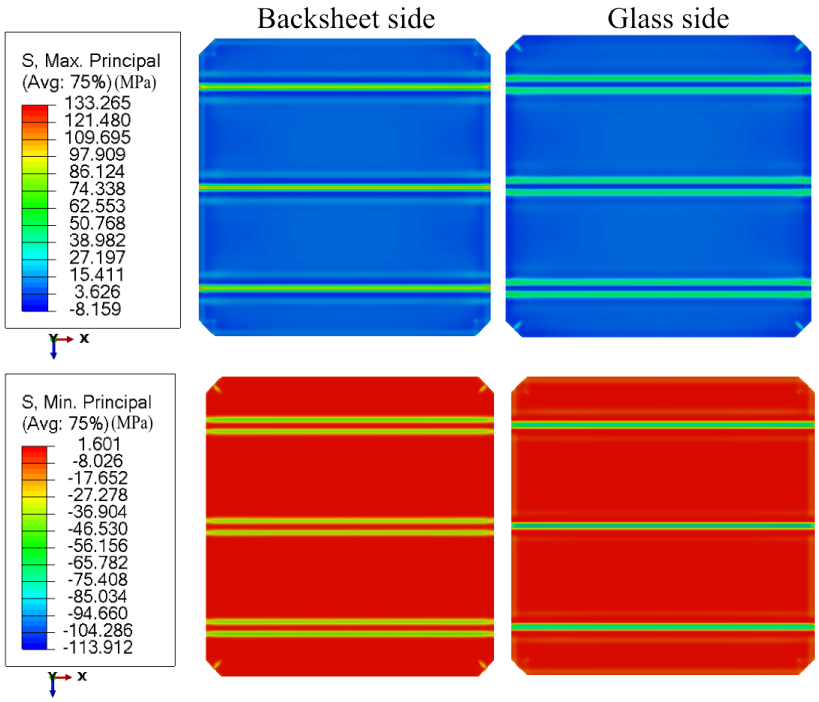

Figure 5.16: Maximal (top) and minimal (bottom) principal stresses distribution in the backsheet side and the glass side of the solar cell at 150°C with either local computing, ritual machine (VM), or cluster

On the backsheet side of the solar cell, the maximal and minimal principal stresses are tensile ones all along the interconnect lines. However, on the glass side of the cell the principal stresses are compressive. Therefore, the solar cell undergoes a bending gradient in its thickness in the interconnection areas. On the other hand, at the borders of the interconnection lines, the maximal and minimal principal stresses level in the cell is reversed with respect to the stresses in the interconnection lines in both cell faces. This means that the cell in the interconnection areas undergoes

local buckling. To better visualize this phenomenon, the maximum principal stress distribution in the cell thickness is presented in Figure 5.17. It is clearly noticeable that the cell around the interconnection zone is undergoing local buckling. This phenomenon is due to the pressure applied on the module by the side of the backsheet, and with the presence of the copper ribbon in the interconnection area, the cell is locally reinforced and bends less due to pressure effect. Hence, the difference in deflection between the interconnection and non-interconnection areas causes a local buckling at the edge of the interconnection area.

Minor edge effects are noticed in the maximal principal stress distribution in Figure 5.16 at the edge of the solar cell and mainly in the edge perpendicular to the interconnection lines. However, these edge effects are more critical in the interconnection areas as presented in Figure 5.17 where the principal maximal stress maximum is found. These edge effects are related to the contact pressure applied by the encapsulant and the backsheet on the edge of the solar cell. Moreover, these effects are more pronounced on the edge perpendicular to the interconnect lines due to the stress concentration in the interconnect lines and the difference in stiffness between the cell and the interconnect line reinforced by the copper ribbons.

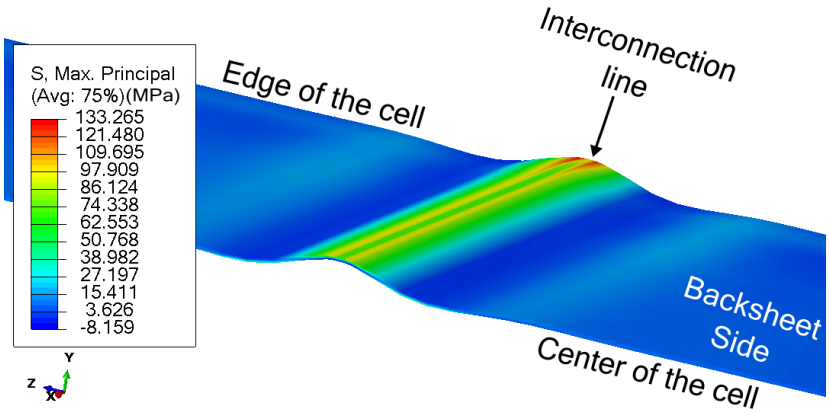

Figure 5.17: Maximal principal stress distribution in the solar cell in interconnection zone at 150°C (the upper face represents the backsheet side of the cell - deformed scaled ×30)

In the literature review on solar cell cracking, the distribution of micro-cracks in solar cells was discussed (see Table 1.3). Several works in the literature have shown that the maximum stresses occur near the edge of the interconnector. This explains that the majority of the microcracks occur at the interconnect lines. The same distribution is observed in our results and the buckling phenomenon can explain the propagation of cracks in these areas.

In a study by Beinert *et al.* [129], residual stresses were measured at the end of lamination using the confocal micro-Raman spectroscopy technique. Their experimental measurements were conducted on a single-cell module quite similar to our geometry in the 3D sub-model. Figure 5.18 shows the experimentally measured residual stress distribution in their study. The interconnection lines are not scanned. As their stress state is measured after lamination (i.e. when the module is at room temperature), the maximum stresses in the cell are compressive ones. However, we are interested in the stress distribution. It can be seen that at the edge of the interconnection lines the stresses are compressive. By moving away from these lines towards the center and the edge of the cell, the stresses become positive, creating a stress concentration.

Comparing this experimental distribution with the numerical distribution obtained in our study, we can withdraw some similarities despite the difference in the stress state, which is logical since in our study we were interested in the stress at the maximum lamination temperature. In both distributions, at the edge of the interconnection lines, the stresses are positive or negative and at a distance from these lines the stress sign changes and is maximal compared to the rest of the solar cell. Moreover, side effects are observed at the edge of the cell along the interconnecting lines, which is similar to our numerical results.

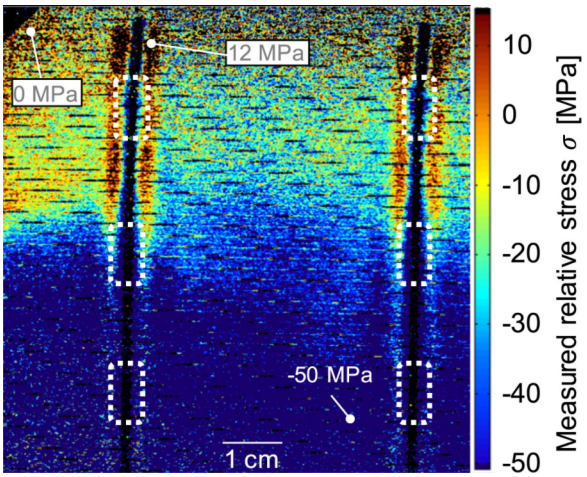

Figure 5.18: Micro-Raman cell scan. The color code represents the interconverted stress relative. The black lines are the metallization fingers and busbars, where no micro-Raman spectra are measured. The dotted white boxes indicate the position of the rear side metallization pads [129]

As discussed earlier, the cell is subjected to local buckling along the interconnecting lines. This numerically observed phenomenon is consistent with the experimental micro-Raman cell scan performed by Beinert et al. [129]. *Therefore, this phenomenon can eventually be at the origin of the microcracks that propagate at the edge of the interconnection lines.*

The presence of copper ribbon in the interconnect lines locally strengthens the cell and makes it less vulnerable to the pressure applied during lamination which forces the components to flatten and adhere well together. However, this causes a concentration of stress in solar cells along these lines and increases their risk of failure. Two parameters that can reduce this effect are either the reduction of the thickness of the copper ribbons or the use of other types of ribbons that have a CTE close to that of the solar cell. In section 2.2.2.2*, some studies of the literature review have shown the advantages of the reduction of the section of the copper ribbons in the decreasing of the residual stresses in the solar cell after soldering. Gabor et al.* [98] *have investigated the possibility of replacing the copper ribbons with Invar ribbons which have a CTE very close to that of the solar cell. Their results showed that Invar can be a promising alternative to copper ribbons.*

5.2.3 The influence of the ECA on the probability of solar cell failure

Solar cell cracking occurs mainly in the interconnect lines as discussed in the literature review in Section 1.2.1. Numerically, in our 2D study, a stress concentration in the interconnection lines was observed. These stress concentrations can eventually decrease if the contact between the ribbon

and the solar cell is not considered perfect by adding an ECA layer between the two components.

Geipel *et al.* [139] investigated the reduction of thermomechanical stresses at the interconnection step using ECA. We have also discussed the level of thermomechanical stress in the ECA interconnection step in Chapter 4. Here, we are interested in studying the effect of ECA on the stress level during lamination. In this study, a comparative study was performed to investigate the stress level when the cell and ribbon are interconnected without or with ECA. The type of ECA was also varied to identify its impact on the thermomechanical stress level. The maximal and minimal principal stresses distribution analysis showed that the solar cell is in tension and compression, respectively. Since tensile stresses are more critical than compressive stresses for brittle materials, this analysis will focus only on the maximal principal stresses where the solar cell is under tension.

Considering these maximum principal stresses in each case of study, a probability of failure is calculated based on the Weibull law introduced in Section 3.3.2. In some works, the size effect is considered in the calculation of the failure probability [30; 150; 205]. It is a variable which allows considering the change of the volume of the sample and the mechanical loading applied on the solar cell [30]. As in this study these two parameters remain invariant between the three cases of study, the size effect is neglected, and the probability of rupture is calculated using the following equation:

$$P_f = 1 - \exp\left[-\left(\frac{\sigma_{I,max}}{\sigma_\theta}\right)^m\right] \tag{5.1}$$

where σ_θ is the characteristic fracture strength, and m is the Weibull modulus. The probability of failure was calculated with respect to the characteristic fracture strength and Weibull modulus of two different types of cells. In this work, the focus is on the SHJ technology and the Weibull parameters calculated in Section 3.3.2 are used. Another type of solar cell is also selected, AL-BSF technology, for the study of failure probability with respect to the maximum principal stress level induced during lamination. The Weibull parameters are summarized in Table 5.5.

Cell technology	**Characteristic fracture strength (MPa)**	**Weibull modulus** m
SHJ	222 (Table 3.5)	8.6 (Table 3.5)
Al-BSF	180 [202]	6.9 [202]

Table 5.5: Weibull parameters for SHJ and Al-BSF solar cells

Figure 5.19 displays the maximum of maximal principal stresses during lamination process at 150°C and the probability of failure with respect to two types of solar cells regarding the type of ECA. The maximum of maximal principal stress in the interconnected cell without ECA is significantly higher by approximately 47 MPa compared to the cells interconnected by ECA. ECA is an acrylate polymer-based material with a glass transition temperature generally lower than the maximum lamination temperature. Therefore, the stiffness of ECA remains well below that of copper and silicon. Moreover, ECA has a coefficient of thermal expansion a hundred times higher than that of silicon and copper. Therefore, these characteristics of the thermomechanical behavior of ECA have a role in the decrease of stress related to the bond between the cell and the copper rib-

bon.

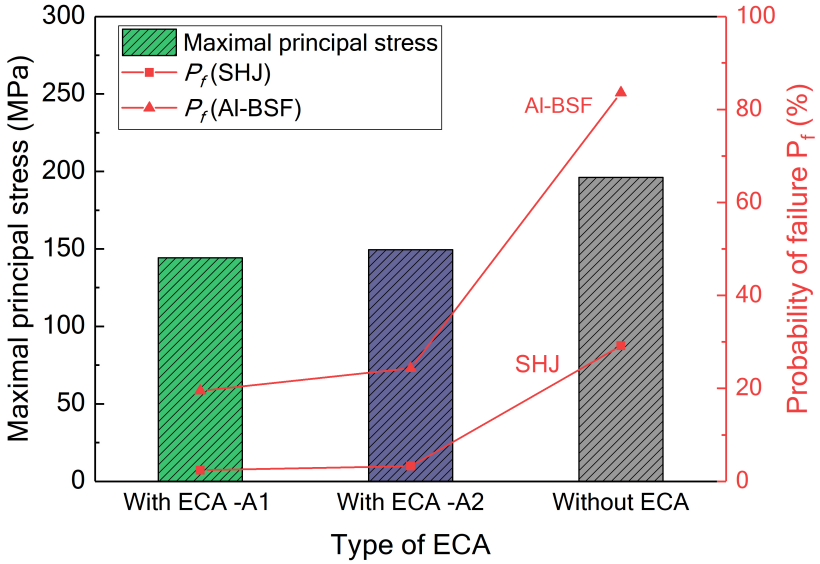

Figure 5.19: Maximum of maximal principal stress in the solar cell in interconnection zone at 150°C, and probability of failure in cell regarding two characteristic fracture strength with respect to the type of ECA

The maximum of maximal principal stress in the solar cell during lamination when ECA-A2 is used is slightly higher than the maximum stress in a cell interconnected by ECA-A1. This is explained by the difference in stiffness between the two ECAs during the lamination process. As shown in Section 3.1.1, ECA-A2 has a glass transition temperature around 95°C and therefore the transition occurs in the lamination temperature range. However, ECA-A1 has a relatively low transition point. Consequently, ECA-A2 has a higher stiffness and does not relax the stresses related to the assembly of the copper and the cell as much as ECA-A1.

The probability of solar cell failure during the lamination process estimated with respect to the failure strength of two types of solar cells is also presented in Figure 5.19. Since the fracture strength of the Al-BSF cell is lower than that of the SHJ cell, the fracture probability in the case of Al-BSF cell is higher. When the cell is interconnected without ECA, the failure probability reaches approximately 84% for the Al-BSF cell, while the probability is limited to ≈ 30% for the SHJ cell. By using ECA to join the cell with the copper ribbon, the stress level decreases so the probability of cell failure in both types of cells decreases considerably. These failure probabilities are quite high since only one cell was considered and the size effect was neglected. However, if several cells are considered taking into account the size effect, the failure probability will necessarily change. We have not conducted experimental studies to verify these numerical observations. Theses aspects are quite intriguing and so encouraging to be further investigated in the future.

Conclusion

The lamination process is the second and final step in the assembly of the PV module components. This assembly is ensured by a combination of mechanical and thermal loading to ensure softening of the encapsulant and adhesion of the protective layers to protect the solar cell matrix. The different components of the PV module involved in this step have a totally different thermomechanical

behavior.

Residual thermomechanical stresses induced in PV modules can affect their performance and lead to a total damage of the structure. Therefore, it is necessary to understand the thermomechanical phenomena that contribute to the creation of these induced stresses. Numerical modeling was used to achieve such purpose.

In this chapter, we have focused on the sub-modeling of the lamination process in order to evaluate the induced thermomechanical stresses. Several studies have been carried out in the literature to study the thermomechanical behavior of PV modules. Few of these works have used realistic material behavior.

In this work, we have estimated the loss of the model accuracy when simplifying the material models of copper ribbons, encapsulant and backsheet. Elastoplastic and viscoelastic models have been used to describe the thermomechanical behavior of copper ribbon and the backsheet and the encapsulant respectively. The results showed **an overestimation or underestimation of the thermomechanical stresses in all components if simplified material laws, such as elastic models, were used. The relaxation of the encapsulant and backsheet protects the solar cell against the deflection applied by the glass. Stress concentrations were observed in the interconnection zones**. These localized stresses allow the potential initiation of microcracks during interconnection followed by propagation and eventually complete failure of the solar cell. In addition, the complex behavior laws do not increase the computation time.

The PV market offers many varieties in component designs and PV module architecture. In this study, we investigated the correlation between the level of induced stresses in the PV module and its architecture. The position of the busbars has an influence on the thermomechanical induced stresses in the solar cell. **Solar cells with busbars offset from the center are less loaded. The non-symmetry of the thermomechanical loading and the structure increases the deflection of the PV module resulting in a higher level of stress in a glass-backsheet module compared to a glass-glass PV module**.

A 3D sub-model was developed to capture the out-of-plane stresses and edge effects induced during the lamination process. The results of the 3D sub-modeling showed that the cell undergoes stresses related to side effects, especially in the edge of the interconnection lines. These **sides effects are related to the contact pressure applied by the other materials at the edges of the cell**.

As mentioned earlier, stress concentrations have been observed in the interconnection areas between the copper ribbon and the solar cell. For this purpose, we have studied the impact of the ECA interconnection technology on these stress concentrations. It was observed that **the presence of ECA between the two components relaxes the stress level induced by the CTE mismatch as the ECA expands greatly and is less stiff. Therefore, the failure probability in the case of an ECA interconnected cell is lower than a solder interconnected cell regardless of the type of solar cell**.

In the two sub-models studied in this chapter, the whole cycle of thermomechanical loading of the lamination process was considered, as the goal was to understand the thermomechanical behavior of the PV module and the assembly of the different components of the PV module. However, this strategy might not be suitable for the investigation of the residual stresses at the end of

the PV module fabrication. This aspect will be addressed in the next chapter.

Chapter 6

Residual deflection of PV module regarding lamination process parameters

Contents

Résumé du chapitre

Les contraintes résiduelles peuvent avoir ont un effet dégradant sur la fiabilité et la durée de vie des modules photovoltaïques (PV). L'évaluation de l'effet des paramètres du procédé de lamination sur la fiabilité des modules PV est une étape clé pour étendre leur durée de vie. Cependant, les méthodes de mesure des contraintes résiduelles sont limitées. Deux méthodes de mesure des contraintes résiduelles à l'échelle locale de la cellule solaire sont disponibles dans la littérature. Toutefois, ces méthodes ne permettent pas une mesure globale de la déflexion du module PV.

Dans ce chapitre, une nouvelle méthode de mesure de la déflexion des modules PV est présentée. Cette méthode consiste à cartographier la surface des deux côtés d'un module PV positionné sur 4 supports ponctuels. La répétition des mesures sur les deux faces vise à compenser l'effet de gravité induit par le poids propre du module PV. La position des supports a été optimisée analytiquement. L'erreur induite par ce protocole de mesure a été estimée numériquement.

Une campagne de mesures expérimentales utilisant ce protocole a été réalisée afin d'étudier l'influence des paramètres du procédé de lamination (architecture, température et type de refroidissement) sur la déflexion des modules PV. Tout d'abord, l'erreur de planéité des plaques de verre utilisées pour fabriquer les modules PV a été mesurée. Il a été constaté que les plaques de verre ne sont pas parfaitement plates et que leur déformation résiduelle n'est pas symétrique.

Ces plaques de verre ont ensuite été utilisées pour fabriquer les modules PV. Les mesures expérimentales sur les modules PV ont montré que pour l'architecture verre-backsheet, la déflexion résiduelle diminue lorsque la température de lamination augmente, ce qui n'est pas observé dans l'architecture verre-verre. Le type de refroidissement a également un effet, étant donné que la déflexion des modules PV refroidis à l'air ambiant est plus élevée que celle des modules PV refroidis sous presse.

Par la suite, un modèle 3D a été développé pour étudier la corrélation entre les mesures expérimentales et numériques. La corrélation entre les mesures expérimentales et numériques de la déflexion résiduelle n'était pas très bonne avec une sous-estimation de la déflexion avec le modèle numérique. Les facteurs influençant cette variation entre les mesures expérimentales et les valeurs numériques ont été discutés. La déflexion résiduelle des plaques de verre a une influence majeure sur cette variation puisque des hypothèses numériques simplificatrices liées à la géométrie ont été considérées. Ces hypothèses considèrent que les composants du module PV sont initialement parfaitement plats et que la structure du module PV est symétrique. Néanmoins, une étude plus approfondie doit être menée pour justifier les différences observées.

Enfin, le niveau de contrainte résiduelle associé à la déflexion numérique des modules PV a été analysé. Les résultats ont montré que les cellules solaires sont sous compression. Les contraintes de compression ne sont pas critiques pour les matériaux fragiles comme le silicium. Cependant, si des rubans d'interconnexion sont ajoutés, ils peuvent induire des concentrations de contraintes positives. Dans ce cas, le risque de défaillance des cellules solaires augmente.

Introduction

Thermomechanical residual stresses have a degrading effect on the reliability and lifetime of photovoltaic (PV) modules. Assessment of the effect of the lamination process parameters on the reliability of PV modules is a key step to extend their lifetime. However, residual stress measurement methods are limited. Tippabhotla *et al.* suggested a synchrotron X-ray micro-diffraction method to evaluate residual stresses in solar cells surface in PV module after interconnection and lamination processes [134]. Beinert *et al.* provided a measurement of thermomechanical stresses in solar cells and PV module by confocal micro-Raman spectroscopy [129]. However, these methods do not allow a global measurement of the deflection of the PV module. Li *et al.* [85] developed a technique to separate the glass plates from the rest of the layers in order to measure their central deflection. However, by eliminating the bonding of the glass to the other layers, the deformation related to the contraction of the glass is neglected. Since it is the glass that governs the contraction of the PV module, the measured deflection could be unrepresentative to that of the PV module.

In this chapter, a new method of measurement of the deflection PV modules will be presented. This method consists in mapping the surface of both sides of a PV module positioned on 4-point supports. The measurement repetition on both sides aims at compensating for the gravity effect induced by the self-weight of the PV module. The position of the supports will be analytically optimized. The error induced by this protocol of measurement will be numerically estimated.

An experimental measurement campaign will be carried out to characterize the impact of lamination process parameters on the residual deflection of the PV modules. First, the initial shape of twelve glass plates will be characterized. Then, the PV modules will be manufactured using the same glass plates while varying architecture, lamination temperature, and cooling type. Using the same method, the residual deflection of these PV modules will be investigated.

Finally, according to our multi-scale modeling strategy (see Figure 6.1), a 3D model which represents the global scale of the PV module will be introduced. This model will allow to study the correlation between the experimental and numerical measurements of residual deflection of PV modules depending on lamination parameters.

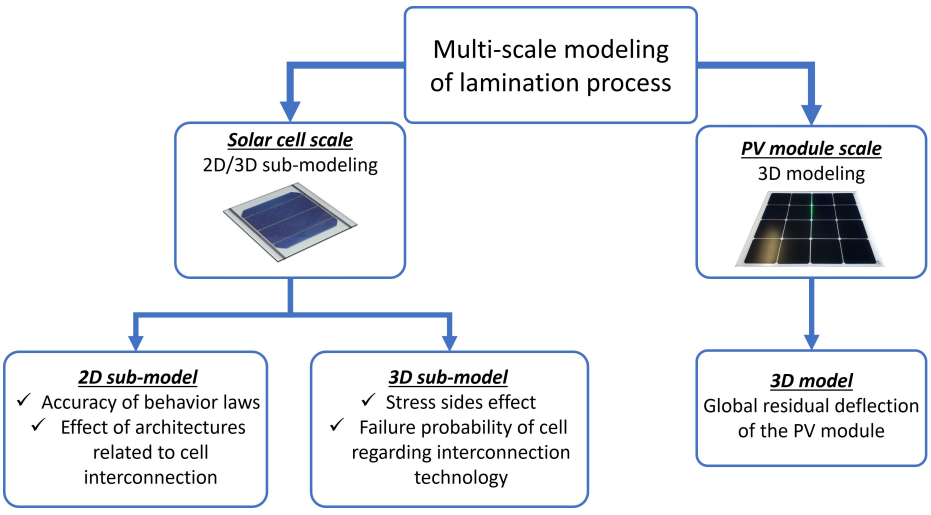

Figure 6.1: Our strategy of multi-scale modeling of lamination process

Some parts of this chapter are quoted verbatim from a conference paper published by Rahmoun et al. [206].

6.1 Experimental measurement method of PV module deflection

The post-lamination thermomechanical residual stresses are translated into a residual deflection of the PV module, which is linked to deflection. In this work, a new method of measuring the global deflection of PV module is developed. Then, this method is validated numerically and experimentally.

Indeed, the deflection (w_x, w_y) of PV module can be measured experimentally using distance sensors (laser or mechanical sensor). Moreover, local orientations (φ_x, φ_y) can be calculated directly using the following equation 6.1 as shown in Figure 6.2 :

$$\varphi_x = \frac{\partial w_x}{\partial y}; \quad \varphi_y = \frac{\partial w_y}{\partial x} \tag{6.1}$$

Then, the variation of local orientation along principal directions is used to calculate local curvature $(\kappa_{xx}, \kappa_{yy})$ in the associated coordinate system as follow:

$$\kappa_{xx} = \frac{\partial \varphi_y}{\partial x}; \quad \kappa_{yy} = \frac{\partial \varphi_x}{\partial y} \tag{6.2}$$

Several assumptions, similar to Kirchhoff-Love [207] thin plate theory can be used to estimate bending strains at the surface of a PV module of thickness t from local curvature:

$$\varepsilon_{xx} = \pm\frac{t}{2}\kappa_{xx}; \quad \varepsilon_{yy} = \pm\frac{t}{2}\kappa_{yy} \tag{6.3}$$

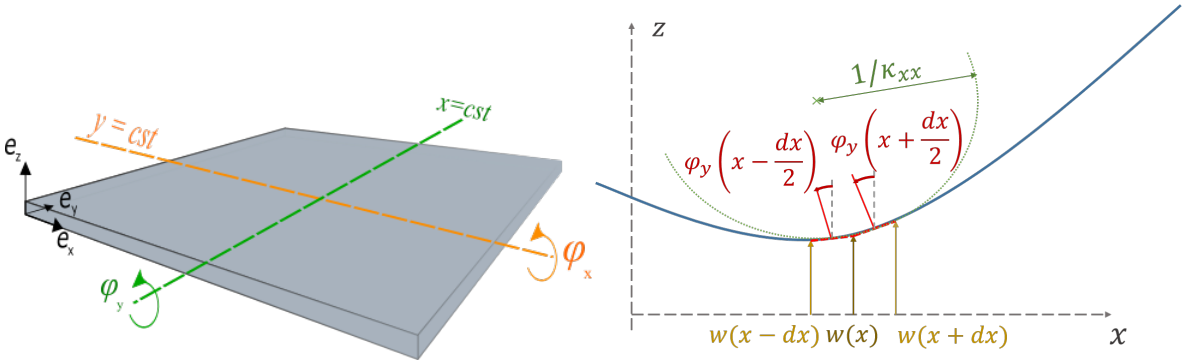

(a) (b)

Figure 6.2: Geometric notations of the problem: (a) Representation of coordinate system and local rotations and (b) Calculation of plate curvature from deflection measure, considering cross-section in (Oxz) plane

In this section, the experimental protocol developed for the estimation of PV module residual deflection is described. The measurement deviation induced by this protocol has been estimated numerically. Afterwards, a first experimental validation of the protocol was carried out on a glass plate and several PV module architectures.

6.1.1 Definition of the experimental protocol

In this section, we describe the experimental protocol developed for the estimation of PV module residual deflection. The main issue is to find a method to measure the deflection without constraining the PV module shape. Indeed, placing it directly on a plane support/table might impose an artificial flatness, while putting it on the edge would constrain the edge shape. The solution adopted was to put the PV module on four punctual supports as presented in Figure 6.3, distributed according to the laminate symmetries. This distribution of supports shall not constrain the measures, assuming the residual deflection to be symmetric. However, gravity effects occur due to the self-weight of the PV module. The additional deflection induced by gravity might even be higher than the residual deflection we are trying to measure if the protocol is not carefully thought out.

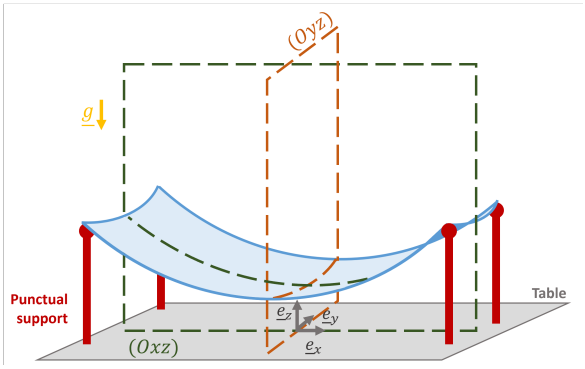

Figure 6.3: Schematic representation of the experimental set-up for the deflection measurement. The symmetry planes are represented in dashed lines.

6.1.1.1 Compensation of gravity effects

This method is inspired from monocrystalline silicon wafers measurement to eliminate the gravity issue. Indeed, SEMI standards [208] suggest to repeat the measure on both sides of the wafer in order to compensate its self-weight (see Figure 6.4). This experimental protocol relies on the assumption that the additional deflection induced by gravity is unchanged by inverting the PV module. Then, both measures contain this gravity contribution with the opposite effect. Thus, the average of both measures shall give the residual deflection, freed of the gravity effects.

6.1.1.2 Supports position optimization

Gravitationally induced deflection strongly depends on the support's position. The analytic study is reduced to a one-dimension (1D) optimization of the support position, along a beam. This simplification offers the right estimation with much easier calculations than a two-dimension (2D) optimization on a plate. The deformation in the transverse direction can be neglected as the PV module is a thin plate. Thus, in the 1D study, the one-point support is simple.

We consider a beam of length 2ℓ, placed on two supports at an equal distance a from the center of the beam (Figure 6.5a). The beam is assumed to be homogeneous, linearly elastic with a Young

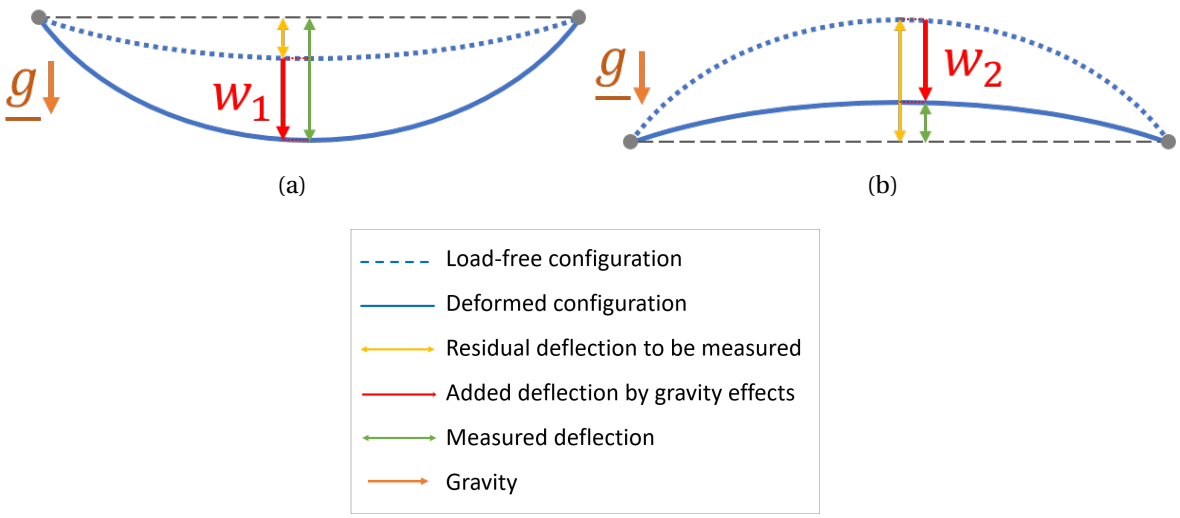

Figure 6.4: Schematic explanation of the experimental protocol used to compensate gravity effects (a) Measurement on side 1 and (b) Measurement on side 2 [206]

modulus E, a moment of inertia I and a linear density λ. The structure undergoes its self-weight, equivalent to an homogeneous linear loading $-\lambda g\, e_y$, where g is the gravitational acceleration. The direction of the beam is denoted by the vector e_x and the origin $x = 0$ is set in its center.

The application of Euler-Bernoulli theory allows to neglect the shear strain. Axial strain of the beam is also neglected with respect to strain coming from bending. Furthermore, small strains assumption is applied. The boundary condition along the symmetry plane is a sliding support with imposed orthogonality.

In the deformed configuration (Figure 6.5b), the deflection at x-axis is denoted by $w(x)$. Particularly, the deflection of interest will be the one in the center of the beam $w_C = w(x = 0)$ and at the end $w_E = w(x = \ell)$.

Castigliano's second theorem is used to calculate directly the deflection at the center and at the end of the beam :

$$w_C = \frac{\lambda g\, a^2}{4EI}\left[\frac{5a^2}{6} - (\ell - a)^2\right] \tag{6.4}$$

$$w_E = \frac{\lambda g(\ell - a)}{2EI}\left[\frac{(\ell - a)^3}{4} + a(\ell - a)^2 - \frac{2a^3}{3}\right] \tag{6.5}$$

Several cases have been considered for the support position, corresponding to different optimization criteria (Figure 6.6):

- **Case 0**: this reference case corresponds to the choice of putting the support at the end of the beam ($a = \ell$). This choice maximizes the deflection in the center w_C, which could be minimized.

- **Case 1**: the second option would be to minimize the deflection in the center with respect to a, where $\partial w_C / \partial a = 0$. However, this minimum corresponds to a negative value of deflection in the center, while the deflection at the end of the beam w_E increases. It occurs with a support around the third of the length: $a = 0.347\ell$.

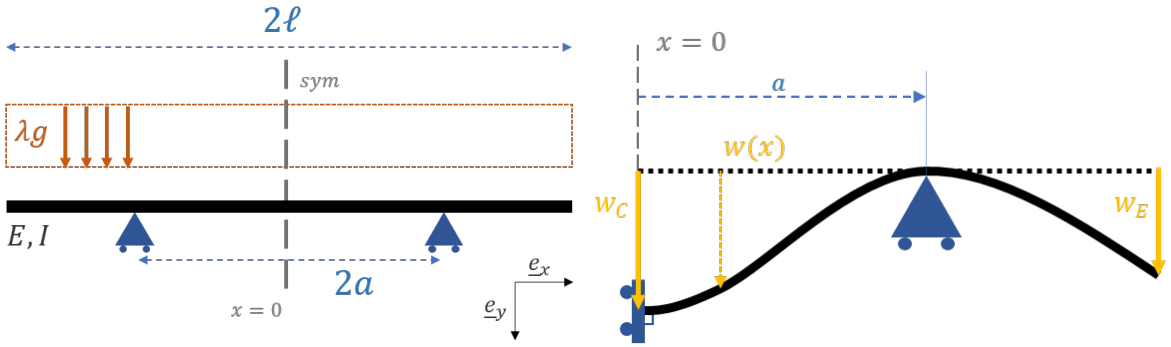

(a) (b)

Figure 6.5: Schematic representation of the problem: (a) loading case (the beam (in black) is placed on two sliding supports (in blue), submitted to self-weight loading (in orange)) and (b) deflection notations (in yellow), describing displacement from initial to deformed configuration (respectively dashed and continuous line) [206]

- **Case 2**: in order to avoid the reverse deflection in the center, another criterion would be to minimize the absolute value of w_C, resulting in $a = 0.523\ell$. However, if this choice ensures a zero deflection at the center of the beam, the deflection at the end of the beam is still not taken into consideration.

- **Case 3**: finally, the most general criteria would be to minimize the maximum deflection along the beam. This case can be expressed mathematically, by defining the optimal position as follows:

$$a_{opt} = \underset{a\in[0,\ell]}{\operatorname{argmin}} \left(\max_{x\in[0,\ell]} w(x) \right) \tag{6.6}$$

  The extreme deflection of the beam is reached either in its center or at its end, depending on the support position. Thus, the optimal value according to this criteria will be respected when $w_C = w_E$, giving $a = 0.554\ell$.

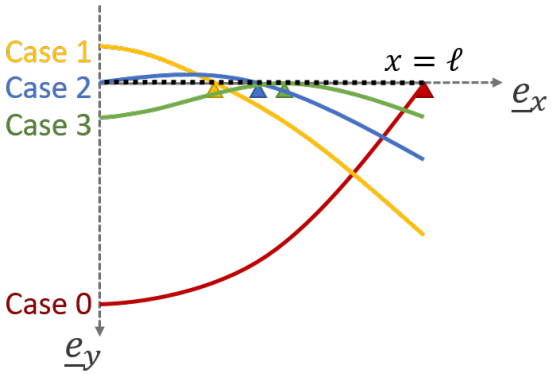

Figure 6.6: Undeformed (in black) and deformed shape of the beam for different cases of support position, corresponding to a choice of optimization criteria [206]

Case 3 was selected as it is the criterion that minimizes the maximum value of deflection along the whole beam. It is important to note that this optimal position is only dependent on the beam length, not on the geometric or material parameters (inertia and stiffness), which only change the

deflection's value. Then, this approach is valid in the most general case.

6.1.2 Numerical validation of experimental protocol

Theoretically it is assumed that the effect of gravity will be identical on both sides. Nevertheless, the validity of this assumption depends on several parameters including the effect of the structure and especially when the PV module has an asymmetrical architecture in the thickness.

A 2D Finite Element (FE) model is defined using Abaqus Software in order to validate the experimental protocol. We assimilate the PV module to a $1m \times 2m$ glass shell plate, as it is the thickest material of the laminate. A constant curvature κ_{xx} is imposed along direction e_x. The curvature is null along the transverse direction e_y (see Figure 6.7a). This arbitrary curvature is meant to represent the residual deformation of PV modules after lamination. We chose a thickness of 3 mm for a glass-backsheet architecture and 6 mm for a glass-glass architecture. The problem has two geometrical symmetries and loading with respect to the planes (Oxz) and (Oyz), at the center of the PV module. Thus, only a quarter of the structure is considered. The structure is submitted to gravity ($g = 9.81\,\mathrm{m/s^2}$), on one side and the other (Figure 6.7b).

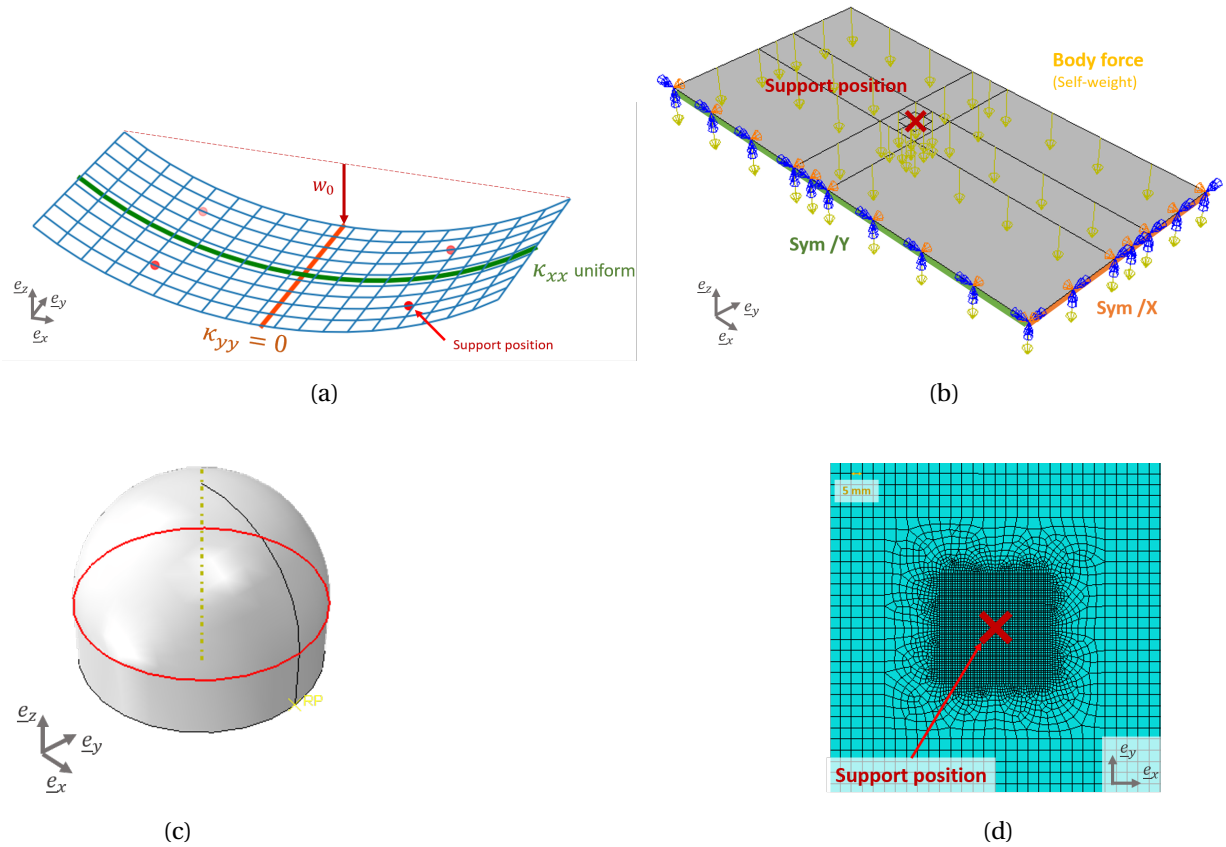

(a) (b)

(c) (d)

Figure 6.7: Description of the numerical model: (a) Geometry of the model, (b) Load description, (c) Support shape, and (d) Mesh refinement near the contact zone

The support is modeled by a 3D discrete rigid half sphere of radius $r = 2\,\mathrm{cm}$ (Figure 6.7c). A contact interaction is defined between the support and the bottom face of the laminate, with normal hard contact and frictionless sliding. Linear quadrilateral shell elements with reduced integration were used to mesh the structure with a characteristic size of $5 \times 5mm^2$. The mesh is

refined near to the contact zone with the support with quadrilateral mesh of size $1 \times 1 mm^2$ (see Figure 6.7d). A mesh analysis was performed to assess the accuracy of the numerical results.
As described in Section 1.1.1.4, tempered glass mechanical behavior can be considered as isotropic linear elastic. The elastic properties used are described in Table 1.2.

In order to assess the validity of the experimental protocol, we compare the initial deflection imposed to the glass plate with the deflection estimated using the approach described in Section 6.1.1.1.
Considering the notations from Figures 6.7a and 6.4, the real deflection we are trying to measure is w_0, while the experimental measure following the protocol will be $w_{exp} = \frac{(w_0 + w_1) + (w_0 - w_2)}{2}$.
Thus, the error criteria for the numerical validation is:

$$\epsilon = \frac{w_{exp} - w_0}{w_0} = \frac{w_1 - w_2}{2 w_0} \tag{6.7}$$

The results are represented in Table 6.1, for a real deflection from 0.1 mm to 10 mm. The numerical error induced by the protocol is inferior to 0.74%. It can also be noticed that the protocol induces an under-estimation of the numerical deflection measurement, as the error is negative. Finally, the results shows also that glass-glass architecture is less affected by structural effects compared to glass-backsheet architecture, as the error is at least 20 times lower.

Residual deflection w_0	**Measurement error** ϵ **(%)**	
(mm)	**Glass-Backsheet**	**Glass-Glass**
0,1	-0,7200	-0,0126
1	-0,7391	-0,0270
10	-0,5817	-0,0297

Table 6.1: Error induced by the experimental protocol for different value of residual deflection, computed with ABAQUS.

6.1.3 Experimental deflection probing

A preliminary study was conducted, in order to prove the relevance of the experimental approach before a larger experimental campaign. The experiments were made using a three-dimensional (3D) coordinate measuring machine "CRYSTA-Apex S 9106" developed by a partner Mitutoyo. This machine offers a high precision probing of up to 7 μm of the measured PV module. The coordinate measurement is performed by a contact inductive distance sensor, moving in the horizontal plane using motorized axes. The machine offers several options for the number and density of measured points. The program chosen is a mapping of the sample surface, with one measurement point every 5 cm.

The samples chosen for this preliminary study are:

1. A glass plate, presumed to be perfectly flat.

2. A laminated glass-backsheet PV module.

3. A glass-free symmetric PV module with polymeric front and back layers, that is particularly bowed. This highly deformed sample demonstrates the ability of the protocol to detect deflection.

The maximum size of the sample was limited by the measuring area of the machine used. Thus, we chose for the glass-backsheet sample a 4 × 4 cells PV module and the associated glass size for samples 1 and 2. The third sample was a mini-module with only 4 cells, which is smaller.

The experimental protocol plans to put the module on four supports, instead of placing it on the machine plate. A rigid frame linking the four supports was made. Stops were added to ensure that the PV module is always placed at the same position. The experimental set up is shown on Figure 6.8.

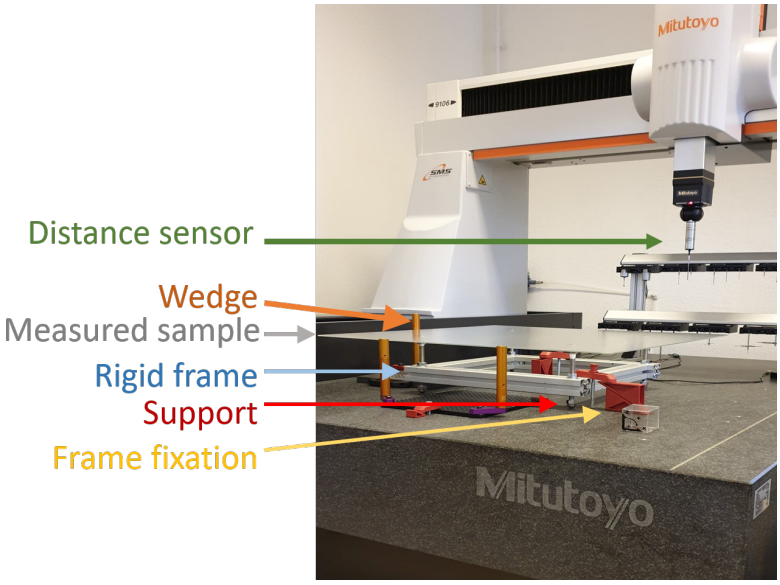

Figure 6.8: Experimental setup for deflection measurement

In order to calculate the real deflection, a Python code was developed to post process data files of the coordinate measurement machine. On each side, a point was measured every 5 cm. By flipping the PV module, an offset was observed between the measurements on each side. Therefore, a linear interpolation was established to compare the deflection at the same point on both sides. For each sample, the real deflection w_0 free of gravity effect was calculated. The effect of gravity w_G was also computed.

Figures 6.9, 6.10, and 6.11 display the experimental results of the deflection measurement in the three samples. We define the flatness error as the distance between maximum and minimum deflection.

Several conclusions can be drawn from the experimental results:

- The glass plate is not flat as expected, with a flatness error of 1.35 mm.
- The deflection of the glass-backsheet sample is smaller than the glass plate (flatness error of 1.15 mm). During lamination, the PV module is heated and pressed. Thus, it might cause stress relaxation in the glass plate.

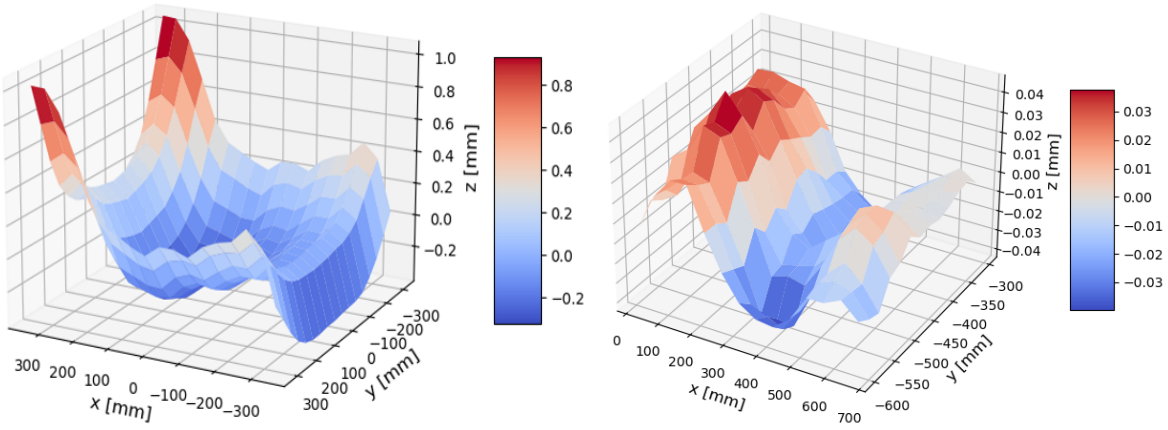

(a) Real deflection w_0 (b) Effect of gravity w_G

Figure 6.9: Experimental results for the glass plate (sample 1)

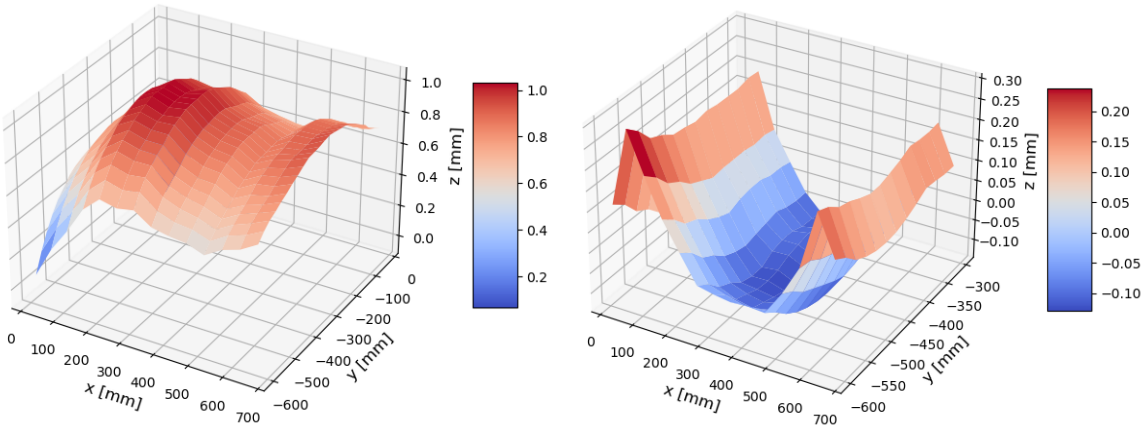

(a) Real deflection w_0 (b) Effect of gravity w_G

Figure 6.10: Experimental results for the glass-backsheet PV module (sample 2)[206]

- The gravity on the 16 cells PV module samples has a bigger effect in the direction x than y, as it is the longer side (4 cm longer, ie 5% of the length).
- The residual deflection of the PV module without glass appears to be much larger than for other samples (21.3 mm). The gravity-induced deflection seems to be inclined in the y direction, due to a mis-centering of solar cells with respect to the composite faces.

Several improvements were brought to this measurement protocol in the parametric study campaign of the lamination process, notably the flatness of the supports, as well as the measurement positions on each side in order to avoid a possible error linked to the linear interpolation between the measurement points.

In this section, a novel method of measuring the global deflection of the PV module was presented. The first validation measurements of the method confirmed some aspects of shape noticed on the tested samples. The results clearly showed that the PV modules are deflected after manufacturing. Furthermore, the measurement results on a glass plate showed that its initial deformation is not symmetrical.

In the following, we will investigate the origin of this deflection of the PV modules, in order to

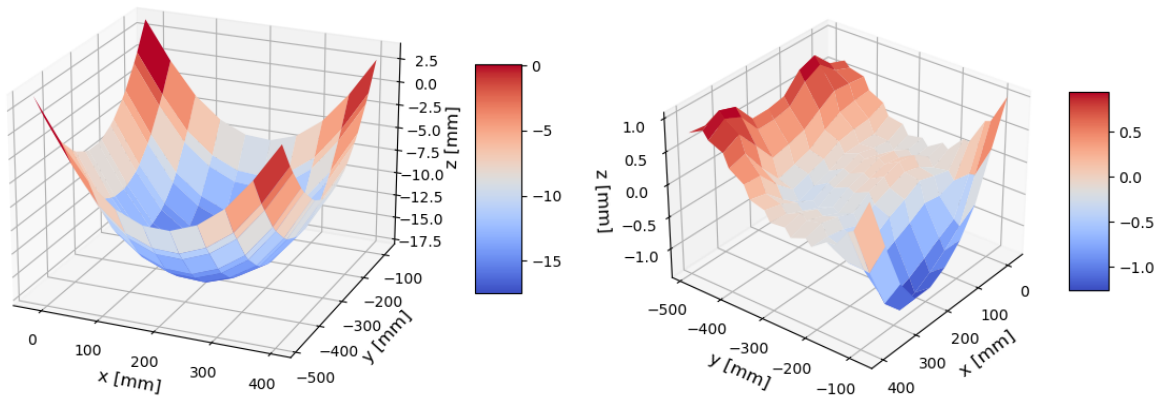

(a) Real deflection w_0 (b) Effect of gravity w_G

Figure 6.11: Experimental results for the glass-backsheet PV module (sample 3)

verify whether this residual deformation is induced by the initial shape of the glass plates or by the lamination process parameters.

6.2 Parametric experimental study of the lamination process and its impact on the residual deflection

6.2.1 Initial deflection of glass plate

As discussed in the previous section, the glass plates are not initially flat. Therefore, a measurement of the initial deflection of the glass plates is necessary before integrating them into the PV module. Using the same protocol presented previously, the initial shape of twelve glass plates was measured. As mentioned previously, the quality of the supports was improved (see Figure 6.12) and the density of the measurement points was increased by keeping the same position on each side to avoid interpolation errors between the measurement points.

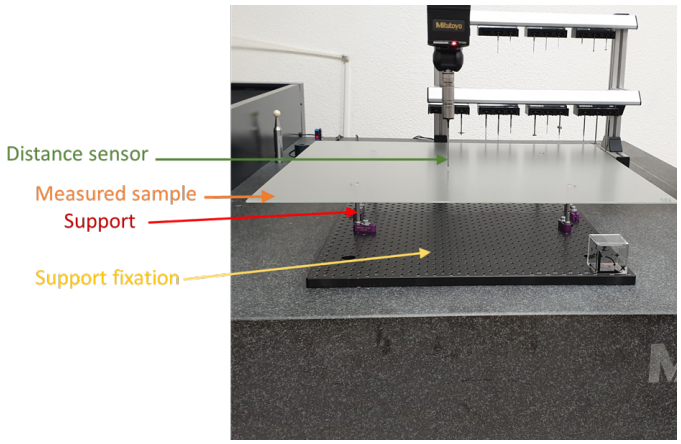

Figure 6.12: The improved experimental set up [206]

Figure 6.13a presents the real deflection w_0 of a glass plate. It can be noticed that the initial shape of the glass plate is not flat and its deflection is not symmetrical. Figure 6.13b shows the flatness error measured for twelve glass plates. The median flatness error in the glass plates is equal

to $1.433mm \pm 0.034$. This residual deflection present in a sampling of glass plates can probably be caused by the nature of the cooling technique after their manufacturing process.

These glass plates were used to manufacture the PV modules for this study. For glass-glass modules, the combined plates have approximately the same flatness error in order to distinguish the effect of the lamination process parameters on their initial deflection.

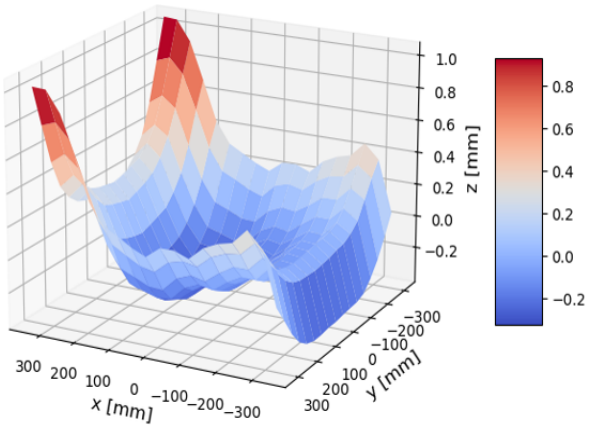

(a)

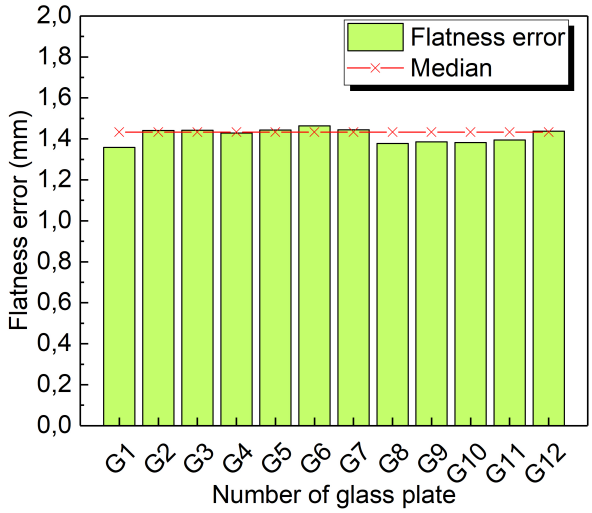

(b)

Figure 6.13: (a) The real deflection w_0 of glass plate G1 and (b) flatness error of the twelve glass plates [206]

6.2.2 Preparation and manufacturing of PV modules

Three parameters of the lamination process were selected for this study.

- The first parameter is the architecture by varying the type of the backside from glass to a PP multilayer polymer.
- The second parameter of study is the maximum lamination temperature. Three temperatures were chosen: 100°C which represents a temperature from which the TPO encapsulant is completely melted, 156°C is the standard lamination temperature, and 170°C which stands for the most optimized recipe temperature with respect to the type of encapsulant tested for a SL lamination process.

- The third parameter is the type of cooling. As mentioned in Section 1.1.2.2.2, in the case of the conventional lamination process the PV module is cooled down in the open air while in the SL process an optional option is developed to control the cooling of the PV module in a cooling press.

Eight 4 × 4 solar cells PV modules were manufactured by combining the three process parameters as shown in Table 6.2. The heterojunction SHJ solar cells were not interconnected. A thermoplastic polyolefin TPO encapsulant was used to encapsulate the PV module layers. For glass-backsheet PV modules, a polypropylene PP backsheet was used. The layers were stacked considering the initial concave shape of the glass plates as shown in Figure 6.14. The glass-glass PV modules have undergone an additional step in the double-sided heating plate compared to the glass-backsheet modules. As stated before in Section 1.1.2.2.2, this is an optional stage developed more especially for glass-glass PV modules, to avoid edge pinching caused by the membrane and to ensure symmetrical heating of the PV module. In this step, the glass-glass PV modules were pressed with a pressure three times higher than the pressure applied in the membrane.

Architecture	**Glass-Glass**				**Glass-Backsheet**			
Combined glass plate	**G10-G9**	**G2-G3**	**G1-G8**	**G5-G6**	**G11**	**G7**	**G4**	**G12**
Temperature of lamination °C	**100**	**156**	**170**	**156**	**100**	**156**	**170**	**156**
Type of cooling	**Cooling press**			**Ambient air**	**Cooling press**			**Ambient air**

Table 6.2: Parameters study of the lamination process [206]

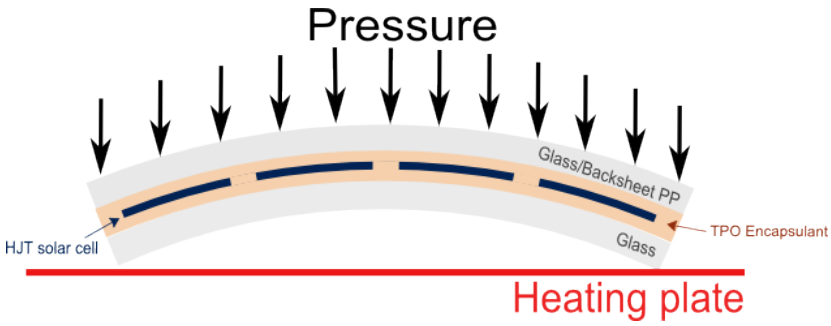

Figure 6.14: Stacking of the layers considering the initial concave shape of the glass plates [206]

6.2.3 Impact of temperature on residual deflection of PV module

Figure 6.15 displays the flatness error of PV modules regarding the architecture, temperature of lamination and type of cooling. For the glass-backsheet architecture, by comparing the flatness error of PV modules cooled down in a cooling press and encapsulated at different temperatures, it is noticed that the higher the lamination temperature is, the less the residual deflection of the PV module will be. The deflection of the "G1" glass used to manufacture the PV module at 100°C is the lowest among the glasses used for the modules laminated at other temperatures. However, the decrease in its deflection is not as remarkable as the other modules.

Nevertheless, for the glass-glass architecture the lowest flatness error is observed in the PV module laminated at 100°C. The initial deflection of the glass plates used to manufacture the modules at 100°C and 170°C is quite close, yet the final flatness error in the module laminated at 170°C is slightly higher than that laminated at 100°C. The module laminated at 156°C with cooling press represents the highest flatness error in this group since the flatness of the "G2" and "G3" glass plates exceeds the median of the flatness errors of all glass plates. Consequently, the temperature effect in this architecture is not correlated to flatness error. The combination of the two glass plates is the main factor behind this, and even though their deflection is quite close, their shape is quite different and asymmetrical. Hence it is not obvious exactly what impact the temperature has on this type of architecture.

It is also observable that the flatness error of all the GBS and GG modules cooled by the cooling press is inferior to the flatness error of the glass plates used for their manufacturing. This confirms the hypothesis that the lamination process relaxes the residual deflection of the glass plates induced during their forming. However, GG modules are less deflected than GBS modules. It is uncertain to judge whether this difference is related to the architecture of the PV module, since GG modules have undergone an additional step in the double-sided heating plate. This stage allows both symmetrical heating and homogeneous surface pressure application compared to the membrane. Thus, this forces the GG modules to flatten.

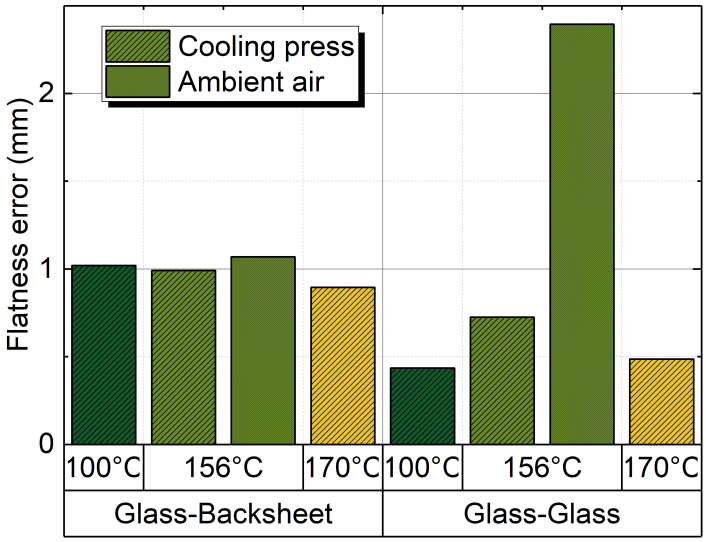

Figure 6.15: Flatness error in PV modules regarding lamination process parameters [206]

Although the GG module laminated at 100°C has a lower deflection than other modules of the same architecture, this does not mean that this is the optimal process temperature for manufacturing this type of PV module. It is necessary to combine the residual deflection with other factors. Figure 6.16 shows a photo of the GG module laminated at 100°C. It can be seen that the encapsulant in some areas still has a fresh surface aspect even though it is well adhered to all layers of the PV module. This surface texture means that the encapsulant has not completely melted despite the lamination temperature exceeding its melting temperature. Since the thickness of the GG module is high, the lamination time in an SL process is not sufficient to transfer the heat needed to fully melt the encapsulant. However, when the temperature is high and well above the melting

point of the encapsulant, the shortened lamination time is sufficient. This phenomenon was not observed in the case of the GBS module, since its thickness is almost 2 times less than that of a GG module.

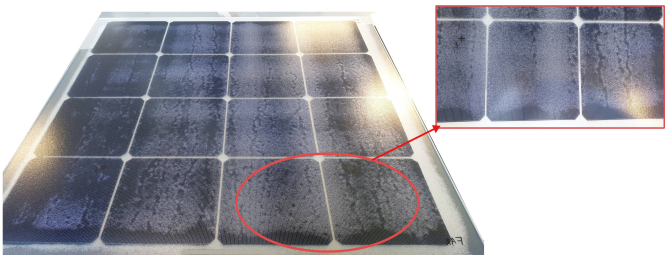

Figure 6.16: Surface aspect of 4 × 4 solar cells GG PV module laminated at 100°C with cooling press

6.2.4 Effect of cooling press on residual deflection

In order to study the impact of the type of cooling on the residual deflection of PV modules, two modules of each architecture were laminated at the same temperature of 156°C and cooled down either in free air or in a cooling press. As explained in Section 1.1.2.2.2, the cooling press allows accelerated cooling of the PV module while maintaining pressure on the PV module to control its flatness.

The results are also presented in Figure 6.15. For both architectures, the highest residual deflection is found for the ambient air cooling case, since in the cooling press stage, a pressure is applied to maintain the flatness of the PV module during cooling. The effect of cooling type is higher in the glass-glass architecture where the flatness error increased by 230% compared to the PV module cooled with the cooling press. This difference is obviously due to the supplementary stage of the double-sided heating plate (HP2) used for GG PV modules, which applies a high pressure compared to the membrane stage. Thus, it forces the module to get more flattened, and when it leaves the double-sided heating plate to cool down in the open air without constraint, it bends drastically.

These experimental results, which show that the cooling press reduces the residual deflection of PV modules, are in good agreement with the results of the study performed by Li *et al.* [85].

The results of flatness measurements of glass plates show a good repeatability of the method developed in this work to study the residual deflection of PV modules. However, in the parametric study of the process, only one module for each parameter was manufactured and its residual deflection was measured. Therefore, the repeatability of the lamination process is not verified.

The cooling press is an acceleration factor in the lamination process that increases the production throughput of PV modules. This study showed that another advantage of the CP is the control of the thermal contraction of the PV module during cooling which results in a low deflection of the PV module compared to a module cooled freely in ambient air. However, it is necessary to investigate whether this pressure to impose flatness and fast cooling does not block the internal

stresses in the PV module. We will investigate this question in the rest of the chapter with the help of a numerical model.

6.3 Numerical measurement of residual deflection

6.3.1 Presentation of the model

6.3.1.1 Geometry of the model and loading conditions

To study numerically the residual deflection of PV modules and to establish the correlation with experimental measurements, a 3D model was developed using the FE Abaqus software. The model represents the geometry of 16 solar cells GBS PV module as shown in Figure 6.17. Based on this assumption, only one quarter of the PV module was modeled by applying symmetry boundary conditions on the symmetric edges. Perfect contact constraints are considered at each interface. A gravity load is applied to the PV module to eliminate rigid body motions. As this model is intended to study the global displacement of the PV module, the interconnectors and the ECA have been omitted considering that their geometry is negligible compared to the PV module dimensions. Transient thermal conditions were applied in the different steps of the simulation. During lamination the PV module is placed on the laminator. For this purpose, a fixed rigid body has been added in contact with the front face of the glass. A normal rigid and tangential frictionless contact is used. Similar to the 3D sub-model, the interferance fit function was used to address the problems of glass penetration in the rigid support.

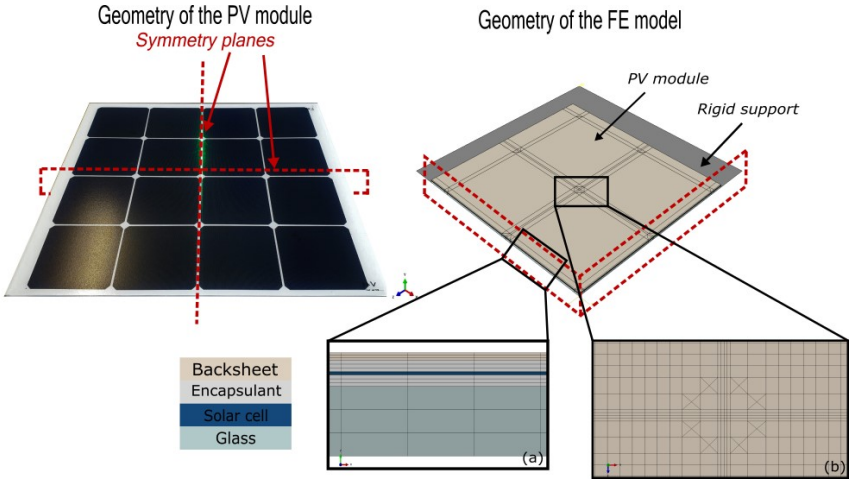

Figure 6.17: Schematic of geometry and FE model of a 16 cells PV module. The enlargement (a) shows the thickness in more details, and enlargement (b) shows mesh details in inter-cell area near pseudo-square shape of solar cells

In this residual deflection analysis, the short lamination process, introduced in Section 1.1.2.2.2, was used in the experimental study to manufacture the PV modules. To closely approximate the experimental conditions, the impact of the sequences of each of the configurations: HP1, HP2, and CP on the numerical residual deflection will be studied hereafter. Numerically, each laminator configuration is modeled in one step using the following boundary conditions:

- Preheating step (I): preheating to 60°C by applying a temperature boundary condition on the outer surface of the glass in contact with the rigid support.
- Vacuum/membrane press HP1 (II): heating to the lamination temperature by applying a temperature boundary condition on the outer surface of the glass in contact with the rigid support, while simultaneously applying a pressure of 300 mbar for one minute in case of GG modules, and for 8 minutes in case of GBS modules.
- Double-sided heating press HP2 (III): this step is only applied to the GG modules. It consists in applying a symmetrical temperature loading on the outer surfaces of the PV module glass plates, while simultaneously applying a pressure of 900 mbar for 8 minutes.
- Double-sided cooling press CP (IV): cooling to room temperature 25°C, by applying a symmetrical temperature loading on the outer surfaces of the PV module glass plates. A simultaneous pressure of 125 mbar was applied on the PV module.

  In the case of ambient air cooling, no pressure is applied and the temperature profile is adapted to ambient air cooling.

The temperature profile applied in each case is extracted from the experimental measurements performed by PV modules instrumented with thermocouples using the same method published in one of our studies [79].

6.3.1.2 Material modeling

In this 3D model, viscoelastic behavior laws were used for the encapsulant, and backsheet. The thermal expansion of the components is considered variable with respect to temperature except for glass where a constant value is defined. In the case of TPT backsheet and solar cell, an orthotropic thermal expansion coefficient is defined. All materials' properties and behaviour laws are detailed in Table 6.3.

Component of PV module	**Young's Modulus (GPa)**	**Poisson's ratio** ν	**Thermal Conductivity** ($W.m^{-1}.K^{-1}$)	**Density** (Kg/m^3)	**CTE** $.10^-6$ ($1/C°$)	**Specific Heat** ($J.Kg^{-1}.K^{-1}$)
Encapsulant TPO-A	G.M. (table A.1)	ν(T)	0.46 (table 3.7)	944*	α(T) (table B.2)	1848.7 (table 3.6)
Backsheet PP	G.M. (table A.1)	ν(T)	0.32 (table 3.7)	2520 [48]	α(T) (table B.1)	1272.11 (table 3.6)
Glass	73 [48]	0.235 [134]	0.937 [48]	2500 [48]	8 [48]	913 [48]
Solar cell	anisotropic elasticity (table 1.1)		130 [48]	2329 [48]	α(T) (table B.1)	677 [48]

G.M., Generalized Maxwell viscoelastic model.

Table 6.3: Material properties of PV modules components. *: provided by manufacturer

6.3.1.3 Model mesh

In this 3D model, coupled temperature-displacement elements were used. Hexahedral elements were used in the model and a combination of hexahedral and prismatic elements was used especially in the pseudo-square area of the solar cell to improve the mesh quality as illustrated in

Figure 6.17. First order linear elements with reduced integration were chosen (3 elements is the minimal number per thickness) where all the materials were assumed thermoelastic.

As discussed previously, 3D models require a large number of elements due to the low thickness/length ratio. Contrary to the 3D submodel, in this 3D model the stress distribution is almost homogeneous in the cell by neglecting the interconnectors which induce a stress concentration. Therefore, a relatively coarse mesh, with with a minimum of 3 elements in the thickness, can ensure a good accuracy of the numerical calculation.

A convergence analysis of the mesh was performed based on the maximum von Mises (VM), maximal principal stresses and maximal vertical displacement during lamination in the solar cell since it represents the most loaded component in the structure. The stresses are taken at the integration points. By reducing the mesh size, the stresses vary by a few hundredths and the displacement by a few thousandths. Since the variation is quite minimal, the analysis will be performed based on the relative error with respect to the most refined mesh case.

Figure 6.18 displays the evolution of relative error of von Mises, maximal principal stresses and maximal displacement with respect to the most refined mesh of 606 120 elements. It can be observed that with a fairly coarse mesh the relative error does not exceed 0.6% in the stresses and 0.04% in the case of displacement. Therefore, a refinement of the mesh is not necessary in this model considering that it increases the computation time. Hence, a mesh with 200 000 elements was chosen as it represents a good accuracy of stress and displacement at the same time.

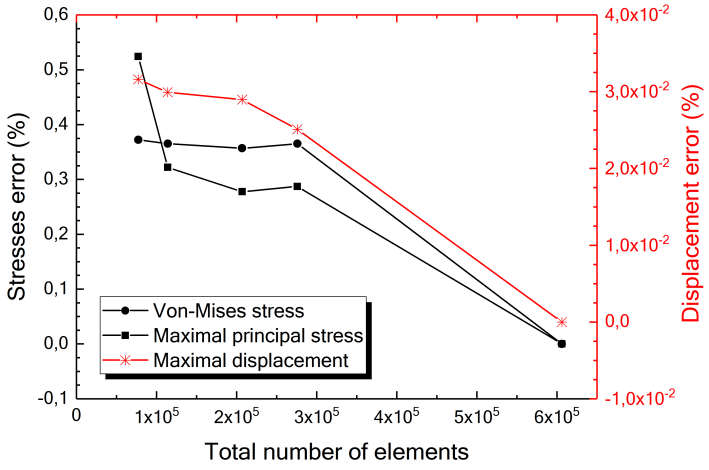

Figure 6.18: Maximum von Mises, maximal principal stresses, and maximal displacement relative error with respect to the number of elements at 150°C in solar cell

6.3.2 Results : correlation with experimental measurements

The 3D model presented above is used to check the correlation between the numerical and experimental measurement of residual deflection and the corresponding level of stress. Several modeling approaches of the lamination process are used in the literature to identify the residual stresses at the end of the process (see Section 2.2.2). Using the sub-models presented in chapter 5, the objective was to study the evolution of the thermomechanical stresses during the process. Therefore, the whole lamination cycle was considered. Here, the purpose is to identify the residual deflection

according to the process parameters. The approach of modeling the whole lamination mechanical and thermal loading cycle used in the sub-models is not necessarily suitable. Therefore, a comparative study between the different approaches was performed in order to identify the right approach that allows an adequate correlation with the experimental measurements.

Four modeling approaches were studied on a GG architecture laminated at 156°C and cooled in ambient air since it represents the most flexed PV module case. The lamination recipe used to manufacture this module is presented in Figure 6.19. The assumptions used for each approach are detailed in the following:

- Approach 1: where the whole lamination process cycle is considered assuming that the stress free temperature is at 25°C.
- Approach 2: where the stress free temperature is assumed at 60°C and the thermomechanical loading from steps II to IV are considered. At this temperature, the encapsulant is normally softened and approaches its molten state, and therefore pressure is applied to the PV module for the first time to ensure good adhesion between the layers. In this step the interface bonds are completely established between the layers.
- Approach 3: where the stress free temperature is assumed at 120°C and the thermomechanical loading from steps III to IV are applied. At 120°C, the encapsulant is completely softened or even melted depending on the maximum lamination temperature used. Thus, an adhesion between the different layers is achieved.
- Approach 4: where only cooling down to room temperature is modeled assuming that the free stress state is at the maximal temperature of lamination 156°C. This is the most widely used approach in the literature [24; 105; 145; 149; 150].

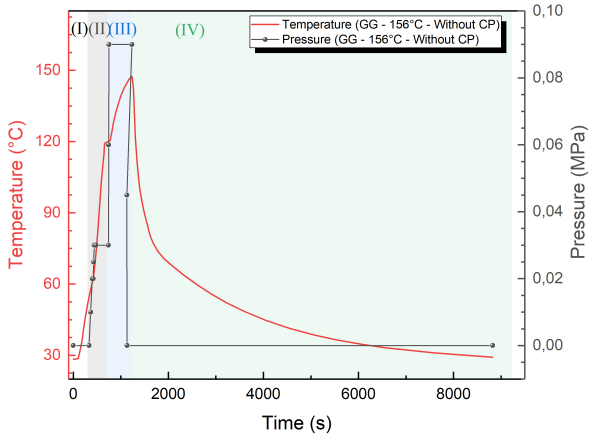

Figure 6.19: Short lamination recipe of GG PV module laminated at 156°C with air ambient cooling

Figure 6.20 displays the numerical flatness error of PV modules laminated at 156°C with and without cooling press as well as the numerical/experimental deviation with respect to the different modeling approaches. Similar to the experimental measurements, the flatness error is defined as the distance between the minimum and the maximum deflection. The minimal numerical flatness error is observed with approach 1, while the maximal error of order of $0.31mm$ is obtained

with approach 4. In approach 1, the temperature in the stress free state is considered to be at 25°C. The materials expand and deform during the temperature increase and shrink during the temperature decrease back to room temperature. This ambient temperature also represents the reference temperature with respect to which the thermal deformation is calculated. Then, when the materials cool down and return to the same initial temperature, all the elastic deformation is reversed and therefore the residual deformation is the consequence of the visco-elastic deformation of the encapsulant which is permanent. Hence, the residual displacement from which the numerical flatness has been calculated is quite small compared to the other approaches studied.

However, with the other approaches, between the temperature of the free stress state and the ambient temperature a temperature gradient is assumed. The higher is this gradient, the higher is the flatness error due to the shrinkage of the structure. Moreover, the numerical/experimental deviation between the flatness errors of the GG PV module laminated without CP decreases between approachs 1 and 4. However, the deviation remains quite high by 87% even with the approach 4 which consists in modeling only of the cooling down to ambient temperature.

When comparing the flatness error between the GG PV module cooled with and without cooling press using approach 4, no significant difference was observed. Although the experimental measurements displayed in Figure 6.15 showed that the GG module cooled without CP deflects much more than the GG module cooled with CP. This explains the decrease of the numerical/experimental deviation in the case of the GG module cooled with CP. Therefore, approach 4 is the most accurate with respect to residual deflection and represents the least deviation from the experimental measurements. In the following, only this approach will be used to study the numerical residual deflection of PV modules.

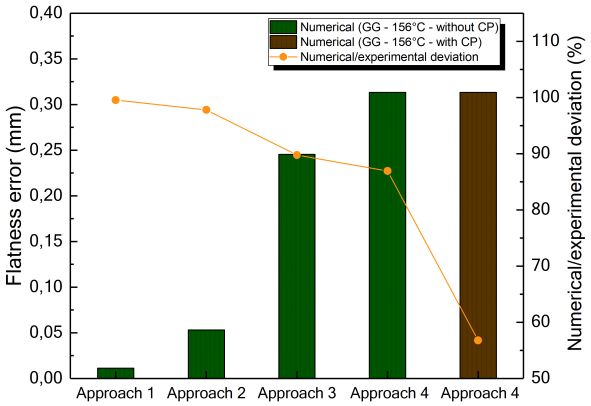

Figure 6.20: Numerical flatness error of GG PV modules laminated at 156°C with and without CP with respect to modeling approaches

Figures 6.21 show the distribution of the experimental and numerical residual deflection of the GG and GBS PV module laminated at 156°C without CP. Despite the deviation noticed between the experimental and numerical deflection measurements, similarities in deflection distributions are observed between the two. In all distributions, the PV module is deflected towards the center and the edges are lifted. The maximum and minimum deflections are mainly observed along the x direction which represents the longer side.

The numerical and experimental displacement distributions in the case of the GBS module are

closer especially on the upper part (see Figures 6.21c, and 6.21d). Numerically, since a symmetry condition has been imposed on the structure, the same deformation is found on the PV module sides. On the other hand, experimentally, since the glass used to manufacture the module was initially deformed and non-symmetrical, the deformation of the lower part is different.

The numerical distribution of the GG PV module gives the illusion that the solar cells increase the stiffness of the PV module. The difference between the minimum and maximum numerical displacement is about 45µm. In the areas where there is no silicon, the encapsulant shrinks more and its thickness varies very slightly compared to the area where cells are present. Thus, the shape of the cells is more visible because of this slight difference in thickness.

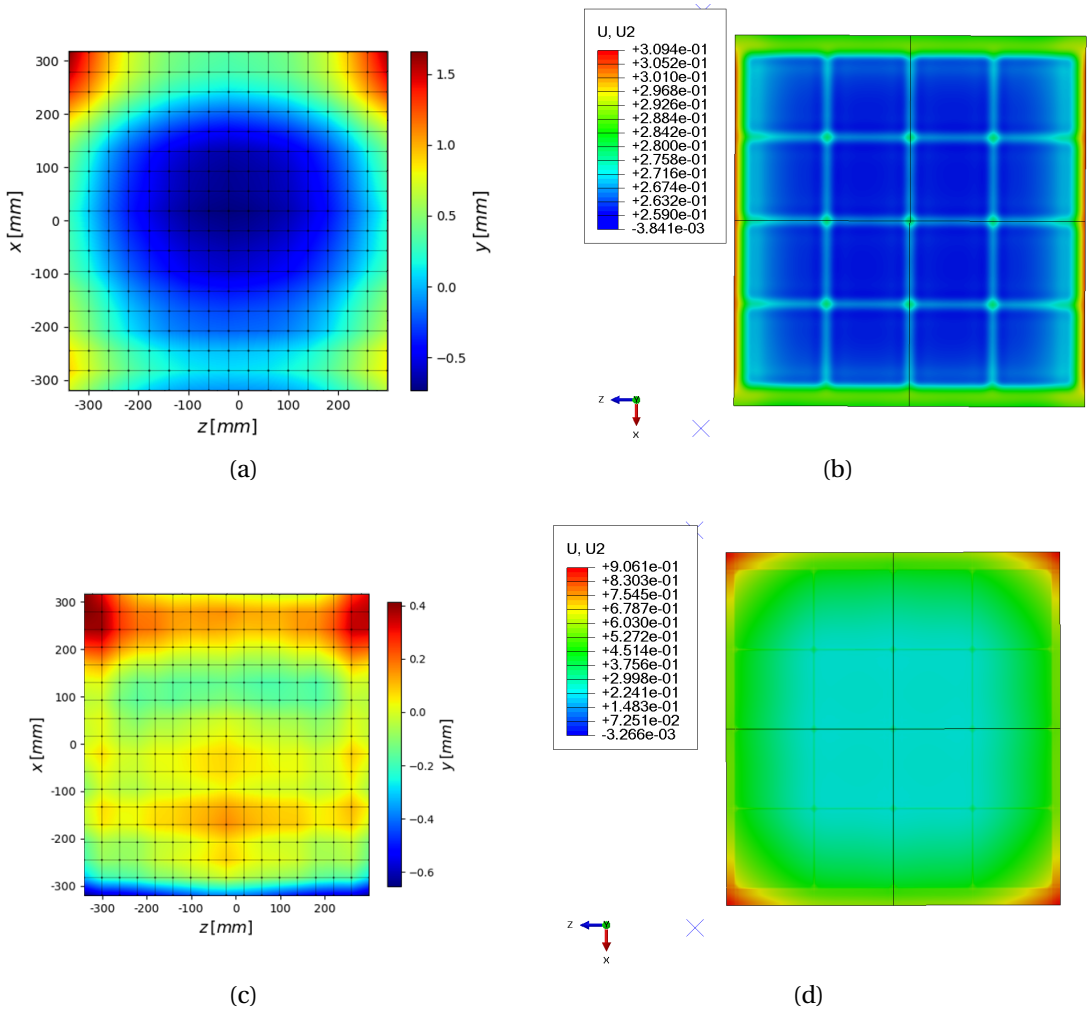

Figure 6.21: Residual experimental deflection distribution of (a) GG and (c) GBS PV modules, and residual numerical deflection distribution of (b) GG and (d) GBS PV modules laminated at 156°C without CP

This deviation between the experiments and the numerical modelling according to the process parameters can be explained by several reasons:

- The deflection of the PV modules is still quite small, of the order of a few millimetres, and therefore the measurement accuracy is a rather critical parameter. Numerically, the scale of accuracy of the displacement is very accurate and allows to capture variations of displacement in the micrometer scale. Experimentally, the accuracy of the measuring machine is

around 7 µm. The experimental method used was studied numerically to identify the accuracy of the protocol which consists in eliminating the effect of gravity. The numerical measurement error with the protocol does not exceed 0.75%. In addition, the measurements performed on the twelve glass plates did not show a large dispersion of the measurement. However, the lack of data on the deflection of the PV modules after lamination according to the process parameters is a factor that may influence the accuracy of the experimental results. As discussed in Section 6.2.4, only one measurement of each type of module was performed. Therefore, the dispersion of experimental measurements on PV modules is a parameter that has not been investigated.

- Experimental measurements on the glass plates before lamination showed that the glass plates are initially not flat and unsymmetrical. Since the initial shape of the glass plates is quite complex, numerically several geometrical simplification assumptions have been made for the development of the numerical model. In the 3D model, all components were initially assumed to be flat. The PV module is assumed to be symmetrical and therefore only a quarter of the PV module is considered. The symmetry boundary conditions artificially stiffen the PV module and the resulting deformation is assumed to be symmetric. The experimental deflection distribution displayed in Figure 6.21a shows that the final deformation of the PV module is not symmetrical. Yet this can be one of the main causes of the observed deviation between numerical and experimental results.

- Concerning the initial flatness of the glass plates, when the glass plates are numerically assumed to be flat, the identified residual deflection is the direct result of the theromechanical loading applied on the PV module during the process. Therefore, in this case the influence of the initial deflection of the glass plates and their shape is neglected. In order to identify the impact of this initial glass plate deflection on the residual deflection of the PV modules, a simplified 2D plane strain model was used as illustrated in Figure 6.22. This model is an approximation of the geometry of a GG PV module composed of two glass plates with a maximum deflection of 1.4 mm in the center. Between these two glass plates two layers of encasulant have been added, the solar cells have been neglected by assuming that their effect on the deflection of the PV module is negligible compared to that of the glass. The same behaviour laws, boundary conditions and mesh used in the 3D model have been chosen also for this 2D model.

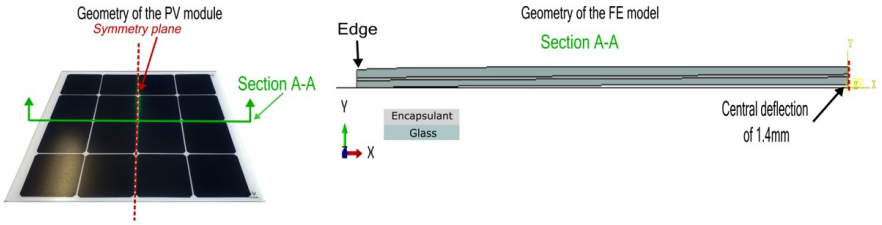

Figure 6.22: Schematic of geometry of the 2D FE model at the center of a 16 cells PV module showing the initial deflection of 1.4mm. Solar cells are not represented

Figure 6.23 displays residual numerical central and edge deflection of GG PV modules lami-

nated at different temperatures with and without CP for PV module laminated at 150°C. We are interested in the central deflection since the 1.4 mm gap of the glass plates has been defined in the center for the initial geometry. And also in order to verify if the same process effects will be obtained numerically when the initial deflection of the glass plates is taken into consideration. The deflection at the edge represents the area where the maximum deflection is observed in the case of the 3D model. Thus, the objective is to check if there is a correlation between the two cases when the geometry is not initially flat.

Analyzing the deflection at the edge of the simplified structure, for the modules laminated at 156°C with and without CP no difference is noticed. This correlates well with the results found with the 3D model with approach 4 shown in Figure 6.20. On the other hand, for the other modules laminated at different temperatures, the modules laminated at a higher temperature have a higher deflection. This means that the higher the lamination temperature, the more the module contracts and lifts at the edges after cooling.

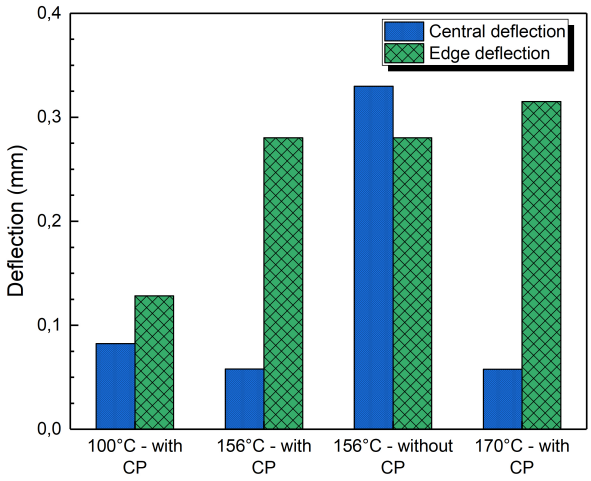

Figure 6.23: Residual numerical central and edge deflection of GG PV modules laminated at different temperatures with and without CP using approach 4

The central deflection is initially equal to 1.4 mm, and therefore the numerical residual deflection clearly reveals the effect of the process parameters that allow to reduce this residual deflection of the glass plates. The results show that the central deflection of the module laminated at 156°C without CP has a much higher residual deflection than the module cooled with CP. This effect correlates well with the experimental results. On the other hand, the temperature effect shows an opposite effect to the one observed on the edges. The module laminated at 100°C has a higher deflection than the modules laminated at 156°c and at 170°c which show an almost identical deflection. Therefore, the modules laminated at high temperature flatten towards the center and curve more towards the edge due to thermal contraction. The cooling press also plays an important role in the flattening of the module towards the center due to the pressure applied on the structure. This effect of temperature correlates well with the experimental results.

The numerically obtained deflection level remains quite small compared to the experimental measurements. The simplified 2D model with a residual deflection of the glass plates has

shown that the experimentally obtained process effects are accurate only if the glass plates are initially curved.

We have detailed all the factors that can be at the origin of the deviation between the experimental measurements and the numerical simulation. The main factor is related to the initial shape of the glass plates. Their initial shape is neglected in the numerical model for simplification reasons. Therefore, if a good correlation between numerical and experimental measurements is to be achieved, simplifying assumptions such as the symmetry and the initial arrow of the glass must be adjusted by taking into account the real initial shape of the glass plates.

The 3D model allows to identify the residual deflection of the PV module during cooling from the lamination temperature considering that the components are initially perfectly flat and that the structure is symmetrical. Therefore, its role is to study the effect of the PV module contraction.

Figure 6.24a summarizes the numerical residual deflection in the GG and GBS PV modules according to the process parameters used for their manufacturing. The deviation from the experimental measurements is also presented. Numerically, it is observed that the GBS modules are more deformed than the GG modules. Which is in good agreement with experimental observations. This is due to the contraction of the module due to the non-symmetry in the thickness of the PV module. It is also noticed that the deviation between experimental and numerical results is lower. This can be explained by the fact that for GBS modules the presence of a single glass plate does not increase the stiffness of the PV module significantly and the module structure can deform freely compared to the GG module. Moreover, for GBS modules the rapid cooling of the cooling press induces a higher thermal contraction than the cooling with ambient air.

Figure 6.24b displays the maximum value of third principal residual stress in the solar cell corresponding to each studied lamination parameters. The cell is under compression after cooling, for this reason the third principal stress is analyzed. It can be seen that for the GBS PV modules with a higher residual deflection, the maximal third principal stress is also higher. Therefore, more the module is contracted, more the cell is subjected to a compressive stress. This is due to the position of the cell offset from the neutral plane in the thickness of the module. However, for GG modules, despite a lower residual deflection, the residual stress level is higher. The presence of the cells between two layers of glass, which are quite rigid, means that a minimum of deflection can compress and apply pressure on the central layers of the module, which have less rigidity, especially the solar cells.

In conclusion, the initial shape of the glass plates has a great influence on the residual deflection of the PV module. In the module manufacturing process flow, no quality control of the glass plates and their flatness is performed. In a sample of twelve glass plates from the same supplier, which have undergone the same fabrication technique, the residual mean deflection is 1.4mm. This means that the probability of a defect in the flatness of the glass plates is not negligible. However, this planarity defect can be reduced using a set of process parameters and ensures a good compromise between initial deflection reduction and thermal contraction due to the thermomechanical loading applied on the PV module during lamination.

The maximum values of the third principal stress associated with each numerical deflection of

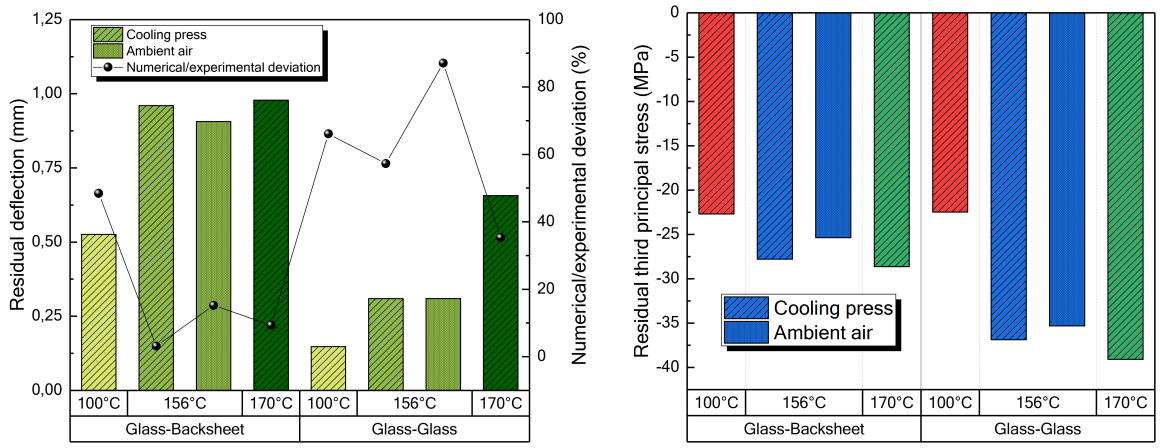

(a) (b)

Figure 6.24: Residual numerical (a) global deflection and (b) maximal value of the third principal stress in solar cell of the GG and GBS PV modules with respect to lamination parameters

the PV modules were analyzed. In all cases the solar cells are subjected to compressive stresses. For brittle materials, like silicon, the compressive stress state is not critical or even beneficial. However, in this study, the interconnect lines were neglected experimentally and numerically. According to the results of chapter 5, the interconnect lines represent critical areas for the solar cells. Hence, the combination of process parameters and stress concentrations along the interconnect lines and their effect on the thermomechanical stresses is an interesting topic for further work.

Conclusion

This chapter presents a new experimental method to measure the global deflection of a PV module using a 3D coordinate machine. An optimization of the supports positions used in the experimental protocol was studied analytically and numerically. Then, a numerical study allowed to estimate the measurement error of the deflection related to the effects of gravity. Finally, experimental measurements were carried out to validate the experimental methodology.

An experimental measurement campaign using this protocol was carried out in order to study the influence of lamination process parameters (architecture, temperature, and type of cooling) on the deflection of the PV modules. **First, the flatness error of the glass plates used to manufacture the PV modules was measured. It was found that the glass plates are not perfectly flat and their residual deformation is not symmetrical.**

Then these glass plates were used to manufacture the PV module. The experimental measurements on PV modules showed that **for glass-backsheet architecture, the residual deflection decreases when the lamination temperature increases, which is not observed in glass-glass architecture. The type of cooling has also an effect, as the deflection of ambient air-cooled PV modules is higher than the one of cooling press-cooled PV modules.**

Afterwards, a 3D model was developed to study the correlation between the experimental and numerical measurements. **The correlation between the experimental and numerical measurements of the residual deflection was not very good with an underestimation of the deflection**

with the numerical model. The factors influencing this deviation between the experimental measurements and the numerical predictions were discussed. **The residual deflection of the glass plates has a major influence in this deviation since numerically simplifying assumptions related to the geometry have been considered.** These assumptions consider that the PV module components are initially perfectly flat and the PV module structure is symmetric. However, further study should be conducted to justify the differences observed.

Finally, the residual stress level associated with the numerical deflection of PV modules was analyzed. The results showed that **the solar cells are under compression. The compressive stresses are not critical for brittle materials like silicon.** However, if interconnection ribbons are added, they can induce positive stress concentrations. In this case, the risk of failure of solar cells increases. Furthermore, the comparison between the deflection and the associated stress level showed that the more the module is deflected, the higher is the stress. Therefore, since the experimental deflection measured on the PV modules is higher than that found numerically, the resulting residual stress level is eventually higher.

In this study, we have developed a novel method to characterize the overall shape of PV modules. We can notice that the problem of the glass plates flatness was not addressed before in the field of PV. Further studies are needed to investigate these aspects and their influences on the reliability of PV modules. Since the deformation of the PV module is not homogeneous, it is complicated to trace the experimental deflection to the residual stress level analytically.

Therefore, it is encouraging to use other methods that allow characterizing the residual stresses at the solar cell scale. Methods such as synchrotron X-ray micro-diffraction and confocal micro-Raman spectroscopy have shown good results as shown in the literature [129; 134]. However, the limited area of analysis remains a limitation for these methods. Recently, Beinert et al. [209] have developed stress sensors integrated in solar cells that allow the monitoring of thermomechanical stresses. More research needs to be done further to assess the feasibility of this method in measuring the residual stresses in PV modules.

General conclusions and prospects

This Ph.D. thesis is a contribution within the strategies emphasized by the International Technology Roadmap for Photovoltaics of 2021 [5] to reduce the cost of PV modules: by reducing the cost of manufacturing processes and increasing the performance and reliability of PV modules. More concretely, this work focused on the identification of first order process parameters that can improve mechanical reliability of PV modules.

To achieve such goal, our objective was to better understand the thermomechanical behavior of PV modules by developing advanced numerical tools identified and validated by an accurate material database. Throughout this dissertation, we have therefore sought to understand the thermomechanical phenomena that are induced during module manufacturing and the process parameters that influence stress distribution and therefore their final reliability. This issue has been mainly approached by developing numerical models implemented by developing representative numerical models and by improving the accuracy of the PV modules components material behavior laws. Experimental measurements of the residual deflection of PV modules with respect to the lamination parameters provided additional insight in term of model validation at the component level.

This general conclusion develops the major achievements of this thesis and suggests future research topics that would be interesting to investigate.

Conclusions

Thermomechanical behavior of PV module components

The first objective highlighted in this work was to characterize the thermomechanical behavior of the PV module components in order to establish the mathematical laws that allow the implementation of the numerical models. The material characterization tests were adapted according to the type of component. DMA measurements were used to characterize the viscoelastic behavior of encapsulants, backsheets, and ECAs. Relaxation tests were performed on the same components to validate the Generalized Maxwell Model identified using DMA tests. Tensile tests were chosen to characterize the elastoplastic behavior of copper ribbons. Then 4-line bending tests were used to characterize the mechanical behavior of SHJ cells. Finally, measurements of the thermal expansion coefficients using DIC technique were conducted.

The main findings of these experimental characterizations are reported as follows:

- The encapsulant and backsheet do not have a long rubbery state. They switch quickly to a flowing state after their glass transition. This is a rather favorable characteristic for the encapsulant since during the manufacturing process it can flow to fill the entire shape of the PV module.

- Copper ribbons exhibit sensitivity to the loading temperature. However, no sensitivity to the loading rate was found. In the literature, only one bilinear plasticity model is available to simulate ribbon behavior. Here, a Johnson-Cook thermo-elastoplastic model was proposed to model the plastic behavior of the ribbons taking into consideration their temperature sensitivity.

- The elastic properties of SHJ cells calculated analytically and numerically, from experimental measurements of 4-lines bending tests, showed similarities with the behavior of silicon wafers. Therefore, the manufacturing process of SHJ cells does not modify the elastic properties of the wafer. Moreover, the fracture behavior of SHJ cells was statistically investigated using a Weibull law. The fracture strength in the busbars direction is higher than the one observed in the perpendicular direction.

- The CTE measurements on the SHJ solar cell have highlighted an anisotropic effect of its thermal expansion. This anisotropy is induced by the silver metallization of the cell since silver expands more than silicon. The expansion of the copper ribbon and the PP backsheet is also linear with anisotropy for the PP. The thermal expansion of laminated encapsulant TPO-A, backsheet TPT, and ECAs A1 and A2, is not linear and strongly depends on their transition temperatures or their processing condition.

All the results presented in this study showed that each component of the PV module has a specific thermomechanical behavior. This difference in materials behaviors is one of the main source of the thermomechanical stresses generation during PV module manufacturing processes.

Optimizing interconnection process parameters

The second underlying objective of this work was to evaluate the level of induced stresses in the ECA bonding interconnection step and in identifying its potential impact on the stress state in the rest of the manufacturing chain. For this purpose, a 2D sub-model of a string of two half cells interconnected with ECA was developed. First, we discussed the level of stresses and thermomechanical strains in a string of two half-cells with a fixed set of process parameters. The analysis was performed on three zones of interest: the zone where the force is applied by the pins, the inter-cell, and an intermediate zone between two pins. Then, the influence of some process parameters (temperature and time of ECA curing, type of ECA, and design of ECA pads) on the stresses induced in the string was analyzed.

The stress distribution analysis showed that the force applied by the pins generates a concentration of stresses in the ribbon and the solar cell resulting in a local deflection of these components. In the inter-cell, the ribbon is sheared due to its geometric shape and the asymmetry of the

structure. In the area where no mechanical loading has been applied the effect of the CTE mismatch is more visible. The level of residual stress induced in the string after cooling is negligible, but the level of thermomechanical stress during the process is not.

Our goal was to identify the ECA interconnection process parameters that have a direct effect on the generation of a critical level of thermomechanical stresses and to propose solutions to optimize the string reliability. The main results are listed below:

- Temperature of ECA curing

  The thermal stress in the solar cell is predominant. A direct effect on the temperature was found, i.e. the higher the process temperature is, the higher thermomechanical stress occurs. Interconnection at 200°C showed stress values that were quite critical and close to the fracture strength of full SHJ cells. However, it has been shown in the literature that half cells have lower fracture strength than full cells [202]. Therefore, the risk of crack initiation is greater. Knowing that the ECA cross-links around 70°C, the process temperature can be optimized in order to prevent reaching critical stress values.

  This temperature optimization must be correlated with a study on the kinetics of ECA crosslinking and also on the adhesion strength of ECA with other components.

- Time of ECA curing and type of ECA

  The time of curing and the type of ECA were considered as second-order parameters since their effect on the internal stress is minimal. Although the two types of ECA used in the study have quite different thermomechanical behaviors, their effect on the induced stresses was almost identical. In the model, the kinetics of cross-linking was neglected. For this reason, the effect of the curing time was neglected.

- Design of ECA pads

  Discontinuity of the ECA pads has a beneficial effect on the stress state in the cell and the copper ribbon either during the process or after cooling. This is related to the reduction of the cell/copper interface bonding and thus less effect related to the CTE mismatch.

  The main critical parameter in the interconnection with disconnected pad is the area of application of the load by the pins, at least for copper. When the load is applied in an area of ECA discontinuity (i.e. inter-pad), the ribbon undergoes a greater bending, which generates more compression on the ECA in the neighboring pads. Moreover, this compression is subsequently transmitted to the solar cell. In the areas where the force is applied at the center of the pad, this phenomenon is not observed. Therefore, the remedy to this problem could be to design the position of the pads to coincide with the position of the pins.

  The design of discontinuous ECA pads contributes to reducing the amount of silver in the module, thus reducing the cost of the PV module. Moreover, from a thermomechanical point of view, this technology induces fewer stresses than continuous pad design, which may improve the mechanical reliability of the string.

Optimizing lamination process parameters

A multi-scale modeling strategy was established to study the thermomechanical behavior of PV modules during lamination. Two sub-models in 2D and 3D were developed to study the stress induced during the process. A 3D model was defined to characterize the post-lamination residual deflection and stresses.

Using the 2D sub-model, we have estimated the loss of model accuracy when simplifying the material models for copper ribbons, encapsulant, and backsheet. Elastoplastic and viscoelastic models have been used to describe the thermomechanical behavior of copper ribbon, backsheet and the encapsulant respectively. The results showed an overestimation or underestimation of the thermomechanical stresses in all components if simplified material laws were used. The relaxation of the encapsulant and backsheet protects the solar cell against the deflection applied by the glass. Stress concentrations were observed in the interconnection zones. These localized stresses might cause the potential initiation of microcracks during interconnection followed by propagation and eventually complete failure of the solar cell. Based on these results, in the rest of our study, constitutive behavior that models with good accuracy the mechanical behavior of components were selected.

A 3D sub-model was developed to capture the out-of-plane stresses and edge effects induced during the lamination process. The results of the 3D sub-modeling showed that the cell undergoes stresses related to side effects, especially at the edge of the interconnection lines. These side effects are related to the contact pressure applied by the other materials at the edges of the cell.

The 2D sub-model was also employed to investigate the correlation between the level of induced stresses in the PV module and its architecture varying solar cell size, number of busbars, and type of rear side. The impact of the ECA interconnection technology on the stress concentrations observed at the interconnection lines was studied using the 3D sub-model.

In order to validate the 3D numerical model, an innovative experimental method measuring the global deflection of the PV module was developed. An experimental measurement campaign was carried out in order to study the influence of short lamination process parameters (architecture, temperature, and type of cooling) on the deflection of the PV modules. First, the flatness error of the glass plates used to manufacture the PV modules was measured. It was found that the glass plates were not perfectly flat and their residual deformation was not symmetrical.

Then residual deflection of PV module was measured after manufacturing. The correlation between the experimental measurements and numerical calculations regarding the residual deflection was not very good with an underestimation of the deflection with the numerical model. The initial flatness of the glass plates has a major influence on this deviation. Moreover, numerical simulation were based on simplified assumptions for the initial geometry. These assumptions consider that the PV module components are initially perfectly flat and the PV module structure is symmetric.

All these studies have identified certain lamination parameters that optimize the mechanical reliability of PV modules. The major results are summarized below:

- Solar cell size and number of busbars

  From a thermomechanical point of view, the increase in cell size does not affect the induced stress state. In this study, the cell size was varied without varying the size of the mini-module. Therefore, in the case where the increase in cell size requires an increase in module size, the effect on the stresses could be different. However, this effect will not be related to the increase of solar cell size but the increase of total PV module size. Therefore, the trend of targeting larger cell size in order to increase the power of the PV module may not have a degrading effect on the mechanical reliability of PV modules.

  The cells with multibusbars showed a lower level of thermomechanical stresses. When the interconnector is offset from the center of the solar cell, the residual stress is lower since the maximum deflection is mainly located in the center of the PV module. Hence, multibusbar technology promises both improved electrical performance and mechanical reliability.

- Architecture

  The effect of the architecture on the thermomechanical behavior of the PV module has been studied at two scales: at the cell scale using the 2D sub-model in conventional lamination, and at the global scale of the PV module with the 3D sub-model in short lamination.

  During a conventional lamination, the non-symmetry of the thermomechanical loading and the structure increases the deflection of the PV module resulting in a higher level of stress in a glass-backsheet module compared to a glass-glass PV module.

  Using a short lamination process, the experimental measurement of residual deflection showed that GG modules are less deformed than GBS modules. Using this lamination technique, GG modules have undergone an additional step in the double-sided heating plate. This stage allows both symmetrical heating and homogeneous surface pressure application compared to the membrane. Thus, this forces the GG modules to flatten. This architecture effect found experimentally was in good agreement with the 3D model.

  The level of third principal residual stresses found numerically in the GG modules in compression was higher than the one of the GBS modules. The compressive stresses for brittle materials like silicon were not harmful, indeed sometimes they were advantageous.

  As discussed in the general introduction, bifacial modules will dominate the market in the future. Numerical and experimental studies conducted in this work show that they also provide mechanical reliability.

- Interconnection technology

  A comparative study was performed to investigate the stress level, during lamination, when the cell and ribbon are interconnected without or with ECA. The type of ECA was also varied to identify its impact on the thermomechanical stress level. The presence of ECA between the two components relaxes the stress level induced by the CTE mismatch as the ECA expands greatly and is less stiff. Therefore, the failure probability in the case of an ECA interconnected cell is lower than a solder interconnected cell regardless of the type of solar cell.

Al-BSF cell showed higher stresses and failure probability than SHJ solar cell as the fracture strength of SHJ is much higher.

The ECA bonding interconnection technology has shown promising results at both the interconnection and laminated stages. Despite the stress relaxation in ECA bonding lines, stress concentrations are still present in this area. Other ways of improvement must be explored.

- Temperature of lamination

  Experimental measurement of PV modules deflection showed that for glass-backsheet architecture, the residual deflection decreases when the lamination temperature increases, which is not observed in glass-glass architecture. The combination of the two glass plates in GG PV modules is the main factor behind this, and even though their deflection is quite close, their shape is quite different and asymmetrical. Hence, the impact the temperature has on this type of architecture is not obvious.

  Numerically, when the initial deflection of the glass plates is taken into consideration, the same temperature effect than the one observed for GBS modules is found for both architectures (i.e. the deflection of the PV module decreases when laminated at high temperature).

  Experimental deflection measurements on twelve random glass plates from the same manufacturer showed that their flatness quality is not controlled. Therefore, in this case, lamination at high temperatures ensures good mechanical reliability of the PV modules by eliminating some of the flatness defects of the glass plates.

- Post-lamination cooling technique

  Using the experimental measurement of PV module post-lamination deflection and numerical 3D model, the effect of two techniques of cooling - cooling press and air ambient cooling - was studied.

  The experimental flatness error of all the GBS and GG modules cooled by the cooling press is inferior to the flatness error of the glass plates used for their manufacturing. Meaning that the lamination process relaxes the residual deflection of the glass plates induced during their forming.

  For both architectures, the highest residual experimental deflection is found for the ambient air cooling case. Since in the cooling press stage, pressure is applied to maintain the flatness of the PV module during cooling.

  The effect of the cooling technique is higher in the glass-glass architecture compared to PV module cooled with the cooling press. This difference is due to the additional stage of the double-sided heating plate (HP2) used for GG PV modules, which applies a high pressure compared to the membrane stage. Thus, it forces the module to get more flattened, and when it leaves the double-sided heating plate to cool down in the open air without constraint, it bends drastically. Similarly, the same effect was found numerically considering the initial deflection of the glass plates.

In addition to reduce of the production time, the cooling press ensures good mechanical reliability of the cooled PV modules and especially of the GG PV modules.

The work accomplished in this thesis has allowed building a large database on the thermomechanical behavior of the PV module components. The numerical models developed have allowed our laboratory to be competitive with the current state of the art by a better understanding of the development of stress concentration for certain interconnection and lamination techniques. More aspects and techniques need to be explored furthermore to reach maturity. The use of advanced numerical tools will be a key point of such progress.

Perspectives

Towards improving ECA bonding interconnection process

As mentioned in the general introduction, the growth of interconnection technology will be severe in the coming years. This growth is related to the willingness to eliminate lead-based soldering technology due to its toxicity and also to the growth of SHJ cell technology. Modeling studies of the interconnection process have provided promising results. However, more work needs to be done to further improve this assembly technique.

According to ITRPV [5], reducing the amount of silver in PV modules is necessary for solar energy to remain competitive. The discontinuous pad deposition technique is one solution among others to achieve this goal. We have shown that discontinuous pads generate less stress than continuous pads.

Studying the adhesion energy and characterizing the fracture at the ECA/cell and ECA/copper interfaces on discontinuous pads is an interesting topic for understanding the fracture behavior of ECAs in this technology.

The growth and capacity increase of solar energy starts with increasing the manufacturing throughput of PV modules. At the string manufacturing scale, the increase in manufacturing rate is conditioned by the cross-linking kinetics of the ECA. This theme of ECA cross-linking, investigated experimentally and numerically, could be a promising way to increase the manufacturing process capacity.

Although the ECA interconnection technology reduces the stress level in the solar cells during lamination, stress concentrations are still observed along the interconnect lines. These stress concentrations must be reduced as they represent a major source of microcracking in solar cells. Some studies in the literature have shown the advantages of the reduction of the section of the copper ribbons in the reduction of the residual stresses in the solar cell after soldering. Gabor *et al.* [98] have investigated the possibility of replacing the copper ribbons with Invar ribbons which have a CTE very close to that of the solar cell. Their results showed that Invar can be a promising alternative to copper ribbons. More efforts should be devoted to studying its alternatives.

Towards improving short lamination process

In 2020, more than 50% of the PV module production units fabs have a production capacity between 1 and 5 GW. By 2031, the manufacturing units fabs with a capacity exceeding 5GW will gain a market share of around 50%.

This increase in capacity requires optimization and automatization of the manufacturing process, especially the lamination process. The short lamination process is a valuable technique to achieve these objectives as it reduces the processing time by 50% [7]. This reduction in production time is ensured by fast heating cycles, especially when TPO type encapsulants are used which require a short heating time compared to EVA, and also by fast cooling.

The effect of this rapid cooling on the micro-structural properties of the encapsulant, optical properties, and the behavior of PV modules under aging are topics not addressed in the literature. Preliminary investigations have been carried out in this work, to understand these phenomena.

The cooling press accelerates the cooling of the PV module by a rate of 5. The analysis of the microstructural properties by DSC of TPO-A encapsulant, extracted from a PV module laminated with CP, showed that the crystallinity of the encapsulant remains constant while the crystallite size increases. This increase in crystallite size reduces the haze factor of the encapsulant by 34%.

PV modules were encapsulated at 156°C with and without CP using the same process parameters chosen to study the residual deflection in chapter 6. However, in these modules interconnected PERC cells were used. Six modules of each lamination cooling technique were manufactured.

They were then subjected to accelerated aging tests including 300 cycles of Thermal Cycling (TC) and 500h of Damp Heat (DH). No degrading effect was observed on the electrical performance of the modules after 300 thermal cycles for the modules cooled with and without cooling press. Modules cooled with CP showed power losses of up to 3% compared to 1% for modules cooled without CP.

These losses in maximal power (P_{max}) are mostly due to open circuit voltage (V_{OC}) losses - about 2% for the worst - and partially due to both short-circuit current (I_{SC}) and Fill Factor (FF) losses. One hypothesis is that the V_{OC} losses could be linked to a deterioration of the cell's passivation during the fast cooling. This deterioration could be harmful and could have been amplified by the environmental ageing conditions. The losses associated with the I_{SC} losses are usually due to optical property changes - typically a yellowing or an opacifying of the front encapsulant, but nothing noticeable in PV modules. Those associated with FF losses are a rise in the string resistance.

The experimental results of this preliminary study and residual deflection measurements for the short lamination process parameters were performed on a limited number of samples. Therefore, the dispersion of the results was not considered. These aspects are quite intriguing and so encouraging to be further investigated in the future.

The results of this thesis were a first step towards the understanding of the thermomechanical behavior during the process. These results could be used for further studies dedicated to the ageing of PV modules in installation.

The numerical models developed in this work can be further enhanced by introducing damage laws to study solar cell failure for instance, or by considering non-perfect interface bonding to study delamination. Moreover, the development of new experimental methods to validate numerical models should be further investigated. In-situ measurements using stress sensors may be a good approach to pursue.

Bibliography

[1] REN21, "Renewables 2021 global status report," 2021. xv, 1

[2] J. F. Weaver, "World has installed 1 TW of solar capacity," in PV magazine, March 2022. 1

[3] M. Ram, D. Bogdanov, A. Aghahosseini, A. Oyewo, A. Gulagi, M. Child, and H.-J. Fell, Global Energy System based on 100% Renewable Energy - Power Sector. study by LUT University and Energy Watch Group, Lappeenranta, Berlin, March 2017. 1

[4] IRENA, Renewable Power Generation Costs in 2020. International Renewable Energy Agency, Abu Dhabi, March 2021. 2

[5] International Technology Roadmap for Photovoltaic (ITRPV), "2020 results," April 2021. 2, 3, 10, 12, 17, 20, 47, 155, 161

[6] A. D. Rose, T. Geipel, D. Erath, A. Kraft, and U. Eitner, "Challenges for the interconnection of crystalline silicon heterojunction solar cells," Photovoltaic International, vol. 40, pp. 78–86, 2018. 2, 12, 17, 18

[7] Bürkle, Lamination Lines Easy-Lam & Ypsator for PV Module & Glass Panel Lamination. 2020. xv, 2, 19, 20, 162

[8] IEC 61215, Crystalline silicon terrestrial photovoltaic (PV) modules - Design qualification and type approval. International Electrochemical Commission, 2nd ed., 2005. 3, 15, 30

[9] R. R. Tummala, E. J. Rymaszewski, and A. G. Klopfenstein, Microelectronics Packaging Handbook: Semiconductor Packaging Part II. Springer Series in Advanced Microelectronics, Springer Science+Business Media Dordrecht, 2nd ed., 1997. 3

[10] S. Liu and Y. Liu, Modeling and simulation for microelectronic packaging assembly: Manufacturing, reability and testing. John Wiley and Sons (Asia), 1st ed., 2011.

[11] Y. Li and D. Goyal, 3D Microelectronic Packaging: From Architectures to Applications. Springer Series in Advanced Microelectronics, Springer Nature Singapore Pte Ltd., 2nd ed., 2021. 3

[12] N. Bosco, M. Springer, and X. He, "Viscoelastic material characterization and modeling of photovoltaic module packaging materials for direct finite-element method input," IEEE Journal of Photovoltaics, vol. 10, no. 5, pp. 1424–1440, 2020. 3, 13, 15, 56, 80, 112

[13] E. J. Schneller, R. P. Brooker, N. S. Shiradkar, M. P. Rodgers, N. G. Dhere, K. O. Davis, H. P. Seigneur, N. Mohajeri, J. Wohlgemuth, G. Scardera, A. C. Rudack, and W. V. Schoenfeld, "Manufacturing metrology for c-Si module reliability and durability part III: Module manufacturing," Renewable and Sustainable Energy Reviews, vol. 59, pp. 992–1016, 2016. xv, 9, 10, 22, 24, 25

[14] A. C. Martins, V. Chapuis, A. Virtuani, H.-Y. Li, L.-E. Perret-Aebi, and C. Ballif, "Thermo-mechanical stability of lightweight glass-free photovoltaic modules based on a composite substrate," Solar Energy Materials and Solar Cells, vol. 187, pp. 82–90, 2018. 9

[15] A. C. Martins, V. Chapuis, A. Virtuani, and C. Ballif, "Robust glass-free lightweight photovoltaic modules with improved resistance to mechanical loads and impact," IEEE Journal of Photovoltaics, vol. 9, no. 1, pp. 245–251, 2019.

[16] M. Li, W. Liu, F. Zhang, X. Zhang, A. A. Abaker Omer, Z. Zhang, Y. Liu, and S. Zhao, "Polymer multilayer film with excellent UV-resistance & high transmittance and its application for glass-free photovoltaic modules," Solar Energy Materials and Solar Cells, vol. 229, p. 111103, 2021. 9

[17] T. Duigou, V. Boichon, X. Brancaz, F. Chabuel, P. Francescato, J. Gaume, M. Lagache, P. Saffré, and L. Tenchine, "VIPV: Process development of integrated photovoltaic cells in a double-curved composite structure for automotive application," in Congrès Polymères pour la mobilité du futur, SIA-SFIP, February 2021. 9

[18] National Center for Photovoltaics NREL, "Best research cell efficiencies." `https://www.nrel.gov/pv/cell-efficiency.html`, 2021. 10

[19] International Technology Roadmap for Photovoltaic (ITRPV), "Trends and Challenges in c-Si PV-an update of the ITRPV ," in Wold Solar Congress, September 2018. 10

[20] C. Battaglia, A. Cuevas, and S. De Wolf, "High-efficiency crystalline silicon solar cells: status and perspectives," Energy & Environmental Science, vol. 9, pp. 1552–1576, 2016. 10

[21] D. Réaux, Cellules photovoltaïques à hétérojonctions de silicium (a-Si H/c-Si): modélisation des défauts et de la recombinaison à l'interface. PhD thesis, Thèse de l'Université Paris-Saclay, June 2017. 10

[22] A. Ebong and N. Chen, "Metallization of crystalline silicon solar cells: A review," in High Capacity Optical Networks and Emerging/Enabling Technologies, pp. 102–109, January 2012. 10

[23] Olympus Scientific Solutions Americas - Industrial Microscop, "Optimizing solar cell manufacturing using high-resolution digital and confocal laser microscopy." `https://www.azom.com/article.aspx?ArticleID=18939`, May 2020. 10

[24] U. Eitner, Thermomechanics of photovoltaic modules. PhD thesis, University Martin-Luther de Halle-Wittenberg, March 2011. xvi, 10, 11, 13, 15, 19, 38, 39, 40, 56, 75, 80, 112, 146

[25] S. K. Chunduri and M. Schmela, "Heterojunction solar technology," in TaiyangNews Advanced module technologies, 2020. 11

[26] S. Schoenfelder, A. Bohne, and J. Bagdahn, "Comparison of test methods for strength characterization of thin solar wafer," in Proceedings of the 22nd European Photovoltaic Solar Energy Conference, vol. 1, p. 1636–1640, September 2007. 11

[27] C. Funke, E. Kullig, M. Kuna, and J. Möller, "Biaxial fracture test of silicon wafers," Advanced Engineering Materials, vol. 6, pp. 594–598, 2004. 11

[28] M. A. Hopcroft, W. D. Nix, and T. W. Kenny, "What is the young's modulus of silicon?," Journal of Microelectromechanical Systems, vol. 19, pp. 229–238, April 2010. xvii, xxi, 11, 77

[29] J. J. Hall, "Electronic effects in the elastic constants of n-type silicon," Physical Review, vol. 161, no. 3, pp. 756–761, 1967. xxi, 11

[30] L. Carton, Mechanical properties of thin silicon wafers for photovoltaic applications: influence of material quality and sawing process. PhD thesis, Thèse de l'Université de Lyon-l'Institut National des Sciences Appliquées de Lyon, December 2020. 11, 75, 79, 123

[31] W. D. J. Callister, Fundamentals of Materials Science and Engineering: An Integrated Approach. Wiley, New York, 5th ed., 2001. 11

[32] G. S. Brady, H. R. Clauser, and J. A. Vaccari, Materials Handbook. McGraw-Hill Professional, 15th ed., 2002. 12, 17, 72, 81

[33] S. K. Chunduri and M. Schmela, "Surprising Developments Leading to Significantly Higher Power Ratings of Solar Modules," in TaiyangNews Advanced Module Technologies, 2019 ed., 2019. 12, 114

[34] S. Wiese, R. Meier, and F. Kraemer, "Mechanical behaviour and fatigue of copper ribbons used as solar cell interconnectors," in Proceedings of the 11th International Thermal, Mechanical Multi-Physics Simulation, and Experiments in Microelectronics and Microsystems (EuroSimE), pp. 1–5, 2010. 12

[35] S. P. Aly, S. Ahzi, N. Barth, and A. Abdallah, "Numerical analysis of the reliability of photovoltaic modules based on the fatigue life of the copper interconnects," Solar Energy, vol. 212, pp. 152–168, 2020.

[36] A. Schubert, R. Dudek, E. Auerswald, A. Gollbardt, B. Michel, and H. Reichl, "Fatigue life models for SnAgCu and SnPb solder joints evaluated by experiments and simulation," in Proceedings of the 53rd Electronic Components and Technology Conference, pp. 603–610, 2003.

[37] A. Eslami Majd and N. N. Ekere, "Crack initiation and growth in PV module interconnection," Solar Energy, vol. 206, pp. 499–507, 2020. 12

[38] V. Poulek, D. Strebkov, I. Persic, and M. Libra, "Towards 50 years lifetime of PV panels laminated with silicone gel technology," Solar Energy, vol. 86, no. 10, pp. 3103–3108, 2012. 12

[39] S. K. chunduri and M. Schmela, "Market survey: Backsheets & encapsulation 2020," in TaiyangNews Advanced module technologies, 2020. xv, 12, 14, 15

[40] S. K. chunduri and M. Schmela, "Bifacial solar technology 2021 edition – part 1," in TaiyangNews Advanced module technologies, 2021. 12

[41] S. K. Chunduri and M. Schmela, "Addressing the needs of different segments: Utility-scale, C&I and rooftops," in TaiyangNews Advanced module technologies, 2021. 12, 21

[42] D. L. King, M. A. Quintana, J. A. Kratochvil, D. E. Ellibee, and B. R. Hansen, "Photovoltaic module performance and durability following long-term field exposure," Progress in Photovoltaics: Research and Applications, vol. 8, no. 2, pp. 241–256, 2000. 13

[43] C. Wiesmeier, I. Haedrich, K.-A. Weiss, and I. Duerr, "Overview of PV module encapsulation materials," Photovoltaics International, vol. 19, pp. 85–92, 2013. 13, 19

[44] M. Paggi and A. Sapora, "An accurate thermoviscoelastic rheological model for Ethylene Vinyl Acetate based on fractional calculus," International Journal of Photoenergy, vol. 2015, pp. 1–7, 2015. 13, 56

[45] Z. Jiang, M. Owen-Bellini, D. Montiel-Chicharro, T. R. Betts, and G. Ralph, "Effect of viscoelasticity of Ethylene Vinyl Acetate encapsulants on photovoltaic module solder joint degradation due to thermomechanical fatigue," Japanese Journal of Applied Physics, vol. 57, pp. 08RG03 1–5, 2019. 13, 56

[46] R. Brueckner., Materials Science and Technology: A Comprehensive Treatment, vol. 9 of Glasses and Amorphous Materials. Wiley-VCH, 1991. xxi, 13

[47] J. E. Purvis, Handbook of Industrial Materials. Glasses and Amorphous Materials, Elsevier Science & Technology, elsevier science ltd ed., 1992. 13

[48] O. Hasan, A. F. M. Arif, and M. U. Siddiqui, "Finite element modeling, analysis, and life prediction of photovoltaic modules," Solar Energy Materials and Solar Cells, vol. 136, pp. 1–1, 2014. xxi, 13, 15, 41, 84, 91, 108, 112, 118, 144

[49] G. Oreski and G. Wallner, "Aging mechanisms of polymeric films for PV encapsulation," Solar Energy, vol. 79, no. 6, pp. 612–617, 2005. Polymeric Materials for Solar Energy Applications. 14

[50] W. Gambogi, "Comparative performance of backsheets for photovoltaic modules," in Proceedings of the 25th European Photovoltaic Solar Energy Conference and Exhibition, September 2010. 14

[51] M. Köntges, S. Kurtz, C. Packard, U. Jahn, K. A. Berger, and K. Kato, Performance and reliability of photovoltaic systems: subtask 3.2: Review of failures of photovoltaic modules: IEA PVPS task 13: external final report IEA-PVPS. International Energy Agency, Photovoltaic Power Systems Programme, 2014. 14

[52] G. Oreski, G. Eder, Y. Voronko, A. Omazic, L. Neumaier, W. Mühleisen, G. Ujvari, R. Ebner, and M. Edler, "Performance of PV modules using co-extruded backsheets based on polypropylene," Solar Energy Materials and Solar Cells, vol. 223, p. 110976, 2021. 14

[53] International Technology Roadmap for Photovoltaic (ITRPV), "Eleventh edition online," April 2020. 15

[54] "Evasol." http://www.evasol.fr accessed on 19/03/2017. xv, 15

[55] C. CARRIERE, Métallisations et interconnexions des cellules solaires pour la fabrication de modules. Projet interne, May 2020. 16, 17

[56] International Technology Roadmap for Photovoltaic (ITRPV), "Results 2018," March 2019. 16

[57] S. Braun, G. Hahn, R. Nissler, C. Pönisch, and D. Habermann, "The multi-busbar design: An overview," Energy Procedia, vol. 43, pp. 86–92, 2013. Proceedings of the 4th Workshop on Metallization for Crystalline Silicon Solar Cells. 16

[58] S. Braun, G. Hahn, R. Nissler, C. Pönisch, and D. Habermann, "Multi-busbar solar cells and modules: High efficiencies and low silver consumption," Energy Procedia, vol. 38, pp. 334–339, 2013. Proceedings of the 3rd International Conference on Crystalline Silicon Photovoltaics. 16

[59] N. Wŏhrle, E. Lohm ŭller, M. Mittag, A. Moldovan, P. Baliozian, T. Fellmeth, K. Krauß, A. Kraft, and R. Preu, "Solar cell demand for bifacial and singulated-cell module architectures," Photovoltaics International, p. 48, 05 2017. 16

[60] A. Faes, M. Despeisse, J. Levrat, J. Champliaud, N. Badel, M. Kiaee, T. Söderström, Y. Yao, R. Grischke, M. Gragert, J. Ufheil, P. Papet, B. Strahm, G. Cattaneo, J. Cattin, Y. Baumgartner, A. Hessler-Wyser, and C. Ballif, "Smartwire solar cell interconnection technology," in Proceedings of the 29th European Photovoltaic Solar Energy Conference and Exhibition, pp. 2555–2561, September 2014. 16

[61] P. Papet, L. Andreetta, D. Lachenal, G. Wahli, J. Meixenberger, B. Legradic, W. Frammelsberger, D. Bätzner, B. Strahm, Y. Yao, and T. Söderström, "New cell metallization patterns for heterojunction solar cells interconnected by the smart wire connection technology," Energy Procedia, vol. 67, pp. 203–209, 2015. Proceedings of the 5th Workshop on Metallization for Crystalline Silicon Solar Cells. 16

[62] L. C. Rendler, A. P. Haryantho, J. Walter, J. Huyeng, A. Kraft, S. Wiese, and U. Eitner, "Wave-shaped wires soldered on the finger grid of solar cells: Solder joint stability under thermal cycling," in AIP Conference Proceedings, vol. 1999, p. 080001, 2018. 16

[63] T. Geipel, D. Eberlein, and A. Kraft, "Lead-free solders for ribbon interconnection of crystalline silicon PERC solar cells with infrared soldering," vol. 2156, p. 020015, 2019. 16

[64] M. Zhang, E. Mu, Q. Chu, H. Xu, and H. Luo, "Influence of Indium on microstructure and properties of Sn-Pb binary alloy applied in photovoltaic ribbon," Journal of Materials Engineering and Performance, vol. 28, pp. 3714–3723, 2019. 16

[65] T. Geipel, M. Moeller, J. Walter, A. Kraft, and U. Eitner, "Intermetallic compounds in solar cell interconnections: Microstructure and growth kinetics," Solar Energy Materials and Solar Cells, vol. 159, pp. 370–388, 2017. 17

[66] N. R. A. Razak, M. A. A. Mohd Salleh, N. Saud, R. M. Said, and M. I. I. Ramli, "Influence of Bismuth in Sn-Based Lead-Free Solder – A Short Review," in Electronic Packaging Interconnect Technology, vol. 273 of Solid State Phenomena, pp. 40–45, Trans Tech Publications Ltd, 6 2018. 17

[67] M. Heimann, P. Klaerner, C. Luechinger, A. Mette, J. Mueller, M. Traeger, T. Barthel, O. Valentin, and P. Wawer, "Ultrasonic bonding of aluminum ribbons to interconnect high-efficiency crystalline-silicon solar cells," Energy Procedia, vol. 27, pp. 670–675, 2012. Proceedings of the 2nd International Conference on Crystalline Silicon Photovoltaics SiliconPV 2012. 17

[68] P. Schmitt, D. Eberlein, C. Ebert, M. Tranitz, U. Eitner, and H. Wirth, "Adhesion of al-metallization in ultra-sonic soldering on the al-rear side of solar cells," Energy Procedia, vol. 38, pp. 380–386, 2013. Proceedings of the 3rd International Conference on Crystalline Silicon Photovoltaics (SiliconPV 2013). 17

[69] J.-S. Jeong, N. Park, and C. Han, "Field failure mechanism study of solder interconnection for crystalline silicon photovoltaic module," Microelectronics Reliability, vol. 52, no. 9, pp. 2326–2330, 2012. Special issue 23rd European symposium on the reliability of electron devices, failure physics and analysis. xv, 17, 24

[70] R. Aradhana, S. Mohanty, and S. K. Nayak, "A review on epoxy-based electrically conductive adhesives," International Journal of Adhesion and Adhesives, vol. 99, p. 102596, 2020. 17, 18

[71] J. B. Charpentier, Micro-structure et mécanique des ICAs à flocons d'argent pour le photovoltaïque. Projet interne, September 2021. 17

[72] M. Mundlein and J. Nicolics, "Modeling of particle arrangement in an isotropically conductive adhesive joint," IEEE Transactions on Components and Packaging Technologies, vol. 28, no. 4, pp. 765–770, 2005. 18

[73] J. E. Morris and J. Liu, Electrically Conductive Adhesives: A Research Status Review, pp. B527–B570. Boston, MA: Springer US, 2007. 18

[74] S. Hoffmann, T. Geipel, M. Meinert, and A. Kraft, "Analysis of peel and shear forces after temperature cycle tests for electrical conductive adhesives," in Proceedings of the 33rd European Photovoltaic Solar Energy Conference and Exhibition, p. 183–186, 2017. 18

[75] D. Lu, Q. Tong, and C. Wong, "Mechanisms underlying the unstable contact resistance of conductive adhesives," IEEE Transactions on Electronics Packaging Manufacturing, vol. 22, no. 3, pp. 228–232, 1999. 18

[76] M. J. Yim, Y. Li, K. sik Moon, K. W. Paik, and C. P. Wong, "Review of recent advances in electrically conductive adhesive materials and technologies in electronic packaging," Journal of Adhesion Science and Technology, vol. 22, no. 14, pp. 1593–1630, 2008. 18

[77] J. Jagt, "Reliability of electrically conductive adhesive joints for surface mount applications: a summary of the state of the art," IEEE Transactions on Components, Packaging, and Manufacturing Technology: Part A, vol. 21, no. 2, pp. 215–225, 1998. 18

[78] J. Schlothauer, M. Ralaiarisoa, A. Morlier, M. Köntges, and B. Röder, "Determination of the cross-linking degree of commercial Ethylene-Vinyl-Acetate polymer by luminescence spectroscopy," Journal of Polymer Research, vol. 21, 04 2014. 19

[79] I. Rahmoun, T. Le Carre, B. Chambion, E. Mofakhami, A. Derrier, J.-L. Bouvard, and P.-O. Bouchard, "3-D Modeling of Thermal Exchange in the PV Module During Lamination: Impact of Architecture, Laminator Configuration, and Lamination Recipe," IEEE Journal of Photovoltaics, pp. 1–7, 2021. xv, 19, 20, 106, 144

[80] International Technology Roadmap for Photovoltaic (ITRPV), "Results 2014," 2015. 19

[81] G. Cattaneo, F. Galliano, V. Chapuis, H.-Y. Li, C. Schlumpf, A. Faes, T. Söderström, Y. Yao, R. Grischke, M. Gragert, C. Ballif, and L.-E. Perret-Aebi, "Encapsulants characterization for novel Photovoltaic modules," in Proceedings of the 29th European Photovoltaic Solar Energy Conference and Exhibition, p. 5, October 2014. 19

[82] S. Sraisth, "Achieving faster lamination process for crystalline photovoltaic modules by using latest lamination technologies," in Proceedings of the 33rd European Photovoltaic Solar Energy Conference and Exhibition, pp. 992 – 997, September 2017. xv, 20

[83] G. Cattaneo, A. Faes, H.-Y. Li, F. Galliano, M. Gragert, Y. Yao, R. Grischke, T. Söderström, M. Despeisse, C. Ballif, and L.-E. Perret-Aebi, "Lamination process and encapsulation materials for glass–glass PV module design," Photovoltaics International, p. 82, March 2015. 19

[84] S. Sraisth, "Lamination technology – PV panels." https://www.energyforum.in/fileadmin/user_upload/india/media_elements/Presentations/20190918_REI_Expo/20190918_Speakers_Corner_PPT/Day_1/02_Robert_Buerkle_Sraisth.pdf, September 2019. xv, 20

[85] H.-Y. Li, L.-E. Perret-Aebi, V. Chapuis, C. Ballif, and Y. Luo, "The effect of cooling press on the encapsulation properties of crystalline photovoltaic modules: residual stress and adhesion," Progress in Photovoltaics: Research and Applications, vol. 23, no. 2, pp. 160–169, 2015. xvi, 20, 41, 44, 45, 129, 142

[86] M. Köntges, S. Kurtz, C. Packard, U. Jahn, K. A. Berger, K. Kato, T. Friesen, H. Liu, and M. V. Iseghem, Performance and reliability of photovoltaic systems: subtask 3.2: Review of failures of photovoltaic modules: IEA PVPS task 13: external final report IEA-PVPS. International Energy Agency, Photovoltaic Power Systems Programme, 2014. xv, 21

[87] A. Richter, "Schadensbilder nach wareneingang und im reklamationsfall," in 8th Workshop "Photovoltaic Module Technology, TÜV Rheinland, Köln, November 2011. 21, 26

[88] K. Schulze, M. Groh, M. Nieß, C. Vodermayer, G. Wotruba, and G. Becker, "Untersuchung von alterungseffekten bei monokristallinen PV-modulen mit mehr als 15 betriebsjahren durch elektrolumineszenz- und leistungsmessung," in Proceedings of 28th Symposium Photovoltaic Solar Energy (OTTI, Staffelstein, Germany), 2012. 21

[89] K. O. Davis, S. R. Kurtz, D. C. Jordan, J. H. Wohlgemuth, and N. Sorloaica-Hickman, "Multi-pronged analysis of degradation rates of photovoltaic modules and arrays deployed in florida," Progress in Photovoltaics: Research and Applications, vol. 21, no. 4, pp. 702–712, 2013. 22

[90] S. Kajari-Schršder, I. Kunze, and M. Kšntges, "Criticality of cracks in pv modules," Energy Procedia, vol. 27, pp. 658–663, 2012. Proceedings of the 2nd International Conference on Crystalline Silicon Photovoltaics. 22

[91] M. Köntges, I. Kunze, S. Kajari-Schröder, X. Breitenmoser, and B. Bjørneklett, "The risk of power loss in crystalline silicon based photovoltaic modules due to micro-cracks," Solar Energy Materials and Solar Cells, vol. 95, no. 4, pp. 1131–1137, 2011.

[92] T. J. Silverman, M. G. Deceglie, M. Owen-Bellini, W. B. Hobbs, and C. Libby, "Cracked solar cell performance depends on module temperature," in Proceedings of the 48th IEEE Photovoltaic Specialists Conference, pp. 1691–1692, 2021. 22

[93] M. Munoz, M. Alonso-García, N. Vela, and F. Chenlo, "Early degradation of silicon PV modules and guaranty conditions," Solar Energy, vol. 85, no. 9, pp. 2264–2274, 2011. 22

[94] L. Lillo-Sánchez, G. López-Lara, J. Vera-Medina, E. Pérez-Aparicio, and I. Lillo-Bravo, "Degradation analysis of photovoltaic modules after operating for 22 years. a case study with comparisons," Solar Energy, vol. 222, pp. 84–94, 2021. 22

[95] S. Deng, Z. Zhang, C. Ju, J. Dong, Z. Xia, X. Yan, T. Xu, and G. Xing, "Research on hot spot risk for high-efficiency solar module," Energy Procedia, vol. 130, pp. 77–86, 2017. Proceedings of the SNEC 11th International Photovoltaic Power Generation Conference & Exhibition. xv, 22, 23

[96] M. Paggi and A. Sapora, "Numerical modelling of microcracking in PV modules induced by thermo-mechanical loads," Energy Procedia, vol. 38, pp. 506–515, 2013. Proceedings of the 3rd International Conference on Crystalline Silicon Photovoltaics. xv, 23

[97] L. Papargyri, M. Theristis, B. Kubicek, T. Krametz, C. Mayr, P. Papanastasiou, and G. E. Georghiou, "Modelling and experimental investigations of microcracks in crystalline silicon photovoltaics: A review," Renewable Energy, vol. 145, pp. 2387–2408, 2020. xxi, 23, 24

[98] A. Gabor, M. Ralli, S. Montminy, L. Alegria, C. Bordonaro, J. Woods, L. Felton, M. Davis, B. Atchley, and T. Williams, "Soldering induced damage to thin si solar cells and detection of cracked cells in modules," in Proceedings of the 21st European Photovoltaic Solar Energy Conference, January 2006. 24, 122, 161

[99] G. Li, M. Akram, Y. Jin, X. Chen, C. Zhu, A. Ahmad, and R. Arshad, "Thermo-mechanical behavior assessment of smart wire connected and busbarpv modules during production, transportation, and subsequent field loading stages," Energy, vol. 168, pp. 931–945, 2019. 24, 33, 41

[100] S. Nasr Esfahani, S. Asghari, and S. Rashid-Nadimi, "A numerical model for soldering process in silicon solar cells," Solar Energy, vol. 148, pp. 49–56, 2017. xv, 24, 33

[101] F. Kraemer, J. Seib, E. Peter, and S. Wiese, "Mechanical stress analysis in photovoltaic cells during the string-ribbon interconnection process," in Proceedings of the 15th International Conference on Thermal, Mechanical and Mulit-Physics Simulation and Experiments in Microelectronics and Microsystems, pp. 1–7, 2014. xvi, 24, 33, 34, 35

[102] L. Rendler, P. Romer, A. Beinert, J. Walter, S. Stecklum, A. Kraft, U. Eitner, and S. Wiese, "Thermomechanical stress in solar cells: Contact pad modeling and reliability analysis," Solar Energy Materials and Solar Cells, vol. 196, pp. 167–177, 2019. xv, 24, 34, 114

[103] H. Shin, E. Han, N. Park, and D. Kim, "Thermal residual stress analysis of soldering and lamination processes for fabrication of crystalline silicon photovoltaic modules," Energies, vol. 11, no. 12, 2018. xvi, 24, 33, 35, 37, 41, 45, 46

[104] M. Israil, S. A. Anwar, and M. Z. Abdullah, "Automatic detection of micro-crack in solar wafers and cells: a review," Transactions of the Institute of Measurement and Control, vol. 35, no. 5, pp. 606–618, 2013. 24

[105] S. Dietrich, M. Pander, M. Sander, S. H. Schulze, and M. Ebert, "Mechanical and thermomechanical assessment of encapsulated solar cells by finite-element-simulation," in SPIE Solar Energy + Technology (N. G. Dhere, J. H. Wohlgemuth, and K. Lynn, eds.), p. 77730F, August 2010. xvi, 24, 39, 40, 45, 47, 114, 146

[106] Q. Zhang, B. Shu, M. Chen, Q. Liang, C. Fan, Z. Feng, and P. Verlinden, "Numerical investigation on residual stress in photovoltaic laminates after lamination," Journal of Mechanical Science and Technology, vol. 29, pp. 655–662, 2015. 41

[107] M. Sander, B. Henke, H. Schwarz, S. Dietrich, S. Schweizer, M. Ebert, and J. Bagdahn, "Characterization of PV modules by combining results of mechanical and electrical analysis methods," Proceedings of SPIE, pp. 777308–777308, August 2010. 24

[108] W. J. R. Song, S. K. Tippabhotla, A. A. O. Tay, and A. S. Budiman, "Numerical simulation of the evolution of stress in solar cells during the entire manufacturing cycle of a conventional silicon wafer based photovoltaic laminate," IEEE Journal of Photovoltaics, vol. 8, no. 1, pp. 210–217, 2018. xvi, 24, 33, 34, 35, 41, 42, 43, 44, 45

[109] W. Song, S. Tippabhotla, A. Tay, and A. Budiman, "Effect of interconnect geometry on the evolution of stresses in a solar photovoltaic laminate during and after lamination," Solar Energy Materials and Solar Cells, vol. 187, pp. 241–248, 2018. 24, 33, 35, 41, 46

[110] M. Israil, "Non-destructive microcracks detection techniques in silicon solar cell," Physical Science International Journal, vol. 4, 2014. 24

[111] T. Liu, P. Ge, W. Bi, and Y. Gao, "Subsurface crack damage in silicon wafers induced by resin bonded diamond wire sawing," Materials Science in Semiconductor Processing, vol. 57, pp. 147–156, 2017. 24

[112] H. Wu, S. Melkote, and S. Danyluk, "Mechanical strength of silicon wafers cut by loose abrasive slurry and fixed abrasive diamond wire sawing," Advanced Engineering Materials, vol. 14, 2012. 24

[113] I. Rogelj, P. Ziger, and P. Eiselt, "Production of PV Ribbon for Photovoltaic Solar Panels: Overview of Product Specifications and Comparison of Production Processes." `http://plasmait.com/wp-content/uploads/2012/10/CabWire-Conference-Nov11-Production-of-PV-Ribbon-Presentation.pdf`, 2011. 24

[114] J. Wendt, M. Träger, M. Mette, A. Pfennig, and B. Jäckel, "The link between mechanical stress induced by soldering and micro damages in silicon solar cells," in Proceedings of the 24th European Photovoltaic Solar Energy Conference, pp. 3420–3423, 2009. 24

[115] J. D. Berghold, T. Geipel, O. Frank, Y. Zemen, and S. Pingel, "Mechanical stability of solar cells within solar panels," in Proceedings of the 24th European Photovoltaic Solar Energy Conference, 2009. 24

[116] M. W. Rowell, S. G. Daroczi, D. W. J. Harwood, and A. M. Gabor, "The effect of laminate construction and temperature cycling on the fracture strength and performance of encapsulated solar cells," in Proceedings of the 7th IEEE World Conference on Photovoltaic Energy Conversion, pp. 3927–3931, 2018. 24

[117] A. M. Gabor, R. Janoch, A. Anselmo, and H. Field, "Solar panel design factors to reduce the impact of cracked cells and the tendency for crack propagation," in NREL PV Module Reliability Workshop, Denver, CO USA, pp. 1–11, 2015. 25

[118] M. Köntges, G. Oreski, U. Jahn, M. Herz, P. Hacke, K.-A. Weiss, G. Razongles, M. Paggi, D. Parlevliet, T. Tanahashi, et al., "Assessment of photovoltaic module failures in the field," IEA PVPS Task, vol. 13, 2017. 25, 26

[119] J. H. Wohlgemuth, P. Hacke, N. Bosco, D. C. Miller, M. D. Kempe, and S. R. Kurtz, "Assessing the causes of encapsulant delamination in PV modules," in Proceedings of the 43rd IEEE Photovoltaic Specialists Conference, pp. 0248–0254, 2016. xv, 25

[120] N. Park, J. Jeong, B. Kang, and D. Kim, "The effect of encapsulant discoloration and delamination on the electrical characteristics of photovoltaic module," Microelectronics Reliability, vol. 53, no. 9, pp. 1818–1822, 2013. European Symposium on Reliability of Electron Devices, Failure Physics and Analysis. 26

[121] H.-Y. Li, R. Theron, G. Röder, T. Turlings, Y. Luo, L. M, C. Ballif, and L.-E. Perret-Aebi, "Insights into the encapsulation process of photovoltaic modules: GC-MS analysis on the curing step of poly(ethylene-co-vinyl acetate) (EVA) encapsulant," Polymers and Polymer Composites, vol. 20, pp. 665–672, 2012. 26

[122] H. Altenbach, J. W. Altenbach, and W. Kissing, Mechanics of composite structural elements. Springer Science & Business Media, 2013. 29

[123] S. E. Bechtel and R. L. Lowe, eds., Fundamentals of Continuum Mechanics. Boston: Academic Press, 2015.

[124] A. B. de Castro., Continuum Thermomechanics. Progress in Mathematical Physics, Birkhäuser Basel, 2005. 29

[125] P. Liu, Chapter 6 - Implicit finite element analysis of the influence of cohesive law parameters for delamination analysis of composite laminates under compression. Damage Modeling of Composite Structures, Elsevier, 2021. 32

[126] C. McCarthy and T. Vaughan, "14 - micromechanical failure analysis of advanced composite materials," in Numerical Modelling of Failure in Advanced Composite Materials (P. P. Camanho and S. R. Hallett, eds.), Woodhead Publishing Series in Composites Science and Engineering, pp. 379–409, Woodhead Publishing, 2015.

[127] A. Turon, P. P. Camanho, A. Soto, and E. V. González, "Analysis of delamination damage in composite structures using cohesive elements," in Comprehensive Composite Materials II (P. W. Beaumont and C. H. Zweben, eds.), pp. 136–156, Oxford: Elsevier, 2018. 32

[128] A. J. Beinert, P. Romer, A. Büchler, V. Haueisen, J. Aktaa, and U. Eitner, "Thermomechanical stress analysis of PV module production processes by Raman spectroscopy and FEM simulation," vol. 124, pp. 464–469, 2017. Proceedings of the 7th International Conference on Silicon Photovoltaics. 33, 35, 39, 112

[129] A. J. Beinert, A. Büchler, P. Romer, V. Haueisen, C. Rendler, Li, M. C. Schubert, M. Heinrich, J. Aktaa, and U. Eitner, "Enabling the measurement of thermomechanical stress in solar cells and PV modules by confocal micro-Raman spectroscopy," Solar Energy Materials and Solar Cells, vol. 193, pp. 351–360, 2019. xvi, xix, 34, 39, 40, 42, 44, 100, 112, 121, 122, 129, 153

[130] S. Dietrich, M. Pander, M. Sander, U. Zeller, and M. Ebert, "Stress analysis of encapsulated solar cells by means of superposition of thermal and mechanical stresses," in Reliability of Photovoltaic Cells, Modules, Components, and Systems VI (N. G. Dhere, J. H. Wohlgemuth, and K. W. Lynn, eds.), vol. 8825, pp. 33 – 42, International Society for Optics and Photonics, SPIE, 2013. 39

[131] S. W. M. Ridhuan, S. K. Tippabhotla, A. A. O. Tay, and A. S. Budiman, "A simulation study of the stresses in crystalline silicon photovoltaic laminates during the soldering and lamination processes along the longitudinal direction," Advanced Engineering Materials, pp. 1–11, 2019. 36, 41

[132] S. K. Tippabhotla, I. Radchenko, W. Song, N. Tamura, A. A. O. Tay, and A. S. Budiman, "Effect of interconnect plasticity on soldering induced residual stress in thin crystalline silicon solar cells," in Proceedings of the 18th IEEE Electronics Packaging Technology Conference, pp. 734–737, 2016. 34, 41, 44, 49

[133] C.-H. Chen, F.-M. Lin, H.-T. Hu, and F.-Y. Yeh, "Residual stress and bow analysis for silicon solar cell induced by soldering," International symposium on solar cell technologies, pp. 1–3, May 2008.

[134] S. K. Tippabhotla, I. Radchenko, W. Song, G. Illya, V. Handara, M. Kunz, N. Tamura, A. A. Tay, and A. S. Budiman, "From cells to laminate: probing and modeling residual stress evolution in thin silicon photovoltaic modules using synchrotron X-ray micro-diffraction experiments and finite element simulations," Progress in Photovoltaics: Research and Applications, vol. 25, no. 9, pp. 791–809, 2017. xvi, 39, 41, 42, 43, 44, 108, 112, 118, 129, 144, 153

[135] S. Wiese, F. Kraemer, N. Betzl, and D. Wald, "Interconnection technologies for photovoltaic modules - analysis of technological and mechanical problems," in Proceedings of the 11th International Thermal, Mechanical Multi-Physics Simulation, and Experiments in Microelectronics and Microsystems, pp. 1–6, 2010. xvi, 33, 35, 36, 37, 38

[136] C. ming Lai, C.-H. Su, and K. moh Lin, "Analysis of the thermal stress and warpage induced by soldering in monocrystalline silicon cells," Applied Thermal Engineering, vol. 55, no. 1, pp. 7–16, 2013. 33

[137] L. C. Rendler, J. Walter, T. Geipel, M. Volk, C. Ebert, and U. Eitner, "Modelling and verification of mechanical stress induced by soldering of wires for multi busbar interconnection," in Proceedings of the 31st European Photovoltaic Solar Energy Conference and Exhibition, pp. 84–88, September 2015. 33

[138] L. C. Rendler, A. Kraft, C. Ebert, U. Eitner, and S. Wiese, "Mechanical stress in solar cells with multi busbar interconnection — parameter study by fem simulation," in Proceedings of the 17th International Conference on Thermal, Mechanical and Multi-Physics Simulation and Experiments in Microelectronics and Microsystems, pp. 1–5, 2016. xv, 33, 34

[139] T. Geipel, C. Rendler, Li, M. Stompe, U. Eitner, and L. Rissing, "Reduction of thermomechanical stress using electrically conductive adhesives," in Proceedings of the 5th International Conference on Silicon Photovoltaics, pp. 346–355, 2015. xv, xvi, 33, 34, 35, 37, 38, 100, 123

[140] D. Eikelboom, J. Bultman, A. Schonecker, M. Meuwissen, M. van den Nieuwenhof, and D. Meier, "Conductive adhesives for low-stress interconnection of thin back-contact solar cells," in Proceedings of the 29th IEEE Photovoltaic Specialists Conference, pp. 403–406, 2002.

[141] M. H. H. Meuwissen, M. van den Nieuwenhof, H. L. A. H. Steijvers, T. Bots, K. M. Broek, and M. J. H. Kloos, "Simulation assisted design of a PV module incorporating electrically conductive adhesive interconnects," in Proceedings of the 21st European Photovoltaic Solar Energy Conference, pp. 2485–2490, 2006. 33, 35, 38

[142] P. Nivelle, J. A. Tsanakas, J. Poortmans, and M. Daenen, "Stress and strain within photovoltaic modules using the finite element method: A critical review," Renewable and Sustainable Energy Reviews, vol. 145, p. 111022, 2021. 36

[143] U. Eitner, P. P. Altermatt, M. Kontges, R. Meyer, and R. Brendel, "A modeling approach to the optimization of interconnects for back contact cells by thermo-mechanical simulations of photovoltaic modules," in Proceedings of the 23rd European Photovoltaic Solar Energy Conference, vol. 8, pp. 2815–2817, September 2008. xvi, 38, 40, 114

[144] U. Eitner, S. Kajari-Schröder, M. Köntges, and R. Brendel, "Non-linear mechanical properties of ethylene-vinyl acetate (EVA) and its relevance to thermomechanics of photovoltaic modules," in Proceedings of the 25th European Photovoltaic Solar Energy Conference, pp. 1–3, September 2010.

[145] U. Eitner, S. Kajari-Schröder, M. Köntges, and H. Altenbach, Thermal Stress and Strain of Solar Cells in Photovoltaic Modules, pp. 453–468. Berlin, Heidelberg: Springer Berlin Heidelberg, 2011. 38, 146

[146] S. Dietrich, M. Sander, M. Pander, and M. Ebert, "Interdependency of mechanical failure rate of encapsulated solar cells and module design parameters," in Proceedings of SPIE - The International Society for Optical Engineering, vol. 8472, October 2012. 39

[147] S. Dietrich, M. Pander, and M. Ebert, "Mechanical challenges of PV - modules and its embedded cells - experiment and finite element analysis," in Proceedings of the 24th European Photovoltaic Solar Energy Conference and Exhibition, pp. 3427–3431, September 2009. 39, 45

[148] A. J. Beinert, M. Ebert, U. Eitner, and J. Aktaa, "Influence of photovoltaic module mounting systems on the thermo-mechanical stresses in solar cells by FEM modelling," in Proceedings of the 32nd European Photovoltaic Solar Energy Conference and Exhibition, pp. 1833–1836, 06 2016. 39

[149] A. J. Beinert, R. Leidl, P. Sommeling, U. Eitner, and J. Aktaa, "FEM-based development of novel back-contact PV modules with ultra-thin solar," in Proceedings of the 33rd European Photovoltaic Solar Energy Conference and Exhibition, pp. 42–47, 2017. 146

[150] A. J. Beinert, P. Romer, M. Heinrich, M. Mittag, J. Aktaa, and D. H. Neuhaus, "The Effect of Cell and Module Dimensions on Thermomechanical Stress in PV Modules," IEEE Journal of Photovoltaics, vol. 10, pp. 70–77, 2020. xvi, 39, 40, 45, 114, 123, 146

[151] A. Pfreundt, A. J. Beinert, L. Mesquita, L. Bauermann, P. Romer, M. Mittag, and D. Yucebas Ayaz, "Post-processing thickness variation of PV module materials and its impact on temperature, mechanical stress and power," in Proceedings of the 36th European Photovoltaic Solar Energy Conference and Exhibition, pp. 935 – 940, September 2019. 39, 46

[152] P. Romer, G. Oreski, A. J. Beinert, D. Neuhaus, and M. Mittag, "More realistic consideration of backsheets coefficient of thermal expansion on thermomechanics of PV modules," in Proceedings of the 37th European Photovoltaic Solar Energy Conference and Exhibition, pp. 772–776, September 2020. 117

[153] M. Heinrich, A. J. Beinert, P. Romer, L. C. Rendler, F. Basler, S. Wendlandt, and D. Neuhaus, "Approaches for a lightweight module with laminated materials," in Proceedings of the 38th European Photovoltaic Solar Energy Conference and Exhibition, pp. 761–764, September 2021.

[154] P. Romer and A. J. Beinert, "Effects of inhomogeneous snow load on the mechanics of a PV module," in Proceedings of the 38th European Photovoltaic Solar Energy Conference and Exhibition, pp. 602 – 606, September 2021.

[155] A. Tummalieh, A. J. Beinert, C. Reichel, M. Mittag, and H. Neuhaus, "Holistic design improvement of the PV module frame: Mechanical, optoelectrical, cost, and life cycle analysis," Progress in Photovoltaics: Research and Applications, pp. 1–11, 2022. 39

[156] S. K. Tippabhotla, N. G. Diesta, X. Zhang, S. Sridhara, C. Stan, N. Tamura, A. A. Tay, and A. Budiman, "Thermomechanical residual stress evaluation in multi-crystalline silicon solar cells of photovoltaic modules with different encapsulation polymers using synchrotron X-ray microdiffraction," Solar Energy Materials and Solar Cells, vol. 193, pp. 387–402, 2019. 41

[157] A. Budiman, S. Anbazhagan, G. Illya, W. Song, R. Sahay, S. Tippabhotla, and A. Tay, "Enabling curvable silicon photovoltaics technology using polycarbonate-sandwiched laminate design," Solar Energy, vol. 220, pp. 462–472, 2021. 41

[158] S. Wiese, R. Meier, F. Kraemer, and J. Bagdahn, "Constitutive behaviour of copper ribbons used in solar cell assembly processes," in Proceedings of the 10th International Conference on Thermal, Mechanical and Multi-Physics Simulation and Experiments in Microelectronics and Microsystems, pp. 1–8, 2009. 41, 72, 111

[159] N. Bosco, M. Springer, J. Liu, S. N. Venkat, R. H. French, and T. Silverman, "Representative modules for accelerated thermal cycling and static load testing," in Proceedings of the 48th IEEE Photovoltaic Specialists Conference, pp. 1298–1300, 2021. 41

[160] N. Bosco, T. J. Silverman, and S. Kurtz, "The influence of PV module materials and design on solder joint thermal fatigue durability," IEEE Journal of Photovoltaics, vol. 6, no. 6, pp. 1407–1412, 2016. 45, 46

[161] Y. Lee and A. A. Tay, "Stress analysis of silicon wafer-based photovoltaic modules under IEC 61215 mechanical load test," Energy Procedia, vol. 33, pp. 265–271, 2013. PV Asia Pacific Conference 2012.

[162] O. Hasan and A. F. M. Arif, "Performance and life prediction model for photovoltaic modules: Effect of encapsulant constitutive behavior," Solar Energy Materials and Solar Cells, vol. 122, pp. 75–87, 2014. 41, 84

[163] M. Springer, J. Hartley, and N. Bosco, "Multiscale modeling of shingled cell photovoltaic modules for reliability assessment of electrically conductive adhesive cell interconnects," IEEE Journal of Photovoltaics, vol. 11, no. 4, pp. 1040–1047, 2021. 41

[164] M. Springer and N. Bosco, "Linear viscoelastic characterization of electrically conductive adhesives used as interconnect in photovoltaic modules," Progress in Photovoltaics: Research and Applications, vol. 28, no. 7, pp. 659–681, 2020. 63, 80, 91, 118

[165] N. Klasen, P. Romer, A. J. Beinert, and A. Kraft, "FEM simulation of deformations in strings of shingled solar cells subjected to mechanical reliability testing," AIP Conference Proceedings, vol. 2156, no. 1, p. 020016, 2019. 41

[166] M. Paggi, S. Kajari-Schröder, and U. Eitner, "Thermomechanical deformations in photovoltaic laminates," The Journal of Strain Analysis for Engineering Design, vol. 46, no. 8, pp. 772–782, 2011. 41

[167] G. H. Sun, S. L. Yan, and G. Chen, "Analytical model of thermal stress for encapsulation and service process of solar cell module," in Manufacturing Science and Engineering I, vol. 97 of Advanced Materials Research, pp. 2699–2702, Trans Tech Publications Ltd, March 2010. 41

[168] S. K. Tippabhotla, W. Song, A. A. Tay, and A. Budiman, "Effect of encapsulants on the thermomechanical residual stress in the back-contact silicon solar cells of photovoltaic modules – A constrained local curvature model," Solar Energy, vol. 182, pp. 134–147, 2019. xvi, 47

[169] N. W. Tschoegl, The Phenomenological Theory of Linear Viscoelastic Behavior: An Introduction. Springer, Berlin, Heidelberg, 1989. 56, 62, 65

[170] W. N. Findley, J. S. Lai, and K. Onaran, "Creep and relaxation of nonlinear viscoelastic materials with an introduction to linear viscoelasticity," ZAMM - Journal of Applied Mathematics and Mechanics / Zeitschrift für Angewandte Mathematik und Mechanik, vol. 58, no. 11, p. 524, 1978. 56, 61

[171] J.-F. Agassant, P. Avenas, J.-P. Sergent, B. Vergnes, and M. Vincent, La mise en forme des matières plastiques. Technique & Documentation - Lavoisier, 3ème édition revue et augmentée ed., Aug 1996. 60, 62, 63

[172] I. Ward and J. Sweeney, An Introduction to The Mechanical Properties of Solid Polymers. Chichester, UK: John Wiley & Sons Ltd, 1993. 60

[173] J. D. Ferry, Viscoelastic properties of polymers. Wiley, New York, 3d ed., 1980. 61, 62

[174] S.-H. Chae, J.-H. Zhao, D. Edwards, and P. Ho, "Characterization of the viscoelasticity of molding compounds in the time domain," Journal of Electronic Materials, vol. 39, pp. 419–425, April 2010. 62, 63, 64

[175] M. L. Williams, R. F. Landel, and J. D. Ferry, "The temperature dependence of relaxation mechanisms in amorphous polymers and other glass-forming liquids," Journal of the American Chemical Society, vol. 77, no. 14, pp. 3701–3707, 1955. 62

[176] I. Emri and N. W. Tschoegl, Generating line spectra from experimental responses. Part I: Relaxation modulus and creep compliance, vol. 32. Rheologica Acta., 1993. 65

[177] N. W. Tschoegl and I. Emri, Generating line spectra from experimental responses. Part II: Storage and loss functions, vol. 32. Rheologica Acta., 1993.

[178] I. Emri and N. W. Tschoegl, Generating line spectra from experimental responses. Part IV: Application to experimental data, vol. 33. Rheologica Acta., 1994. 65

[179] S. Bhattacharjee, A. K. Swamy, and J. S. Daniel, "Continuous relaxation and retardation spectrum method for viscoelastic characterization of asphalt concrete," Mechanics of Time-Dependent Materials, vol. 16, p. 287–305, August 2012. 65

[180] B. Babaei, A. Davarian, K. M. Pryse, E. L. Elson, and G. M. Genin, "Efficient and optimized identification of Generalized Maxwell viscoelastic relaxation spectra," Journal of the Mechanical Behavior of Biomedical Materials, vol. 55, pp. 32–41, April 2016. 65

[181] A. Takeh and S. Shanbhag, "A computer program to extract the continuous and discrete relaxation spectra from dynamic viscoelastic measurements," Applied Rheology, vol. 23, p. 24628, April 2013. 65

[182] J. Honerkamp and J. Weese, "A nonlinear regularization method for the calculation of relaxation spectra," Rheologica Acta, vol. 32, pp. 65–73, 1993. 65

[183] M. Baumgaertel and H. Winter, "Determination of discrete relaxation and retardation time spectra from dynamic mechanical data," Rheologica Acta, vol. 28, p. 511–519, 1989. 65

[184] KILONEWTON SAS, "Logiciel vic-3d." `https://www.kilonewton.fr/correlation_images/vic_3d.html`. 70

[185] H. Ledbetter, "Elastic constants of polycrystalline copper at low temperatures. relationship to single-crystal elastic constants," physica status solidi (a), vol. 66, pp. 477–484, 1981. 72

[186] G. R. Johnson and W. H. Cook, "A constitutive model and data for metals subjected to large strains, high strain rates and high temperatures," in Proceedings of the 7th International Symposium on Ballistics, vol. 21, p. 541–547, 1983. 73

[187] R. Jain, K. P. Surjya, and B. S. Singh, Numerical modeling methodologies for friction stir welding process. Woodhead Publishing Reviews: Mechanical Engineering Series, Butterworth-Heinemann, 2017. 73

[188] M. Smith, ABAQUS/Standard User's Manual, Version 6.9. United States: Dassault Systèmes Simulia Corp, 2009. xix, 74, 77, 108, 118

[189] M. E. Barkey and Y.-L. Lee, Chapter 8 - Strain-Based Multiaxial Fatigue Analysis. Butterworth-Heinemann, 2012. 74

[190] R. Riva, Essais de flexion 4 lignes sur cellules PV - Série 4. Livrable interne, September 2018. 75

[191] L. Zhao, A. Maynadier, and D. Nelias, "Stiffness and fracture analysis of photovoltaic grade silicon plates," International Journal of Solids and Structures, vol. 97-98, pp. 355–369, 2016. xvii, 76, 77

[192] W. Weibull, "A Statistical Distribution Function of Wide Applicability," ASME Journal of Applied Mechanics, vol. 18, pp. 293–297, 1951. 78

[193] R. A. Fisher and E. J. Russell, "On the mathematical foundations of theoretical statistics," Philosophical Transactions of the Royal Society of London, vol. 222, no. 594-604, pp. 309–368, 1922. 79

[194] A. Khalili and K. Kromp, "Statistical properties of Weibull estimators," Journal of Materials Science, vol. 26, no. 594-604, pp. 6741–6752, 1991. 79

[195] STANDARD ASTM C 1239-07, Reporting Uniaxial Strength Data and Estimating Weibull Distribution Parameters for Advanced Ceramics. ASTM, 2007. xxi, 79, 80

[196] A. Salahouelhadj and M. Gonzalez, "CTE measurements for 3D package substrates using Digital Image Correlation," in Proceedings of the 17th International Conference on Thermal, Mechanical and Multi-Physics Simulation and Experiments in Microelectronics and Microsystems, pp. 1–6, 2016. 80

[197] P. Bing, X. Hui-min, H. Tao, and A. Asundi, "Measurement of coefficient of thermal expansion of films using digital image correlation method," Polymer Testing, vol. 28, no. 1, pp. 75–83, 2009.

[198] Y. Wang and W. Tong, "A high resolution DIC technique for measuring small thermal expansion of film specimens," Optics and Lasers in Engineering, vol. 51, no. 1, pp. 30–33, 2013. 80

[199] A. Savitzky and M. J. E. Golay, "Smoothing and differentiation of data by simplified least squares procedures," Analytical Chemistry, vol. 36, no. 8, pp. 1627–1639, 1964. 83, V

[200] T. A. Instruments, Performing MDSC Heat Capacity Calibration. Manuel, 2006. 83

[201] L. Rivière, Analyse des mécanismes de conduction thermique dans les composites structuraux PEEK/particules submicroniques d'argent. PhD thesis, Thése de l'Université Paul Sabatier - Toulouse III, 2016. 84

[202] F. Kaule, M. Pander, M. Turek, M. Grimm, E. Hofmueller, and S. Schoenfelder, "Mechanical damage of half-cell cutting technologies in solar cells and module laminates," in AIP Conference Proceedings, vol. 1999, p. 020013, August 2018. 96, 123, 157

[203] L. Theunissen, B. Willems, J. Burke, D. Tonini, M. Galiazzo, and A. Henckens, "Electrically conductive adhesives as cell interconnection material in shingled module technology," AIP Conference Proceedings, vol. 1999, no. 1, p. 080003, 2018. 97

[204] I. Rahmoun, J.-L. Bouvard, A. Derrier, and P.-O. Bouchard, "Modeling of the lamination process: impact of behavior laws and design of photovoltaic module component," Renewable Energy, 2022. 106

[205] S. Dietrich, M. Pander, M. Sander, M. Ebert, and J. Bagdahn, "Introducing a reliability concept based on probabilistic material data of glass for PV modules," in Proceedings of the 26th European Photovoltaic Solar Energy Conference and Exhibition, 09 2011. 123

[206] I. Rahmoun, T. Le Carre, B. Chambion, E. Mofakhami, A. Derrier, J.-L. Bouvard, and P.-O. Bouchard, "Enabling measurement of PV module curvature: Towards characterization of thermomechanical residual stresses," in Proceedings of the 38th

European Photovoltaic Solar Energy Conference and Exhibition, pp. 864 – 869, November 2021. xix, xx, xxi, 130, 132, 133, 137, 138, 139, 140, 141

[207] S. P. Timošenko and S. Woinowsky-Krieger, Theory of Plates and Shells. New York: Engineering Societies Monographs, McGraw-Hill, 2nd reissued ed., 1987. 130

[208] SEMI M1-0302, Specifications for Polished Monocrystalline Silicon Wafers. Semi, 2001. 131

[209] A. J. Beinert, M. Imm, J. Benick, F. Becker, S. Seitz, M. Heinrich, O. Paul, S. W. Glunz, J. Aktaa, U. Eitner, and H. Neuhaus, "Silicon solar cell–integrated stress and temperature sensors for photovoltaic modules," Progress in Photovoltaics: Research and Applications, vol. 28, no. 7, pp. 717–724, 2020. 153

[210] OriginPro, "Algorithms (smooth)." `https://www.originlab.com/doc/Origin-Help/Smooth-Algorithm#:~:text=The%20Savitzky-Golay%20method%20The%20Savitzky-Golay%20method%20performs%20a,the%20value%20of%20the%20polynomial%20at%20position%20i.`, 2022. V, VI

Appendix A

Generalized Maxwell model - Prony series

The following table display the Prony series terms of each material. These Prony series terms are calculated based on the fitting curves using Generalized Maxwell model presented in Section 3.1.3. Two shift functions - WLF and Arrhenius - were chosen to represent the TTS depending over the large range of temperature for encapsulant TPO-A and EVA, and backsheets TPT and PP. While WLF shift function was used for ECA A1 and A2.

Table A.1: The parameters of the Generalized Maxwell viscoelastic model: Prony pairs, WLF and Arrhenius constants

	TPT		**PP**		**TPO-A**		**EVA**		**ECA-A1**		**ECA-A2**	
T_{ref}(°C)	110		20		20		20		-30		85	
C_1	53.92		48.99		100		54.66		50.65		64.3758	
C_2(°C)	300		200		293.87		159.73		288.39		700	
T_{ref}(°C)	110		20		20		20		-		-	
E(J/mol)	131 964.8		107 093.69		116 948.65		125 886.97		-		-	
G_0(MPa)	1721.45		1755.75		577.69		580.23		6537.53		3388.62	
	τ_i	g_i	τ_i	g_i	τ_i	g_i	τ_i	g_i	τ_i	g_i	τ_i	g_i
	6.57E-30	1.95E-01	2.43E-20	6.65E-02	2.08E-22	8.44E-02	3.23E-23	7.86E-02	2.29E-15	1.24E-01	1.18E-19	6.27E-02
	5.66E-27	6.70E-02	6.41E-19	4.12E-02	7.60E-21	5.42E-02	1.29E-21	4.93E-02	5.14E-14	4.05E-02	1.24E-18	2.20E-02
	2.93E-24	4.60E-02	1.03E-17	4.78E-02	1.71E-19	5.45E-02	3.10E-20	5.61E-02	7.97E-13	4.34E-02	9.56E-18	2.26E-02
	1.52E-21	3.42E-02	1.45E-16	4.79E-02	3.58E-18	6.66E-02	6.76E-19	6.86E-02	1.10E-11	3.71E-02	6.66E-17	2.09E-02
	7.07E-19	3.89E-02	2.03E-15	4.33E-02	6.26E-17	8.78E-02	1.26E-17	8.90E-02	1.47E-10	3.70E-02	4.51E-16	1.90E-02
	2.43E-16	4.83E-02	2.82E-14	4.23E-02	8.39E-16	1.10E-01	1.78E-16	1.14E-01	1.88E-09	3.52E-02	3.05E-15	1.94E-02
	6.29E-14	5.27E-02	3.63E-13	4.41E-02	8.54E-15	1.19E-01	1.85E-15	1.23E-01	2.34E-08	3.40E-02	2.02E-14	1.95E-02
	1.35E-11	5.11E-02	4.21E-12	4.43E-02	7.03E-14	1.14E-01	1.54E-14	1.20E-01	2.82E-07	3.61E-02	1.32E-13	2.01E-02
	2.54E-09	4.92E-02	4.81E-11	3.95E-02	5.17E-13	9.77E-02	1.13E-13	1.01E-01	3.14E-06	3.98E-02	8.32E-13	2.23E-02
	3.96E-07	5.08E-02	5.56E-10	3.71E-02	3.79E-12	7.32E-02	8.13E-13	7.68E-02	3.19E-05	4.52E-02	5.08E-12	2.31E-02
	4.55E-05	5.51E-02	6.08E-09	3.63E-02	3.04E-11	4.93E-02	6.23E-12	5.15E-02	2.68E-04	5.64E-02	3.01E-11	2.52E-02
	3.67E-03	5.75E-02	6.31E-08	3.52E-02	2.78E-10	3.08E-02	5.51E-11	2.99E-02	1.83E-03	5.86E-02	1.73E-10	2.65E-02

Continued on next page

Table A.1 – continued from previous page

τ_i	g_i	τ_i	g_i	τ_i	g_i	τ_i	g_i	τ_i	g_i	τ_i	g_i
2.18E-01	5.67E-02	6.31E-07	3.43E-02	2.89E-09	1.85E-02	5.90E-10	1.55E-02	1.11E-02	6.02E-02	9.44E-10	2.85E-02
1.05E+01	5.05E-02	5.93E-06	3.39E-02	3.31E-08	1.13E-02	7.26E-09	8.52E-03	6.48E-02	5.31E-02	4.87E-09	3.00E-02
4.74E+02	4.18E-02	5.27E-05	3.23E-02	4.05E-07	7.00E-03	9.63E-08	4.70E-03	3.96E-01	4.50E-02	2.46E-08	2.84E-02
2.31E+04	2.95E-02	4.61E-04	2.96E-02	5.21E-06	4.54E-03	1.38E-06	2.79E-03	2.55E+00	3.90E-02	1.26E-07	2.69E-02
1.62E+06	1.60E-02	4.04E-03	2.69E-02	7.01E-05	3.02E-03	2.13E-05	1.74E-03	1.72E+01	3.19E-02	6.43E-07	2.70E-02
2.44E+08	7.83E-03	3.57E-02	2.40E-02	9.91E-04	2.08E-03	3.23E-04	1.34E-03	1.20E+02	2.75E-02	3.18E-06	2.68E-02
2.28E+10	1.04E-02	3.20E-01	2.18E-02	1.45E-02	1.55E-03	4.80E-03	9.75E-04	8.33E+02	2.39E-02	1.52E-05	2.71E-02
1.03E+12	6.48E-03	2.88E+00	1.98E-02	2.13E-01	1.22E-03	7.07E-02	8.16E-04	5.74E+03	2.08E-02	6.98E-05	2.78E-02
4.81E+13	3.56E-03	2.56E+01	1.91E-02	3.03E+00	1.08E-03	1.01E+00	6.57E-04	3.88E+04	1.83E-02	3.10E-04	2.82E-02
		2.12E+02	1.85E-02	4.08E+01	9.57E-04	1.41E+01	5.81E-04	2.57E+05	1.62E-02	1.32E-03	2.90E-02
		1.77E+03	1.69E-02	5.29E+02	8.35E-04	1.90E+02	4.91E-04	1.66E+06	1.39E-02	5.31E-03	3.03E-02
		1.41E+04	1.70E-02	6.54E+03	7.82E-04	2.43E+03	4.65E-04	1.06E+07	1.21E-02	1.98E-02	3.16E-02
		1.07E+05	1.59E-02	7.72E+04	6.96E-04	2.87E+04	4.34E-04	6.54E+07	1.04E-02	6.87E-02	3.26E-02
		8.13E+05	1.50E-02	8.80E+05	6.18E-04	3.12E+05	4.02E-04	3.95E+08	8.76E-03	2.26E-01	3.33E-02
		5.87E+06	1.47E-02	9.66E+06	5.74E-04	2.77E+06	4.34E-04	2.36E+09	7.17E-03	7.13E-01	3.22E-02
		4.04E+07	1.37E-02	1.05E+08	4.85E-04	2.27E+07	3.46E-04	1.39E+10	5.77E-03	2.15E+00	3.14E-02
		2.78E+08	1.27E-02	1.16E+09	4.14E-04	2.05E+08	2.72E-04	8.12E+10	4.45E-03	6.13E+00	3.19E-02
		1.89E+09	1.18E-02	1.23E+10	4.04E-04	1.81E+09	2.61E-04	4.74E+11	3.29E-03	1.65E+01	3.22E-02
		1.27E+10	1.08E-02	1.24E+11	3.56E-04	1.51E+10	1.95E-04	2.80E+12	2.16E-03	4.26E+01	2.87E-02
		8.47E+10	9.91E-03	1.21E+12	3.09E-04	1.24E+11	1.71E-04	1.75E+13	1.55E-03	1.09E+02	2.76E-02
		5.62E+11	9.00E-03	1.16E+13	2.96E-04	1.01E+12	1.47E-04	1.25E+14	6.96E-04	2.83E+02	2.17E-02

Continued on next page

Table A.1 – continued from previous page

τ_i	g_i	τ_i	g_i	τ_i	g_i	τ_i	g_i	τ_i	g_i	τ_i	g_i
		3.73E+12	8.12E-03	1.09E+14	2.47E-04	7.51E+12	1.09E-04	9.17E+14	7.60E-04	7.54E+02	2.16E-02
		2.48E+13	7.30E-03	1.01E+15	2.17E-04	4.81E+13	1.11E-04	7.33E+15	2.28E-04	2.10E+03	1.42E-02
		1.65E+14	6.54E-03	8.96E+15	2.12E-04					6.20E+03	1.35E-02
		1.10E+15	5.83E-03	7.62E+16	1.71E-04					1.97E+04	6.12E-03
		7.19E+15	5.27E-03	6.15E+17	1.55E-04					6.76E+04	6.44E-03
		4.60E+16	4.75E-03	4.65E+18	1.53E-04					2.58E+05	1.73E-03
		2.88E+17	4.21E-03	3.49E+19	1.29E-04					1.17E+06	2.16E-03
		1.74E+18	3.79E-03	2.58E+20	6.87E-05						
		1.03E+19	3.20E-03	1.56E+21	1.43E-04						
		6.26E+19	2.66E-03	9.18E+21	5.76E-05						
		4.20E+20	2.19E-03								
		3.03E+21	2.16E-03								
		1.15E+22	3.40E-03								

Appendix B

Savitzky-Golay smoothing method for CTE calculation

The CTE measurement using DIC technique described in Section 3.4.1 showed that the thermal strains for some materials - for instance encapsulant TPO-A, ECAs and backsheet TPT- were not linear. Thus, a parabolic fit was not suitable for CTE calculation. Therefore, the smoothing Savitzky-Golay method [199] was adopted to calculate CTE of these materials.

The Savitzky-Golay smoothing method performs a polynomial regression to input points denoted $\{f_i \mid i = 1,2,\ldots,\mathrm{N}\}$ within a moving window. Then, the output smoothed data points g_i denoted $\{g_i \mid i = 1,2,\ldots,\mathrm{N}\}$ are computed as the value of the polynomial at position i from $\{f_m \mid i - floor(npts/2) < m < i + floor(npts/2)\}$ [210].

where $npts$ is the value of the points of window variable and m is the number of smoothed data.

First, the thermal strain curves are smoothed using the Savitzky-Golay method. Polynomials of order 2 have been used for polynomial regression. The smoothed curves for each sample of the tested materials are shown in Figure B.1.

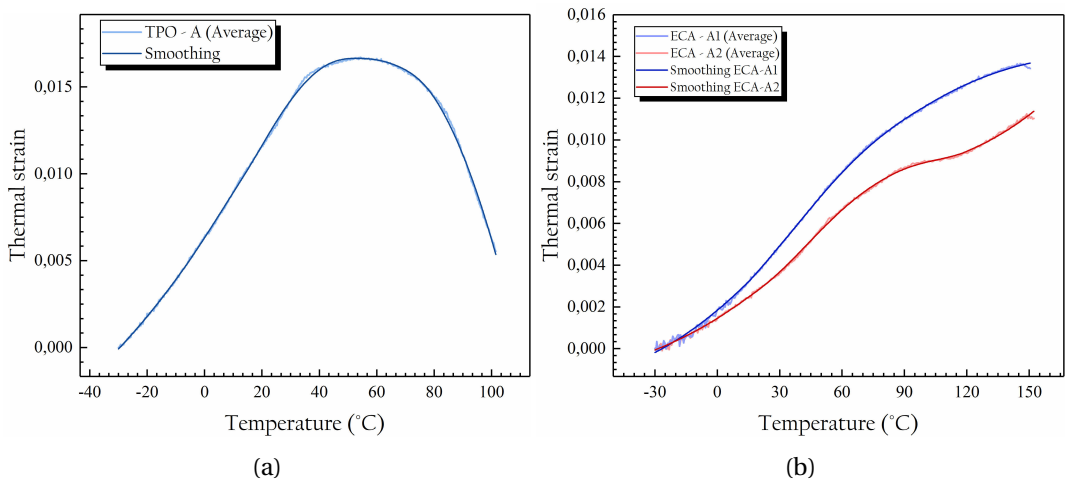

Figure B.1: Thermal strain and smoothing of curves using the Savitzky-Golay method of (a) encapsulant TPO-A and (b) ECAs A1 and A2

Afterwards, the evolution of the CTE with respect to temperature is deduced from the first order derivative of these smoothed curves. OriginPro software [210] was used to perform this calculations. Figure B.2 represents the CTE measurements for the TPO-A encapsulant and the A1 and A2 ECAs. The analysis of results were detailed in Section 3.4.1.

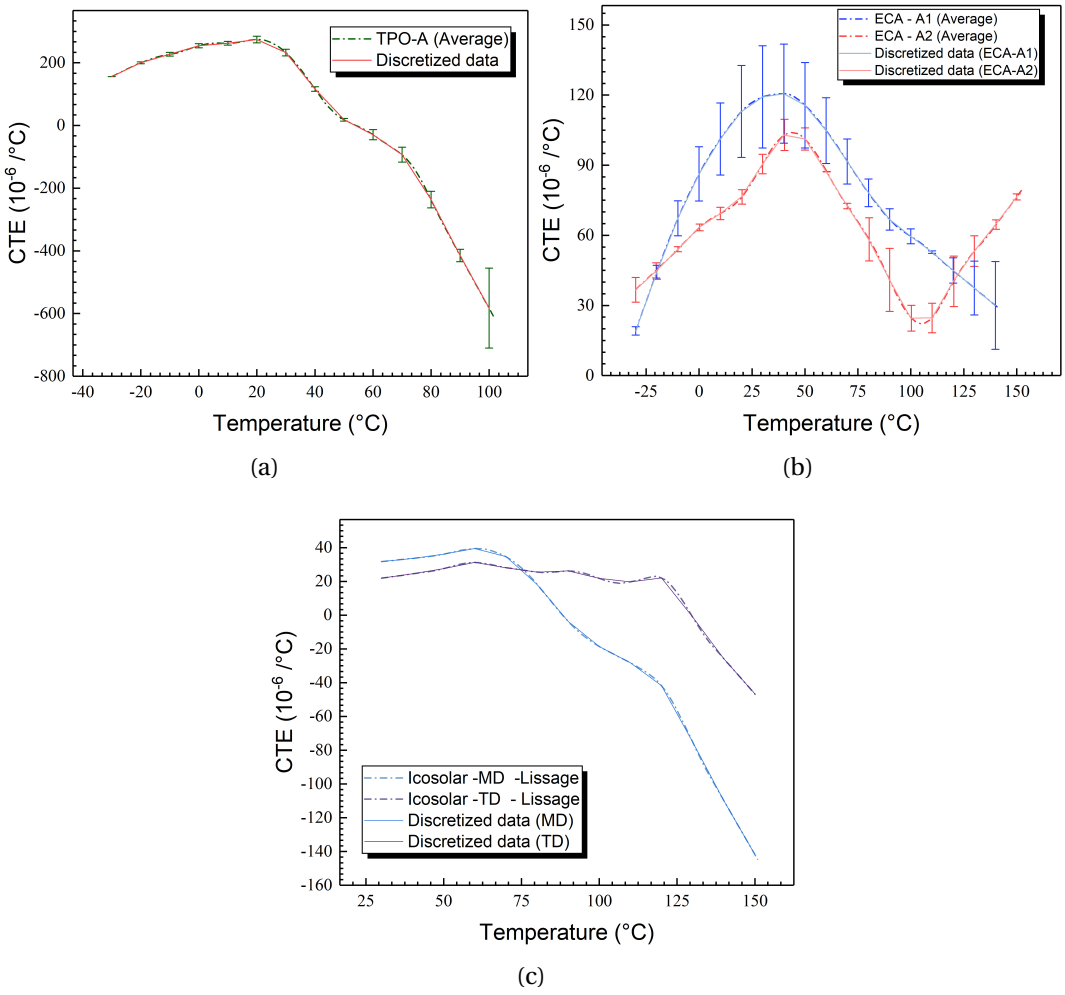

Figure B.2: Coefficient of thermal expansion (CTE) of (a) encapsulant TPO-A, (b) ECAs A1 and A2, and c backsheet TPT

For materials with linear thermal expansion (solar cell, backsheet PP, and copper ribbon), the CTE is calculated using the following equation as described in Section 3.4.1:

$$\alpha_{th} = \frac{\partial \varepsilon_{\text{th}}}{\partial \text{T}} = c_1 + 2c_2\text{T} + 3c_3\text{T}^2 \tag{B.1}$$

The coefficients used to calculate the CTE for these materials are summarized in Table B.1. However, for the other materials that have a non-linear CTE curve, and calculated by the Savitzky-Golay smoothing method, discretized data based on the raw data are used in numerical model directly to ensure good accuracy of the thermal behavior of the materials.

Coefficient		$c_1(1/°C)$	$c_2((1/°C)^2)$	$c_3((1/°C)^3)$
Solar cell	MD	2.001E-06	4.276E-6	-
	TD	1.640E-06	7.279E-09	-
PP	MD	6.399E-05	1.396e-07	4.490E-10
	TD	7.821E-05	7.706E-09	9.277E-10
Copper ribbon		1.232E-05	2.325E-08	-

Table B.1: Coefficient of thermal expansion fit for PV module components with linear CTE

Temperature °C	CTE $\alpha_{th} \times 10^{-6}(1/°C)$				
	TPO-A	ECA-A1	ECA-A2	TPT	
				MD	TD
-30	155.78	19.13	36.71	-	-
-20	199.78	44.23	45.04	-	-
-10	226.91	67.29	54.07	-	-
0	254.27	86.27	63.39	-	-
10	262.16	101.20	69.34	-	-
20	274.28	112.99	76.46	-	-
30	232.40	119.24	90.52	31.69	21.87
40	115.98	120.62	102.96	33.63	24.44
50	18.21	115.67	101.20	36.14	27.56
60	-29.69	104.83	87.21	39.41	31.19
70	-93.36	91.58	72.54	34.64	28.11
80	-236.72	78.18	58.24	18.26	25.53
90	-414.76	66.81	40.92	-3.66	26.27
100	-582.73	59.55	24.56	-18.60	21.75
110	-	52.83	24.64	-28.23	19.71
120	-	44.97	40.29	-41.77	22.10
130	-	37.43	53.23	-75.18	-1.17
140	-	29.97	64.59	-109.79	-25.75
150	-	-	76.44	-141.81	-46.69

Table B.2: Coefficient of thermal expansion for PV module components with non-linear CTE

RÉSUMÉ

Les modules photovoltaïques (PV) sont constitués de couches photovoltaïques actives (Silicium, passivation), de couches d'encapsulation protectrice (polymères) et de plaques de verre. La performance et la durée de vie des modules PV dépendent en partie de leur capacité à résister à différentes contraintes environnementales, liées aux phénomènes thermomécaniques, physiques, chimiques et/ou électriques. Dans le cadre de ce travail, nous nous intéresserons plus particulièrement aux contraintes résiduelles induites lors de la fabrication. Celle-ci comporte l'interconnexion électrique entre les cellules PV du module, par soudage ou collage de lignes conductrices, et l'encapsulation protectrice par des couches de polymères et de verre par le procédé de lamination (pressage à chaud). Ces contraintes résiduelles peuvent être à l'origine de défaillances observées sur les modules (délamination, fissure des cellules, rupture d'interconnexions…etc.), soit dès la fabrication soit, en s'ajoutant aux contraintes de service, au cours de la vie des modules PV. L'enjeu de ce travail de thèse sera de modéliser les procédés d'encapsulation et d'interconnexion des cellules afin de mieux comprendre leur influence sur les principales défaillances observées sur les modules.

MOTS CLÉS

Module photovoltaique, Procédé de lamination, Procédé d'interconnexion, Modélisation thermomécanique, Contraintes résiduelles

ABSTRACT

Photovoltaic (PV) modules consist of active photovoltaic layers (Silicon, passivation), protective encapsulation layers (polymers) and glass plates. The performance and service life of PV modules depends on their ability to withstand various environmental constraints related to thermomechanical, physical, chemical and / or electrical phenomena. In the context of this work, we will focus on the residual stresses induced during manufacturing. This comprises the electrical interconnection between the PV module cells, by welding or adhesive bonding of conductive lines, and the protective encapsulation by layers of polymers and glasses using lamination process (hot pressing). The induced residual stresses can be at the origin of failures observed on the modules (delamination, cell cracking, breakage of interconnections ...etc.), either at the manufacturing stage or during the lifetime of the modules due to the service constraints. The objective of this PhD thesis will be to model the encapsulation and interconnection processes of cells to better understand their influence on the main failures observed on the modules.

KEYWORDS

Photovoltaic module, Lamination process, Interconnection process, Thermomechanical modeling, Residual stresses